LIQUID-CRYSTAL TUNABLE FILTER SPECTRAL IMAGING FOR DISCRIMINATION BETWEEN NORMAL AND NEOPLASTIC TISSUES IN THE BRAIN

By

Steven Charles Gebhart

Dissertation

Submitted to the Faculty of the

Graduate School of Vanderbilt University

in partial fulfillment of the requirements

for the degree of

DOCTOR OF PHILOSOPHY

in

Biomedical Engineering

December, 2006

Nashville, Tennessee

Approved:

Anita Mahadevan-Jansen

E. Duco Jansen

Robert L. Galloway

Reid C. Thompson

Wei-Chiang Lin

Tuan Vo-Dinh

To my sister Julie,

who watches over, protects, and guides me from heaven.

I love you and miss you every day.

To the rest of my family,

for their patience and unending support

during this journey of discovery.

ACKNOWLEDGEMENTS

First, I would like to acknowledge the members of my PhD committee for their time and sacrifice throughout my 7-year graduate school tenure. I would like to thank Bob Galloway for originally attracting me to Vanderbilt, for his mentorship during my Master's research, for housing me in his lab, and for always being available for advice or a chat about Duke basketball. I would like to thank Wei-Chiang Lin for all of his tutelage and guidance during my early days in the biomedical optics lab; you single-handedly allowed me to ascend the learning curve more rapidly than would have otherwise been possible. I would like to thank Duco Jansen for his mentorship during both phases of my research and for his continual willingness to hear out and help flesh out my crazy research or data analysis ideas. I would like to thank Reid Thompson for his perpetual excitement about participating in this project and utmost for his patience in the operating room as I painstakingly acquired my spectral imaging data; he represents the epitome of what a biomedical engineer hopes for in a clinical collaborator. I would like to thank Tuan Vo-Dinh for his willingness to partner with our lab during the early days of this project, for inviting me to spend a week in his lab to conduct filter comparison studies, and for his continued involvement in the fulfillment of this research. Finally, I would like to thank my adviser Anita Mahadevan-Jansen for giving me the opportunity to train under her tutelage, not least of which was painstakingly teaching me how to write as a scientist should, and more importantly for pushing me to pursue and complete a project of which I can be truly proud.

I would be remiss if I did not acknowledge all of my friends and co-workers inside and outside of Vanderbilt, in the biomedical optics and SNARL labs, in the nursing staff of the neurosurgery department, in the physics machine shop, and in the biomedical engineering faculty and front office. You each contributed to the success of this research project in various ways but even more-so helped me to grow personally as well as professionally. Whether doing homework for classes, taking undergrads out for drinks after completion of their instrumentation projects, playing soccer (especially at Ed and Cathy's wedding), going to dinner at conferences, hosting BBQs and Halloween parties, dominating intramural sports, or simply relaxing with a beer after a long week of work, you have all made my seven years at Vanderbilt more enjoyable than graduate school probably ought to be and I take a host of lifelong memories with me because of them.

Foremost, I would like to acknowledge my wonderful family for their unending patience, unwavering support, and their ability to push me at every level of my education, in graduate school simply by constantly asking the one question that every graduate student dreads, “So how much longer until you’re finished?” I am the most blessed person in the world to have a close family which I deeply love. I never could have achieved this without them; they share this achievement with me.

TABLE OF CONTENTS

Appendix

LIST OF TABLES

LIST OF FIGURES

CHAPTER I

INTRODUCTION

Motivation

The American Cancer Society estimates that 18,820 new cases of and 12,820 deaths from malignant brain tumors will be reported in the United States in 2006 with a five-year survival rate of 33% [1]. The average survival time for adults with infiltrating glioblastoma multiforme is only 12-18 months with a 5.1% three-year survival rate [2]. The current three-prong attack for brain tumor treatment is surgical resection of maximum tumor volume followed by radiation and chemotherapy. However, the blood-brain barrier often prevents cancer-targeting drugs from reaching the tumor, rendering chemotherapy ineffective; and while surgery and radiation therapy can effectively treat the tumor core, the fingerlike protrusions at the margins of infiltrating tumors make treating the entire tumor near impossible. The extent of surgical margin resection for both low-grade and high-grade tumors has been repeatedly correlated to patient quality of life and mortality [3-7], but is currently limited by the surgeon's ability to discriminate between normal tissue and tumor margins during surgery. To this end, tools and techniques are constantly being developed to help locate the tumor and identify its margins during a resection procedure, to maximize tumor mass resection without sacrificing neurologic function.

Current methods for intra-operative tumor localization are limited in their ability to differentiate normal brain from tumor margins. Visual inspection can be highly subjective and inconclusive, especially when dealing with low-grade tumors or diffuse tumor margins which often resemble normal neural tissue. On-site pathology is more histologically reliable but is expensive, is far from real-time, and does not spatially demarcate margin extent. Three-dimensional surgical navigation with x-ray computed tomography (CT) or magnetic resonance imaging (MRI) is extremely useful in tumor localization and debulking [8, 9] but limited in its margin sensitivity, as tumor cells have been found outside of delineated image margins in many documented cases [10]. Furthermore, deformation of brain tissue subsequent to craniotomy, retraction, and debulking by as much as a centimeter degrades the accuracy of surgical navigation based upon pre-operative images [11, 12]. Real-time intra-operative ultrasound overcomes limitations from brain deformation and can detect tumor margins because brain

tumors are usually hyperechoic relative to normal tissue, but it is less likely to be able to differentiate tumor from peritumoral edema, which is also hyperechoic [13, 14] and poor image resolution hinders correlation between image features and surgical position. Due to the inherent limitations of these adopted tumor visualization techniques, significant residual tumor cells frequently remain after resection [3, 5], emphasizing the need to develop an objective, on-site, real-time imaging system that is capable of detecting the margins of brain tumors with high sensitivity. It should be noted that such a system is not a replacement of current existing techniques; it will fill a significant need existing in current practice of brain tumor resection.

Statement of Problem

Optical spectroscopy has the capability to provide real-time, on-site detection of tissue changes associated with the progression of disease. Over the past 20 years, the investigation of optical spectroscopy to differentiate between normal and diseased tissues has grown tremendously and been extended to a host of bodily tissues [15-17], with our research group at the forefront of applying autofluorescence and diffuse reflectance spectroscopy for tissue discrimination in the brain [18-20]. However, the majority of these investigations employ fiber-optic probe-based spectroscopy systems designed for retrospective, proof-of-principle studies aimed to correlate spectral features to histopathological diagnoses of sample biopsies at single-point interrogation sites. While these clinical trials are sufficient to demonstrate the capability of optical biopsy to detect tissue changes with disease, similar to on-site pathology, probe-based spectroscopy provides no information as to the spatial extent of disease and therefore is of limited clinical use for therapy guidance.

The extension of probe-based spectroscopy to spectral imaging seeks to overcome this limitation by acquiring spectral information at every point within a two-dimensional field of view on the tissue surface, thereby giving an objective, comprehensive snapshot of tissue pathology in real time. To realize significant utility as a therapy guidance tool, spectral imaging must be capable of rapid image acquisition with a convenient interface for seamless integration into the clinical environment. The effects of the transition to imaging on measured spectral lineshape must be investigated to determine if spectral differences between tissue types observed with probe-based spectroscopy are conserved. Finally, the accuracy with which spectral imaging

is capable of differentiating between normal and tumor tissues in the brain must be assessed, most notably at the tumor margins.

Overview

The objectives of the original research proposal were designed to translate existing fiber-optic probe-based spectroscopy to spectral imaging capable of spatially resolved, macroscopic tissue interrogation *in vivo*. While the development of spectral imaging technology is not novel in its own right, its clinical application using combined tissue autofluorescence and diffuse reflectance for intra-operative brain tumor core and margin detection and surgical resection guidance remains unaccomplished. The primary goal of my research project was to assess the efficacy of using spectral imaging to rapidly and accurately demarcate tumor margins during surgery. As outlined above, successful translation from spectroscopy to imaging requires seamless integration of spectral imaging into the clinical environment, thorough investigation into the effects of such a translation on fluorescence and diffuse reflectance lineshape, and demonstration of high diagnostic accuracy of tumor margins from spectral imaging data.

Chapter 2 provides background information to understand the biology and pathology of brain tumors, their growth and development, and the current techniques in their diagnosis and treatment. With emphasis on how optical biopsy methods overcome limitations in current tumor localization techniques, the principles behind optical spectroscopy and its application to brain tissue discrimination are summarized. The chapter concludes with a description of the impetus to extend optical spectroscopy to spectral imaging, the challenges inherent to such a translation, and the selection of and principles behind liquid-crystal tunable filter spectral imaging which is used throughout my research project.

Chapter 3 describes the *in vitro* measurement of absorption and reduced scattering spectra for white matter, gray matter, and glioma samples. The mean optical property spectra are correlated to diffuse reflectance spectral features from probe-based spectroscopy and are used to develop gelatin-based phantoms which mimic human brain tissues in chapter 4 and to provide practical soft-tissue optical property limits for the investigations in chapters 5 and 6.

Building upon the preliminary results of our research group in brain tissue diagnosis using probe-based spectroscopy, chapter 4 describes the design, construction, and testing of a liquid-crystal tunable filter spectral imaging system for clinical use in the operating room. The

system is thoroughly characterized in terms of linearity, field of view, resolution, and sensitivity and functionally tested in terms of image acquisition time and its capability to spectrally discriminate between phantom and brain tissues *in vitro* and *in vivo*.

Chapters 5 and 6 investigate the potential effects of the translation from fiber-optic probe-based spectroscopy to non-contact spectral imaging on measured spectral lineshape. Upon the discovery of a significant disparity between probe-based and imaging lineshapes in fluorescence and diffuse reflectance spectra, the disparity is definitively attributed to inherent differences in the excitation-collection geometry of the two systems. The behavior of the lineshape disparity is subsequently investigated in terms of sample optical properties, incident excitation angle, and emission collection angles in chapter 5 and in terms of sample optical properties and the distribution of source-detector separation distances in chapter 6.

Ultimately, the capability of the spectral imaging system to intra-operatively differentiate glioma tissues from normal cortex was assessed clinically in a retrospective study in Chapter 7. Spectral features in imaging fluorescence and diffuse reflectance spectra are correlated to histopathological diagnoses of human brain tissue biopsies to determine discrimination sensitivity and specificity for brain tumor demarcation and utility for surgical resection guidance.

A summary of and conclusions from the dissertation as well as future directions for the research are outlined in chapter 8.

References

1. A. Jemal, et al, "Cancer statistics, 2006," CA Cancer J Clin **56**, 106-30 (2006).
2. C.B.T.R.o.t.U. States, "Primary Brain Tumors in the United States Statistical Report, 1998-2002 Years Data Collected," http://www.cbtrus.org, 2005-2006. Accessed on April 27, 2006.
3. M. Ammirati, et al, "Effect of the extent of surgical resection on survival and quality of life in patients with supratentorial glioblastomas and anaplastic astrocytomas," Neurosurgery **21**, 201-6. (1987).
4. M.C. Chamberlain and P.A. Kormanik, "Practical guidelines for the treatment of malignant gliomas," West J Med **168**, 114-20. (1998).
5. A. Kowalczuk, et al, "Quantitative imaging study of extent of surgical resection and prognosis of malignant astrocytomas," Neurosurgery **41**, 1028-36 (1997).
6. M.T. Selch, et al, "Gangliogliomas: experience with 34 patients and review of the literature," Am J Clin Oncol **21**, 557-64. (1998).

7. S.A. Toms, D.Z. Ferson, and R. Sawaya, "Basic surgical techniques in the resection of malignant gliomas," J Neurooncol **42**, 215-26. (1999).

8. R.J. Maciunas, *Interactive Image-Guided Neurosurgery*. 1993, Park Ridge, IL: American Association of Neurological Surgeons.

9. R.J. Maciunas, *Minimally Invasive Therapy of the Brain*, ed. A.D. Salles and R. Lufkin. 1997, New York: Thieme Medical Publishers, Inc.

10. P.D. LeRoux, et al, "A comparison between preoperative magnetic resonance and intraoperative ultrasound tumor volumes and margins," J Clin Ultrasound **22**, 29-36. (1994).

11. D.L. Hill, et al, "Measurement of intraoperative brain surface deformation under a craniotomy," Neurosurgery **43**, 514-26; discussion 527-8. (1998).

12. N.L. Dorward, et al, "Postimaging brain distortion: magnitude, correlates, and impact on neuronavigation," J Neurosurg **88**, 656-62. (1998).

13. L.M. Auer and V.V. Velthoven, *Intraoperative Ultrasound Imaging in Neurosurgery: Comparison with CT and MRI*. 1990, Berlin: Springer-Verlag.

14. J.E. Knake, et al, "Neurosurgical applications of intraoperative ultrasound," Radiological Clinics of North America **23**, 73-90 (1985).

15. R. Richards-Kortum and E. Sevick-Muraca, "Quantitative optical spectroscopy for tissue diagnosis," Annu Rev Phys Chem **47**, 555-606 (1996).

16. N. Ramanujam, "Fluorescence spectroscopy of neoplastic and non-neoplastic tissues," Neoplasia **2**, 89-117. (2000).

17. A. Mahadevan-Jansen and R. Richards-Kortum, "Raman spectroscopy for the detection of cancers and precancers," Journal of Biomedical Optics **1**, 31-70 (1996).

18. W.-C. Lin, et al, "In vivo brain tumor demarcation using optical spectroscopy," Photochem Photobiol **73**, 396-402. (2001).

19. W.-C. Lin, et al, "Brain tumor demarcation using optical spectroscopy; an in vitro study," J Biomed Opt **5**, 214-20. (2000).

20. S.A. Toms, et al, "Intraoperative optical spectroscopy identifies infiltrating glioma margins with high sensitivity," Neurosurgery **57**, 382-91 (2005).

CHAPTER II

OVERCOMING CURRENT LIMITATIONS IN BRAIN TUMOR MARGIN LOCALIZATION WITH OPTICAL BIOPSY

Neurobiology of Brain Tumors

Basic Neuroanatomy and Physiology

The central nervous system consists of the brain and spinal cord. Since the major goal of this dissertation is improved surgical guidance of tumor resection within the brain, this background will not involve information regarding the spinal cord and its associated tumors. The main parts of the brain which can be affected by tumors include the cerebrum, cerebellum, brain stem, and basal ganglia (Figure 1). The cerebrum is responsible for higher cognition, initiation of gross bodily movement, and interpretation of sensory information. The cerebrum primarily consists of white matter surrounded by an outer layer of gray matter, known as the cortex (Figure 1a). Gray matter consists of neuronal cell bodies which perform the information processing in the brain while the white matter consists of neuronal axons which transmit the information from the cortex to other areas of the brain or to the rest of the body. The thickness of the cortex generally varies between one and four millimeters. The cerebrum is divided laterally into two hemispheres which contain frontal (cognition, olfactory, speech, and gross bodily movement), parietal (somatosensory interpretation, written language), occipital (vision), and temporal

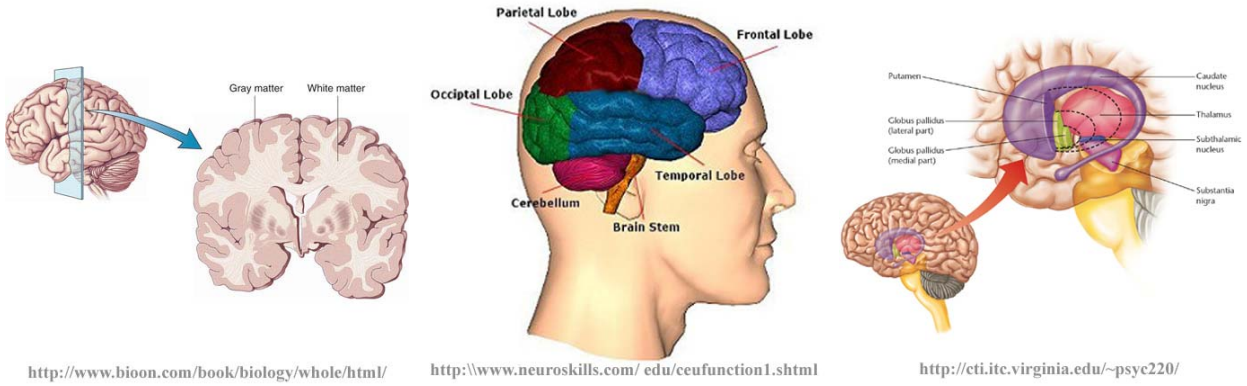

(a) **(b)** **(c)**

Figure 1. Gross neuroanatomy of the brain depicting the (a) cerebral lobes, cerebellum, and brain stem, (b) gray matter cortex and underlying white matter, and (c) basal ganglia.

(hearing, interpretation of verbal language) lobes (Figure 1b). The cerebellum (Figure 1b), located below the occipital lobes, between the temporal lobes, and behind the brainstem, controls somatic motor function such as muscle tone, coordination of movements, and maintenance of balance. The brain stem (Figure 1b) is located at the base of the brain where it connects to the spinal cord. It controls involuntary movements such as breathing and heartbeat and provides motor and sensory information for the head and neck via the cranial nerves. The basal ganglia (Figure 1c) are comprised of three regions of subcortical gray matter – the putamen, caudate, and globus pallidus – which serve to inhibit muscles during movement, carry out subconscious motor programs, and are affected in diseases such as Parkinson's disease and Hodgkin's chorea.

Other anatomical landmarks of the brain which can be afflicted with brain tumors or serve as topographical landmarks for their classification are the meninges, the tentorium cerebelli, and the cranial nerves (Figure 2). The meninges consist of three membranes – the dura mater (outermost), arachnoid (middle), and pia (innermost) – which surround the brain to serve as a capsule against infection (Figure 2a). While any of the three membranes can be the source of tumor development, tumors of the meninges (meningiomas) most frequently derive from the arachnoid membrane. The tentorium cerebelli is a fold of the dura mater which separates the cerebellum from the cerebral occipital and temporal lobes. Tumors located above the tentorium cerebelli which afflict the cerebral hemispheres are denoted supratentorial, whereas tumors

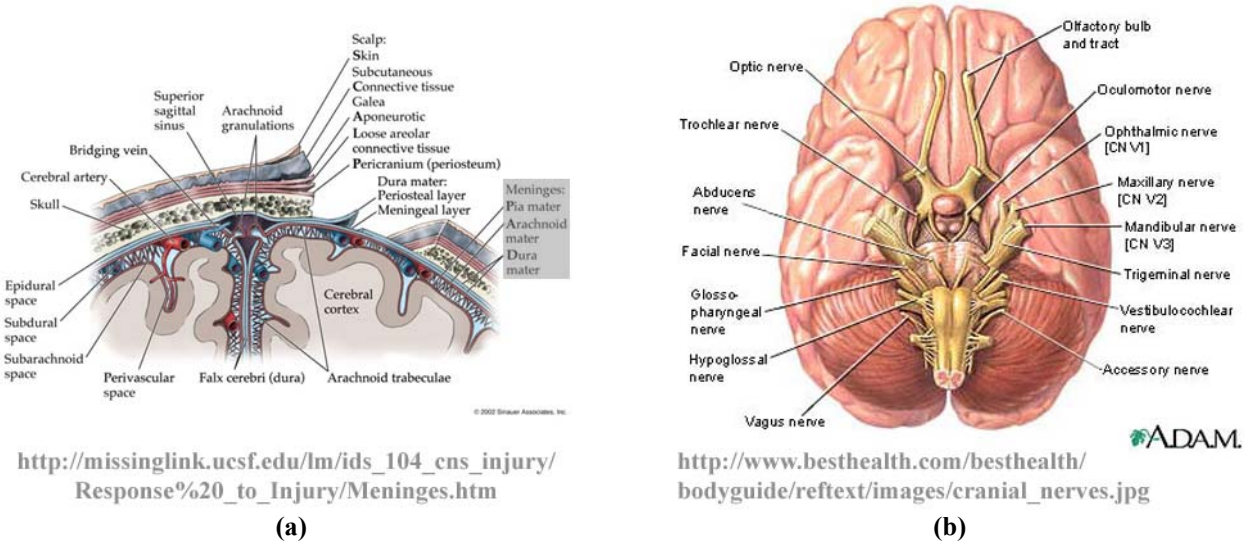

http://missinglink.ucsf.edu/lm/ids_104_cns_injury/Response%20_to_Injury/Meninges.htm

http://www.besthealth.com/besthealth/bodyguide/reftext/images/cranial_nerves.jpg

(a) **(b)**

Figure 2. Gross neuroanatomy of the brain depicting the (a) meninges and (b) cranial nerves.

below it which afflict the brainstem are denoted infratentorial. The cranial nerves (Figure 2b) transmit sensory information and signals to control motor movement for structures of the head and neck and can be the source of brain tumors which develop from the Schwann cells (schwannomas) that myelinate them.

Physiologically, different types of brain tumors are categorized by the cells from which they develop [1]. As will be discussed in detail in the next section, a large proportion of primary and primary malignant brain tumors develop from glial cells [3], of which there are three types:

- **Astrocytes** support and nourish neurons and supply phagocytic behavior to repair brain injury. Astrocytic proliferation following brain injury, known as gliosis, can be histologically confused with neoplastic transformation in a brain tumor.
- **Oligodendrocytes** produce myelin to sheath neuronal axons of the central nervous system and increase transduction velocities of neuronal signals.
- **Ependymal cells** line the ventricles of the brain and serve to circulate cerebrospinal fluid through the cerebrospinal fluid pathway.

While not an exhaustive list, other types of cells found within the central nervous system which can lead to brain tumor development are:

- **Neurons** receive and transmit electrical signals for communication between various areas of the brain and between the brain and the rest of the body.
- **Schwann cells** are similar to oligodendrocytes in that they myelinate neuronal axons but are limited to the cranial nerves.
- **Lymphocytes** serve to fight infection and while very few are found in the central nervous system, they can be the source of primary brain tumor development.

One of the most important physiologic structures of the central nervous system in terms of its impact on brain tumor diagnosis and treatment is the blood-brain barrier. The gaps between endothelial cells within the brain vasculature are smaller than elsewhere in the body, allowing free diffusion of gases such as oxygen and carbon dioxide and lipid soluble substances such as alcohol and nicotine, but preventing passage of most foreign molecules not essential for normal brain function. While blood-brain barrier minimizes the risk for brain injury due to foreign agents, it makes treating brain injury or disease more difficult since it blocks antibiotics such as penicillin used to fight infection. The blood-brain barrier can also negatively impact brain tumor diagnosis and treatment since exogenous contrast agents for various imaging modalities and

chemotherapy agents for tumor therapy are rendered ineffective. While high-grade brain tumors often compromise the blood-brain barrier, the breakdown is rarely complete, requiring higher doses of contrast or chemotherapeutic agents than necessary in other organs of the body, and the blood-brain barrier is usually intact in low-grade tumors and at the tumor margins.

Anatomy, Physiology, and Pathology of Brain Tumors

Brain tumors can develop from a single abnormal cell with the ability to reproduce rapidly and proliferate. While different brain tumor types display different characteristics, there are many common properties between them. As the tumor begins to develop and grow outward from the parent cell, the daughter cells closely resemble the size and shape of the original parent cell. But as more mutations are randomly incorporated in the cells' DNA, the cells begin to adopt various shapes and sizes which are often indicative of the type of tumor and the grade of the tumor can often be estimated by the resemblance to (or lack thereof) the derivative cell type. Despite irregular shapes and sizes, tumors often exhibit higher cell densities than normal tissue due to rapid cell replication. The final tumor stage often comes when additional genetic mutations turn the tumor malignant, which is followed by even more rapid proliferation and quick fatality of the host.

One of the most universal characteristics of cancer is its high metabolism for rapid cellular proliferation. To accommodate increased metabolism, tumors develop nucleocytoplasmic abnormalities such as mitotic figures (spindle fibres) on the cellular level and neovascularization on the gross level, evident by small, highly convoluted capillaries at the periphery of the tumor. However, when the tumor becomes too large for the small vessels to maintain, necrotic zones will develop at the tumor core while the outer edges of the tumor continue to feed and proliferate.

The architecture of brain tumors can vary from being well encapsulated, facilitating complete resection, to extending finger-like columns of tumor cells into the surrounding white and gray matter several centimeters from the tumor core, creating what are known as infiltrating tumor margins. While treatment of well-encapsulated benign tumors can be relatively straight-forward through surgical resection or radiation therapy, treating infiltrating malignant tumors is limited by the tradeoff between aggressive removal of the tumor core and margins and conservative resection to ensure minimal removal of normal brain tissue and prevent

neurological deficit for the patient. As will be discussed in greater detail in the next section, limitations in the ability to differentiate between normal and tumor margin tissue for margin localization during resection surgery often prompt neurosurgeons to adopt a more conservative resection strategy by removing the tumor core but leaving the margins intact, especially in regions of eloquent brain tissue (parenchyma).

Given the large number of central nervous system tumors, a complete description of every tumor type is impossible here. Tumors of the central nervous system can be separated into intracranial and intraspinal tumors. Since the targeted disease of this dissertation is brain cancer, this section will be limited to intracranial tumors, with a brief description of the most frequent types in adults. As mentioned previously, intracranial tumors can be topographically separated into supratentorial or infratentorial depending upon their location relative to the tentorium cerebelli and can be histologically separated as primary or secondary. Primary intracranial tumors derive from cells native to the central nervous system and are classified according to their derivative cell (Table 1). Secondary tumors develop due to metastases from cancers elsewhere in the body, accounting for 20-25% of intracranial tumors and most commonly deriving from cancers of the lung (44%), breast (10%), kidneys (7%), and alimentary tract (6%). For prognostic purposes, intracranial tumors are also classified according to their malignancy on a scale (grade

Table 1. Simplified histological classification of primary intracranial tumors. Reproduced from [1].

Histological elements normally present within the cranial cavity	Cellular Derivatives of the Neural Tube	Glial cells	Astrocytes	Astrocytomas
				Glioblastomas
			Oligodendrocytes	Oligodendrogliomas
			Ependymocytes	Ependymomas
				Choroid plexus papillomas
				Colloid cysts
		Neurons		Medulloblastomas
				Gangliogliomas
		Pinealocytes		Pineocytomas
				Pineoblastomas
	Cellular Derivatives of the Neural Crest	Schwann cells		Schwannomas
				Neurofibromas
		Arachnoid cells		Meningiomas
		Melanocytes		Melanomas
	Other Cells	Connective tissue cells		Sarcomas
		Reticuloendothelial cells		Reticulum-cell sarcomas
		Vascular cells		Hemangioblastomas
		Glomus jugulare cells		Glomus jugulare tumors
		Adenohypophyseal cells		Pituitary adenomas
Intracranial embryonal remnants	Ectodermal Derivatives			Craniopharyngiomas
				Cholesteatomas
	Notochord			Chordomas
	Adipose cells			Lipomas
	Germ cells			Germinomas
	Derived from 3 germ layers			Teratomas

I-IV) developed by the World Health Organization and as to whether they are parenchymatous, afflicting eloquent areas of the brain.

The most common intracranial tumors found in adults are:

- **Astrocytomas** are histologically benign tumors deriving from astrocytes which are susceptible to malignant change (anaplastic astrocytoma, glioblastoma). They comprise 9.8% of all primary intracranial tumors and 25% of gliomas [3].
- **Glioblastomas** are malignant, rapidly fatal, astrocytic tumors which arise from astrocytomas or *de novo*. They comprise 20.3% of primary intracranial tumors and 50.7% of gliomas [3]. The cerebral hemispheres, basal ganglia, and commissural pathways are sites of predilection. The tumors lack a capsule, resulting in rapid infiltration with possible meningeal invasion and high incidence of recurrence even after apparent total resection.
- **Oligodendrogliomas** are benign tumors arising from oligodendrocytes and are usually found in the cerebral hemispheres. They comprise 3.7% of primary intracranial tumors and 9.2% of gliomas [3]. The prognosis is regarded as relatively favorable but they can undergo malignant change.
- **Ependymomas** are benign tumors arising from ependymal cells and occur at any level of the ventricular system. They comprise 2.3% of primary intracranial tumors and 5.6% of gliomas [3]. They are well circumscribed but can easily metastasize within the central nervous system via the cerebrospinal fluid pathway and can undergo malignant change.

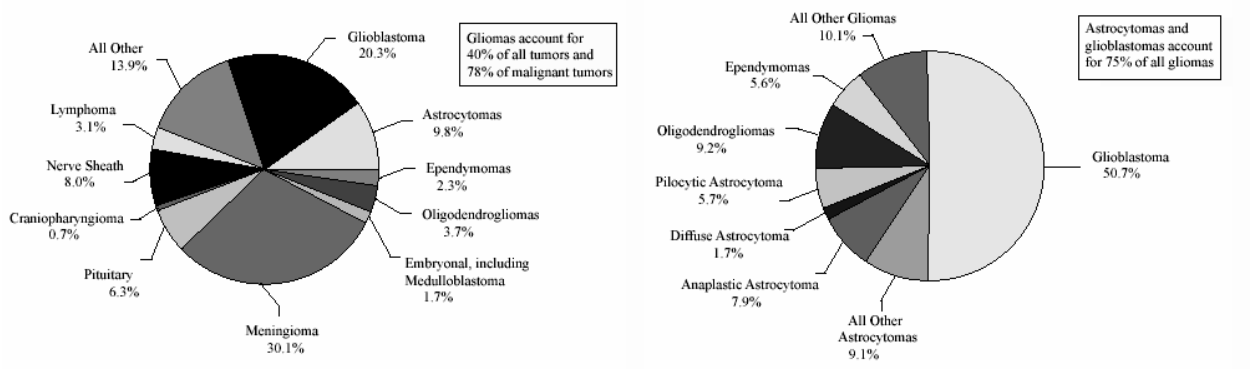

Figure 3. Distribution of all primary brain and CNS (a) tumors by histology and (b) gliomas by histology subtype. Reproduced from [3].

- **Meningiomas** are benign tumors originating from the meninges surrounding the brain, most often from arachnoidal cells. They comprise 30.1% of primary intracranial tumors and afflict females 2-fold more often than males [3]. Meningiomas can recur even after apparent total resection but remain histologically benign.
- **Schwannomas** are benign tumors arising from Schwann cells and are usually found on the cranial nerves, especially the vestibulocochlear (acoustic schwannoma) and facial nerves. Schwannomas comprise 8.0% of primary intracranial tumors [3] and may recur but remain histologically benign.
- **Pituitary tumors** arise in the pituitary gland and comprise 6.3% of primary intracranial tumors [3]. They are generally classified as functionally inactive (chromophobe) or hormone secreting, with several varieties depending upon the derivative cell type (somatotropic, corticotropic, melanotropic, thyrotropic, prolactin-secreting).

As will be described in greater detail in the next section, treatment of infiltrating gliomas is often ineffective due to limitations in the real-time differentiation between normal and tumor margin tissue during surgery to achieve complete tumor removal without sacrificing patient neurologic function. Given that gliomas represent 40% of primary intracranial tumors and 78% of those tumors which are malignant [3], improved glioma resection is a significant area of study in the field of neurosurgery. The research in this dissertation focuses on developing a real-time, objective imaging system to demarcate glioma margins and overcome the limitations in current margin localization techniques, which are outlined in the following section.

Current Methods in Brain Tumor Diagnosis and Treatment

Brain Tumor Diagnosis

Currently, routine tests for the sake of screening for central nervous system tumors do not exist. The majority of central nervous system tumors are diagnosed during doctor visits for tumor-related symptoms usually resulting from increased intracranial pressure subsequent to tumor growth. Increased pressure commonly causes headaches and seizures, but can also lead to nausea and vomiting. The types of symptoms rarely identify the type of tumor but can often

reflect its location. For example, tumors which afflict the basal ganglia may affect fine muscle movement while those of the brain stem may affect the cranial nerves and sensory or motor information in the head and neck. A positive side effect of symptomatic diagnosis is that tumors in more eloquent areas of the brain which must be treated early before malignant transformation are the first to present with visible signs and symptoms.

The standard procedure to determine tumor topography and histology is tomographic imaging followed by either stereotactic biopsy or biopsy during surgical resection. Tomographic imaging provides the location and extent of the tumor for radiation, surgical, and possible stereotactic biopsy guidance. Stereotactic biopsy and subsequent confirmed histology of the tumor can be incorporated into the treatment plan and contribute to patient prognosis.

The three most widely used modalities for brain tumor imaging are x-ray computed tomography (CT), magnetic resonance imaging (MRI), and positron emission tomography (PET) (Figure 4). X-ray CT and MRI give three-dimensional soft tissue information, x-ray CT in terms of relative absorption of x-rays and MRI in terms of the relative concentrations of protons, most often in the form of water. Magnetic resonance imaging is often preferred to x-ray CT for surgical planning because exogenous contrast agents such as gadolinium collect in brain tumors with a compromised blood-brain barrier and T2-weighted MR images highlight edematous zones which are often correlated with infiltrating tumor margins [4]. Neurosurgeons use the core and margin information and their proximity to eloquent brain tissue to determine the extent to which they plan to resect the tumor during surgery.

While x-ray CT and MRI provide tomographic images of brain anatomy, PET provides

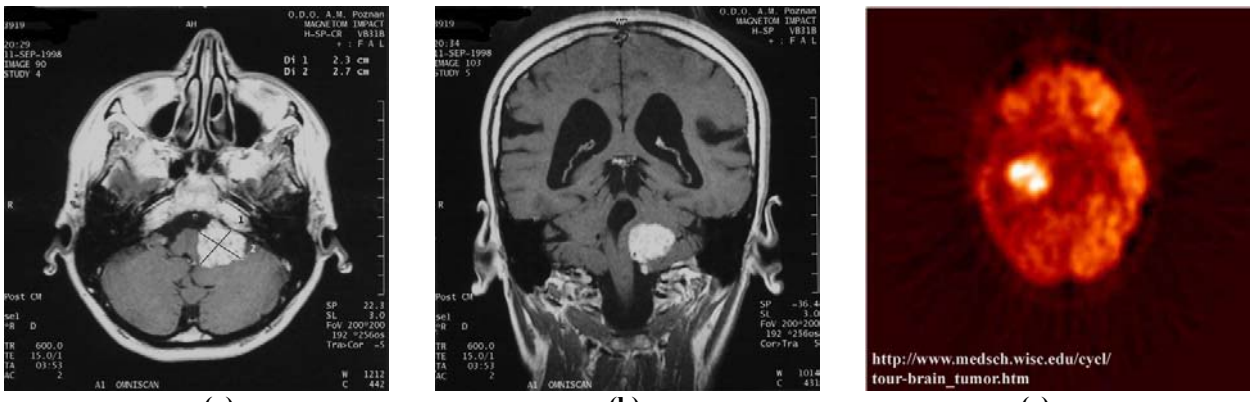

(a) **(b)** **(c)**

Figure 4. Example (a) x-ray CT, (b) MR, and (c) PET images of brain tumors. X-ray CT and MR images copied from http://ampat.amu.edu.pl/przyp/case1/CASE1.HTM.

three-dimensional information on tissue metabolism. PET measures the concentration of exogenously administered radioactive glucose, which unlike many radionucleide tracers used in nuclear medicine is capable of crossing the blood-brain barrier via transport by specialized proteins. Since most tumors are aggressive and highly metabolic, they appear as hotspots on the PET images and their intensity can indicate the grade of the tumor; however, the inherent poor resolution of PET imaging limits their clinical applicability for surgical planning or margin identification.

Neurosurgical biopsies are administered stereotactically or during surgery to help guide surgical decisions to formulate the subsequent treatment plan. In stereotactic biopsy, a biopsy needle is guided to the tumor using tumor location from CT or MR images and trajectory information from a stereotactic frame rigidly attached to the patient's skull or frameless stereotaxy with a surgical navigation system. In either case, a small sample of tumor tissue is extracted from the tumor core, withdrawn with the biopsy needle, and sent to pathology for histopathological diagnosis. Intra-operative biopsies can be repeatedly acquired to determine the extent of tumor margin resection, but biopsy diagnosis from pathology can take on the order of 15-20 minutes, making the process relatively inefficient.

Brain Tumor Treatment

Depending on tumor location and histology, the current three-prong attack for brain tumor treatment is surgical resection of maximum tumor volume followed by radiation and/or chemotherapy. Resection surgery alone has a mortality rate of 1% to 2% and morbidity rate of only 25% for neurological deficit [5]; therefore, the relief of tumor-related symptoms is often enough to warrant resection surgery. Surgical resection combined with radiation therapy is often sufficient to cure many benign tumors such as meningiomas, some ependymomas, gangliogliomas, and cerebellar astrocytomas, especially if the tumors are well encapsulated. However, for malignant tumors such as anaplastic astrocytomas and glioblastomas with infiltrating margins, the current treatment methods are rarely curative, tumor recurrence is common, and the doctor's goals are predominantly palliative, to reduce the patient's tumor-related symptoms and extend his/her life as long as possible.

The crux of surgical resection is the amount of tumor which should be removed. For benign, well-encapsulated tumors, complete tumor removal only comes into question in areas of

eloquent cortex. For malignant tumors with infiltrating margins, the extents of tumor core and margin resection have been repeatedly correlated to patient quality of life and mortality [4-8]. Several studies indicate that complete tumor core resection significantly improves 2-year survival rate, median survival time, and mean functional ability (as measured by the Karnofsky Performance Scale) relative to subtotal resection [5, 6]. While complete resection of the tumor core is feasible, complete tumor margin resection as indicated by gadolinium contrast enhancement in post-operative MRI is achieved in less than 20% of infiltrating tumor surgeries [7, 9], generally due to limitations in the ability to differentiate between normal and margin tissue during surgery. Visual inspection can be highly subjective and inconclusive, especially when dealing with low-grade tumors or diffuse tumor margins which often resemble normal neural tissue. On-site pathology is more histologically reliable but is expensive, is far from real-time, and does not spatially demarcate margin extent. Three-dimensional surgical navigation with x-ray CT or MRI is extremely useful in tumor localization and debulking [10, 11] but limited in its margin sensitivity, as tumor cells have been found outside of delineated image margins in many documented cases [12]. Furthermore, deformation of brain tissue subsequent to craniotomy, retraction, and debulking by as much as a centimeter degrades the accuracy of surgical navigation based upon pre-operative images [13, 14]. Real-time intra-operative ultrasound overcomes limitations from brain deformation and can detect tumor margins because brain tumors are usually hyperechoic relative to normal tissue, but it is less likely to be able to differentiate tumor from peritumoral edema, which is also hyperechoic [15, 16] and poor image resolution hinders correlation between image features and surgical position. Due to the inherent limitations of these adopted tumor visualization techniques, significant residual tumor cells frequently remain after resection [6, 7]. This limited success rate of complete margin resection prompts surgeons to adopt a conservative approach to margin removal [4] since the costs of speech, motor, or other functions which significantly affect patient quality of life far outweigh removal of a small percentage of tumor margin which most likely fails to lead to complete margin resection.

As mentioned above, radiation therapy and chemotherapy are often used to kill residual tumor and tumor margins after surgical resection. The two main types of radiation therapy are external beam radiation focuses an outside beam of radiation on the targeted tumor tissue and interstitial radiotherapy, or brachytherapy, which places radioactive seeds directly within the

tumor to impose a higher radiation dose on the tumor cells without damage to intervening normal tissue. Some studies have found that radiation therapy is more effective on rapidly growing cells [8], so doctors often reserve radiation therapy for high-grade tumors. While some brain tumors can be treated completely with radiation therapy (medulloblastomas), complete treatment of the fingerlike protrusions at the margins of infiltrating gliomas is nearly impossible; however, radiation therapy is always used for glioma treatment, with doses between 5,000 and 6,000 cGy [5, 7, 8] administered for a 3-cm radius around the tumor core [5].

Chemotherapy is predominantly reserved for treatment of high-grade tumors and lymphomas and many times combined with radiation therapy to increase survival rates [5]. Chemotherapeutic agents target and kill rapidly dividing cells such as high-grade tumor cells, but which can lead to severe side effects by targeting bone marrow, endothelial cells in the mouth and intestines, and hair follicles or damaging the heart, kidneys, and peripheral nerves. For treatment of malignant gliomas, carmustine and lomustine nitrosoureas and oral procarbazine are generally regarded as the most chemotherapeutic agents; however, as any foreign agent attempting to enter brain tissue, an intact blood-brain barrier blocks these cancer-targeting drugs from reaching the tissue, rendering chemotherapy ineffective for treatment of low-grade gliomas or infiltrating tumor margins.

Due to the inability of radiation therapy to target diffuse tumor margins and of chemotherapy to penetrate the blood-brain barrier intact in these tissue regions, treatment of infiltrating tumor margins for malignant gliomas is limited to surgical resection. The extent of surgical margin resection is dependent upon the surgeon's ability to discriminate between normal tissue and tumor margins during surgery. Current methods of intra-operative tumor margin localization are severely limited either in their sensitivity (visual inspection, MRI), efficiency and spatial demarcation (on-site pathology), or accuracy (ultrasound), leading to complete tumor resection in less than 20% of glioma patients and emphasizing the need for a real-time, objective, non-invasive technique to map out brain tumor margins with high sensitivity and specificity.

Optical Spectroscopy for Intra-operative Brain Tumor Detection

Principles of Fluorescence and Diffuse Reflectance Spectroscopy

A potential candidate for objective brain tumor margin visualization is an imaging system with contrast based on optical spectroscopy which can quickly and non-intrusively detect tissue changes associated with the progression of disease. Fluorescence spectroscopy and diffuse reflectance spectroscopy have been investigated in recent years for the development of new clinical diagnostic tools. Intrinsic fluorescence or autofluorescence spectra have been shown to differ between normal and neoplastic tissues in various organ systems possibly due to changes in fluorophore concentration or environment with the progression of disease [17]. Studies which exploit spectral differences for tissue discrimination have been carried out for the brain [18-21], bronchus [22], colon [23], cervix [24], bladder [25], esophagus [26], skin [27], breast [28], and arterial wall [29]. Exogenous fluorescent dyes, most notably hematoporphyrin derivatives (Photofrin, 5-aminoluvolinic acid), have also been shown to selectively collect in tumor tissue and have been used for enhancement of fluorescent contrast between normal and neoplastic tissue in animal models [30] as well as in the human lung [31] and colon [32]. While exogenous dyes have also been applied in the brain [9, 33, 34], the need for the disruption of the blood-brain barrier give exogenous dyes poor sensitivity for detection of low-grade tumors and tumor margins, a limitation which is described in greater detail below.

While fluorescence spectroscopy provides information about the chemical and morphological composition of tissue, diffuse reflectance spectroscopy yields information about tissue absorption and scattering [35]. During the progression from normal to neoplastic, tissue undergoes many structural as well as chemical changes at the cellular and subcellular level, altering the optical properties of the tissue and thereby enabling tissue discrimination with diffuse reflectance spectroscopy. The most drastic changes within a tissue diffuse reflectance spectrum between 400 and 600 nm frequently result from the amount of blood concentration or oxygenation within the tissue. Since cancers often develop neovascularization to sustain a high metabolism and generally shift to more anaerobic cellular respiration, diffuse reflectance spectroscopy has the potential to detect cancerous tissue from its blood absorption “signature.” Diffuse reflectance spectroscopy has been studied for tissue discrimination in the bladder [36], breast [37], colon [38], and skin [39, 40]. Although diffuse reflectance spectroscopy has not been

used for brain tissue discrimination, optical properties of normal and malignant brain tissue were found to be significantly different [41, 42]. Thus by combining fluorescence with diffuse reflectance spectroscopy, optical techniques can be used for brain tumor margin detection.

Fluorescence and Diffuse Reflectance Spectroscopy in the Brain

The first effort to guide glioma resection in the brain with optical techniques employed exogenous fluorescence subsequent to systemic administration of 5-aminoluvolinic acid (5-ALA) [9, 33], one of the precursors to hematoporphyrins along the heme biosynthesis pathway. Photosensitizers such as 5-ALA when administered systemically or topically, have been shown to selectively collect in tumor tissues. While 5-ALA itself is not fluorescent, its porphyrin derivatives exhibit strong red fluorescence in response to blue excitation light, making them useful for photodynamic therapy and potentially as a means to demarcate tumor borders. As mentioned previously, the clinical utility of any technique for glioma resection guidance depends on its ability to highlight infiltrating tumor margins from the surrounding normal brain tissue. To assess this capability *in vivo*, Stummer et al administered 5-ALA to patients before tumor resection surgery and acquired tissue biopsies from fluorescent and non-fluorescent regions along the tumor margins. The presence of fluorescence was correlated to histopathological diagnosis, and the presence of residual porphyrin fluorescence was correlated to residual gadolinium contrast enhancement in post-operative MRI as a measure of the extent of tumor resection. Over the course of two separate studies which involved 61 patients and acquired 353 biopsy samples, porphyrin fluorescence possessed a sensitivity of 85%, specificity of 98%, positive predictive value (PPV) of 100% and negative predictive value (NPV) of 60% for the presence of tumor cells in the biopsy samples. High diagnostic sensitivity and specificity indicate sensitive detection without false prediction of the presence of tumor, leading to a high PPV which signifies excellent safety to avoid neurologic deficit. However, the low NVP indicates that biopsy samples without fluorescence often contained tumor tissue, suggesting limited efficacy for positive tumor margin demarcation. While the results demonstrate good correlation between residual fluorescence and residual MR contrast enhancement, the correlation simply follows from the fact that margin demarcation with porphyrin fluorescence is limited in much the same manner as with contrast-enhanced MRI. Since gadolinium and 5-ALA are both polar molecules which cannot freely cross the blood-brain barrier [43], contrast enhancement in both modalities

is only present in regions where the blood-brain barrier has been breached, such that neither modality enhances infiltrating tumor margins or low-grade gliomas.

While exogenous contrast methods are spatially correlated to the integrity of the blood-brain barrier, autofluorescence and diffuse reflectance spectroscopy probe intrinsic tissue contrast, giving them the potential to overcome limitations of exogenous contrast by demarcating infiltrating tumor margins based upon the inherent changes in tissue structure and biochemistry subsequent to tumor invasion. The capability to optically detect intrinsic tissue changes with tumor progression using autofluorescence spectroscopy was first assessed by Chung et al [20]. Fluorescence excitation-emission matrices (EEMs) were measured *ex vivo* and *in vitro* for white matter, gray matter, and a variety of primary intracranial tumors, including various grades of gliomas. The EEMs showed three distinct groups of excitation-emission peaks in brain tissue: 1) 360 nm excitation, 470 nm emission, attributed to NAD(P)H fluorescence; 2) 440 nm excitation, 520 nm emission, attributed to flavin fluorescence; and 3) 490 nm excitation, 630 nm emission, attributed to intrinsic porphyrin fluorescence. In terms of differences in autofluorescence between tissue types, the measurements demonstrated greater fluorescence emission in white matter than gray matter, with peak intensity ratios which ranged from 1.7 to 2.7, and significantly greater NAD(P)H fluorescence intensity in normal brain than in glioma tissues.

Similar changes in fluorescence intensity were observed by Bottiroli et al during measurement of autofluorescence emission spectra *in vivo* from cortex, white matter, and tumor tissues in three glioblastoma patients [21]. With 366-nm excitation, peak autofluorescence emission occurred between 445 and 465 nm and was attributed to NAD(P)H. The measured spectra showed significant changes in fluorescence intensity and lineshape between normal and tumor tissues, with greater intensity in white matter than tumor, slightly greater intensity in cortex than tumor, and a red-shift in the peak fluorescence wavelength for tumor relative to normal tissues. Since the free form of NAD(P)H, which is associated with anaerobic metabolism, has a 30% lower fluorescence quantum yield and a shift in its fluorescence peak from 440 to 465 nm relative to bound NAD(P)H [44, 45], spectral differences from tumor tissue were attributed to an impairment in metabolic equilibrium from damage to the aerobic machinery and a shift toward anaerobic respiration in tumor cells.

Subsequent to the findings of Chung et al and Bottiroli et al, our research group conducted an *in vitro* study to quantitatively determine how accurately combined fluorescence

and diffuse reflectance spectroscopy could differentiate between normal and tumor tissues in the brain [18] Fluorescence EEMs as well as diffuse reflectance and fluorescence spectra with 337 nm excitation were measured from normal, glioma, and secondary tumors acquired from twenty patients, and spectral differences were correlated to histopathological diagnosis to develop empirical discrimination algorithms from the observed spectral differences between tissue groups. Measured diffuse reflectance spectra possessed lineshapes which were strongly modulated by the oxy/deoxy-hemoglobin absorption bands at 415, 542, and 577 nm and intensities which were significantly higher in white matter than in gray matter or tumor, which were similar. While fluorescence EEMs demonstrated no peaks at 440/520 or 490/630 nm excitation-emission as observed by Chung et al and tumor fluorescence was not red-shifted relative to normal tissues as observed by Bottiroli et al, fluorescence emission at 460 nm was less intense in tumor relative to normal tissues, consistent with previous results. Based on these spectral differences, primary brain tumors were accurately differentiated from white and gray matter using the difference in fluorescence intensity at 460 nm alone (97% sensitivity, 96% specificity, biased results), while the diffuse reflectance intensity at 625 nm and the ratio of fluorescence to diffuse reflectance at 460 nm were capable of separating secondary tumors from normal brain tissues (94% sensitivity, 90% specificity, biased results).

To determine the true clinical utility of optical spectroscopy for tumor resection guidance, our research group is in the middle of a multi-center clinical study to determine the diagnostic accuracy of combined fluorescence and diffuse reflectance spectroscopy for discriminating between normal and tumor margin tissues *in vivo* [19, 46, 47]. During craniotomy procedures for glioma resection or temporal lobectomy, multiple gray matter, white matter, tumor core, and tumor margin sites are selected for spectral measurement with a portable spectroscopic system [19]. Excitation light from a pulsed nitrogen laser (fluorescence) and halogen lamp (diffuse reflectance) are sequentially delivered to a point on the tissue surface by two of seven fibers within a handheld, beam-steered, fiber-optic probe. The other five fibers in the probe are used to collect remitted fluorescence and diffuse reflectance from the tissue surface and deliver it to a spectrograph for spectral measurement. Spectra are grouped as normal, tumor core, or tumor margin according to gold-standard histopathological diagnosis of tissue biopsies acquired at the interrogation site and analyzed to determine spectral differences between tissue groups. Despite only subtle spectroscopic differences between normal and tumor tissues, initial

reports using multivariate analysis of fluorescence and diffuse reflectance spectra measured from 184 tissue sites in 35 of more than 125 patients measured to date demonstrate a diagnostic accuracy of 100%, 96%, and 94% for normal, tumor core, and tumor margin tissue samples, with only 2 out of 35 tumor margin sites misclassified as normal [46]. These results indicate not only the promising capability of combined autofluorescence and diffuse reflectance spectroscopy to provide contrast between normal and tumor tissues in the brain, but also its ability to overcome the limitations of current tumor margin localization techniques, accurately differentiate infiltrating tumor margins from surrounding normal brain tissue, and potentially affect more complete glioma resection.

Spectral Imaging Development

Fiber-optic probe-based spectroscopy is useful for correlating spectral features to histopathological diagnosis at a specific interrogation site, to prove the principle that optical spectroscopy has the capability to rapidly, objectively, and non-invasively differentiate between tissue types. However, probe-based spectroscopy has limited clinical applicability since it produces single-point diagnostic measurements without providing spatial information regarding the extent of tumor margins, information which is necessary to efficiently guide tumor resection. For optical biopsy to be clinically useful, single-point spectroscopy systems must be extended to spectral imaging in which spectral information is acquired at every pixel within a two-dimensional field of view, yielding spatial and spectral tissue information for a comprehensive snapshot of tissue pathology during surgery.

Successful translation from probe-based spectroscopy to macroscopic spectral imaging depends on three main factors: 1) reasonable image acquisition time of autofluorescence and diffuse reflectance despite significant decreases in excitation irradiance due to larger target areas, 2) a convenient clinical interface for seamless integration into the surgical setting, and 3) maintenance of accurate spectral discrimination between tissue types. While spectral discrimination capability will be discussed in the last section of this background, speed of spectral image acquisition and creating a versatile, compact imaging system for use in the operating room depend to a large degree on optical design and spectral imaging implementation. The following section outlines the various modalities for spectral imaging and the selection process of liquid-crystal tunable filter spectral imaging for this research project.

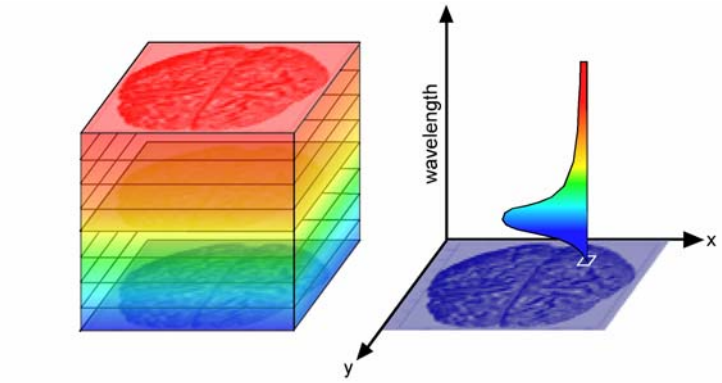

Figure 5. Spectral image data cube with two dimensions (x,y) of spatial information and one dimension (wavelength) of spectral information.

Spectral Imaging Modalities

Acquiring spatially resolved spectral information via spectral imaging yields three-dimensional data cubes with two dimensions of spatial information and one dimension which varies with wavelength (Figure 5). Spectral imaging methods have long been used in the fields of astronomy [48-50], remote sensing [51-53], and chemical compound analysis [54-56] to elucidate the composition and characteristics of terrestrial, atmospheric, and extra-terrestrial objects. Spectral imaging systems developed more recently for life science applications have been coupled to benchtop microscopes for fluorescence *in situ* hybridization [57-60], general cell visualization [61-63], and fluorescent-protein cell trafficking (FRET) [64, 65]. The surge of optical methods for tissue discrimination have led to many optical imaging systems for tissue contrast; however, few of the systems designed to date perform true spectral imaging, a term generally reserved for the acquisition of **detailed** spectral information at every pixel, and none have been quantitatively tested for guidance of disease management. Most tissue-based optical imaging systems acquire limited spectral information (a few emission bands), trading decreased spectral information for increased frame rates by employing filter-based assemblies containing bandpass-filter wheels, dichroic filters, and/or beamsplitters and oftentimes optically implementing tissue classification algorithms in hardware [66, 67]. These systems have been most commonly applied to exploit the preferential deposition of exogenous fluorescent dyes to tumor tissue [30, 68, 69] and to target the hemoglobin absorption bands of soft tissue for perfusion imaging [70, 71]. While the speed of these optical imaging systems is impressive, hardware acquisition of partial spectral information limits the complexity of viable classification

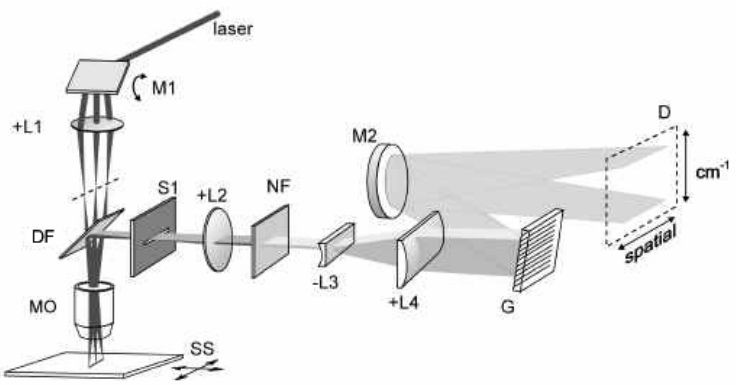

Figure 6. Schematic of line-scanning spectral imaging system [2] demonstrating single-line excitation and collection and dispersion of the spectral components of the collected line across the second dimension of the CCD camera.

algorithms, which are often unique to a given organ system, further requiring a separate imaging system for each tissue type.

Spectral imaging systems capable of good resolution across all three dimensions can be grouped according to the method by which they acquire three dimensions of information using a two-dimensional optical detector (CCD camera): line-scanning, tunable-filters, and multiplexing methods such as Fourier-transform interferometry. Line-scanning systems (Figure 6) utilize motors to scan a 1-D excitation-collection line across the tissue surface. At each scan position, the line of light collected from the tissue surface is aligned along one dimension of the CCD array while a grating disperses the spectral components along the orthogonal dimension. Thus, each image acquired by the CCD camera contains the complete spectra from one spatial row of the image, and successive CCD frames are acquired as the excitation-collection line is scanned across the tissue surface. Line-scanning methods are simple to implement; however, the motors often cause vibration artifacts within the images and the images require as many CCD frames as the spatial dimensionality of the image, resulting in time-consuming data readout from the camera.

Tunable-filter spectral imaging systems [72-74] continuously excite and collect emission from the entire tissue surface and employ an electronically tunable bandpass filter, such as a liquid-crystal tunable filter (LCTF) or an acousto-optic tunable filter (AOTF), to transmit or diffract, respectively, one band of the emission spectrum to the CCD camera at a time. In this way, tunable filter spectral imaging systems use the filter to directly parse the wavelength dimension of the spectral image. A frame of CCD data is acquired for each band of the emission spectrum, using the entire CCD array for spatial resolution. The spectral dimension of the image

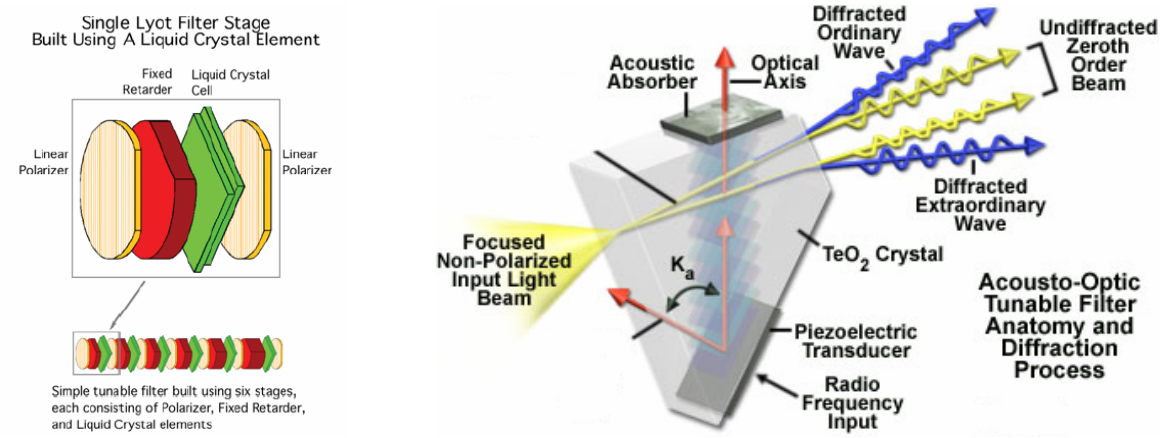

(a) **(b)**

Figure 7. Schematics showing (a) the construction of a liquid-crystal tunable filter (www.cri-inc.com) and (b) the principles of operation for an acousto-optic tunable filter (www.olympusfluoview.com/products/aotfproducts.html).

is constructed by acquiring successive CCD frames as the filter tuning wavelength is swept across the spectral range of interest. The most recent generations of these filters possess a wide spectral range across the visible or infrared regions of the spectrum with excellent spectral resolution (±5 nm) and can be tuned on the order of microseconds (AOTF) to milliseconds (LCTF).

Liquid-crystal tunable filters are constructed from a stack of linear polarizers with interspersed layers of liquid crystals and birefringent crystals (Figure 7a). The retardance (R) of each stage, defined as the product of its thickness (d) and the difference between its ordinary (n_o) and extraordinary (n_e) indices of refraction

$$R = d\left(n_o - n_e\right), \tag{1}$$

can be modulated by applying a voltage to the liquid crystal and changing its extraordinary index of refraction. Altering the stage's retardance affects the phase delay between the ordinary and extraordinary light rays emerging from the stage, thereby changing its transmission (T) as a function of wavelength (λ)

$$T = \frac{1}{2}\cos^2\left(x\right), \tag{2}$$

where

$$x = \frac{R}{\lambda}.$$

The thicknesses (d) of the birefringent crystals in the filter stack and the voltages applied to the liquid crystals are often selected to produce a binary series of retardances – R, 2R, 4R, etc. –

such that all of the stages transmit the selected passband while destructive interference at the other wavelengths "trims" the stopband light. The number of stages employed in the filter dictates the width of the passband and the degree of stopband attenuation.

The advantage to LCTF implementation in a spectral imaging system is the simplicity in the optical design. Without disturbance of the passband beam or moving parts to create vibration artifacts in the images, the system requires only a camera lens to focus the transmitted light onto the CCD focal plane. However, the peak transmission of liquid-crystal devices for co-polarized light ranges from 5% (at 400 nm) to 60% (at 700 nm) across the visible spectrum, and a major drawback to any filter-based imaging system is the inherent trade-off between the system's optical throughput (3-10%) – defined as the fraction of light collected by the imaging system which is ultimately detected by the camera – and its spectral resolution.

Acousto-optic tunable filters apply radio-frequency (RF) acoustic waves to modulate the index of refraction of the filter crystal. If the incident wavelength satisfies a momentum-matching condition based upon the frequency of the RF wave, the linear polarization states of the incoming light are diffracted to the opposite state and the light is deflected upon its exit from the crystal, with two symmetrically diffracted passband beams and a transmitted zero-order stopband beam exiting the filter (Figure 7b). Since the diffracted and zero-order beams must be separated for spectral imaging, optical design of AOTF systems requires either:

1) a long object distance to allow physical separation of the diffracted and zero-order beams; or,
2) orthogonally oriented polarizers on either side of the filter to polarize the input light and allow only orthogonally oriented output light (i.e. the passband) to reach the camera.

Although AOTF diffraction efficiency is on the order of 90-95% for polarized input light (and 70% for unpolarized light), both beam separation solutions result in a loss of at least 50% of the light collected from the sample.

Multiplexing methods for optical measurements were first developed for spectral analysis in the infrared region of the electromagnetic spectrum due to a dearth of low-noise infrared detectors. Rather than isolating and measuring individual spectral bands of a signal, multiplexing methods weigh the spectral components in groups using orthogonal basis functions (cosines in the case of Fourier spectroscopy) and measure the total intensity of each weighted group.

Measuring multiple spectral components simultaneously and back-calculating their intensities from the weighted measurements provides greater optical throughput than spectrometer and filter-based systems with subsequent increase in signal-to-noise for equivalent integration times.

Fourier-based imaging systems use Michelson or Sagnac interferometers where the optical path difference (OPD) between two beams created and subsequently recombined by a 50/50 beamsplitter is varied between successive CCD frames (Figure 8a). Varying the OPD modulates the interference pattern seen by the CCD camera, building interferograms at each pixel as the OPD is shifted and the CCD frames are acquired. After complete image acquisition, each pixel interferogram represents the Fourier transform of the pixel spectrum and can be individually converted to such via the inverse Fourier transform (Figure 8b). Employing a beamsplitter-based interferometer for multiplexing provides a theoretical system optical throughput of 50% (half the light is lost back out the entrance port) over the entire spectrum and a multiplex advantage of $\sqrt{N/8}$ (N = number of frames) over measuring the wavelengths individually with a filter system. However, considerable overhead is expended in image acquisition time since spectral extraction must be performed for every spatial pixel within the image. This process requires N^2 additions or multiplications at each pixel, a process that can become computationally intensive for a highly resolved image. Also, the relationship between sampling the interferogram and the spectrum is not intuitive, to the point that certain combinations of image acquisition parameters can lead to incomplete spectra or images with

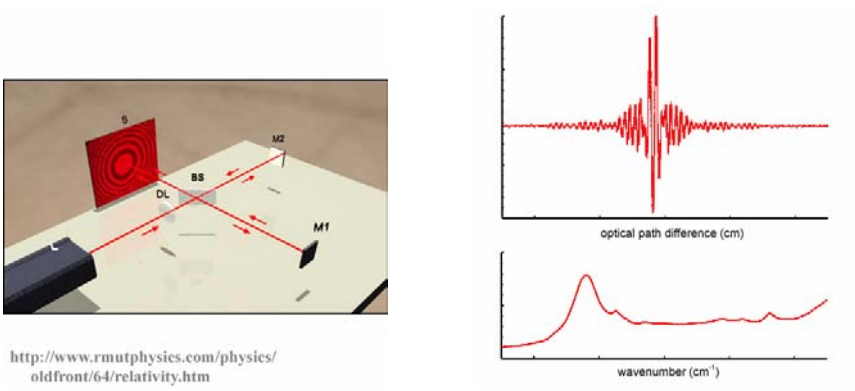

(a) **(b)**

Figure 8. (a) Michelson interferometer with laser input showing interference fringes as a result of changes in optical path difference with radial position. In spectral imaging, one of the mirrors is replaced with the sample of interest, and the other mirror is scanned along the optical axis to create multiple OPD values. (b) Example inverse Fourier transformation from interferogram as a function of optical path difference to spectrum as a function of wavenumber (inverse of wavelength).

spatial harmonics. Furthermore, the optical designs of multiplexing systems are somewhat complex and system performance is often extremely sensitive to optical alignment.

As part of a previous project, our research group evaluated three benchtop spectral imaging systems to determine which system was most amenable to rapid autofluorescence imaging in a clinical setting [75]. A detailed description of this evaluation can be found in Appendix A. The three systems employed an acousto-optic tunable filter (AOTF), a liquid-crystal tunable filter (LCTF), and a Fourier multiplexer, respectively, for resolution of the spectral image dimension. Briefly, the systems were quantitatively compared in terms of optical throughput and imaging signal-to-noise ratio in strong reflectance and weak autofluorescence images. While the Fourier system enjoyed the highest optical throughput, the LCTF system generated the highest signal-to-noise ratio in both types of imaging and proved to be the most versatile with the simplest optical design. It was based upon this evaluation that our research group chose to develop a LCTF spectral imaging system for clinical implementation in this research project.

Precise resection of brain tumors in functionally or anatomically eloquent areas or deep-seated regions of the brain often requires enhanced tumor visualization and access. To this end, the neurosurgical field has increasingly exploited adjuncts such as endoscopes, operating microscopes, and neuro-navigational systems to affect more complete and accurate tumor resection. The flexibility of endoscopes facilitates neurosurgical access to and visualization of lesions in hard-to-reach areas of the brain with less tissue manipulation than conventional retraction [76]. Neuro-endoscopes have been employed for access to intraventricular lesions [77], for a transnasal approach to the brainstem [78, 79], and with ultrasound guidance for a variety of lesion treatments [80, 81]. The magnification and illumination of operating microscopes make them indispensable for precise resection of brain tumors such as brainstem and motor strip gliomas and acoustic neuromas which abut cranial nerves. Use of operating microscopes has become so routine for tumor resection that several image-guided surgical systems have been developed for direct microscopic interface. These systems [82-85] have been investigated for treatment of general gliomas, cerebral arteriovenous malformations, acoustic neuromas, and brainstem neoplasms. While not directly interfaced, operating microscopes have also been used in conjunction with image-guided surgery systems for epilepsy treatment and resection of gliomas, pituitary tumors [86], and supratentorial cavernomas [87], and have even

been employed with new intra-operative MR imaging systems [88-90]. With the increased use of operating microscopes, endoscopes, and microscope-based navigation systems during neurosurgery, the ultimate objective of this research project is to develop a spectral imaging camera head with variable interfaces that may be selected based on tumor type, location, and surgical need. For my dissertation research project, as a logical first step for resection guidance of gliomas which predominantly present within the cerebral hemispheres, coupling the spectral imaging system to a standard operating microscope will help affect a seamless integration of efficient spectral diagnosis into the surgical setting.

Effects of the Translation from Probe-Based Spectroscopy to Spectral Imaging

Ideally, non-contact spectral imaging would produce fluorescence and diffuse reflectance lineshapes equivalent to probe-based spectroscopy; otherwise, time and resources spent developing discrimination algorithms based upon spectral differences observed in probe-based data during large, multi-patient clinical studies are squandered, since new imaging-based algorithms must be determined. Investigators in the field of probe-based spectroscopy and spectral imaging have always been diligent in accounting for spectral variations in source illumination and detector sensitivity to remove the effects on measured lineshape of factors extrinsic to the sample, suggesting at first glance that producing equivalent lineshapes between probe-based spectroscopy and spectral imaging is as simple as applying the standard spectral calibration procedure outlined in every optical biopsy manuscript to our spectral imaging system. However, investigations over the past 20 years have repeatedly demonstrated that measured spectral lineshape is equally affected by the excitation-collection geometry of the measurement system, even for probe-based spectroscopy measurements. The results of these investigations indicate that spectral lineshape is modulated by two main factors. First, the sample optical properties dictate the impulse response of light distribution within the tissue in terms of the relative propagation and attenuation of different wavelengths and the subsequent intensity, spatial distribution, and angular profile of light emitted from the tissue surface. Second, the excitation-collection geometry of the measurement system dictates the convolution of that impulse response with the spatial dimensions of the excitation and collection regions and the excitation-collection angles to determine what fraction of the light emitted at each wavelength is ultimately measured. Therefore, an excitation-collection geometry which involves spectral

variations in the fraction of remitted light collected by the system impacts the measured spectral lineshape despite correction for excitation spectrum and detector sensitivity.

The transition from probe-based spectroscopy to spectral imaging often involves a drastic shift in excitation-collection geometry, both spatially and in terms of angular relationship to the tissue surface (Figure 9). Spectroscopy probes often contain multiple fibers, some of which are used for excitation delivery and the rest for emission collection. Direct contact of the probe tip with the tissue surface and the specific configuration of the probe – the relative positions of the excitation and collection fibers, the gap between the fiber tips and the tissue surface, and the fiber polish angles – produce consistent excitation and collection angles for every sample but

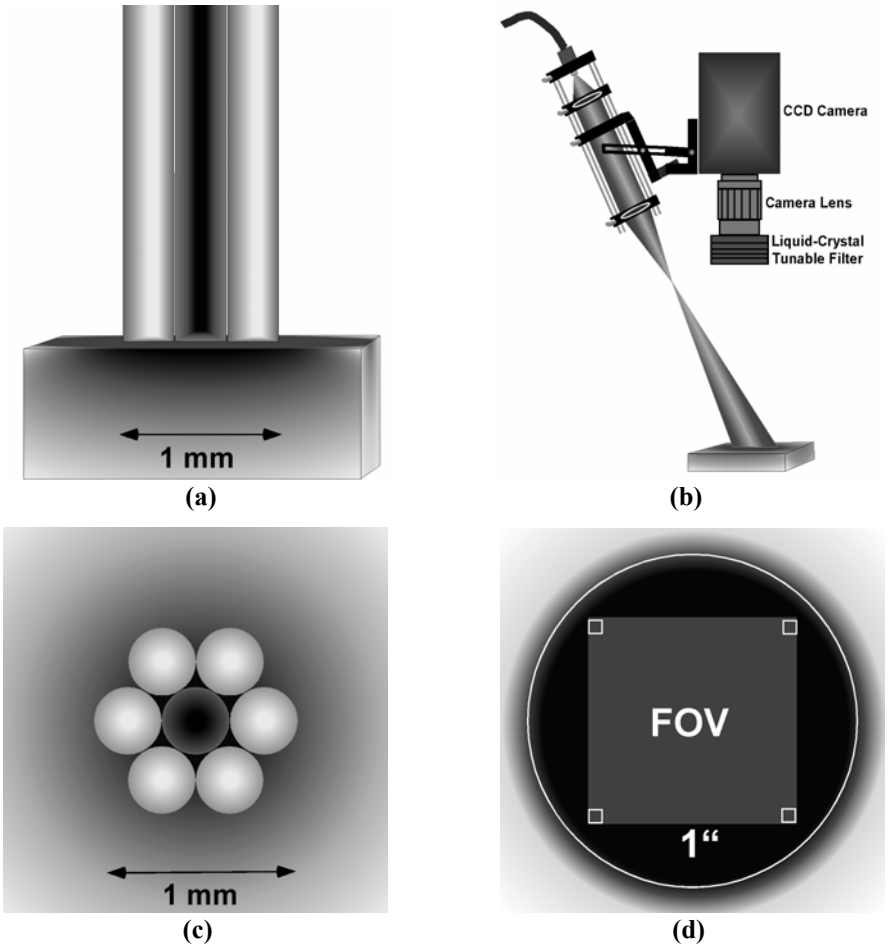

Figure 9. Excitation-collection geometries for example probe-based spectroscopy and non-contact spectral imaging systems. (a) Fiber-optic probe with a single excitation fiber, fibers polished normally, and direct contact between the fibers and the tissue surface. (b) Spectral imaging system with non-contact excitation and collection. (c) Cross-section of the probe-tissue interface for a six-around-one probe configuration with a central excitation fiber and six surrounding collection fibers relative to the light distribution in the tissue. (d) Spectral imaging field of view and individual pixels relative to the excitation spotsize and subsequent light distribution.

create a unique set of source-detector separation distances (Figure 9a,c). Since the spatial distribution of light remitted from tissue varies with optical properties, its relative relationship to the fiber configuration will vary with wavelength, such that lineshapes measured with probe-based spectroscopy will be influenced by spectral variations in collection efficiency.

While multiple modalities exist for spectral imaging implementation, most spectral imaging systems acquire spectral data with non-contact excitation and collection (Figure 9b). When the excitation spot is much larger than the system field of view, as is often the case, each pixel in the image can be treated as a small collection region surrounded by a semi-infinite excitation spot (Figure 9d), and its spatial excitation-collection geometry as a convolution of all possible source-detector separation distances. However, non-contact imaging produces a geometry whose excitation and collection angles vary not only from image to image but across pixels within a single image when the sample surface topography is non-uniform. Therefore, while the collection efficiency of spectral imaging is not sensitive to optical property variations in the spatial distribution of remitted light, it is sensitive to the relative relationship between the excitation-collection angles and the angular emission profile of remitted light. If angular profiles of surface emission for a given excitation angle depend upon sample optical properties, angular emission will vary between wavelengths and their relative measured intensities will be modulated by detector collection that is limited to a narrow range of emission angles. If angular emission profiles depend upon incident excitation angle, an undulating sample surface can similarly induce spectral distortions within imaging spectra and extrinsic differences between them.

While previous studies in the literature, outlined below, have investigated fluorescence and diffuse reflectance propagation with results which hint at some of the aforementioned effects of excitation-collection measurement geometry on measured spectral lineshape, no group has examined the effect of the shift in spatial and angular excitation-collection geometry from probe-based spectroscopy to non-contact spectral imaging. As such, there exists a need to characterize fluorescence and diffuse reflectance propagation and angular emission profiles as functions of incident excitation angle and sample optical properties to predict the potential effects of such a transition on discrimination accuracy between tissue types.

Correlations of fluorescence and diffuse reflectance angular emission to the optical properties of tissue and to the incident angle of excitation light have not been thoroughly

explored in the literature. Using Monte Carlo simulation, Qu et al reported "nearly Lambertian" angular emission profiles for fluorescence and diffuse reflectance when excitation is normal to the tissue surface [91]. Angular emission profiles for diffuse reflectance deviated from Lambertian behavior when the excitation was delivered at oblique angles (30° and 75° with respect to the surface normal) such that the emission was biased away from the source, indicating that angular emission of diffuse reflectance may be dependent on sample optical properties when the excitation is delivered at an oblique excitation angle. Churmakov et al reported similar roughly Lambertian emission behavior for diffuse reflectance when excited normal to the surface [92]. While these results hint at angular emission profiles of diffuse reflectance which are dependent upon incident excitation angle, neither group examined fluorescence emission behavior, investigated the correlation between angular emission and sample optical properties, or provided a detailed explanation for the behavior of the bias.

Research into diffuse reflectance propagation in tissue began with one-dimensional depth-resolved investigations in which diffuse reflectance was modeled as a function of optical properties using photon migration theory [93]. Several groups have also simulated or measured radially resolved profiles of diffuse reflectance for wide ranges of optical properties, but the results were used to develop inverse models for *in vivo* optical property determination [41, 94]. The authors concentrated on producing calibrated data for specific collection geometries and did not extend their findings to how profile changes with optical properties might affect clinically measured spectra. Bargo et al [95, 96] measured the collection efficiency of a single excitation-collection fiber and of an excitation-collection fiber pair as a function of optical properties and separation distance, but defined collection efficiency as the fraction of light impinging on the face of the collection fiber that falls within its acceptance cone, without investigating how the absolute emission intensity varies with optical properties (i.e. wavelength) and would thereby also affect diffuse reflectance lineshape.

While several studies have demonstrated changes in diffuse reflectance lineshape subsequent to a shift in excitation-collection geometry, the causes for the behavior were not thoroughly examined. Liu et al [97] simulated and experimentally measured diffuse reflectance for a subset of discrete optical property values and three different probe geometries, but did not discuss how the collection efficiencies of the specific probe geometries varied with wavelength. A subsequent paper from the same research group [98] used one of the investigated probes to

demonstrate that fluorescence and diffuse reflectance lineshapes from breast tissue change between three source-detector separation distances. However, the source of the disparities is not discussed other than to ascribe them to probing different depths of the tissue (the spectra from the different separation distances are used as independent inputs to a tissue classification scheme). Not surprisingly, the classification results show that the three sets of spectra yield similar discrimination success rates since there is "no apparent structural change in breast tissue with increasing depth," i.e. breast tissue is not layered.

The only studies in the literature which have examined the combined effects of optical properties and excitation-collection geometry on diffuse reflectance lineshape were conducted by Schmitt and Kumar [99, 100]. Diffuse reflectance spectra were measured in the near infrared for a single excitation-collection fiber pair in an effort to determine how collected emission varied with separation distance (d = 1-6 mm) for various optical properties (μ_a = 0-1.0 mm^{-1}, μ_s' = 0.5-2.0 mm^{-1}). They demonstrated that diffuse reflectance lineshape varies with source-detector separation distance and explained the shifts using diffusion theory. However, diffusion-based predictions broke down at small source-detector separation distances and thus far, no group has validated their results in the visible spectrum where increased scattering and absorption and the shorter source-detector separation distances of most fiber-optic probes (d = 0-1 mm) render diffusion theory inaccurate.

Recent investigations into fluorescence propagation can be divided into two major categories: those that investigate depth-resolved fluorescence [101-106] and those that seek to extract intrinsic fluorescence information from fluorescence measurements [107-111]. Depth-resolved fluorescence investigations predominantly aim to identify probe geometries which will collect fluorescence from specific layers in epithelial tissues, but they rarely worry about how optical properties and probe geometry affect the lineshape. While extracting intrinsic fluorescence information from fluorescence measurements recognizes the effects of optical properties on lineshape, and actually seeks to remove those effects, most of the methods nullify the effects of probe geometry by using diffuse reflectance information for fluorescence correction. Since the fluorescence and diffuse reflectance spectra are generally collected with the same excitation-collection geometry, diffuse reflectance is similarly modulated, eliminating any wavelength-specific geometry effects.

While depth-resolved and intrinsic fluorescence studies provide knowledge into fluorescence behavior, neither of them give insight into how tissue optical properties and excitation-collection geometry combine to modulate fluorescence lineshape. Surprisingly, while the recent investigations outlined above have strayed from the issue, two of the **first** investigations into fluorescence propagation initially demonstrated a dependence of fluorescence lineshape on excitation-collection geometry. Richards-Kortum et al [112] compared measured fluorescence spectra from regions inside and outside of the excitation spot. Keijzer et al [113] simulated and measured fluorescence spectra as a function of radial distance from the source. Both studies found that fluorescence lineshape drastically changes as collection is moved out of and further from the excitation spot. Shifts in lineshape are attributed to increased probing depth as the source-detector separation distance increases, subjecting the fluorescence to greater modulations from absorption. Since then, other groups have observed similar results [114, 115], but none have investigated spectral lineshapes measured with traditional fiber-optic probe configurations or non-contact imaging systems.

The high mortality rate for patients with malignant infiltrating gliomas due to tumor recurrence demonstrates the clinical need for more complete tumor margin resection, which has been repeatedly correlated to patient quality of life and survival. Limitations in current localization methods for infiltrating tumor margins emphasize the need for an intra-operative, objective method to spatially demarcate glioma margins for surgical resection guidance. Combined fluorescence and diffuse reflectance spectroscopy has proven capable of differentiating normal and tumor tissues in the brain and, more importantly, of discriminating infiltrating tumor margins from surrounding normal tissue. However, fiber-optic probe-based spectroscopy does not provide spatially resolved diagnostic information necessary to intra-operatively guide tumor resection, calling for an extension of probe-based spectroscopy to spectral imaging for a comprehensive snapshot of tissue pathology during surgery. The translation from spectroscopy to imaging involves a drastic shift in measurement excitation-collection geometry, with subsequent effects on measured spectral lineshapes that have been suggested in the literature but never thoroughly examined or characterized. The effect of excitation-collection geometry on diagnostic accuracy must be assessed by developing discrimination algorithms specific to spectral imaging data for differentiation between normal

and neoplastic brain tissues, in order to definitively determine the clinical utility of combined fluorescence and diffuse reflectance spectral imaging for infiltrating tumor margin resection guidance. The studies outlined in the subsequent five manuscripts have been designed to address these needs.

References

1. R. Escourolle and J. Poirier, *Manual of Basic Neuropathology*. 1978, Philadelphia: W.B. Saunders Company.
2. C. Otto and J. Greve, "Progress in instrumentation for Raman micro-spectroscopy and Raman imaging for cellular biophysics," Internet Journal of Vibrational Spectroscopy **2**, (1998).
3. "Brain Tumor Registry Statistics," http://www.cbtrus.org, Accessed on April 27, 2006.
4. S.A. Toms, D.Z. Ferson, and R. Sawaya, "Basic surgical techniques in the resection of malignant gliomas," J Neurooncol **42**, 215-26. (1999).
5. M.C. Chamberlain and P.A. Kormanik, "Practical guidelines for the treatment of malignant gliomas," West J Med **168**, 114-20. (1998).
6. M. Ammirati, et al, "Effect of the extent of surgical resection on survival and quality of life in patients with supratentorial glioblastomas and anaplastic astrocytomas," Neurosurgery **21**, 201-6. (1987).
7. A. Kowalczuk, et al, "Quantitative imaging study of extent of surgical resection and prognosis of malignant astrocytomas," Neurosurgery **41**, 1028-36 (1997).
8. M.T. Selch, et al, "Gangliogliomas: experience with 34 patients and review of the literature," Am J Clin Oncol **21**, 557-64. (1998).
9. W. Stummer, et al, "Intraoperative detection of malignant gliomas by 5-aminolevulinic acid-induced porphyrin fluorescence," Neurosurgery **42**, 518-25; discussion 525-6. (1998).
10. R.J. Maciunas, *Interactive Image-Guided Neurosurgery*. 1993, Park Ridge, IL: American Association of Neurological Surgeons.
11. R.J. Maciunas, *Minimally Invasive Therapy of the Brain*, ed. A.D. Salles and R. Lufkin. 1997, New York: Thieme Medical Publishers, Inc.
12. P.D. LeRoux, et al, "A comparison between preoperative magnetic resonance and intraoperative ultrasound tumor volumes and margins," J Clin Ultrasound **22**, 29-36. (1994).
13. D.L. Hill, et al, "Measurement of intraoperative brain surface deformation under a craniotomy," Neurosurgery **43**, 514-26; discussion 527-8. (1998).
14. N.L. Dorward, et al, "Postimaging brain distortion: magnitude, correlates, and impact on neuronavigation," J Neurosurg **88**, 656-62. (1998).

15. L.M. Auer and V.V. Velthoven, *Intraoperative Ultrasound Imaging in Neurosurgery: Comparison with CT and MRI*. 1990, Berlin: Springer-Verlag.

16. J.E. Knake, et al, "Neurosurgical applications of intraoperative ultrasound," Radiological Clinics of North America **23**, 73-90 (1985).

17. J.R. Lakowicz, *Principles of Fluorescence Spectroscopy*. 1983, New York: Plenum Press.

18. W.-C. Lin, et al, "Brain tumor demarcation using optical spectroscopy; an in vitro study," J Biomed Opt **5**, 214-20. (2000).

19. W.-C. Lin, et al, "In vivo brain tumor demarcation using optical spectroscopy," Photochem Photobiol **73**, 396-402. (2001).

20. Y.G. Chung, et al, "Diagnostic potential of laser-induced autofluorescence emission in brain tissue," J Korean Med Sci **12**, 135-42. (1997).

21. G. Bottiroli, et al, "Brain tissue autofluorescence: an aid for intraoperative delineation of tumor resection margins," Cancer Detect Prev **22**, 330-9 (1998).

22. M. Zellweger, et al, "In vivo autofluorescence spectroscopy of human bronchial tissue to optimize the detection and imaging of early cancers," J Biomed Opt **6**, 41-51. (2001).

23. R. Richards-Kortum, et al, "Spectroscopic diagnosis of colonic dysplasia," Photochem Photobiol **53**, 777-86. (1991).

24. N. Ramanujam, et al, "Cervical precancer detection using a multivariate statistical algorithm based on laser-induced fluorescence spectra at multiple excitation wavelengths," Photochem Photobiol **64**, 720-35. (1996).

25. M.A. D'Hallewin, L. Baert, and H. Vanherzeele, "Fluorescence imaging of bladder cancer," Acta Urol Belg **62**, 49-52. (1994).

26. M. Panjehpour, et al, "Spectroscopic diagnosis of esophageal cancer: new classification model, improved measurement system," Gastrointest Endosc **41**, 577-581 (1995).

27. B.W. Chwirot, et al, "Detection of melanomas by digital imaging of spectrally resolved ultraviolet light-induced autofluorescence of human skin," Eur J Cancer **34**, 1730-4. (1998).

28. P.K. Gupta, S.K. Majumder, and A. Uppal, "Breast cancer diagnosis using N2 laser excited autofluorescence spectroscopy," Lasers Surg Med **21**, 417-22 (1997).

29. S. Warren, et al, "Combined ultrasound and fluorescence spectroscopy for physico-chemical imaging of atherosclerosis," IEEE Trans Biomed Eng **42**, 121-32. (1995).

30. V.V. Lazarev, et al, "Detection of premalignant oral lesions in hamsters with an endoscopic fluorescence imaging system," Cancer **85**, 1421-9. (1999).

31. R. Baumgartner, et al, "Inhalation of 5-aminolevulinic acid: a new technique for fluorescence detection of early stage lung cancer," J Photochem Photobiol B **36**, 169-74. (1996).

32. G. Siboni, et al, "Spectral imaging of MC540 during murine and human colon carcinoma cell differentiation," J Histochem Cytochem **49**, 147-53. (2001).

33. W. Stummer, et al, "Fluorescence-guided resection of glioblastoma multiforme by using 5-aminolevulinic acid-induced porphyrins: a prospective study in 52 consecutive patients," Journal of Neurosurgery **93**, 1003-1013 (2000).

34. H.B. Sarnat, et al, "Gliosis and glioma distinguished by acridine orange," Can J Neurol Sci **14**, 31-5. (1987).

35. I.J. Bigio and J.R. Mourant, "Ultraviolet and visible spectroscopies for tissue diagnostics: fluorescence spectroscopy and elastic-scattering spectroscopy," Phys Med Biol **42**, 803-14. (1997).

36. J.R. Mourant, et al, "Spectroscopic diagnosis of bladder cancer with elastic light scattering," Lasers Surg Med **17**, 350-7 (1995).

37. I.J. Bigio, et al, "Diagnosis of breast cancer using elastic-scattering spectroscopy: preliminary clinical results," J Biomed Opt **5**, 221-8. (2000).

38. G.E. Zhengfang, K.T. Schomacker, and N.S. Nishioka, "Identification of Colonic Dysplasia and Neoplasia by Diffuse Reflectance Spectroscopy and Pattern Recognition Techniques," Applied Spectroscopy **52**, 833-839 (1998).

39. S. Tomatis, et al, "Spectrophotometric imaging of cutaneous pigmented lesions: discriminant analysis, optical properties and histological characteristics," J Photochem Photobiol B **42**, 32-9. (1998).

40. R. Marchesini, et al, "In vivo spectrophotometric evaluation of neoplastic and non-neoplastic skin pigmented lesions. III. CCD camera-based reflectance imaging," Photochem Photobiol **62**, 151-4. (1995).

41. F. Bevilacqua, et al, "In vivo local determination of tissue optical properties: applications to human brain," Applied Optics **38**, 4939-4950 (1999).

42. H.R. Eggert and V. Blazek, "Optical properties of human brain tissue, meninges, and brain tumors in the spectral range of 200 to 900 nm," Neurosurgery **21**, 459-64. (1987).

43. L. Terr and L.P. Weiner, "An autoradiographic study of delta-aminolevulinic acid uptake by mouse brain," Exp Neurol **79**, 564-8 (1983).

44. T. Galeotti, et al, "Fluorescence Studies of Nad(P)H Binding in Intact Cells," Hoppe-Seylers Zeitschrift Fur Physiologische Chemie **351**, 274-& (1970).

45. J.M. Salmon, et al, "Microspectrofluorometric Approach to the Study of Free Bound Nad(P)H Ratio as Metabolic Indicator in Various Cell-Types," Photochemistry and Photobiology **36**, 585-593 (1982).

46. S.K. Majumder, et al, "A probability-based multi-class diagnostic algorithm for iIn-vivo optical separation of tumor margin and tumor from normal human brain tissue," Applied Spectroscopy ((in review)).

47. S.A. Toms, et al, "Intraoperative optical spectroscopy identifies infiltrating glioma margins with high sensitivity," Neurosurgery **57**, 382-91 (2005).

48. D.A. Glenar, et al, "Spectral imaging of martian water ice clouds and their diurnal behavior during the 1999 aphelion season (L-s=130 degrees)," Icarus **161**, 297-318 (2003).

49. E.E. Kim, et al, "A high-resolution multi-spectral imaging system for small satellites," Acta Astronautica **52**, 813-818 (2003).

50. C.L. Miskey and F.C. Bruhweiler, "STIS spectral imagery of the ob stars in NGC 604. I. Description of the extraction technique for a crowded stellar field," Astronomical Journal **125**, 3071-3081 (2003).

51. M. Galand, et al, "Electron and proton aurora observed spectroscopically in the far ultraviolet," Journal of Geophysical Research-Space Physics **107**, art. no.-1129 (2002).

52. J.P. Kerekes and J.E. Baum, "Spectral imaging system analytical model for subpixel object detection," Ieee Transactions on Geoscience and Remote Sensing **40**, 1088-1101 (2002).

53. S.N. White, et al, "Ambient light emission from hydrothermal vents on the Mid-Atlantic Ridge," Geophysical Research Letters **29**, art. no.-1744 (2002).

54. A. Kulcke, et al, "On-line classification of synthetic polymers using near infrared spectral imaging," Journal of near Infrared Spectroscopy **11**, 71-81 (2003).

55. J. Howard, et al, "Coherence-imaging approach to time-resolved charge-exchange recombination spectroscopy in high-temperature plasma," Review of Scientific Instruments **74**, 2060-2063 (2003).

56. D.R. Demers, et al, "Spectroscopic ion beam imaging for investigations into magnetic field mapping of a plasma," Review of Scientific Instruments **74**, 2103-2106 (2003).

57. M.L. Slovak, et al, "Targeting multiple genetic aberrations in isolated tumor cells by spectral fluorescence in situ hybridization," Cancer Detection and Prevention **26**, 171-179 (2002).

58. A.H.N. Hopman, et al, "Improved identification of multicolor chromogenic in situ hybridisation signals by the application of new spectral imaging methods," Cytometry 51-51 (2002).

59. S.I. Tsunoda, et al, "Novel spectral Imaging system combined with confocal laser microscopy for FISH analysis of interphase nuclei," Cytometry 139-139 (2002).

60. H.U.G. Weier, et al, "Towards a full karyotype screening of interphase cells: 'FISH and chip' technology," Molecular and Cellular Endocrinology **183**, S41-S45 (2001).

61. D. Maiti, S. Sennoune, and R. Martinez-Zaguilan, "Proton gradients in human breast cancer cells determined by confocal, multiphoton, and spectral imaging microscopy," Faseb Journal **17**, A467-A467 (2003).

62. A.N. Papadakis, et al, "A novel spectral microscope system: Application in quantitative pathology," Ieee Transactions on Biomedical Engineering **50**, 207-217 (2003).

63. A. Synytsya, et al, "In vitro interaction of macrocyclic photosensitizers with intact mitochondria: a spectroscopic study," Biochimica Et Biophysica Acta-General Subjects **1620**, 85-96 (2003).

64. L. Greenbaum, D. Schwartz, and Z. Malik, "Spectrally resolved microscopy of GFP trafficking," Journal of Histochemistry & Cytochemistry **50**, 1205-1212 (2002).

65. T. Haraguchi, et al, "Spectral imaging fluorescence microscopy," Genes to Cells **7**, 881-887 (2002).

66. J.N.Y. Qu, H.P. Chang, and S.M. Xiong, "Fluorescence spectral imaging for characterization of tissue based on multivariate statistical analysis," Journal of the Optical Society of America a-Optics Image Science and Vision **19**, 1823-1831 (2002).

67. N. Ramanujam, et al, "Fast and noninvasive fluorescence imaging of biological tissues in vivo using a flying-spot scanner," IEEE Trans Biomed Eng **48**, 1034-41. (2001).

68. S. Andersson-Engels, et al, "Preliminary evaluation of two fluorescence imaging methods for the detection and the delineation of basal cell carcinomas of the skin," Lasers Surg Med **26**, 76-82 (2000).

69. J. Hewett, et al, "The application of a compact multispectral imaging system with integrated excitation source to in vivo monitoring of fluorescence during topical photodynamic therapy of superficial skin cancers," Photochem Photobiol **73**, 278-82. (2001).

70. R.G. Nadeau and W. Groner, "The role of a new noninvasive imaging technology in the diagnosis of anemia," J Nutr **131**, 1610S-4S. (2001).

71. U. Thomale, et al, "Visualization of rat pial microcirculation using the novel orthogonal polarized spectral (OPS) imaging after brain injury," J Neurosci Methods **108**, 85-90. (2001).

72. O. Khait, S. Smirnov, and C.D. Tran, "Multispectral imaging microscope with millisecond time resolution," Anal Chem **73**, 732-9. (2001).

73. C.D. Tran, "Development and analytical applications of multispectral imaging techniques: an overview," Fresenius J Anal Chem **369**, 313-9. (2001).

74. C. Balas, "A novel optical imaging method for the early detection, quantitative grading, and mapping of cancerous and precancerous lesions of cervix," IEEE Trans Biomed Eng **48**, 96-104. (2001).

75. S. Gebhart, et al. "Instrumentation considerations in spectral imaging for tissue demarcation: comparing three methods of spectral resolution," in *SPIE Photonics West, Spectral Imaging: Instrumentation, Applications, and Analysis III*, San Jose, CA, 2005: Bellingham, WA.

76. G. Fries and A. Perneczky, "Endoscope-assisted brain surgery: part 2--analysis of 380 procedures," Neurosurgery **42**, 226-31; discussion 231-2 (1998).

77. L. Zamorano, C. Chavantes, and F. Moure, "Endoscopic stereotactic interventions in the treatment of brain lesions," Acta Neurochir Suppl (Wien) **61**, 92-7 (1994).

78. D.B. Moreland, et al, "Endoscopic resection of pituitary lesions through the nostril," Semin Perioper Nurs **7**, 193-9 (1998).

79. S.S. Nasseri, et al, "A combined, minimally invasive transnasal approach to the sella turcica," Am J Rhinol **12**, 409-16 (1998).

80. M. Strowitzki, M. Kiefer, and W.I. Steudel, "A new method of ultrasonic guidance of neuroendoscopic procedures. Technical note," J Neurosurg **96**, 628-32 (2002).

81. K.D. Resch, "Endo-neuro-sonography: first clinical series (52 cases)," Childs Nerv Syst **19**, 137-44 (2003).

82. M. Nakamura, et al, "Image-guided microsurgery with the Mehrkoordinaten Manipulator system for cerebral arteriovenous malformations," J Clin Neurosci **7 Suppl 1**, 10-3 (2000).

83. A. Samii, et al, "Navigation-guided opening of the internal auditory canal via the retrosigmoid route for acoustic neuroma surgery: cadaveric, radiological, and preliminary clinical study," Neurosurgery **47**, 382-7; discussion 388 (2000).

84. M.F. Levesque and F. Parker, "MKM-guided resection of diffuse brainstem neoplasms," Stereotact Funct Neurosurg **73**, 15-8 (1999).

85. K. Roessler, et al, "Image-guided neurosurgery comparing a pointer device system with a navigating microscope: a retrospective analysis of 208 cases," Minim Invasive Neurosurg **41**, 53-7 (1998).

86. C. Nimsky, et al, "Low-field magnetic resonance imaging for intraoperative use in neurosurgery: a 5-year experience," Eur Radiol **12**, 2690-703 (2002).

87. P. Jannin, et al, "[Sulcal identification and neuronavigation in supratentorial cavernoma surgery]," Neurochirurgie **46**, 534-9; discussion 539-40 (2000).

88. R. Steinmeier, et al, "Intraoperative magnetic resonance imaging with the magnetom open scanner: concepts, neurosurgical indications, and procedures: a preliminary report," Neurosurgery **43**, 739-47; discussion 747-8 (1998).

89. V. Seifert, et al, "Open MRI-guided neurosurgery," Acta Neurochir (Wien) **141**, 455-64 (1999).

90. E. Alexander, 3rd, et al, "The present and future role of intraoperative MRI in neurosurgical procedures," Stereotact Funct Neurosurg **68**, 10-7 (1997).

91. J.Y. Qu, Z. Huang, and J. Hua, "Excitation-and-collection geometry insensitive fluorescence imaging of tissue-simulating turbid media," Applied Optics **39**, 3344-3356 (2000).

92. D.Y. Churmakov, I.V. Meglinski, and D.A. Greenhalgh, "Influence of refractive index matching on the photon diffuse reflectance," Phys Med Biol **47**, 4271-85 (2002).

93. J. Wu, et al, "Diffuse Reflectance from Turbid Media - an Analytical Model of Photon Migration," Applied Optics **32**, 1115-1121 (1993).

94. T.J. Pfefer, et al, "Reflectance-based determination of optical properties in highly attenuating tissue," J Biomed Opt **8**, 206-15 (2003).

95. P.R. Bargo, S.A. Prahl, and S.L. Jacques, "Optical properties effects upon the collection efficiency of optical fibers in different probe configurations," Ieee Journal of Selected Topics in Quantum Electronics **9**, 314-321 (2003).

96. P.R. Bargo, S.A. Prahl, and S.L. Jacques, "Collection efficiency of a single optical fiber in turbid media," Applied Optics **42**, 3187-3197 (2003).

97. Q. Liu, C.F. Zhu, and N. Ramanujam, "Experimental validation of Monte Carlo modeling of fluorescence in tissues in the UV-visible spectrum," Journal of Biomedical Optics **8**, 223-236 (2003).

98. C.F. Zhu, et al, "Use of a multiseparation fiber optic probe for the optical diagnosis of breast cancer," Journal of Biomedical Optics **10**, - (2005).

99. J.M. Schmitt and G. Kumar, "Spectral distortions in near-infrared spectroscopy of turbid materials," Applied Spectroscopy **50**, 1066-1073 (1996).

100. G. Kumar and J.M. Schmitt, "Optimal probe geometry for near-infrared spectroscopy of biological tissue," Applied Optics **36**, 2286-2293 (1997).

101. A.J. Welch, et al, "Propagation of fluorescent light," Lasers Surg Med **21**, 166-78 (1997).

102. T.J. Pfefer, L.S. Matchette, and R. Drezek, "Influence of illumination-collection geometry on fluorescence spectroscopy in multilayer tissue," Medical & Biological Engineering & Computing **42**, 669-673 (2004).

103. T.J. Pfefer, et al, "Selective detection of fluorophore layers in turbid media: the role of fiber-optic probe design," Optics Letters **28**, 120-122 (2003).

104. T.J. Pfefer, et al, "Multiple-fiber probe design for fluorescence spectroscopy in tissue," Applied Optics **41**, 4712-4721 (2002).

105. C.F. Zhu, Q. Liu, and N. Ramanujam, "Effect of fiber optic probe geometry on depth-resolved fluorescence measurements from epithelial tissues: a Monte Carlo simulation," Journal of Biomedical Optics **8**, 237-247 (2003).

106. S.K. Chang, et al, "Analytical model to describe fluorescence spectra of normal and preneoplastic epithelial tissue: comparison with Monte Carlo simulations and clinical measurements," Journal of Biomedical Optics **9**, 511-522 (2004).

107. J. Wu, M.S. Feld, and R.P. Rava, "Analytical Model for extracting intrinsic fluorescence in turbid media," Applied Optics **32**, 3585-3595 (1993).

108. A.J. Durkin, et al, "Relation between Fluorescence-Spectra of Dilute and Turbid Samples," Applied Optics **33**, 414-423 (1994).

109. C.M. Gardner, S.L. Jacques, and A.J. Welch, "Fluorescence spectroscopy of tissue: recovery of instrinsic fluorescence from measured fluorescence," Applied Optics **35**, 1780-1792 (1996).

110. Q.G. Zhang, et al, "Turbidity-free fluorescence spectroscopy of biological tissue," Optics Letters **25**, 1451-1453 (2000).

111. M.G. Muller, et al, "Intrinsic fluorescence spectroscopy in turbid media: disentangling effects of scattering and absorption," Applied Optics **40**, 4633-4646 (2001).

112. R. Richards-Kortum, et al, "Spectral diagnosis of atherosclerosis using an optical fiber laser catheter," Am Heart J **118**, 381-91 (1989).

113. M. Keijzer, et al, "Fluorescence spectroscopy of turbid media: autofluorescence of the human aorta," Applied Optics **28**, 4286-4292 (1989).

114. S. Avrillier, et al, "Influence of the emission-reception geometry in laser-induced fluorescence spectra from turbid media," Applied Optics **37**, 2781-2787 (1998).

115. J. Swartling, et al, "Fluorescence spectra provide information on the depth of fluorescent lesions in tissue," Applied Optics **44**, 1934-1941 (2005).

CHAPTER III

IN VITRO DETERMINATION OF NORMAL AND NEOPLASTIC HUMAN BRAIN TISSUE OPTICAL PROPERTIES USING INVERSE ADDING-DOUBLING

Abstract

To complement a project toward the development of real-time optical biopsy for brain tissue discrimination and surgical resection guidance, the optical properties of various brain tissues were measured *in vitro* and correlated to features within clinical diffuse reflectance tissue spectra measured *in vivo*. Reflectance and transmission spectra of *in vitro* brain tissue samples were measured with a single-integrating-sphere spectrometer for wavelengths 400 to 1300 nm and converted to absorption and reduced scattering spectra using an inverse adding-doubling technique. Optical property spectra were classified as deriving from white matter, gray matter, or glioma tissue according to histopathologic diagnosis and mean absorption and reduced scattering spectra were calculated for the three tissue categories. Absolute reduced scattering and absorption values and their relative differences between histopathological groups agreed with previously reported results with the exception that absorption coefficients were often overestimated, most likely due to biologic variability or unaccounted light loss during reflectance/transmission measurement. Absorption spectra for the three tissue classes were dominated by hemoglobin absorption below 600 nm and water absorption above 900 nm and generally determined the shape of corresponding clinical diffuse reflectance spectra. Reduced scattering spectral shapes followed the power curve predicted by the Rayleigh limit of Mie scattering theory. While tissue absorption governed the shape of clinical diffuse reflectance spectra, reduced scattering determined their relative emission intensities between the three tissue categories.

Introduction

Diffuse reflectance spectroscopy is directly related to tissue absorption and scattering [1]. Because optical property differences between tissue types directly affect tissue diffuse reflectance, optical property spectra have the capability to explain feature disparities in diffuse reflectance spectra observed between normal and neoplastic tissues. The most obvious change within a diffuse reflectance spectrum during the progression from normal to neoplastic

frequently correlates to an increase in blood absorption related to the development of neo-vascularization inherent to tumor tissue. Our research group is focused on the development of using combined fluorescence and diffuse reflectance spectroscopy for brain tumor demarcation. We are currently in the process of acquiring spectra from a large multi-center clinical study in order to develop an unbiased discrimination method for differentiation between human brain tissue types [2-4]. It is therefore of extreme interest to us to understand the effect of optical properties on diffuse reflectance spectra of normal and malignant brain tissues, which in turn affect the performance of this method in tissue discrimination.

Optical properties of normal and neoplastic brain tissues have been measured, reported, and compiled [5] within the literature multiple times, both at discrete wavelengths tailored for specific applications [6, 7] as well as over large spectral ranges [8-10]. However, many of these reports measure penetration depths and effective attenuation coefficients [5, 11, 12] which combine the individual contributions of absorption and scattering into a single tissue parameter, making it difficult to correlate their individual contributions to diffuse reflectance spectral features. Some reports measure optical properties or related parameters at isolated wavelengths which cannot be used to explain inter-tissue *spectral* feature disparities. Finally, some employ indirect methods to determine optical properties, such as Kubelka-Munk (which assumes isotropic scattering), that *approximate* the light transport equation and are subsequently limited in their accuracy and ability to predict soft tissue behavior.

Inverse Monte Carlo (IMC) methods can be used to determine independent absorption, scattering, and anisotropy coefficients over any spectral range, without any simplifications that might limit their accuracy. This iterative method of light propagation repeatedly adjusts the sample optical properties until the Monte Carlo predictions for diffuse reflectance as well as diffused and collimated transmission converge to experimental values for a given wavelength. Due to its ability to compensate for different measurement and sample geometries and to account for sources of experimental error such as light lost out the sides of the sample, IMC is currently regarded as the most robust, versatile, and accurate optical property determination method available. However, large computation times are needed to acquire adequate signal-to-noise ratio from the Monte Carlo simulations and ensure proper convergence to the correct optical properties at each wavelength within the spectral range of interest. Thus, the measurement efficiency of IMC is poor, limiting researchers to its use at a few isolated wavelengths or across

spectral regions for only a handful of tissue samples. Bevilacqua et al [6] reported *in vivo* optical properties of brain tissues at four near-infrared wavelengths from a total of eight different tissue sites within two patients. Yaroslavsky et al [10] measured IMC absorption and scattering spectra (360-1100 nm) for a limited number of tumor and normal brain tissues which may not accurately represent true population values (biased results) and the inherent inter-patient variability that confounds most researchers.

The inverse adding-doubling (IAD) method developed by Prahl et al [13] represents a numerical solution to the radiative transport equation which can be used to calculate the absorption (μ_a) and reduced scattering (μ_s') coefficients of a sample from measurements of reflectance (R) and transmission (T). The program predicts R and T from the sample for a given albedo, optical thickness, and scattering anisotropy using the forward adding-doubling method. The predictions for R and T are then compared to the actual measurements, and the derived optical parameters are adjusted to obtain more accurate predictions. The process is repeated until the predicted and measured values match within a specified tolerance. These final optical parameters can then be used to calculate absorption and reduced scattering coefficients for the sample. If collimated transmission is independently measured from the sample, the IAD program is able to separate the contributions of scattering and anisotropy to reduced scattering, giving an estimate for the anisotropy factor and allowing subsequent calculation of the scattering coefficient. The main advantage to the IAD method is its combination of fast computation and validity over practically all albedo values. It has been used for optical property determination within a host of tissues [14], using double [15] and single integrating spheres [16] for reflectance and transmission measurement, and its accuracy has been validated by multiple research groups [13, 15, 17].

In this paper, we present results from a study of the optical properties from normal and tumor brain tissues *in vitro*. Transmission and reflectance were measured from 83 samples of human white matter, gray matter, and glioma tissues from 400-1300 nm using a spectrophotometer, and the optical properties were calculated using an inverse adding-doubling method that has the accuracy equivalent to IMC determination and efficiency sufficient to interrogate a large population of tissue samples [13, 17]. Calculated brain tissue optical properties were compared to previously published optical property values determined by IMC [6, 10]. The results were subsequently correlated to features observed *in vivo* within clinical diffuse

reflectance spectra from the three tissue classes in an effort to elucidate the tissue differences which underlie the spectral feature disparities between normal and neoplastic brain tissues.

Materials and Methods

Optical Property Spectral Measurement in vitro

Eighty-three brain tissue samples were acquired during open craniotomy for tumor resection or temporal lobectomy. The samples were snap-frozen in liquid nitrogen after tissue removal and stored at –80ºC until *in vitro* measurement. Immediately prior to measurement, the samples were thawed for 10 minutes in a 25ºC, 7.4 pH phosphate buffer saline solution to remove residual blood. The samples were then mounted between two glass microscope slides and compressed in order to yield adequate surface area (greater than 80% of the port size). Surface tension with the microscope slides trapped the saline between the slides, keeping the samples well-hydrated during the measurements; and spacers were placed between the microscope slides to maintain a constant sample thickness throughout the measurements. The thickness of the samples ranged from 0.22 to 1.25 mm. Total reflectance (diffuse + specular) and total transmission (diffuse + collimated) spectra were measured from 400 to 1300 nm at four sites on each tissue sample using a Perkin-Elmer Lambda 900 Spectrophotometer with a single 150-mm-diameter integrating sphere. The four reflectance and transmittance spectra were averaged and composite spectra were created for each tissue sample. The mean spectra were filtered with a high-order low-pass digital filter to remove system noise without losing spectral features.

An inverse adding-doubling technique developed by Prahl et al [13] was used to determine the dimensionless albedo (α) and optical thickness (τ) spectra from the mean reflectance and transmission spectra for each sample. Four quadrature points were used in the IAD calculation and the indices of refraction of tissue and the glass slides were estimated to be 1.40 and 1.54, respectively. Since collimated transmission spectra were not obtained in these measurements, a fixed anisotropy coefficient (g = 0.85) [10] was assumed for every wavelength and for every sample. The absorption and reduced scattering spectra were calculated from the albedo, optical thickness, and assumed anisotropy coefficient using

$$\mu_s' = \frac{\alpha\tau}{d}(1-g)$$

$$\mu_a = \frac{(1-\alpha)\tau}{d}$$

where d is the sample thickness. The measurement protocol was independently validated by comparing measured transmission and reflectance measurements and subsequent IAD-calculated reduced scattering and absorption spectra to predictions from Beer's Law and Mie scattering theory for solutions of polystyrene microspheres and various chromophores. The assumption that the anisotropy value has negligible effect on IAD-predicted reduced scattering coefficients was also verified for a range of measured reflectance and transmission values.

Optical property spectra were calculated for 83 brain tissue samples acquired from 12 patients. After measurement, each sample was fixed in formalin and sent to histology for tissue classification. Samples were classified as white matter, gray matter, or glioma. Mean and standard error of the absorption and reduced scattering spectra were calculated for each tissue category.

Diffuse Reflectance Spectral Measurement in vivo

The optical properties calculated in this work were compared to *in vivo* diffuse reflectance spectra measured as part of an on-going clinical study [2-4] at Vanderbilt University Medical Center. All patients undergoing open craniotomy for primary tumor resection or temporal lobectomy were recruited equally without age, race, and gender preference and written consent was obtained from each patient under a protocol approved by the Vanderbilt Institutional Review Board. Patients with recurrent brain tumor were not particularly selected. Fluorescence and diffuse reflectance spectra (400-800 nm) were measured using a portable spectroscopic system consisting of a nitrogen laser for fluorescence excitation, a white light source for diffuse reflectance, and a spectrometer all controlled by a computer. A detailed description of the instrument can be found elsewhere [2]. Light delivery and collection was measured using an optical probe consisting of seven, 300-micron (core) optical fibers in a six-around-one configuration with the fluorescence and diffuse reflectance excitation fibers located on opposite sides of the outer ring of fibers.

Six to ten sites were investigated for each patient by the participating neurosurgeons. These sites usually included cortical tissues, brain tumor core, tumor margins, and normal brain tissues distal to the tumor bed as defined by intraoperative ultrasound and a surgical navigation system. The fiber-optic probe was placed lightly in contact with the surface of the investigated

site and three optical spectra (baseline, fluorescence, and diffuse reflectance) were sequentially acquired. Upon completion of spectral acquisition, a punch biopsy was taken from each investigated site and placed in formalin. The tip of the fiber-optic probe was maintained clean using saline-moisturized gauze throughout the study to avoid blood clot formation, which would induce artifacts within the measured spectra. Reference measurements were performed at the end of each study to monitor and account for any variations in system performance between experiments. This allowed spectral calibration and therefore direct spectral comparison between different patients. Biopsy samples were sent for histopathological processing and read by a consulting neuro-pathologist.

All spectra were processed to eliminate inherent artifacts. The baseline spectrum was first subtracted from each emission spectrum. Calibration factors, derived from a standard calibration procedure, were then multiplied to the baseline-corrected spectra to remove wavelength-dependent characteristics of the spectroscopic system. Processed spectra were then correlated to their corresponding histological identities and mean diffuse reflectance spectra were calculated for the three tissue classes: white matter (n = 55), gray matter (n = 58), and core glioma tissues (n = 82).

Correlating spectral features between *in vitro* optical property measurements and *in vivo* diffuse reflectance spectra relies upon the assumption that *in vitro* optical properties are a reasonable approximation of the *in vivo* optical properties which yield the measured diffuse reflectance spectra. To validate this assumption, Monte Carlo simulation was used to estimate diffuse reflectance emission spectra from bulk white matter, gray matter, and tumor tissues with optical properties equivalent to our mean measured absorption and reduced scattering spectra. Briefly, diffuse reflectance emission was simulated using a grid of optical property pairs (μ_a, μ_s') that spanned the mean optical property spectra from the three tissue classes. Each simulation in the grid generated a single diffuse reflectance intensity, ultimately creating a diffuse reflectance emission surface as a function of absorption and reduced scattering. This surface was interpolated using the measured absorption and reduced scattering spectra from the three tissue groups to produce simulated diffuse reflectance spectra. The three simulated diffuse reflectance spectra were uniformly scaled by the factor necessary to give the measured and simulated spectra from white matter equivalent average emission intensities between 600 and 800 nm. The scaling

was performed for comparison purposes while maintaining spectral lineshape as well as relative emission intensities between the three tissue categories.

Statistical Spectral Comparison

Student's t-tests (two-tailed, unequal variance) were applied to the diffuse reflectance and optical property spectra to determine regions of significant spectral differences between tissue categories. Each tissue category was individually compared to the other two (i.e. white matter vs. gray matter; white matter vs. tumor; gray matter vs. tumor), and the calibrated diffuse reflectance intensities and optical property values at each investigated wavelength were treated as independent measurements. The null hypotheses were tested using a Student's t-test at each wavelength and p-value spectra were compiled for the mean diffuse reflectance, absorption, and reduced scattering spectra between the tissue categories.

Results

Based on histology, which served as the gold standard for all comparisons, the 83 tissue samples were identified to 19 white matter samples, 25 gray matter samples, and 39 gliomas.

Optical Property Spectral Measurement in vitro

Figure 1a shows the absorption coefficient spectra for the three tissue categories. The absorption bands of hemoglobin below 600 nm and water above 900 nm dominate the spectra, with consistently low absorption over the spectral range known as the "therapeutic window" ($600 < \lambda < 1000$ nm). All three spectra demonstrate peak absorption bands around 425 nm and 550 nm characteristic of oxy- and deoxy-hemoglobin. From visual inspection, these findings are similar to results reported by Eggert and Blazek [8] using Kubelka-Munk theory and by Yaroslavsky et al [10] using an IMC technique, but contain more pronounced hemoglobin absorption features.

The reduced scattering coefficient spectra (figure 1b) generally decrease with increasing wavelength, consistent with Rayleigh scattering theory and previously published results [10]. The gray-matter and tumor spectra contain a scattering peak at a wavelength (420 nm) coincident with peak hemoglobin absorption, behavior which contrasts previous reports which showed no deviation from the monotonic decrease predicted by Rayleigh scattering theory. The relative

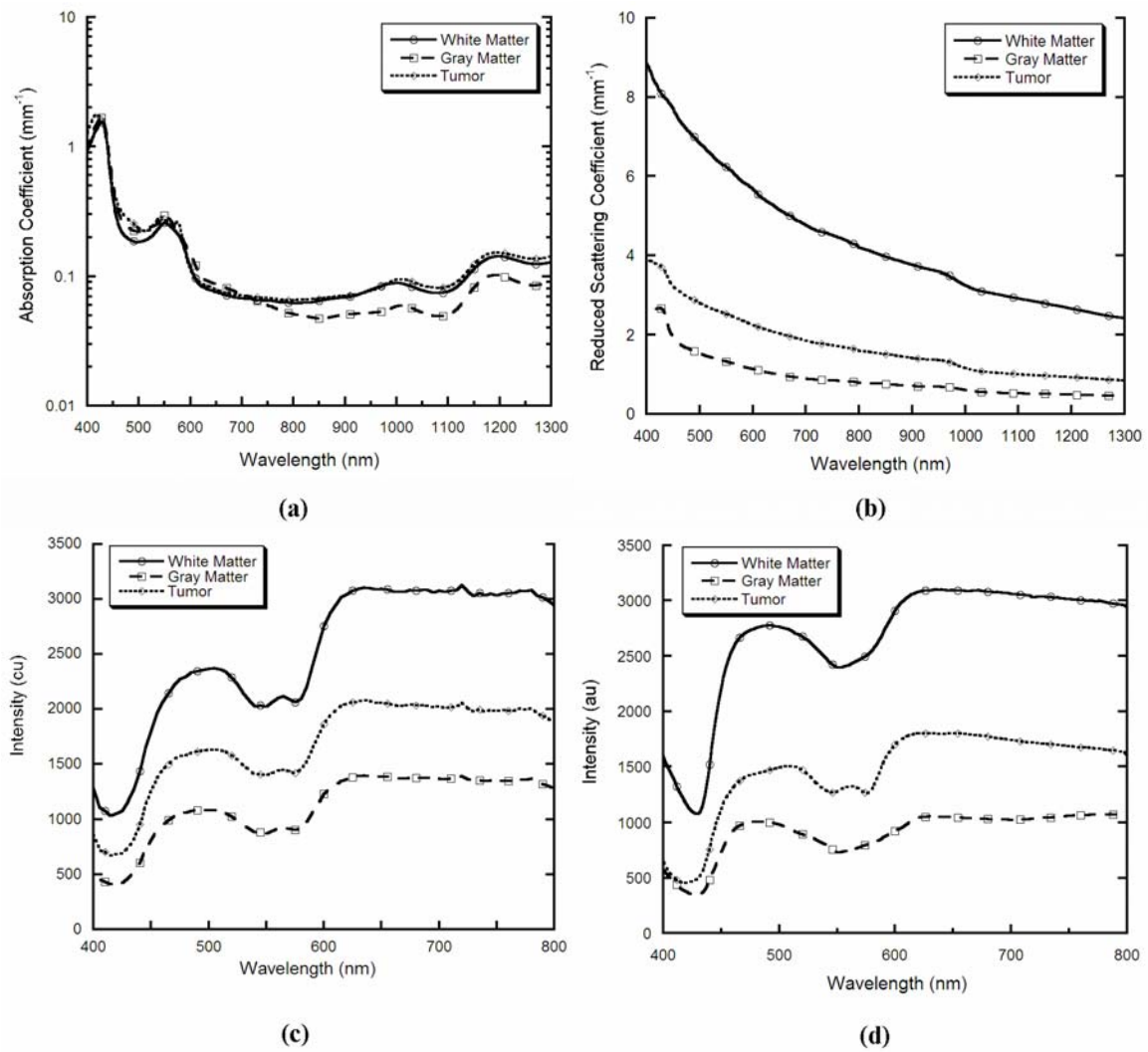

Figure 1. Mean experimental (a) absorption coefficient, (b) reduced scattering coefficient, and (c) diffuse reflectance spectra for white matter, gray matter, and glioma tissues. (d) Mean predicted diffuse reflectance spectra using Monte Carlo simulation based upon the mean experimental absorption and reduced scattering coefficient spectra in (a) and (b). Simulated diffuse reflectance spectra have been normalized for comparison purposes while maintaining the relative intensities between tissue classes.

levels of reduced scattering are highest for white matter and lowest for gray matter for all investigated wavelengths, consistent with Yaroslavsky et al.

Diffuse Reflectance Spectral Measurement in vivo

The mean *in vivo* diffuse reflectance spectra between 400 and 800 nm measured from white matter, gray matter, and tumor tissues in the multi-patient clinical study (figure 1c) possess similar spectral shapes but different relative intensities, with white matter boasting the highest diffuse reflectance, gray matter the lowest, and tumor tissue between the two. This trend

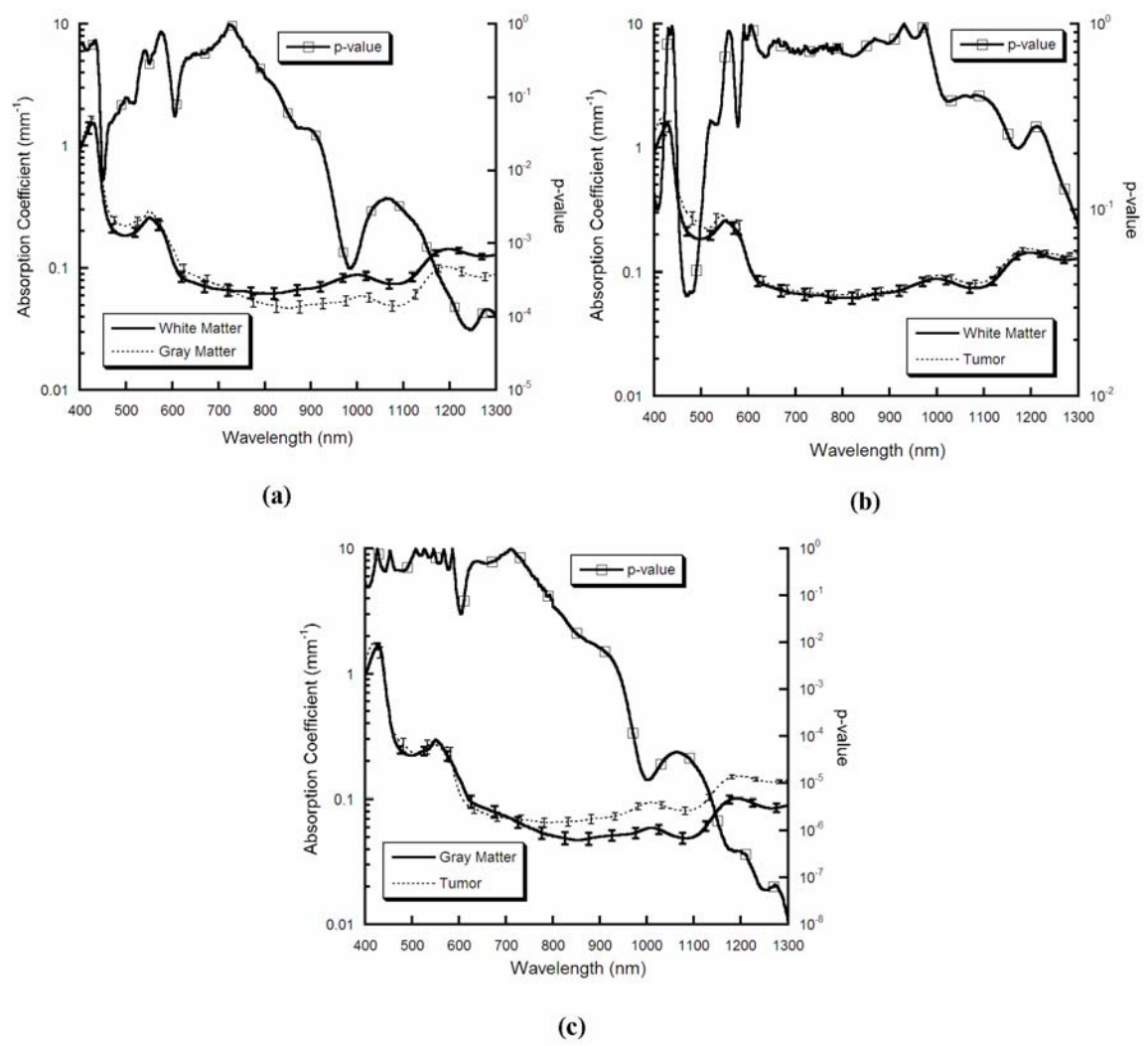

Figure 2. Mean (± one standard error) absorption coefficient spectra comparing (a) white and gray matter, (b) white matter and tumor, and (c) gray matter and tumor. P-values derive from two-tailed t-tests comparing the mean spectra.

coincides with that observed in the reduced scattering properties measured *in vitro*, suggesting that relative diffuse reflectance magnitude is dictated by the degree of tissue scattering. The diffuse reflectance spectra contain three pronounced valleys near 420 nm, 540 nm, and 580 nm, corresponding to strong oxy- and deoxy-hemoglobin absorption, hence high blood content in the *in vivo* interrogated tissue volumes. The maximum diffuse reflectance consistently occurs between 600 and 800 nm, coincident with the low-absorption therapeutic window. These observations suggest that the spectral shape of diffuse reflectance is affected by tissue absorption.

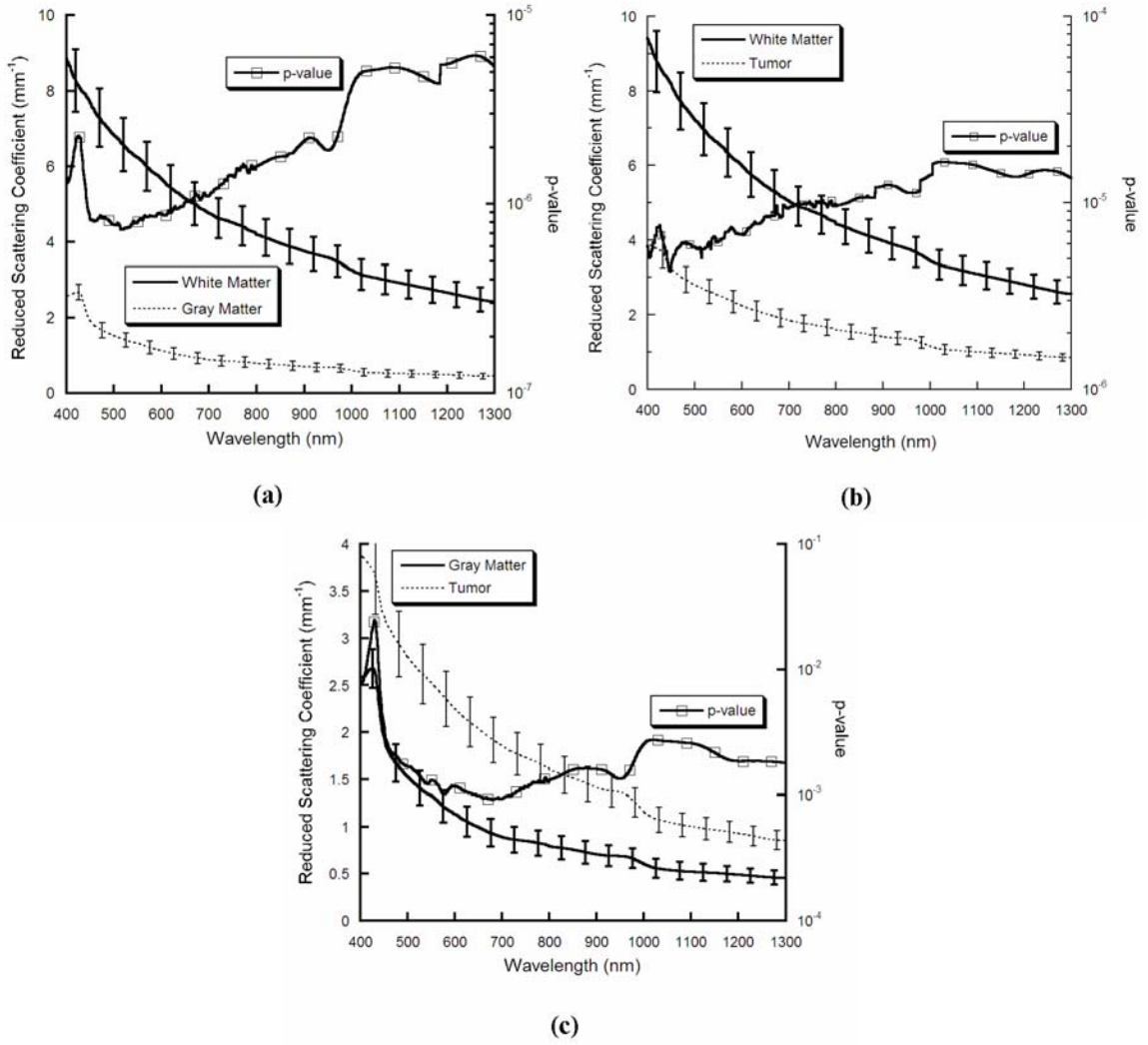

Figure 3. Mean (± one standard error) reduced scattering coefficient spectra comparing (a) white and gray matter, (b) white matter and tumor, and (c) gray matter and tumor. P-values derive from two-tailed t-tests comparing the mean spectra.

This research relies upon the assumption that *in vitro* brain tissue samples are a reasonable approximation of the *in vivo* environment, and as such, that the *in vitro* optical property measurements in Figure 1a and b correlate to *in vivo* optical properties which yield the diffuse reflectance spectra shown in Figure 1c. To validate this assumption, Monte Carlo simulation was used to estimate diffuse reflectance emission spectra (Figure 1d) from bulk white matter, gray matter, and tumor tissues with optical properties equivalent to our mean absorption and reduced scattering spectra. Comparing figures 1c and 1d, several differences are observed between the measured and simulated diffuse reflectance spectra from white and gray matter and

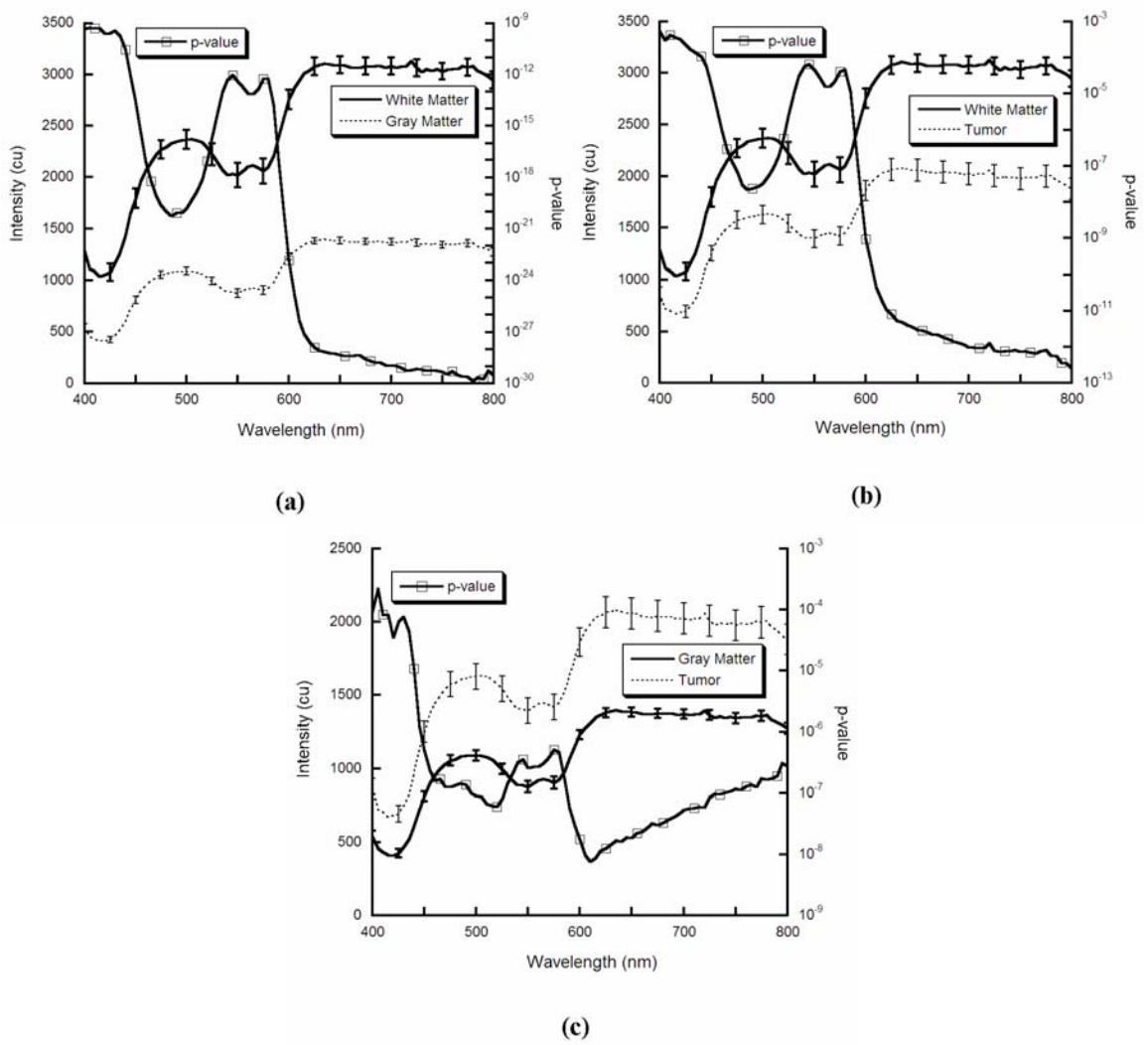

Figure 4. Mean (± one standard error) diffuse reflectance spectra comparing (a) white and gray matter, (b) white matter and tumor, and (c) gray matter and tumor. P-values derive from two-tailed t-tests comparing the mean spectra.

tumor. Besides the obvious disparity in oxy- and deoxy-hemoglobin absorption behavior in the white and gray matter spectra, another significant contributor may be assumptions made in specifying the excitation-collection geometry of the diffuse reflectance measurements in the Monte Carlo simulations. Despite these minor differences, the similarity in general lineshape and relative emission intensities between tissue categories indicates that the optical property spectra measured *in vitro* correlate to brain tissue optical properties *in vivo*.

Statistical Spectral Comparison

Student's t-tests were applied to the diffuse reflectance and optical property coefficient spectra to highlight the statistically significant differences between the tissue categories. Large regions of overlap between the mean (± one standard error) absorption spectra of the three tissue classes (figure 2) result in only discrete ranges where the differences are statistically significant ($p < .01$). White and gray matter absorption spectra are significantly different above 936 nm; white matter and tumor differences are not significant for any wavelength range; and gray matter and tumor are significantly different at all wavelengths above 882 nm. These results indicate that blood absorption is similar in all three tissue classes while water absorption is significantly lower in gray matter relative to white matter and tumor tissue.

The mean white matter reduced scattering spectrum is significantly higher than gray matter and tumor tissue reduced scattering (figures 3a,b) for all wavelengths. Differences between gray matter and tumor tissue scattering (figure 3c) are less appreciable with statistical significance only found above 438 nm ($p < .01$). It is important to note that while the standard errors appear largest for white matter, its coefficients of variance (COVs) are the smallest, while tumor tissue boasts the largest COVs.

The mean (± one standard error) white and gray matter diffuse reflectance spectra (figure 4a) do not intersect at any wavelengths, yielding significance values below 10^{-9} over the entire spectral range. While the mean tumor tissue spectrum falls between the mean gray and white matter spectra (figure 4b,c), the mean spectral differences were still significant ($p < .001$) for all wavelengths. For the three inter-class comparisons, the p-value spectra appeared inversely related to the diffuse reflectance intensities, suggesting that diffuse reflectance dispersion results from variable blood content (and therefore absorption) between samples and/or from the increased impact of system noise where measured diffuse reflectance intensities are reduced. This behavior is consistent with the absorption coefficient measurements where the largest p-values were found at the hemoglobin absorption peaks.

Discussion

In this study, we report optical properties of normal and tumor brain tissues obtained using an inverse adding-doubling model, a method that has never been used to study brain tissues. This method has been proven more accurate and versatile than Kubelka-Munk theory and

more efficient than inverse Monte Carlo techniques [13]. While efficiency lends little weight to scientific significance, it allowed measurement from over 80 tissue samples and thus provided mean optical property spectra which complements those reported by Yaroslavsky et al [10]. Further, IAD yields absolute optical property coefficients which can be used to simulate photon migration within brain tissue. Such simulations can be exploited to extract intrinsic fluorescence information from tissue fluorescence spectra [18], for optical tomography image reconstruction, and to design fiber-optic arrangements for spectroscopy probes [19] seeking to selectively amplify spectral differences between normal and neoplastic tissues. Since the purpose of our study here is to aid in the understanding and development of optical methods for brain tumor demarcation, the previous demonstration of the utility of IAD for enhancing optical biopsy methods validate the use of this method in this study.

Previous reports on brain tissue optical properties found in the literature can be classified into two categories: (1) those that report optical properties at isolated wavelengths and (2) those that report full optical property spectra over a wide wavelength range. Unfortunately, dispersion within both groups can complicate validating new study results relative to published ones. Optical property coefficients for human brain tissue reported in literature vary between 94% (white matter reduced scattering at 630 nm) and 171% (gray matter absorption at 630 nm) in measurements of equivalent tissue types at similar wavelengths [7, 10]. These disparities can typically be traced back to experimental details or to limitations in the method of optical property determination from experimental measurements. For example, Kubelka-Munk theory [8, 9] assumes isotropic scattering even though tissue scattering is forward biased. **Thus, in the current study, any comparisons to previously published reports will emphasize relative optical property trends between tissue categories, as opposed to magnitudes of the coefficients.** For simplicity, any comparisons will be limited to optical properties published using IMC [6, 10].

In terms of relative differences in optical properties between tissue classes, the results presented here agree with the spectra reported by Yaroslavsky et al [10]. Both methods report the presence of equivalent hemoglobin absorption between white and gray matter, with significantly higher reduced scattering and water absorption in white matter. Bevilacqua et al [6] reported the optical properties of human gray matter *in vivo* at four near-infrared wavelengths using IMC simulation of diffuse reflectance data for multiple source-detector separations. As demonstrated

Table 1. Comparison of (a) mean reduced scattering coefficients and (b) mean absorption coefficients of white and gray matter measured by inverse adding-doubling (IAD) and inverse Monte Carlo (IMC). Percent differences are calculated as the ratio of the difference to the mean of the two measurements.

(a)	White Matter			Gray Matter		
Wavelength (nm)	IAD	IMC	% Difference	IAD	IMC	% Difference
450[a]	7.71	9.24	-18.1%	1.94	1.40	32.0%
510[a]	6.72	8.09	-18.6%	1.48	1.27	15.2%
630[a]	5.34	6.54	-20.3%	1.04	0.99	5.2%
670[a]	5.01	6.02	-18.3%	0.95	0.84	12.1%
674[b]				0.94	1.00	-6.2%
811[b]				0.78	0.87	-10.5%
849[b]				0.76	0.87	-13.9%
850[a]	3.97	4.10	-3.3%			
956[b]				0.69	0.86	-22.7%
1064[a]	3.02	3.26	-7.7%	0.53	0.57	-6.7%

[a] IMC values acquired from Yaroslavsky *et al* (2002)
[b] IMC values acquired from Bevilacqua *et al* (1999)

(b)	White Matter			Gray Matter		
Wavelength (nm)	IAD	IMC	% Difference	IAD	IMC	% Difference
450[a]	0.396	0.14	95.5%	0.516	0.07	152.2%
510[a]	0.187	0.10	60.6%	0.227	0.04	140.1%
630[a]	0.081	0.08	1.2%	0.093	0.02	129.2%
670[a]	0.071	0.07	1.5%	0.081	0.02	120.7%
674[b]				0.080	0.02	120.0%
811[b]				0.050	0.02	85.7%
849[b]				0.047	< 0.01	129.8%
850[a]	0.064	0.10	-43.5%			
956[b]				0.052	0.02	88.9%
1064[a]	0.075	0.10	-28.6%	0.050	0.05	0.3%

[a] IMC values acquired from Yaroslavsky *et al* (2002)
[b] IMC values acquired from Bevilacqua *et al* (1999)

in table 1a, the absolute magnitude of reduced scattering reported here agree with previously published values, generally staying within 20%. However, as shown in table 1b, our measurements for the absolute magnitude of absorption generally overestimate previous results, most significantly at the hemoglobin absorption bands for white and gray matter and within the therapeutic window ($600 < \lambda < 1000$ nm) for gray matter.

While differences between published reports can be due to simple biologic variability in the measured samples, potential sources of error in optical property measurement include artifacts induced by sample preparation, limitations in measurement technique, and assumptions in the inversion technique (e.g. IAD, IMC, Kubelka-Munk). The findings of Roggan et al [20]

are often cited when discussing the effects of sample preparation on tissue optical properties; however, the trends in the optical properties reported here are not consistent with the effects observed by Roggan et al. Using a single-integrating sphere combined with IMC to measure the optical properties of porcine liver tissue, Roggan et al determined that snap freezing tissue samples in liquid nitrogen produces changes in absorption and reduced scattering coefficients which are statistically insignificant, although it produces significant decreases in the scattering coefficient. Roggan et al also investigated the effect of soaking samples in saline (e.g. for thawing purposes) prior to measurement and observed a marked decrease in absorption due to washing out the chromophores. However, in a quick comparison study as part of this research, it was observed that snap freezing, tissue storage, and thawing in saline had minimal effect on our measured *in vitro* optical properties as compared to four tissue samples measured *ex vivo* (immediately after resection) which were subject to none of those measures. In fact, the *ex vivo* samples exhibited *higher* reduced scattering and *lower* absorption than the mean spectra reported here for the respective tissue categories, results counter to the findings of Roggan et al, suggesting the differences evident in Table 1 are not due to these sample preparation details.

The overestimation in absorption coefficient relative to previously published reports (Table 1b) may be due to tissue compression or to light loss out the ports of the integrating sphere during reflectance and transmission measurement. According to Chan et al [21], tissue compression between microscope slides can lead to an increase in scattering and absorption due to decreased tissue volume and therefore an increase in scatterer and chromophore concentration. However, it should be noted that many researchers in the optical property field operate under the assumption that tissue is incompressible [22] and not subject to these effects. One of the most significant experimental errors in the determination of optical properties using integrating sphere reflectance and transmission measurements is light lost out the entrance and exit ports due to insufficient sample size [17]. If the sample diameter is not sufficient to completely cover the ports of the integrating sphere, significant light losses will occur, resulting in underestimation of transmission and reflection and overestimation of IAD-predicted absorption. Given the small size of human brain tissue samples that can be reasonably acquired, compression was required to maximally cover the entrance and exit ports (diameter = 1 inch) of the integrating sphere. Since complete port coverage was not always possible, our measurements may be subject to these artifacts and the absorption coefficients reported here may overestimate true, *in vivo* brain tissue

optical properties, consistent with the overestimation evident in Table 1b. Further, since this artifact is more significant in gray matter than white matter, overestimated absorption may also explain why the relative levels of simulated diffuse reflectance between gray matter and white matter are less than that measured *in vivo* (Figures 1c,d).

An area of particular concern in comparing our optical property spectra with those published by Yaroslavsky et al is the presence of a peak at 420 nm within IAD-calculated scattering spectra that corresponds to peak hemoglobin absorption. This is unlike IMC scattering which demonstrates monotonic decreases with wavelength characteristic of the Rayleigh limit of Mie scattering. To investigate possible sources of this inter-parameter "crosstalk," a problem which is well-known in optical tomography [23-26], IAD was used to calculate albedo and optical thickness for all possible combinations of measured reflectance and transmission. A (dimensionless) scattering coefficient surface was then created (from the product of albedo and optical thickness) as a function of reflectance and transmission such that measured reflectance and transmission spectra can be overlaid on the surface contours (Figure 5). Comparing spectra of samples with crosstalk to those without suggests that crosstalk occurs when hemoglobin absorption at 420 nm affects a larger decrease in transmission than in reflectance, causing the crosstalk curves to ascend the scattering contours, subsequently creating local maxima in the scattering spectra. Statistically, the drop in transmission relative to reflectance from the long wavelengths (650 to 1300 nm) to the hemoglobin peak is significantly larger in gray matter samples that exhibit crosstalk ($p < 0.05$). As such, crosstalk seen in the gray matter and tumor scattering spectra may be caused by inherent limitations or non-linearities in the measurement of low reflectance levels which result from high absorption and low scattering. This theory is supported by the facts that this crosstalk is most consistently present within gray matter samples which have the lowest scattering and is strongest within tumor samples which have the highest peak absorption. It should be noted that a reduced scattering surface calculated using an IMC technique possesses the same basic contours (results not shown) as the IAD-predicted surface in Figure 5, such that we would expect IMC to produce similar crosstalk when given identical reflectance-transmission spectra. Unfortunately, without a number of calibrated reflectance standards, it is difficult to experimentally validate the linearity of reflectance measurements in an integrating sphere setup.

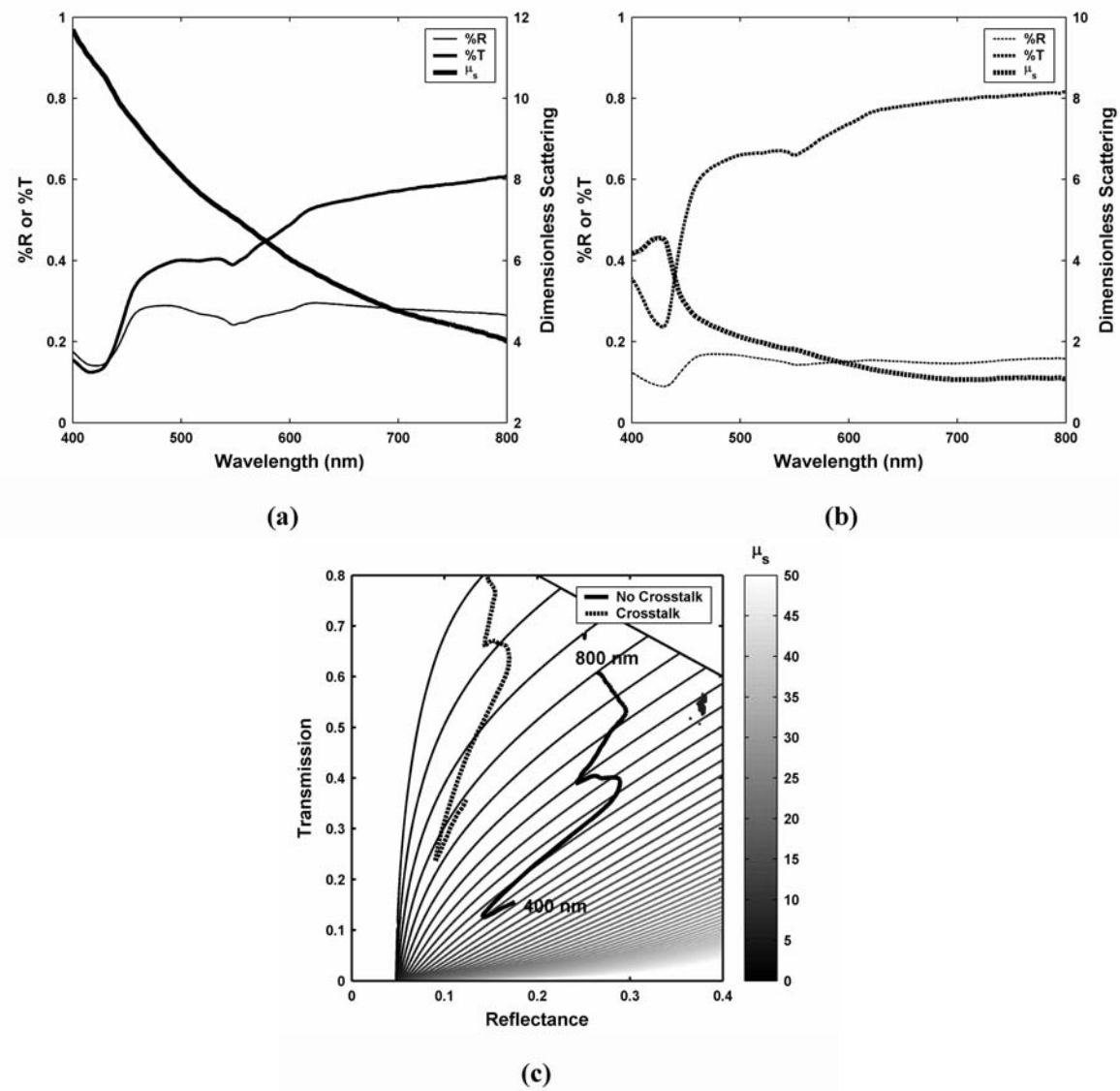

Figure 5. Reflectance, transmission, and dimensionless scattering spectra for gray matter samples (a) without crosstalk and (b) with crosstalk. (c) Dimensionless scattering map predicted by IAD as a function of measured reflectance and transmission. Dimensionless scattering is the product of albedo and optical thickness. Other parameters (indices of refraction, scattering anisotropy) in the IAD model were kept constant with previous methods. Reflectance-transmission curves from the gray matter samples with and without crosstalk have been overlaid. Contours are spaced in one-unit increments from 1 (top left) to 50 (bottom right).

Inspection of the mean absorption spectra suggests that tissue absorption dictates the line shape of diffuse reflectance spectra between the three tissue categories but has little effect on their relative emission magnitudes. Brain tissue absorption spectra are dominated by the characteristic hemoglobin and water absorption bands, with global maxima near 420 nm (hemoglobin) and local maxima near 550 nm (hemoglobin), 1000 nm (water), and 1200 nm

(water). While the diffuse reflectance spectra were not measured to encompass the water absorption peaks, blood absorption created emission valleys near 420 and 550 nm and relatively constant emission over the low-absorption therapeutic window. In terms of magnitude, the tissue absorption spectra depict equivalent levels of hemoglobin-related absorption (below 600 nm) between white and gray matter and tumor tissue, with lowest water-related absorption (above 1000 nm) in gray matter. The diffuse reflectance spectra, on the other hand, demonstrated significantly higher emission for white matter and lowest emission for gray matter over the entire spectral range.

It was observed that the mean white and gray matter absorption spectra exhibited a single absorption peak at 550 nm characteristic of deoxy-hemoglobin (Hb). In addition, normal brain tissues possessed absorption peaks at 420 nm which were red-shifted compared to the corresponding peak within the mean tumor spectrum. A closer scrutiny of the individual tissue sample spectra show that 3 of 19 white matter samples, 0 of 25 gray matter samples, and 22 of 39 tumor samples show oxy-hemoglobin (HbO_2) double-peak absorption at 550 nm. Thus, while tumor samples indeed possessed the highest percentage of samples with characteristic HbO_2 absorption, that percentage was still less than 60%. While the low proportion of HbO_2 within the tissue samples is unexpected due to tissue exposure to room air, it is not without precedent as the same effect has been previously observed both *in vitro* and *in vivo* during our clinical spectroscopy study. Unfortunately, the cause behind whether HbO_2 or Hb absorption appears within tissue spectra is currently unknown and appears to be random in nature. It may be correlated to the local environment of the sample during clinical measurement or to sample extraction. Often during brain tissue resection for tumor removal or temporal lobectomy, neurosurgeons will employ electro-cautery to stop bleeding from broken vessels. Heat diffusion to the blood within surrounding tissue areas during cauterization could cause hemoglobin denaturation and thereby affect its ability to bind oxygen. The random nature of hemoglobin absorption could therefore be linked to the degree of tissue heating prior to measurement. Regardless of its underlying mechanism, the random presentation of hemoglobin absorption within diffuse reflectance and absorption spectra impairs tissue discrimination based upon absorption profile shape.

The majority of primary *infiltrating* brain tumors derive from glial cells which serve to support neuron cell bodies (astrocytes and microglia) and myelinate their axons

(oligodendrocytes) and are predominantly found within white matter, gray matter cortex, and the basal ganglia. As such, one might expect infiltrating glioma tumor samples (especially samples taken at the tumor margins) to be comprised of mixtures of tumor and white or gray matter. It logically follows that the *mean* level of tumor scattering would lie between that of the two normal tissue types. This observation is supported by two experimental facts: (1) the population of reduced scattering spectra from individual tumor samples spans the white and gray matter mean spectra, and (2) reduced scattering of tumor tissues shows the largest dispersion among the three tissue types. This observation also suggests that a discrimination algorithm to differentiate between tumor and normal tissues should first separate tissues by the absolute intensity of their diffuse reflectance emission, effectively performing an initial classification according to their derivative normal tissue (white or gray matter).

Figure 1b demonstrates that gray matter exhibits lower scattering as compared to white matter. Gray matter and cortical tissue consist of neuron cell bodies, while white matter consists predominantly of myelinated axons which travel between gray matter cell bodies and their targets. The radii of axons are significantly smaller (10-100X) than their neuron cell bodies, with a higher density, which contribute to greater scattering according to Mie theory. Other reports postulate that the higher scattering of white over gray matter is due to myelination of the white matter axons (rather than their size relative to gray matter cell bodies) [8, 9]. This was based on an earlier report by Svaasand and Ellingsen [12] that compared scattering between adult and neonatal white matter and concluded that myelination increases scattering relative to unmyelinated axons.

Correlation between relative levels of diffuse reflectance intensity and reduced scattering coefficient suggest that differences in diffuse reflectance between tissue categories result from variations in reduced scattering. Tissue scattering derives from microscopic refractive-index heterogeneities in the cells and cellular components. Theories from scattering measurements on other tissues have attributed differential scattering of normal and neoplastic tissues to increase in the number of mitochondria [27], increase in the nuclear to cytoplasm ratio [28], decondensation of the DNA in the nucleus [29], and fibrous tissue compositional changes [29]. However, none of these reports definitively correlate tissue scattering differences to one or more specific tissue changes which occur during the progression from normal to neoplasia. Full investigation into how the various cellular, sub-cellular, and extra-cellular components of brain tissue (as well as

their changes during tumor development and proliferation) contribute to brain tissue scattering and correlate to scattering differences between normal and cancerous brain tissues is beyond the scope of this paper. Nevertheless, known tissue changes with tumor development and their effects on tissue scattering as predicted by Rayleigh and Mie scattering theory can lead to possible explanations.

The measured reduced scattering spectra of brain tissue presented here demonstrate the marked inverse relationship between scattering and wavelength predicted by the Rayleigh limit of Mie scattering and show significantly different ($p < .01$) reduced scattering coefficients between all three tissue classes over the spectral range of diffuse reflectance measurement (400 nm $< \lambda <$ 800 nm). Mie scattering theory predicts a general scattering decrease as wavelength increases relative to the scattering radius when the light is scattered by tissue components which are on the order of or much smaller than its wavelength ($r <\approx \lambda$). On the other hand, for particles with $r \gg \lambda$, scattering possesses no strong relationship to the wavelength of the light. For these scatterers, Mie theory predicts a general decrease in scattering, increase in anisotropy, and a subsequently large decrease in reduced scattering as the scattering radius increases. Based on the aspects of this theory, the difference in scattering magnitude observed in our *in vitro* data could be the result of disparities in the concentration or in the size distribution of scatterers between tissue categories. The concentration and/or size distribution of the large tissue scatterers such as cells, nuclei, mitochondria, and bilipid membranes are known to vary between tissue categories due to differences in general tissue composition of white and gray matter and the cellular transformations with tumor progression. Rapid cell proliferation during tumor growth produces cells of variable shapes and sizes within the tissue. This random cell morphology within tumor tissue allows its malignancy to be graded by the visual similarity of tumor cells to their parent cell; however it also prevents dense cell packing. Further, to facilitate rapid cellular replication, malignant tumor cell nuclei are often larger than normal [30, 31] to accommodate de-condensed DNA [29], effectively decreasing the scattering from cell nuclei. These decreases in scattering can be offset by the presence of increased numbers of mitoses and multiple nuclei in a cell [30, 31], giving additional scattering centers. Since tumors are known to develop neo-vascularization in order to sustain a heightened metabolism, one might expect the number of mitochondria per cell to increase with tumor progression. Surprisingly, the opposite effect has been observed. While low-grade tumors such as oligodendrogliomas and astroctyomas will contain more

mitochondria [32], perhaps as a compensation mechanism since many can be atypical or damaged [33], the tumor cells of glioblastomas (high-grade) tend to contain *fewer* mitochondria. They transition from oxidative phosphorylation to glycolytic respiration [34], possibly in response to further damage to the mitochondria and its associated "respiratory machinery" of oxidative phosphorylation [35]. These shifts in concentration and/or radius of the various tissue scatterers may explain the relative levels of reduced scattering (highest in white matter, lowest in gray matter) that is consistent with the tenets of Mie scattering theory. Tissue and cell culture studies are currently in progress to thoroughly investigate the specific effects of these cellular changes on tissue scattering, absorption, and subsequent diffuse reflectance as a function of wavelength.

Conclusion

In this study we present absolute and relative reduced scattering and absorption coefficients of brain tissue using the inverse-adding doubling method which agree with previously published results using inverse Monte Carlo techniques. The major areas of disagreement correspond to higher absorption values and inter-parameter crosstalk in our spectra at the hemoglobin absorption bands. The results presented in this study demonstrate that while the shape of clinical diffuse reflectance spectra is mainly governed by sample absorption, the emission intensities of different tissue categories are determined by relative magnitudes of reduced scattering. Brain tissue absorption spectra are dominated by hemoglobin absorption bands for wavelengths below 600 nm and water absorption bands at wavelengths above 900 nm. Reduced scattering spectra represent a combination of Rayleigh and Mie scattering with significant spectral differences most likely deriving from density and size disparities in Mie scatterers between the tissue categories. While there are some differences observed in the magnitude of diffuse reflectance from measured and simulated tissue spectra, they show similar trends in relative emission profiles between tissue categories and general line shape, supporting the fundamental basis of this study which is to correlate *in vivo* diffuse reflectance spectra to inherent tissue optical properties based on *in vitro* measurements. Optical properties of tissue represent only one of the factors which govern laser-tissue interactions; other players such as fluorophore concentrations, fibrous tissues, perfusion, and thermodynamic properties will hopefully further provide spectral differences needed for a reliable, objective, real-time optical

diagnosis system for brain tissue using combined fluorescence and diffuse reflectance spectroscopy.

Acknowledgments

We would like to acknowledge the National Institutes of Health for funding this research (RO1 Grant CA85989). We would also like to acknowledge Dr. Mahlon Johnson for his work determining the pathology of our tissue samples.

References

1. I.J. Bigio and J.R. Mourant, "Ultraviolet and visible spectroscopies for tissue diagnostics: fluorescence spectroscopy and elastic-scattering spectroscopy," Phys Med Biol **42**, 803-14. (1997).
2. W.-C. Lin, et al, "In vivo brain tumor demarcation using optical spectroscopy," Photochem Photobiol **73**, 396-402. (2001).
3. W.-C. Lin, et al, "Brain tumor demarcation using optical spectroscopy; an in vitro study," J Biomed Opt **5**, 214-20. (2000).
4. W.-C. Lin, et al, "Intraoperative Application of Optical Spectroscopy in the Presence of Blood," IEEE Journal of Selected Topics in Quantum Electronics **7**, 996-1003 (2001).
5. W.F. Cheong, S.A. Prahl, and A.J. Welch, "A Review of the Optical-Properties of Biological Tissues," Ieee Journal of Quantum Electronics **26**, 2166-2185 (1990).
6. F. Bevilacqua, et al, "In vivo local determination of tissue optical properties: applications to human brain," Applied Optics **38**, 4939-4950 (1999).
7. R. Splinter, et al, "In vitro optical properties of human and canine brain and urinary bladder tissues at 633 nm," Lasers Surg Med **9**, 37-41 (1989).
8. H.R. Eggert and V. Blazek, "Optical properties of human brain tissue, meninges, and brain tumors in the spectral range of 200 to 900 nm," Neurosurgery **21**, 459-64. (1987).
9. H.R. Eggert and V. Blazek, "Optical properties of normal human intracranial tissues in the spectral range of 400 to 2500 nm," Adv Exp Med Biol **333**, 47-55 (1993).
10. A.N. Yaroslavsky, et al, "Optical properties of selected native and coagulated human brain tissues in vitro in the visible and near infrared spectral range," Phys Med Biol **47**, 2059-73. (2002).
11. W.F. Cheong, "Summary of Optical Properties" in *Optical-Thermal Response of Laser-Irradiated Tissue*, M.J.C. van Gemert, ed. (Plenum Press, New York 1995).
12. L.O. Svaasand and R. Ellingsen, "Optical properties of human brain," Photochem Photobiol **38**, 293-9. (1983).
13. S. Prahl, M. van Gemert, and A. Welch, "Determining the optical properties of turbid media by using the adding-doubling method," Applied Optics **32**, 559-568 (1993).

14. J.F. Beek, et al, "In vitro double-integrating-sphere optical properties of tissues between 630 and 1064 nm," Phys Med Biol **42**, 2255-61 (1997).

15. T.L. Troy and S.N. Thennadil, "Optical properties of human skin in the near infrared wavelength range of 1000 to 2200 nm," J Biomed Opt **6**, 167-76 (2001).

16. A.N. Bashkatov, et al, "Optical properties of human skin, subcutaneous and mucous tissues in the wavelength range from 400 to 2000 nm," Journal of Physics D-Applied Physics **38**, 2543-2555 (2005).

17. J.W. Pickering, et al, "Double-Integrating-Sphere System for Measuring the Optical-Properties of Tissue," Applied Optics **32**, 399-410 (1993).

18. C.M. Gardner, S.L. Jacques, and A.J. Welch, "Fluorescence spectroscopy of tissue: recovery of instrinsic fluorescence from measured fluorescence," Applied Optics **35**, 1780-1792 (1996).

19. U. Utzinger and R.R. Richards-Kortum, "Fiber optic probes for biomedical optical spectroscopy," Journal of Biomedical Optics **8**, 121-147 (2003).

20. A. Roggan, et al, "The effect of preparation technique on the optical parameters of biological tissue," Applied Physics B-Lasers and Optics **69**, 445-453 (1999).

21. E.K. Chan, et al, "Effects of compression on soft tissue optical properties," Ieee Journal of Selected Topics in Quantum Electronics **2**, 943-950 (1996).

22. Y.C. Fung, *Biomechanics: mechanical properties of living tissues*. 2nd ed. 1993, New York: Springer-Verlag.

23. P.K. Yalavarthy, et al, "Experimental investigation of perturbation Monte-Carlo based derivative estimation for imaging low-scattering tissue," Optics Express **13**, 985-997 (2005).

24. J.C. Ye, et al, "Modified distorted Born iterative method with an approximate Frechet derivative for optical diffusion tomography," Journal of the Optical Society of America a-Optics Image Science and Vision **16**, 1814-1826 (1999).

25. Y.L. Pei, H.L. Graber, and R.L. Barbour, "Normalized-constraint algorithm for minimizing inter-parameter crosstalk in DC optical tomography," Optics Express **9**, 97-109 (2001).

26. S.R. Arridge and W.R.B. Lionheart, "Nonuniqueness in diffusion-based optical tomography," Optics Letters **23**, 882-884 (1998).

27. B. Beauvoit, T. Kitai, and B. Chance, "Contribution of the mitochondrial compartment to the optical properties of the rat liver: a theoretical and practical approach," Biophys J **67**, 2501-10. (1994).

28. J.R. Mourant, et al, "Spectroscopic diagnosis of bladder cancer with elastic light scattering," Lasers Surg Med **17**, 350-7 (1995).

29. R. Richards-Kortum and E. Sevick-Muraca, "Quantitative optical spectroscopy for tissue diagnosis," Annu Rev Phys Chem **47**, 555-606 (1996).

30. D. Schiffer, *Brain Tumors: Biology, Pathology, and Clinical References*. 2nd ed. 1997, Berlin: Springer-Verlag.

31. S. Zacks, *Atlas of Neuropathology*. 1971, New York: Harper and Row.

32. J. Cervos-Navarro and N. Pehlivan, "Ultrastructure of oligodendrogliomas," Acta Neuropathol Suppl (Berl) **7**, 91-3 (1981).

33. J.S. Carew and P. Huang, "Mitochondrial defects in cancer," Mol Cancer **1**, 9 (2002).

34. S. Oudard, et al, "High glycolysis in gliomas despite low hexokinase transcription and activity correlated to chromosome 10 loss," Br J Cancer **74**, 839-45 (1996).

35. O. Warburg, *The metabolism of tumours*. 1930, London: Arnold Constable.

CHAPTER IV

LIQUID-CRYSTAL TUNABLE FILTER SPECTRAL IMAGING FOR BRAIN TUMOR DEMARCATION: SYSTEM CHARACTERIZATION

Abstract

Past studies have demonstrated that combined fluorescence and diffuse reflectance spectroscopy can successfully discriminate between normal, tumor core, and tumor margin tissues in the brain. To achieve efficient, real-time surgical resection guidance with optical biopsy, probe-based spectroscopy must be extended to spectral imaging to spatially demarcate the tumor margins. This paper describes the design and characterization of a combined fluorescence and diffuse reflectance imaging system which uses liquid-crystal tunable filter technology. Experiments were conducted to quantitatively determine the linearity, field of view, spatial and spectral resolution, and wavelength sensitivity of the imaging system. Spectral images were acquired from tissue phantoms, mouse brain *in vitro*, and human cortex *in vivo* for functional testing of the system. The spectral imaging system produces measured intensities that are linear with sample emission intensity and integration time and possesses a one-inch field of view for a seven-inch object distance. The spectral resolution is linear with wavelength and the spatial resolution is pixel-limited. Sensitivity spectra for the imaging system provide a guide for the distribution of total image integration time between wavelengths. Functional tests *in vitro* demonstrate the capability to spectrally discriminate between brain tissues based on exogenous fluorescence contrast or endogenous tissue composition. *In-vivo* imaging captures adequate fluorescence and diffuse reflectance intensities within a clinically viable two-minute imaging timeframe and demonstrates the importance of hemostasis to acquired signal strengths and imaging speed.

Introduction

The American Cancer Society estimates that 18,820 new cases of and 12,820 deaths from brain tumors were reported in the United States in 2006 [1]. Gliomas comprise 40% of primary brain tumors and 78% of malignant tumors, with a five-year survival rate of only 33% and a 12-18 month average survival time and 5.1% three-year survival rate for infiltrating glioblastomas [2]. The current three-prong attack for brain tumor treatment is surgical resection of maximum

tumor volume followed by radiation and chemotherapy. However, the blood-brain barrier often prevents cancer-targeting drugs from reaching the tumor, rendering chemotherapy ineffective; and while surgery and radiation therapy can effectively treat the tumor core, the fingerlike protrusions at the margins of infiltrating tumors make treating the entire tumor near impossible. The extent of surgical resection at these tumor margins for both low-grade and high-grade gliomas has been repeatedly correlated to patient quality of life and mortality [3-7]; but complete tumor resection is achieved in less than 20% of patients diagnosed with infiltrating gliomas due to limitation in the surgeon's ability to discriminate between normal tissue and tumor margins during surgery. To this end, tools and techniques are constantly being developed to help locate the tumor and identify its margins during a resection procedure, to maximize tumor mass resection without sacrificing neurologic function.

Current methods for intra-operative tumor localization are limited in their ability to differentiate normal brain from tumor margins. Visual inspection can be highly subjective and inconclusive, especially when dealing with low-grade tumors or diffuse tumor margins which often resemble normal neural tissue. On-site pathology is more histologically reliable but is expensive, is far from real-time, and does not spatially demarcate margin extent. Three-dimensional surgical navigation with x-ray computed tomography (CT) or magnetic resonance imaging (MRI) is extremely useful in tumor localization and debulking [8, 9] but limited in its margin sensitivity, as tumor cells have been found outside of delineated image margins in many documented cases [10]. Furthermore, deformation of brain tissue subsequent to craniotomy, retraction, and debulking by as much as a centimeter degrades the accuracy of surgical navigation based upon pre-operative images [11, 12]. Real-time intra-operative ultrasound is not subject to complications from brain deformation and is capable of detecting tumor margins because brain tumors are often hyperechoic relative to normal tissue; but ultrasound imaging is frequently unable to differentiate tumor from peritumoral edema, which is also hyperechoic [13, 14], and poor image resolution hinders correlation between image features and surgical position. Due to the inherent limitations of these adopted tumor visualization techniques, significant residual tumor cells frequently remain after resection [3, 5], emphasizing the need to develop an objective, on-site, real-time imaging system that is capable of detecting the margins of brain tumors with high sensitivity.

A potential candidate for objective brain tumor margin visualization is an imaging system with contrast based on optical spectroscopy which can quickly and non-intrusively detect tissue changes associated with the progression of disease. Our research group is currently in the middle of a multi-center, retrospective pre-clinical study to investigate the capability of combined autofluorescence and diffuse reflectance spectroscopy to discriminate between normal and malignant tissues in the human brain *in vivo* [15-18]. In this study, optical spectra are measured from multiple gray matter, white matter, tumor core, and tumor margin sites with a portable spectroscopic system [16] during craniotomy procedures for glioma resection or temporal lobectomy. Excitation light from a pulsed nitrogen laser (fluorescence) and a halogen lamp (diffuse reflectance) are sequentially delivered to a point on the tissue surface by two of seven fibers within a handheld fiber-optic probe. The remaining five fibers in the probe are used to collect remitted fluorescence and diffuse reflectance from the tissue surface and deliver it to a spectrograph for spectral measurement. Spectra are grouped as normal, tumor core, or tumor margin according to gold-standard histopathological diagnosis of tissue biopsies acquired at the interrogation site and analyzed to determine spectral differences between tissue groups. Preliminary analysis of the *in-vivo* spectroscopic differences between normal and tumor tissues demonstrates an unbiased diagnostic accuracy of 100%, 96%, and 94% for normal, tumor core, and tumor margin tissue samples using multivariate statistics, indicating the promising capability of optical spectroscopy to provide intrinsic contrast between normal and tumor tissues in the brain [15].

While fiber-optic probe-based spectroscopy is useful for correlating spectral features to histopathological diagnosis at a specific interrogation site, it produces a single-point measurement on the tissue surface without providing the spatial extent of tumor margins, information that is necessary to efficiently guide tumor resection. Therefore, for optical biopsy to be clinically useful, single-point spectroscopy systems must be translated to spectral imaging in which spectral information is acquired at every pixel within a two-dimensional field of view, yielding spatial and spectral tissue information for a comprehensive snapshot of tissue pathology during surgery. Successful translation from probe-based spectroscopy to macroscopic spectral imaging depends upon maintenance of accurate spectral discrimination between tissue types with a reasonable image acquisition time despite significant decreases in excitation irradiance due to larger target areas. Ideally, spectral imaging would produce equivalent fluorescence and diffuse

reflectance lineshapes to probe-based spectroscopy in order to exploit discrimination algorithms developed from probe-based measurements. However, initial comparisons of probe-based and imaging spectra have shown significant disparities in fluorescence and diffuse reflectance lineshape due to inherent differences in excitation-collection geometry, behavior which has been thoroughly investigated and is described in a separate paper [19]. The ability for spectral imaging to discriminate between normal and tumor tissues in the brain must be independently validated during a separate retrospective pre-clinical study currently being conducted by our research group. As such, preliminary functional testing for clinical efficacy which is tested and reported in this paper boils down to the ability of a spectral imaging system to produce spectral contrast between tissue types in an image acquisition time that is clinically viable.

Speed of spectral image acquisition depends to a large degree on optical design and spectral imaging implementation. Many optical and hyper-spectral imaging systems designed to date for tissue interrogation acquire limited spectral information (a few emission bands), trading decreased spectral information for increased frame rates by employing filter-based assemblies containing bandpass-filter wheels, dichroic filters, and/or beamsplitters and oftentimes optically implementing tissue classification algorithms in hardware [20, 21]. These systems have been most commonly applied to exploit the preferential deposition of exogenous fluorescent dyes to tumor tissue [22-24] and to target the hemoglobin absorption bands of soft tissue for perfusion imaging [25, 26]. While the speed of these optical or hyper-spectral imaging systems is impressive, hardware acquisition of partial spectral information limits the complexity of viable classification algorithms, which are often unique to a given organ system and yet to be determined for imaging-based tissue discrimination in the brain. Contrary to these methods, our research group sought to develop a true spectral imaging system capable of acquiring full fluorescence and diffuse reflectance information at every pixel within a macroscopic field of view to clinically determine a robust diagnostic algorithm for intra-operative discrimination between normal and tumor tissue in the brain.

Imaging with full spectral information can be implemented in a variety of modalities, from line-scanning to tunable-filter to multiplexing methods. As part of a previous project, our research group evaluated three benchtop spectral imaging systems based on an acousto-optic tunable filter (AOTF), a liquid-crystal tunable filter (LCTF), and a Fourier multiplexer [27]. The three systems were quantitatively compared in terms of optical throughput and imaging signal-

to-noise ratio for strong reflectance and weak autofluorescence images to determine the system that was most amenable to rapid autofluorescence and diffuse reflectance imaging in a clinical setting. While the Fourier system enjoyed the highest optical throughput, the LCTF system generated the highest signal-to-noise ratio in both types of imaging and proved to be the most versatile. Based on this comparison, a LCTF spectral imaging system was developed for clinical implementation and optimized for brain tissue autofluorescence and diffuse reflectance imaging.

Liquid-crystal tunable filters are constructed from a stack of linear polarizers with interspersed layers of liquid crystals and birefringent crystals. The retardance (R) of each stage is defined as the product of its thickness (d) and the difference between its ordinary (n_o) and extraordinary (n_e) indices of refraction – $R = d(n_o - n_e)$ – which can be modulated by applying a voltage to the liquid crystal and changing its extraordinary index of refraction [28]. Altering the stage's retardance affects the phase delay between the ordinary and extraordinary light rays emerging from the stage, thereby changing its transmission (T) as a function of wavelength (λ) as $T = 0.5\cos^2(x)$ where $x = dR/\lambda$ [28]. The thicknesses (d) of the birefringent crystals in the filter stack and the voltages applied to the liquid crystals are often selected to produce a binary series of retardances such that all of the stages transmit the selected passband while destructive interference at the other wavelengths "trims" the stopband light. The number of stages employed in the filter dictates the width of the passband and the degree of stopband attenuation.

Liquid-crystal tunable filter spectral imaging systems [29-32] use the filter to directly parse the wavelength dimension of the spectral image. A frame of CCD data is acquired while the LCTF passes a single band of the emission spectrum to the camera, using the entire CCD array for spatial resolution. The spectral dimension of the image is constructed by acquiring successive CCD frames as the filter tuning wavelength is swept across the spectral range of interest. The major advantages to LCTF-based spectral imaging systems are their simple design and their versatility. The entire collection leg of the imaging system can be comprised of three components: the filter, a collection lens, and a CCD camera. The major drawback to tunable-filter systems is the inherent tradeoff between spectral resolution and optical throughput. Since only one band of the collected emission is passed to the CCD camera, the majority of collected emission is lost. However, the random-access tuning capability of the filter allows spectral interrogation at exactly and only those wavelengths that are deemed diagnostically significant.

Many of the spectral imaging systems developed to date for medical applications have been designed for investigation of tissue sections to augment information provided by traditional staining methods and white-light microscopy during pathology [33-35]. Several research groups have also constructed tunable-filter spectral imaging systems for *in-vivo* tissue interrogation. Martin et al have developed an endoscope-based spectral imaging system which can be interfaced with an AOTF or LCTF for spectral resolution of fluorescence images while simultaneously acquiring color reflectance images with a second, color CCD camera [36, 37]. The researchers have correlated imaging spectra to spectrofluorimetry and probe-based spectroscopy data and demonstrated differences in fluorescence intensity and lineshape between normal and malignant tissues for mouse skin and an implanted mouse tumor model. Orfanoudaki et al have developed a similar LCTF-based spectral imaging colposcope to interrogate cervical tissue after aceto-whitening using reflectance imaging [31, 38]. While the efforts of these research groups lays the groundwork for spectral imaging *in vivo*, both imaging systems produce single-mode (i.e. diffuse reflectance or fluorescence) spectral images and have been coupled to specialty optical scopes designed for gastroenterology or cervical/lower GI applications.

This paper describes the first macroscopic, dual-mode, fluorescence and diffuse reflectance spectral imaging system, using a liquid-crystal tunable filter, designed in a simple lens-plus-detector configuration to image tissue in the clinical environment, and optimized for human brain tissue discrimination. The clinical efficacy of such a stand-alone system depends on its ability to rapidly and faithfully measure the fluorescence and diffuse reflectance behavior of human brain tissue during tumor resection surgery. While a companion paper investigates the effects of the transition from probe-based spectroscopy to spectral imaging on fluorescence and diffuse reflectance lineshapes [19], this paper presents results from a battery of tests designed to quantitatively characterize the system parameters important for spectral imaging performance, including the linearity of its measured intensities, its field of view, its spatial and spectral resolution, and its system sensitivity as a function of wavelength. For a more direct evaluation of clinical efficacy, spectral images were measured from tissue phantoms designed to optically mimic human brain tissue, mouse brain tissue samples *in vitro*, and human cortex *in vivo* during tumor resection surgery, to determine the functional capability of the imaging system to spectrally discriminate between tissue types based on exogenous fluorescence and endogenous

tissue composition and the speed with which macroscopic autofluorescence and diffuse reflectance images can be acquired *in vivo*.

Materials and Methods

System Description

The clinical imaging system was designed to perform dual-mode fluorescence and diffuse reflectance spectral imaging. The collection head of the imaging system is comprised of three components: a Varispec VIS-20 liquid-crystal tunable filter (CRI, Inc.), a variable focal length (f = 28-80 mm) camera lens (Nikon), and a 512 x 512 pixel PhotonMax CCD camera (Princeton Instruments). As shown in Figure 1a, the system is connected to a Wild Heerbrugg M690 operating microscope (Leica), which contains a side assembly originally designed for a second set of oculars. The oculars were removed and the spectral imaging system was mounted in place. The focal length and fine focus of the imaging system collection lens are easily adjusted to align the focal planes of the imaging system and primary oculars. Microscope focus is adjusted via

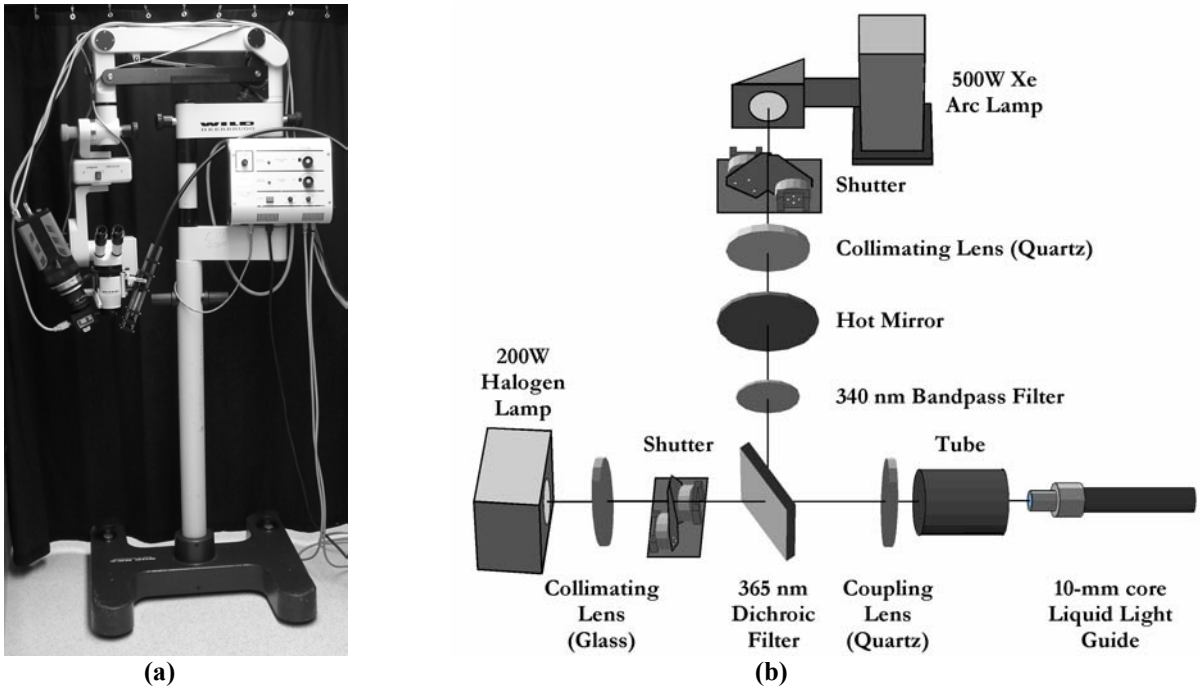

(a) **(b)**

Figure 1. (a) Picture of LCTF spectral imaging system coupled to the side assembly of a Wild Heerbrugg M690 operating microscope. (b) Schematic of excitation optics for fluorescence and diffuse reflectance imaging.

motorized translation of the entire microscope head (including the imaging system), rather than by movement of the focusing optics in the microscope, such that the distance between the microscope head and focal plane is maintained. This ensures that once the microscope and imaging focal planes are aligned, as the surgeon focuses on a tissue target with the primary oculars, the spectral imaging system is always focused on the same object.

Fluorescence and diffuse reflectance excitation (Figure 1b) are provided by a 500 W xenon arc lamp (Thermo-Oriel) and a 200 W halogen lamp (Luxtec), respectively. Fluorescence excitation light is filtered by a hot mirror and 340 nm bandpass filter (Chroma) to simulate nitrogen laser excitation from the probe-based spectroscopy system. A 365 nm dichroic filter allows light from both excitation sources to be coupled into a 10-mm core diameter liquid light guide (Steiner and Martins), which delivers the excitation light to the sample at the microscope head. Shutters (Electro-optical Products) along both beam paths allow automated switching between the two excitation sources for dual-mode imaging and baseline correction for ambient light. The entire system, including LCTF tuning, CCD camera communication, shutter control, and data handling, is controlled with a custom C-based computer program with graphical user interface controls from the Fast Light Toolkit.

System Characterization

A battery of tests was designed to characterize the parameters of the LCTF spectral imaging system important for clinical spectral imaging performance. Confirming the linearity of measured intensities with sample emission intensity and integration time ensures that relative measured intensities directly correlate to relative emission levels and that image intensities can be normalized for changes in integration time. Measuring the field of view as a function of object distance provides the necessary distance between the imaging system and focal plane of the microscope to produce a target 25-mm field of view. Gauging the spatial resolution of the imaging system determines the spatial extent of visible tissue features and whether the optics of the LCTF pushes this extent above the pixel limits of the CCD camera. Comparing the spectral resolution of the imaging and probe-based spectroscopy systems predicts whether fluorescence and diffuse reflectance spectral features within imaging data will be broadened relative to probe-based spectra. Finally, quantifying the wavelength sensitivity of the imaging system not only

allows for wavelength correction of measured imaging spectra but also predicts the relative signal-to-noise levels between wavelengths in the spectrum.

For any detection system, it is important to know whether the system output is linear with the system inputs. For a spectral imaging system, the output is the digital count of measured intensity, and two of the most significant inputs are the sample emission intensity and the integration time over which that intensity is allowed to impinge on the CCD array. To determine the linearity of measured intensity with sample emission, spectral images of a 99% diffuse reflectance standard (Spectralon, LabSphere) under halogen-lamp illumination were acquired from 400 to 720 nm in 5 nm steps with a 10 ms integration time per wavelength. The light intensity emitted from the sample was varied by placing neutral density filters between the liquid light guide and sample, effectively diminishing the excitation power. Spectral images and corresponding baseline images with no excitation were acquired for fourteen filter combinations whose optical density (OD) varied from 0 to 3.5. To determine the linearity of measured intensity with integration time, twelve spectral images were similarly acquired but with a constant excitation power and integration times which varied from 1 to 5000 ms per wavelength. For the two sets of variable emission and variable integration images, mean spectra were calculated for each spectral image and normalized relative to the maximum intensity image spectra (0 OD for variable emission, 5000 ms for variable integration). Regression lines were fit to the data in a least-squares sense and regression coefficients were calculated with each wavelength treated independently.

The field of view of the spectral imaging system was characterized as a function of sample distance from the distal face of the LCTF. A two-dimensional phantom was constructed consisting of a Cartesian grid of lines on a flat piece of plastic, spaced 1 mm apart. In these experiments, the phantom was placed at various distances from the distal face of the LCTF, from 250 mm away down to the point at which the system was no longer able to focus on the phantom. At each position of the phantom, the system was focused on the phantom with the origin (0,0) positioned at the corner of the system field of view. An image of the phantom was subsequently acquired under ambient illumination with the filter tuned to 600 nm. For image acquisition at long object distances, the focal length of the camera lens was set to its maximal focal length (f = 80 mm). Once the object distance became too short such that the imaging

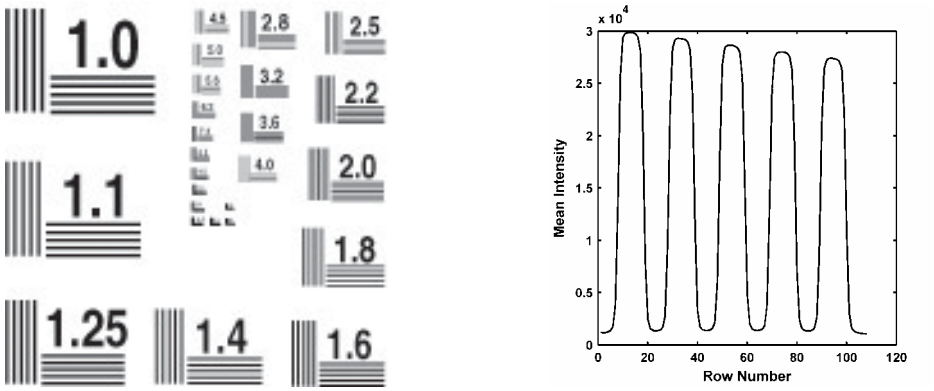

(a) **(b)**

Figure 2. (a) NBS 1963A spatial resolution target. (b) Example intensity profile calculated by averaging the measured intensity across a set of rulings for all wavelengths.

system could no longer focus on the phantom, the focal length was shortened until the phantom came into focus.

The spectral resolution of the imaging system was defined to be the full-width at half-maximum (FWHM) of the mean spectrum from an image of a monochromatic input. To measure the spectral resolution as a function of wavelength, a pulsed nitrogen laser with tunable dye module (Oriel) and various fluorescent dyes were used to create multiple laser wavelengths across the tuning range of the LCTF (400 to 720 nm). Laser light was coupled into and delivered via fiber optic cable to create a roughly 10-mm-diameter excitation spot on a 99% diffuse reflectance standard. Baseline and spectral images were acquired of the laser spot for each of twenty-eight different laser wavelengths using a 1-nm increment between CCD frames. Mean spectra and their corresponding FWHM values were calculated for each of the images.

The spatial resolution of any imaging system is traditionally defined to be the separation distance between two objects below which the system can no longer distinguish them as separate. The spatial resolution of the spectral imaging system was characterized using a negative NBS 1963A target (Figure 2a, Edmund Industrial Optics) with rulings varying from 1.0 to 16.0 line pairs per millimeter (lp/mm). For each image acquisition, the spatial resolution target was placed 180 mm from the distal face of the filter, a sample distance which yields the target field of view of 25 mm, according to prior measurements. For a bright background to the negative resolution target, the halogen lamp was used to illuminate a diffuse reflectance standard below the target. To quantify the capability of distinguishing adjacent lines in each ruling as separate, mean intensity profiles (Figure 2b) were calculated across the rows/columns along each

ruling and across all wavelengths. The five peak intensities and the four minimum intensities were extracted from the profile and a peak-to-valley (PVR) ratio was calculated. The spatial resolution of the imaging system was defined to be the separation distance between the lines in a ruling which produces a PVR equal to the square root of two, below which it is assumed that the system can no longer distinguish adjacent lines as separate objects.

The wavelength sensitivity of the spectral imaging system was characterized using a NIST calibration lamp with known spectral output. A spectral image of direct illumination from the lamp and a baseline image were acquired from 400 to 720 nm in 1 nm increments. Integration times were varied at each wavelength to acquire signal measurements at roughly half the dynamic range of the CCD camera for all regions of the spectrum. Measured spectra were subsequently corrected for differences in integration time during post-processing. The sensitivity of the imaging system for fluorescence was defined as the ratio of the true lamp output spectrum to the mean measured spectrum across the image. Calibration for diffuse reflectance imaging was conducted separately since diffuse reflectance spectra must also be corrected for the excitation spectrum of the halogen lamp. To do so, spectral and baseline images of the halogen lamp output were acquired similar to the NIST lamp images, from 400 to 720 nm in 1 nm increments and with variable integration times between wavelengths. The sensitivity of the imaging system for diffuse reflectance imaging was defined as the inverse of the measured spectrum averaged across the image.

Functional System Testing

Functional tests for most spectral imaging systems in the literature involve demonstration of measured spectral contrast between normal and diseased states in the tissue of interest. Many such applications involve visibly observable changes which can be easily correlated to measured spectral features, such as selective uptake of fluorescent dyes by tumor tissue or aceto-whitening of abnormal tissues in the cervix. The first functional test is designed to parallel exogenous dye applications by establishing discrimination capability between brain tissue phantoms with stark optical contrast in fluorescence and diffuse reflectance. The second test demonstrates spectral contrast of the largest source of endogenous contrast in brain tissues, the difference in scattering between white and gray matter, by correlating fluorescence and diffuse reflectance features between white and gray matter tissues to myelin and cell-body staining in the mouse brain.

Based on our clinical experience with probe-based spectroscopy, subtle spectral differences between normal brain and tumor tissues require multivariate statistical analysis to determine discrimination accuracy. As such, an additional functional test demonstrates that high-quality autofluorescence and diffuse reflectance images can be acquired from human brain tissue *in vivo* within a clinically viable timeframe. The images validate the subtle differences in spectral features between normal human cortex and an infiltrating cortical glioma, solidifying the need for large-scale clinical testing with the imaging system to determine its ability to discriminate between normal and tumor tissues in the brain and improve surgical resection guidance.

Spectral image measurement during functional testing began with acquisition of the fluorescence spectral image data cube, followed by acquisition of the fluorescence baseline, diffuse reflectance, and diffuse reflectance baseline images. Spectral image data cubes were constructed from successive CCD frames acquired as the tuning wavelength of the LCTF was scanned across its spectral range, with one CCD frame acquisition per filter wavelength. Integration times were varied at each wavelength to compensate for disparities in system sensitivity as measured previously. Baseline images were acquired with no sample excitation using identical integration times as their respective fluorescence and diffuse reflectance images to correct for ambient illumination and CCD dark current. After measurement, imaging data was baseline subtracted and corrected for variations at each wavelength in system sensitivity and integration time. To create two-dimensional grayscale or color images from three-dimensional spectral image data, spectral intensities were summed on a pixel-by-pixel basis across all wavelengths (grayscale) or using a custom weighted integration scheme (color). Summed intensities were subsequently normalized to maximize the grayscale/color contrast across the image pixels while maintaining the relative intensities between color channels.

Since human brain tissue cannot be readily acquired for system testing *in vitro*, tissue phantoms were developed to optically mimic human brain tissues (white matter, gray matter, glioma) with regard to reduced scattering, absorption, and autofluorescence. Published mean reduced scattering and absorption spectra for white matter, gray matter, and glioma tissues [39] were used as the target values for phantom development. Within a substrate of Bloom Type A gelatin (Vyse Gelatin), bovine hemoglobin (Sigma-Aldrich) was employed for absorption, polystyrene microspheres (Polysciences) for reduced scattering, and Stilbene 420 (Exciton) for fluorescence. The concentrations of these components for the three tissue types are outlined in

Table 1. Phantom components for white matter, gray matter, and tumor tissues. All component concentrations are given per milliliter of the total phantom volume. Polystyrene microsphere concentrations represent the number of milliliters of 2.65% stock microsphere solution per milliliter of total phantom volume.

Tissue Type	Bovine Hemoglobin	Polystyrene Microspheres (d = 0.1 μm)	Polystyrene Microspheres (d = 0.5 μm)	Stilbene 420
White Matter	2.5 mg/mL	0.300 mL/mL	0.300 mL/mL	5.0 μg/mL
Gray Matter	2.5 mg/mL	0.083 mL/mL	0.083 mL/mL	5.0 μg/mL
Tumor	2.5 mg/mL	0.150 mL/mL	0.150 mL/mL	3.5 μg/mL

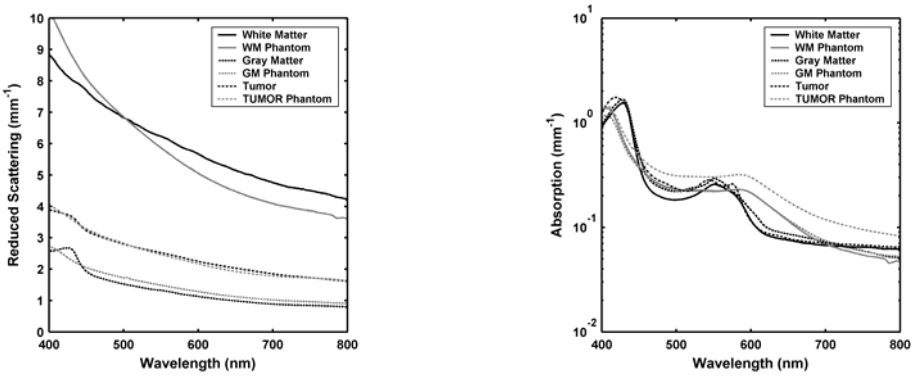

Figure 3. Measured (a) reduced scattering and (b) absorption spectra from white matter, gray matter, and tumor tissues [39] and phantoms using a single-integrating-sphere spectrophotometer and inverse adding-doubling technique [40].

Table 1. It should be noted that all concentrations were empirically determined from optical property measurements (using the standard integrating sphere and inverse adding-doubling technique as described in [40]) on the tissue phantoms and subsequent comparison to the previously measured spectra (Figure 3). Fluorescent dye concentrations were empirically determined by comparing fluorescence measurements from phantom tissues to those measured *in vivo* with a probe-based spectroscopy system as part of a separate project [18]. While the peak fluorescence intensity *in vivo* has been found to be generally constant between tissue types, the concentration of fluorescent dye was decreased in the tumor tissue phantom to provide exogenous spectral contrast between normal and tumor tissues for system testing.

A phantom was created using the three phantom types to simulate a frontal slice through the brain with a large tumor deeply seated within the white matter. Fluorescence and diffuse reflectance spectral images (and corresponding baseline images) were acquired from 400 to 720 nm with the tuning wavelength incremented in 20 and 10 nm steps, respectively. Integration times were varied at each wavelength to acquire measured signals roughly half the dynamic

range of the CCD camera at every wavelength. The total image integration times were 190 seconds for fluorescence and 13.76 seconds for diffuse reflectance. To further increase the signal-to-noise ratio in the fluorescence images, 2 x 2 pixel binning was utilized.

To demonstrate the capability of the imaging system to produce spectral contrast between white and gray matter tissue, an intact brain from a euthanized FVB wild-type mouse was studied. The brain tissue was snap-frozen in liquid nitrogen immediately after removal and stored at -80°C until image measurement. Prior to measurement, the brain was thawed in phosphate buffered saline to room temperature and sliced along a frontal plane through the rostral diencephalon to expose the underlying white matter. Similar to the phantom measurements, fluorescence and diffuse reflectance (plus baseline) spectral images were acquired *in vitro* from 400 to 720 nm in 20 and 10 nm steps, respectively. Fluorescence was acquired using an integration time of 30 seconds at each wavelength between 400-500 nm and 10 seconds between 520-720 nm. Diffuse reflectance was measured using integration times that varied from 5 seconds at 400 nm to 5 ms at 720 nm. The total integration time to acquire the entire spectral data cube was 5 minutes for fluorescence and 15 seconds for diffuse reflectance with no pixel binning employed in either image. It is important to note that while the mouse brain did not span the entire field of view of the imaging system, an 80-mm focal length and 180-mm object distance were maintained for a 25-mm field of view which correlates to the spatial resolution characterization.

For the ultimate functional test, fluorescence and diffuse reflectance images were acquired *in vivo* from the cortical surface of a human brain tumor patient undergoing craniotomy for glioma resection. The image acquisition protocol was approved by the Vanderbilt University Institutional Review Board. Subsequent to craniotomy and duratomy, the imaging system was covered in a sterile drape and positioned roughly seven inches above the patient's brain surface by the attending neurosurgeon. The system field of view was focused on a cortical surface region near the edge of the craniotomy such that both normal cortex and glioma tissue were visible. Spectral and baseline images were acquired from the brain surface with integration times which varied inversely with system sensitivity at each wavelength. Sample integration times were 4 seconds at 460 nm for fluorescence and 8 ms at 580 nm for diffuse reflectance. Total integration times for diffuse reflectance and fluorescence spectral images were 15 and 45 seconds, respectively, and 4 x 4 pixel binning was employed only for fluorescence imaging. Diffuse

reflectance images were acquired from 400 to 720 nm in 10 nm increments, while fluorescence images were acquired every 20 nm except between 440-480 nm where a 10-nm increment was used and 600-720 nm where a 40-nm increment was used.

Results

System Characterization

Measured intensity from the spectral imaging system is linear with both emission intensity and integration time. Sample results at 600 nm are shown in Figure 4 and the regression statistics averaged over all wavelengths are outlined in Table 2. Linearity was assessed before and after baseline subtraction, which effectively eliminated the non-zero offset from ambient illumination and dark current within the CCD camera observed in the measurements.

The field of view (FOV) for the imaging system was found to be linear with object distance measured from the distal face of the LCTF (Figure 5). For a collection-lens focal length equal to 80 mm, the system FOV varied from 20 to 36 mm over object distances which ranged

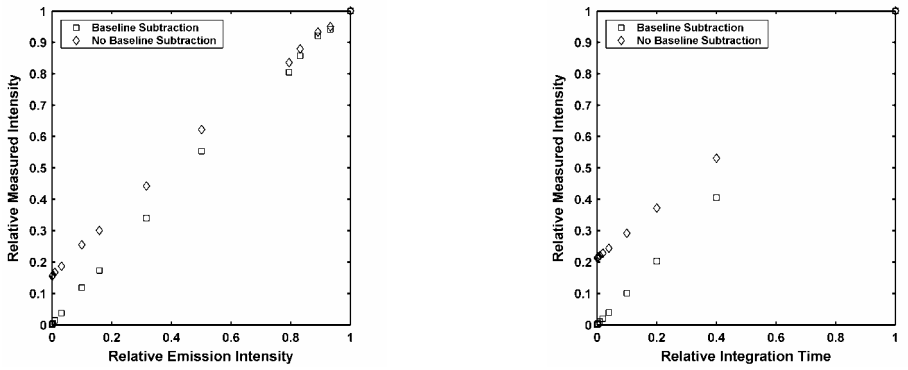

Figure 4. Linearity measurements at 600 nm for (a) constant integration time, variable sample emission and (b) constant sample emission, variable integration time. Measured intensities, ideal emission intensities, and integration times are normalized relative to the maximum intensity images in each set of measurements (OD= 0 and 5000 ms integration).

Table 2. Regressions statistics for linearity measurements, averaged across all wavelengths.

Variable Emission Intensity						**Variable Integration Time**					
Baseline Subtracted			*No Baseline Subtraction*			*Baseline Subtracted*			*No Baseline Subtraction*		
m	**b**	**R^2**	**m**	**b**	**R^2**	**m**	**b**	**R^2**	**m**	**b**	**R^2**
0.9932	0.0174	0.9990	0.6526	0.3557	0.9990	0.9919	0.0097	0.9996	0.5918	0.4087	0.9991

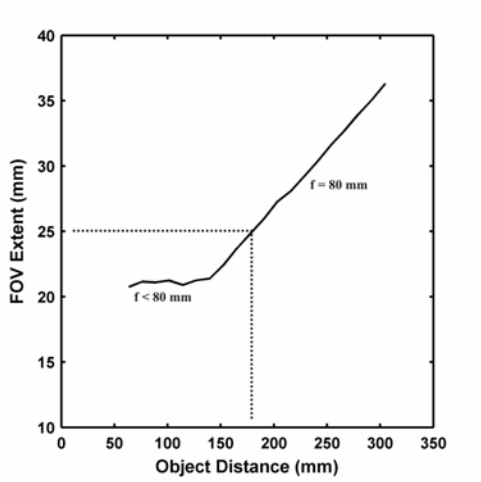

Figure 5. Imaging system field of view as a function of object distance from the distal face of the LCTF.

from 140 to 305 mm (5.5" to 10"). For object distances shorter than 140 mm, the system FOV was held constant at 20 mm while the lens focal length was shortened to focus on the sample. An object distance of 178 mm (7.0") allowed a system FOV of 25.4 mm (1.0"). Thus, the imaging system was coupled to the microscope with this target FOV and object distance, placing the LCTF 178 mm from the focal plane of the microscope.

The spectral resolution of the imaging system was determined to be linear with tuning wavelength of the LCTF. The mean imaging spectra acquired from the laser spots (Figure 6a) demonstrate increasing width as a function of peak emission wavelength, with a bandwidth that varies as ~λ/12, from 6.75 nm at 400 nm to 35.1 nm at 720 nm (Figure 6b). The spectral

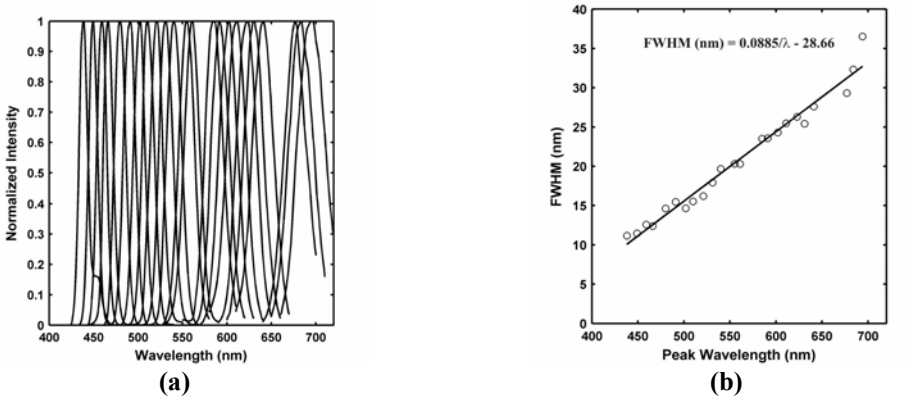

Figure 6. (a) Mean imaging spectra of various laser inputs across the spectral range of the LCTF. (b) Measured spectral bandwidth of imaging system as function of peak emission intensity.

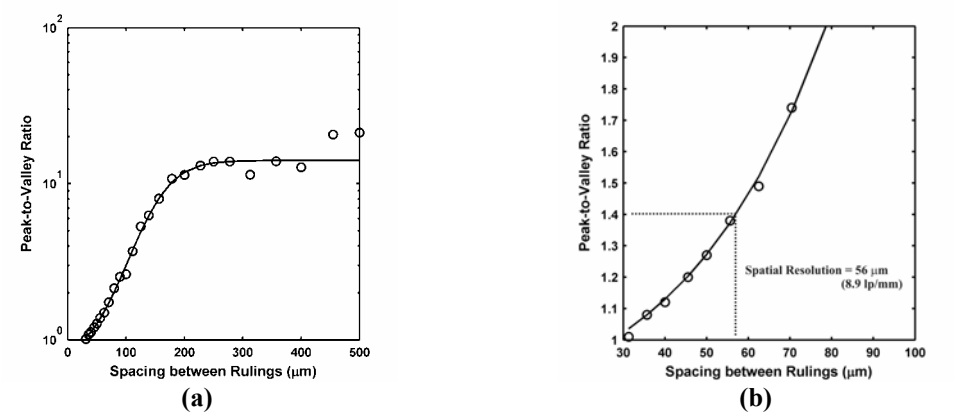

Figure 7. (a) Sigmoid relationship between the measured peak-to-valley ratios as a function of separation distance between rulings. (b) Zoomed view of sigmoid curve centered around region where separation distance yields a PVR equal to the square root of two.

resolution at 550 nm was measured to be 20.32 nm, which agrees with the nominal hardware specifications of the LCTF (FWHM = 20 nm at 550 nm).

The spatial resolution of the imaging system proved to be pixel-limited. The measured peak-to-valley ratios followed a sigmoid curve as a function of the spacing between adjacent lines (Figure 7a). A separation distance equal to 56 μm (8.9 lp/mm) yielded a PVR equal to the square root of two (Figure 7b). Given the 25.4 mm field of view and 512 x 512 pixel array of the CCD camera, pixel-limited spatial resolution can be calculated to be 49.6 μm, roughly equivalent to the measured spatial resolution.

The wavelength sensitivity of the imaging system demonstrated large dynamic ranges for

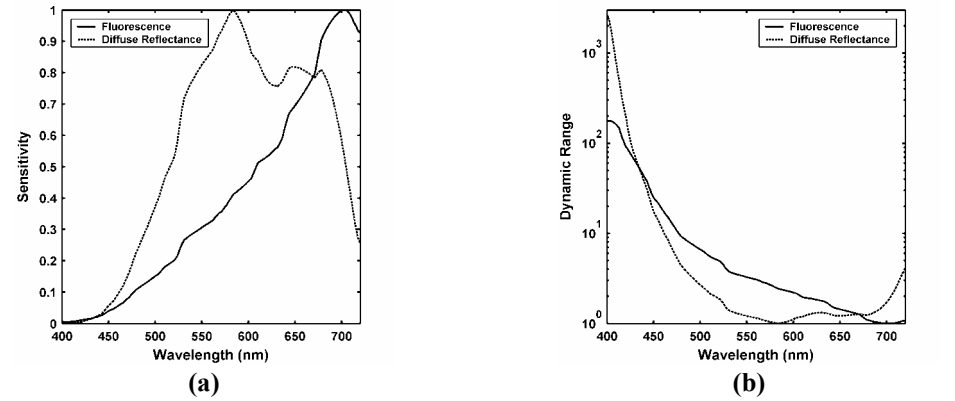

Figure 8. Wavelength (a) sensitivity and (b) dynamic range spectra of the spectral imaging system for fluorescence and diffuse reflectance.

both fluorescence and diffuse reflectance (Figure 8). The sensitivity of the collection leg of the imaging system (fluorescence) is highest at 702 nm and lowest at 400 nm, with a dynamic range of 177. The dynamic range for diffuse reflectance is exacerbated by the excitation spectrum of the halogen lamp, which peaks near 680 nm and is lowest at 400 nm, resulting in a dynamic range of 2650. However, since the gradient from 680 to 400 nm in the halogen excitation spectrum is smaller than the equivalent gradient in the fluorescence sensitivity curve, the peak sensitivity for diffuse reflectance is significantly blue-shifted from 702 to 584 nm.

Functional system testing

Diffuse reflectance and fluorescence spectral images (Figure 9a,b) of the brain tissue

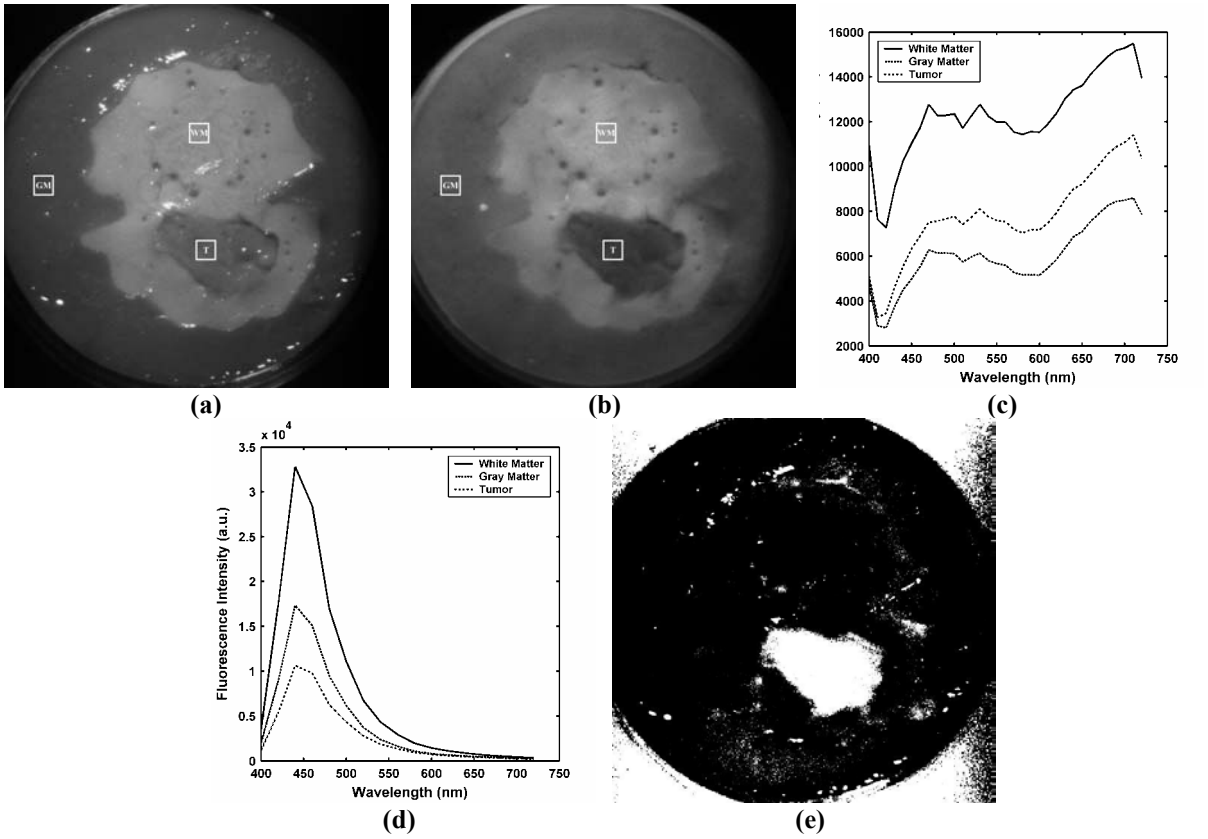

Figure 9. (a) Diffuse reflectance and (b) fluorescence spectral images of a brain tissue phantom *in vitro*. Displayed image intensities reflect a direct integration across all wavelengths of the diffuse reflectance and fluorescence spectral image intensities. (c) Diffuse reflectance spectra (averaged over the boxed 20 x 20 pixel regions) for the three tissue types. (d) Fluorescence spectra over the same regions. (e) Discrimination image depicting normal (black) and tumor (white) tissues, created from the ratio of fluorescence at 460 nm to diffuse reflectance at 700 nm (F_{460}/Rd_{700}). Pixels with $F_{460}/Rd_{700} < 1.15$ were classified as tumor, with $F_{460}/Rd_{700} > 1.35$ classified as normal, and with $1.15 < F_{460}/Rd_{700} < 1.35$ classified as transitional areas (gray).

phantom demonstrate the spatial resolution of the system and its capability to provide spectral contrast necessary to visualize sharp transitions and spectral differences between white matter, gray matter, and glioma phantom tissues. Mean imaging spectra calculated across the boxed 20 x 20 pixel regions (Figure 9c,d) show spectral lineshapes with varying magnitudes between the tissues for fluorescence and diffuse reflectance. Fluorescence intensity peaked between 440 and 460 nm for all three tissues with white matter boasting the highest fluorescence intensity. Based on the spectral differences between the normal and tumor tissues, an empirical algorithm was developed to demonstrate the capability to spectrally demarcate the tumor from the surrounding normal tissue using spectral imaging data. The ratio of fluorescence at 460 nm (F_{460}) to the diffuse reflectance at 700 nm (Rd_{700}) with a threshold of 1.25 effectively highlighted the tumor tissue (Figure 9e), showing that the LCTF spectral imaging system is capable of spectrally discriminating between tissues based on exogenous fluorescence.

Diffuse reflectance and fluorescence images from the *in-vitro* mouse brain illustrate sharp spectral contrast between gray and white matter tissues (Figure 10a,b). Spectral image features also show good correlation to tissue structures evident in a composite Nissl- and myelin-stained frontal section (Figure 10c) through the rostral diencephalon of the mouse neuroanatomy [41]. Raw spectra (Figure 10d) measured from white and gray matter regions without correction for integration time or wavelength sensitivity show measured fluorescence levels near 20,000 counts (of a 16-bit dynamic range). Corrected spectra (Figure 10e) demonstrate peak fluorescence between 460 and 480 nm, diffuse reflectance which varies inversely with hemoglobin absorption, and greater diffuse reflectance in white matter.

When comparing the spectral images to the mouse-brain atlas, the diffuse reflectance spectral image shows low-scattering gray matter structures that correlate to a high concentration of cell bodies (positive Nissl staining), such as the cortical tissue surface, basal ganglia, hippocampus, and diencephalon (thalamus and hypothalamus). High-scattering white matter fiber tracts (positive myelin staining) are also clearly visible, most notably the corpus callosum connecting the two cortical hemispheres and the internal capsule running between the basal ganglia and diencephalon. The spatial resolution and spectral contrast in the diffuse reflectance image are sensitive enough to visualize even subtle anatomic features such as the white matter striations from the corpus callosum into the cortex (e.g. into the cingulate gyrus along the midline) and from the internal capsule into the motor nuclei of the basal ganglia and into the

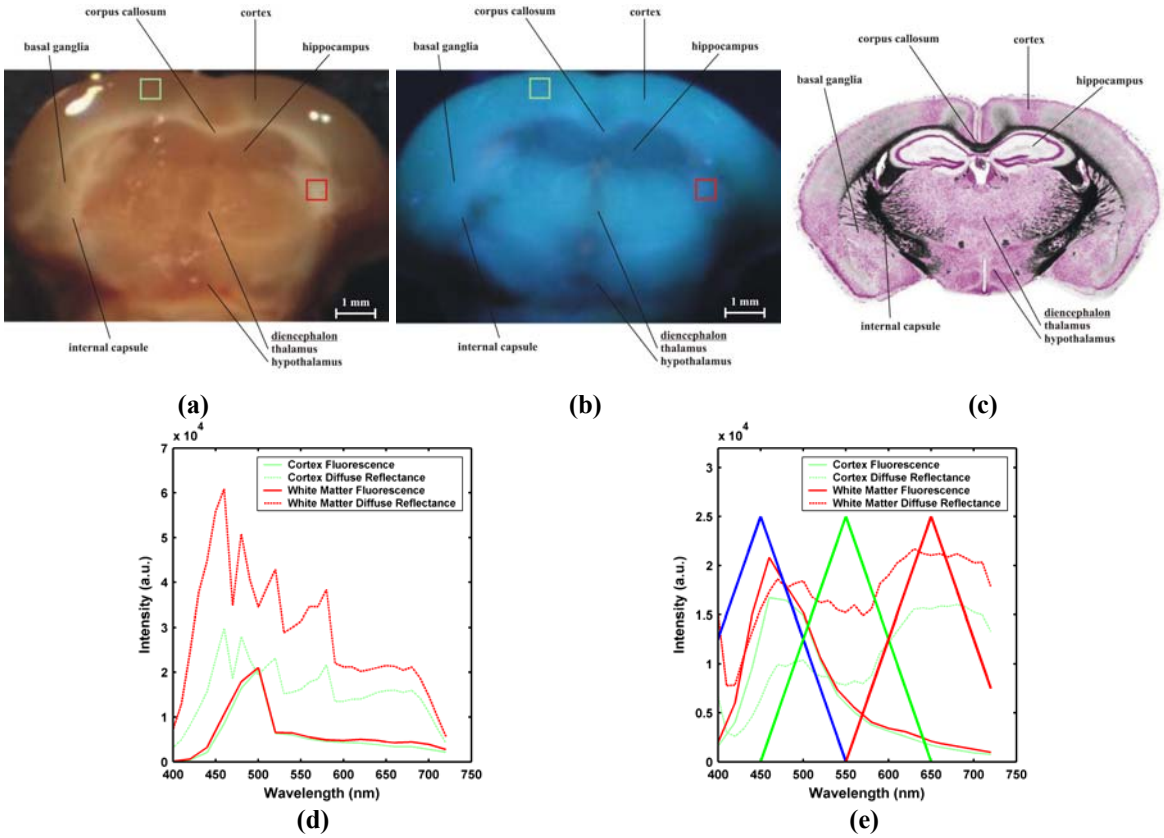

Figure 10. (a) Diffuse reflectance and (b) fluorescence spectral images of a frontal slice of mouse brain imaged *in vitro*. Displayed color intensities reflect a weighted integration scheme, shown in (e), of the diffuse reflectance and fluorescence spectral image intensities. (c) Composite Nissl (pink) and myelin (black) stained frontal section through the rostral diencephalon of the mouse brain [19] (d) Raw fluorescence and diffuse reflectance spectra for white and gray matter tissues (10 x 10 pixel regions) before correction for integration time and system sensitivity as a function of wavelength. (e) Fluorescence and diffuse reflectance spectra after correction and the custom integration scheme (solid thick lines) employed to produce color images from spectral imaging data.

motor and sensory nuclei of the thalamus. The fluorescence images show increased emission levels with increased concentration of cell bodies and increased tissue scattering, consistent with the results from phantom tissues (Figure 9). The cortex (high cell body content, low scattering) and white matter structures (low cell body content, high scattering) show equivalent levels of fluorescence emission, while the hippocampus (low cell body content, low scattering) shows very little fluorescence and the thalamus (high cell body content, moderate scattering from white matter tracts) demonstrates the highest fluorescence intensity. Though not readily visible, a line of fluorescence contrast even exists within the low-emission hippocampus which corresponds to the contour of high cell concentration evident in the stained section.

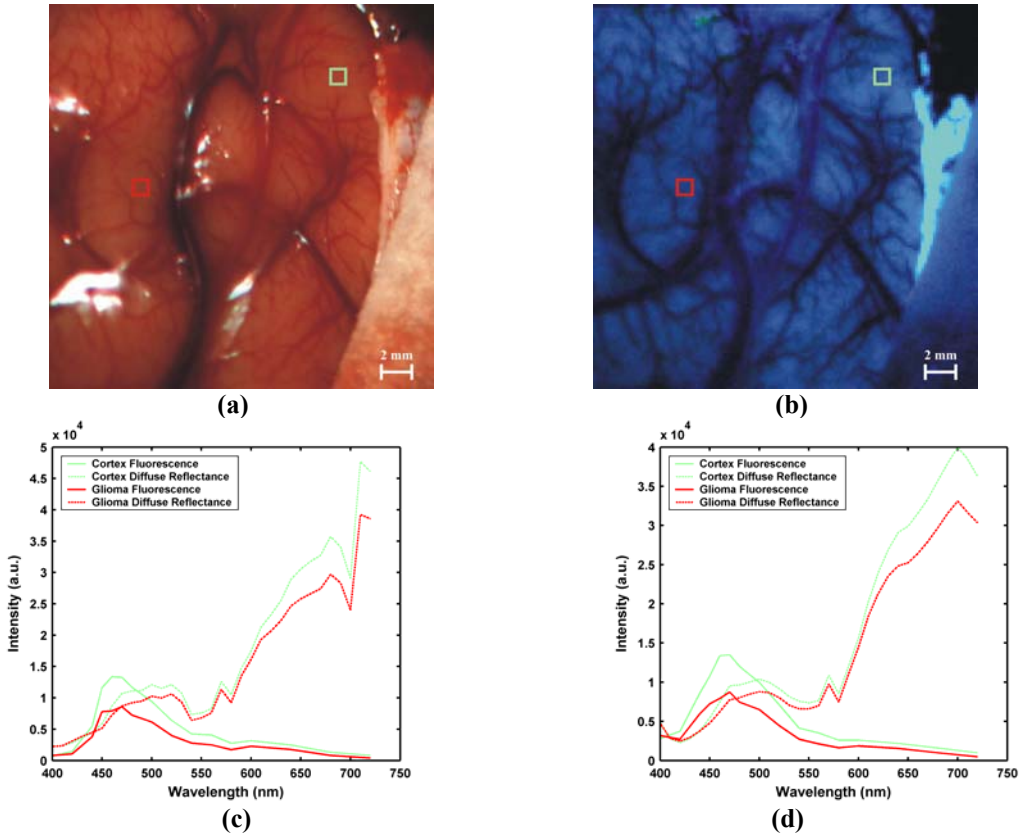

Figure 11. *In vivo* (a) diffuse reflectance and (b) fluorescence spectral images of the cortical surface of a human brain tumor patient. (c) Raw fluorescence and diffuse reflectance spectra (20 x 20 pixel regions) from tumor (left of major blood vessel vertically bisecting the image) and normal cortex (right) before correction for integration time and system sensitivity as a function of wavelength. (d) Fluorescence and diffuse reflectance spectra after correction.

The *in vivo* diffuse reflectance and fluorescence images (Figure 11a,b) provide good visualization of the large blood vessels and pial microcirculation along the cortical surface of the human brain. Based on the images and the mean spectra (Figure 11d), there appear to be only subtle differences (as expected) in fluorescence and diffuse reflectance between the tumor tissue to the left of the major blood vessel bisecting the image and the normal cortex to the right. The raw spectra (Figure 11c) show measured fluorescence intensities near 15,000 counts with diffuse reflectance intensities near 10,000 counts in the blue region of the spectrum and 40,000 counts in the red region. The corrected spectra (Figure 11d) demonstrate peak fluorescence between 460 and 470 nm and greater contrast between the blue and red regions of the spectrum than the *in-vitro* mouse brain measurements, both in diffuse reflectance spectra and in the peak fluorescence emission intensity relative to diffuse reflectance at 700 nm.

Discussion

While single-point spectroscopy measurements are ideal for proof-of-principle clinical studies in which measured spectra can be correlated to histopathologic diagnoses of punch tissue biopsies, they are an inefficient means to provide surgical resection guidance. This limitation calls for the extension of single-point spectroscopy to spectral imaging which acquires equivalent spectroscopic information at every pixel across a two-dimensional imaging surface, giving a spatial snapshot of tissue pathology during surgery. The spectral imaging system described in this paper is capable of combined fluorescence and diffuse reflectance spectral imaging coupled to an operating microscope for seamless integration into the clinical environment. The battery of tests designed to characterize the imaging system parameters have revealed measured intensities which are linear with sample emission intensity and integration time, a 25-mm field of view for a 180-mm object distance, spectral resolution which is linear with wavelength, spatial resolution which is pixel-limited, and fluorescence and diffuse reflectance sensitivities with large dynamic ranges. Consistent with the goals of the functional tests, *in-vitro* images of phantom and mouse brain tissue showed excellent spatial resolution for visualization of fine tissue structures and spectral contrast based on exogenous fluorescence and endogenous tissue differences for successful spectral discrimination between tissue types. *In-vivo* imaging of the cortical surface in a human brain tumor patient proved that high signal-to-noise ratio images can be acquired within a clinically viable, two-minute imaging timeframe, resulting in minimum disruption during surgery for clinical data acquisition.

By the strictest definition of linearity, spectral imaging in the presence of dark current CCD noise is linear if baseline subtraction is performed. The linearity of the imaging system was characterized to ascertain whether increases in integration time or emission intensity increase the measured intensity by the same factor. For plots of *normalized* measured intensity versus *normalized* emission intensity or integration time, a linear system conforming to such a definition yields a slope of one and an intercept of zero, criteria which are satisfied when baseline subtraction is used to eliminate the offset due to dark current noise in the CCD camera. Strict linearity has two main advantages. First, wavelength *ratios* performed on a pixel-by-pixel basis directly correlate to differences in emission intensity and are immune to emission changes due to spatial variations in excitation light and surface topography, allowing simple correction for these effects. Second, and more importantly, unique integration times can be used at the

different wavelengths in the spectral image, and simple normalization of the measured spectra can be used to correct for these varied integration times during post-processing. Given the large dynamic range in system sensitivity for fluorescence (177) and diffuse reflectance (2650), variable integration times are necessary to acquire reasonable signal levels at all wavelengths in the images, which can subsequently be accounted for with normalization, as was performed during functional system testing.

The wavelength sensitivity of a detection system is normally reserved to correct measured spectra for system response. Given the linearity of the imaging system with integration time, the system sensitivity can also be used to guide how the total image integration time is distributed between wavelengths. The sensitivity measurements suggest that the majority of image integration time should be devoted to the blue region of the spectrum where sensitivity is lowest (Figure 8). Employing integration times which vary inversely with system sensitivity (such that the correction for wavelength sensitivity and integration time offset one another) ensured that measured signal levels were independent of the system response, directly correlated to tissue emission intensity, and created raw measured spectra (Figure 11c) that were similar in shape to the corrected spectra (Figure 11d).

Spatial and spectral resolution characterization aims to determine whether these system limits distort spectral imaging data from true sample behavior. Spectral resolution of the imaging system (10 to 35 nm) acts as a low-pass filter on the spectral lineshape, effectively widening spectral features with narrow bandwidths. Modeling a spectral peak and the system passband as Gaussian functions, the width of the peak as measured by the system can be calculated as the quadratic sum of the true peak width and the passband width [32]. To broaden a spectral peak by 10%, the spectral resolution must be greater than 46% of the original peak width. Fluorescence and diffuse reflectance spectra are traditionally composed of broadband features (i.e. widths > 50 nm), and those with the narrowest bandwidth, NADH fluorescence at 460 nm and the hemoglobin absorption bands at 420 and 540 nm (542, 578 nm for oxy-hemoglobin), occur in regions of the spectrum where the system spectral resolution is lowest (10-20 nm). As such, the distortion of fluorescence and diffuse reflectance spectral features from their true lineshapes can be considered negligible.

Given the resolution demonstrated in the mouse brain and human cortical surface images, pixel-limited spatial resolution of the imaging system (56 μm with no binning) will have

minimal effect on tissue discrimination and surgical resection guidance. While the spatial resolution is larger than individual neurons and glial cells in the brain and thus subject to partial volume effects over multiple cells, current methods of tumor resection are incapable of single-cell removal; therefore, neurosurgeons are often interested in macroscopic more than microscopic discrimination. Further, it has been demonstrated that photon diffusion from areas as far as 10 mm from a given pixel can influence spectral imaging lineshape [19]. Therefore, partial volume effects in spectral imaging will be influenced less by the pixel size in the CCD camera and more by the scattering of light through the tissue, even when the effective pixel size is increased with pixel binning.

The question often arises regarding the effect of the polarization capability of the LCTF on measured spectral lineshape and the steps taken to correct for such distortions. Since excitation light delivered by the spectral imaging system is randomly polarized and brain tissue is fairly homogeneous with no known birefringence characteristics, the light remitted from the tissue surface is assumed to be randomly polarized across the entire tissue surface and for all wavelengths in the spectrum. Therefore, the polarization capability of the LCTF only serves to reduce the throughput of the spectral imaging system, without affecting the measured lineshapes of the imaging spectra, to the point that roughly 5-15% of blue light remitted from the tissue reaches the CCD camera for detection. It is important to note that imaging tissues with known birefringence (e.g. muscle) will be sensitive to the orientation of the LCTF relative to the optical axis of the tissue, with the potential for spectral distortion due to birefringence variations with wavelength.

Spectra from fluorescence and diffuse reflectance images of the tissue phantom (Figure 9) and the mouse brain (Figure 10) agree with expectations based on the known optical properties (Figure 3), fluorophore concentrations (Table 1), and cellular composition (Figure 10c) for the various tissue types observed in the images. The diffuse reflectance spectral lineshapes are inversely related to the tissue absorption spectra, while equivalent absorption levels between white matter, gray matter, and tumor tissues lead to a direct correlation between the magnitude of reduced scattering and measured diffuse reflectance intensity. Reduced scattering also increases fluorescence intensity, as demonstrated in the phantom images by higher fluorescence in the white matter than gray matter despite equivalent fluorophore concentrations in the two tissues. Equivalent fluorescence levels between gray matter and white

matter in mouse brain tissue coupled with higher reduced scatting in white matter suggests higher fluorescence generation in gray matter tissue, perhaps due to a higher concentration of cell-body content and subsequently NADH.

The spectral images acquired *in vitro* from the tissue phantom and mouse brain tissue demonstrate the capability of the system to spectrally discriminate between brain tissues based on exogenous fluorescence (Figure 9) and endogenous tissue chromophores (Figure 10). Simple weighted integration of spectral intensities (Figure 10e) to produce pixel-by-pixel color information was sufficient to create stark visible disparities between white matter and gray matter in the mouse brain images (Figure 10a,b) with no optimization of spectral differences. For the mock discrimination scenario in Figure 9e, the ratio of fluorescence at 460 nm (F_{460}) to the diffuse reflectance at 700 nm (Rd_{700}) with a threshold of 1.25 was capable of accurately separating normal from tumor tissue. The discrimination algorithm was based on fluorescence intensity while presumably correcting this intensity for spatial variations in excitation intensity and surface topography and for the disparate levels of scattering between the tissue types. It should be noted that the major sources of error in the discrimination image correspond to regions where specular reflectance is highlighted and where air bubbles are present on the surface of the phantom which reduce the fluorescence emission. Based on these results, spectral discrimination with our dual-mode LCTF spectral imaging system is at least on par with other imaging systems in the literature capable of 1) creating visible image contrast from disparities in endogenous tissue chromophores and 2) tissue discrimination based on spectral differences from exogenous tissue fluorescence.

The *in-vitro* and *in-vivo* brain tissue images indicate that acquiring full fluorescence and diffuse reflectance information with good signal intensities *in vivo* is feasible in a clinically viable timeframe, resulting in minimal disruption during surgery. The fluorescence, diffuse reflectance, and baseline images measured from mouse brain tissue *in vitro* used 10.5 minutes of total integration time to produce image intensities which spanned a third of the 16-bit dynamic range of the CCD camera (max intensity = 65535). Exploiting 4 x 4 pixel binning during *in-vivo* testing reduced the total image integration time for fluorescence from five minutes to forty-five seconds. Image acquisition overhead associated with data readout from the CCD (100 ms for a full CCD frame) and LCTF tuning (50 ms for each wavelength) diminishes the benefit of pixel binning for diffuse reflectance imaging, decreasing the acquisition time for a 33-wavelength

image from 20 s (15 s integration, 5 s overhead) to 6 seconds (1 s integration, 5 s overhead). With these reduced imaging times, the fluorescence, diffuse reflectance, and their associated baseline images can be acquired in 120 seconds, and given the pixel-limited spatial resolution of the imaging system, still yield a 200 μm spatial resolution sufficient for macroscopic tumor resection guidance.

In addition to the *in-vitro* mouse brain images demonstrating that rapid imaging is feasible, the *in-vivo* images reveal the power of superficial blood contamination and tissue perfusion to absorb fluorescence emission at 460 nm and affect measured signal levels, behavior which is consistent with our clinical experiences with probe-based spectroscopy [16, 42]. Fluorescence image intensity is reduced in all blood vessels regardless of size, and a thin layer of blood is enough to completely absorb the bright fluorescence from the cranium at the right of the image. Similarly, a small blood vessel traverses the internal capsule to the left of the *in-vitro* mouse brain images; despite its small size to the point of near invisibility, the vessel creates a distinct line of low-emission in the fluorescence image. The *in-vivo* fluorescence images were acquired with 4x4 pixel binning and a 7.5-fold decrease in integration time at 460 nm, resulting in a two-fold increase in collection power at 460 nm relative to the mouse brain images. The raw *in-vivo* spectra show a two-fold *decrease* in peak fluorescence intensity relative to the mouse brain spectra (Figures 10d & 11c). Hemoglobin absorbs greater in the blue-green (400 – 600 nm) than the red region (600 – 720 nm) of the spectrum, such that the ratio in diffuse reflectance intensity between these regions indicates the relative level of blood absorption in the measured spectrum. The increase in that ratio from 2-fold *in vitro* (Figure 10e) to nearly 4-fold *in vivo* (Figure 11d) indicates the increased presence of blood absorption *in vivo*, consistent with previous results [16]. Given that superficial blood is not apparent in the images, the decrease in measured fluorescence intensity *in vivo* can be attributed to increased blood perfusion in the live tissue, requiring increased image acquisition times *in vivo* relative to the *in-vitro* scenario to achieve equivalent signal levels.

As mentioned in the introduction, successful translation from probe-based spectroscopy to macroscopic spectral imaging hinges on reasonable image acquisition time and accurate spectral discrimination between tissues. The results in this paper demonstrate the ability of our dual-mode LCTF spectral imaging system to acquire fluorescence and diffuse reflectance images *in vivo* within a clinically viable, two-minute imaging timeframe with excellent spatial

resolution, diffuse reflectance contrast indicative of even small anatomic transitions between white and gray matter, and fluorescence contrast indicative of cellular composition. The imaging results in this paper breed confidence in our ultimate ability to delineate tumor margins in the brain in the face of subtle spectral differences between normal brain and tumor tissues. Success in such an endeavor will require careful investigation into the normal and tumor spectral lineshapes as measured by spectral imaging and multivariate statistical analysis of patient imaging data through a large, well-designed retrospective clinical study. Pre-clinical spectral image data acquisition for this study has already begun; the results from the investigations described in this paper will serve to guide us as we move further toward clinical spectral imaging for intra-operative brain tumor resection guidance.

Conclusion

This paper outlines the imaging characteristics of a combined fluorescence and diffuse reflectance spectral imaging system designed for clinical brain tissue diagnosis and tumor resection guidance. Its simple design around a liquid-crystal tunable filter, its linearity of measured intensity with emission intensity and integration time, and its pixel-limited spatial resolution make it a versatile imaging system for clinical tissue diagnosis. It can acquire spectral information at specific wavelengths deemed diagnostically significant, employ integration times which vary with wavelength to acquire good signal-to-noise across the spectral range of interest, and utilize pixel binning to increase signal levels while maintaining sufficient spatial resolution for surgical guidance. Using this system, phantom tissues can be distinguished based on exogenous fluorescence variations and white and gray matter can be differentiated based upon spectral differences subsequent to disparities in scattering and cell-body concentration. *In-vivo* testing indicates that high-quality autofluorescence and diffuse reflectance images can be acquired from brain tissue within a clinically viable, two-minute imaging timeframe during surgery, and tissue perfusion and superficial blood contamination continue to play an important role along this front. These results will help guide data collection during a large pre-clinical study designed to determine the efficacy of combined fluorescence and diffuse reflectance spectral imaging to spectrally discriminate between normal and glioma tissues in the brain for tumor margin demarcation and surgical resection guidance.

Acknowledgements

We would like to acknowledge the National Institutes of Health for their research funding (Grant R01 CA85989). We would also like to thank John Fellenstein and Robert Patchin for their help in construction of the spectral imaging system. Finally, we would like to acknowledge the members of the nursing staff in the Vanderbilt Department of Neurosurgery for their aide and patience in the operating room during spectral image acquisition.

References

1. A. Jemal, et al, "Cancer statistics, 2006," CA Cancer J Clin **56**, 106-30 (2006).
2. C.B.T.R.o.t.U. States, "Primary Brain Tumors in the United States Statistical Report, 1998-2002 Years Data Collected," http://www.cbtrus.org, 2005-2006. Accessed on April 27, 2006.
3. M. Ammirati, et al, "Effect of the extent of surgical resection on survival and quality of life in patients with supratentorial glioblastomas and anaplastic astrocytomas," Neurosurgery **21**, 201-6. (1987).
4. M.C. Chamberlain and P.A. Kormanik, "Practical guidelines for the treatment of malignant gliomas," West J Med **168**, 114-20. (1998).
5. A. Kowalczuk, et al, "Quantitative imaging study of extent of surgical resection and prognosis of malignant astrocytomas," Neurosurgery **41**, 1028-36 (1997).
6. M.T. Selch, et al, "Gangliogliomas: experience with 34 patients and review of the literature," Am J Clin Oncol **21**, 557-64. (1998).
7. S.A. Toms, D.Z. Ferson, and R. Sawaya, "Basic surgical techniques in the resection of malignant gliomas," J Neurooncol **42**, 215-26. (1999).
8. R.J. Maciunas, *Interactive Image-Guided Neurosurgery*. 1993, Park Ridge, IL: American Association of Neurological Surgeons.
9. R.J. Maciunas, *Minimally Invasive Therapy of the Brain*, ed. A.D. Salles and R. Lufkin. 1997, New York: Thieme Medical Publishers, Inc.
10. P.D. LeRoux, et al, "A comparison between preoperative magnetic resonance and intraoperative ultrasound tumor volumes and margins," J Clin Ultrasound **22**, 29-36. (1994).
11. D.L. Hill, et al, "Measurement of intraoperative brain surface deformation under a craniotomy," Neurosurgery **43**, 514-26; discussion 527-8. (1998).
12. N.L. Dorward, et al, "Postimaging brain distortion: magnitude, correlates, and impact on neuronavigation," J Neurosurg **88**, 656-62. (1998).
13. L.M. Auer and V.V. Velthoven, *Intraoperative Ultrasound Imaging in Neurosurgery: Comparison with CT and MRI*. 1990, Berlin: Springer-Verlag.

14. J.E. Knake, et al, "Neurosurgical applications of intraoperative ultrasound," Radiological Clinics of North America **23**, 73-90 (1985).

15. S.K. Majumder, et al, "A probability-based multi-class diagnostic algorithm for iIn-vivo optical separation of tumor margin and tumor from normal human brain tissue," Applied Spectroscopy (in review).

16. W.-C. Lin, et al, "In vivo brain tumor demarcation using optical spectroscopy," Photochem Photobiol **73**, 396-402. (2001).

17. W.-C. Lin, et al, "Brain tumor demarcation using optical spectroscopy; an in vitro study," J Biomed Opt **5**, 214-20. (2000).

18. S.A. Toms, et al, "Intraoperative optical spectroscopy identifies infiltrating glioma margins with high sensitivity," Neurosurgery **57**, 382-91 (2005).

19. S.C. Gebhart and A. Mahadevan-Jansen, "Comparison of spectral variation from spectroscopy to spectral imaging," Applied Optics (in press).

20. J.N.Y. Qu, H.P. Chang, and S.M. Xiong, "Fluorescence spectral imaging for characterization of tissue based on multivariate statistical analysis," Journal of the Optical Society of America a-Optics Image Science and Vision **19**, 1823-1831 (2002).

21. N. Ramanujam, et al, "Fast and noninvasive fluorescence imaging of biological tissues in vivo using a flying-spot scanner," IEEE Trans Biomed Eng **48**, 1034-41. (2001).

22. S. Andersson-Engels, et al, "Preliminary evaluation of two fluorescence imaging methods for the detection and the delineation of basal cell carcinomas of the skin," Lasers Surg Med **26**, 76-82 (2000).

23. V.V. Lazarev, et al, "Detection of premalignant oral lesions in hamsters with an endoscopic fluorescence imaging system," Cancer **85**, 1421-9. (1999).

24. J. Hewett, et al, "The application of a compact multispectral imaging system with integrated excitation source to in vivo monitoring of fluorescence during topical photodynamic therapy of superficial skin cancers," Photochem Photobiol **73**, 278-82. (2001).

25. R.G. Nadeau and W. Groner, "The role of a new noninvasive imaging technology in the diagnosis of anemia," J Nutr **131**, 1610S-4S. (2001).

26. U. Thomale, et al, "Visualization of rat pial microcirculation using the novel orthogonal polarized spectral (OPS) imaging after brain injury," J Neurosci Methods **108**, 85-90. (2001).

27. S. Gebhart, et al. "Instrumentation considerations in spectral imaging for tissue demarcation: comparing three methods of spectral resolution," in *SPIE Photonics West, Spectral Imaging: Instrumentation, Applications, and Analysis III*, San Jose, CA, 2005: Bellingham, WA.

28. H.R. Morris, C.C. Hoyt, and P.J. Treado, "Imaging Spectrometers for Fluorescence and Raman Microscopy - Acoustooptic and Liquid-Crystal Tunable Filters," Applied Spectroscopy **48**, 857-866 (1994).

29. O. Khait, S. Smirnov, and C.D. Tran, "Multispectral imaging microscope with millisecond time resolution," Anal Chem **73**, 732-9. (2001).

30. C.D. Tran, "Development and analytical applications of multispectral imaging techniques: an overview," Fresenius J Anal Chem **369**, 313-9. (2001).

31. C. Balas, "A novel optical imaging method for the early detection, quantitative grading, and mapping of cancerous and precancerous lesions of cervix," IEEE Trans Biomed Eng **48**, 96-104. (2001).

32. S.C. Gebhart, W.-C. Lin, and A. Mahadevan-Jansen. "Characterization of a Spectral Imaging System," in *SPIE Photonics West, Spectral Imaging: Instrumentation, Applications and Analysis II*, San Jose, CA, 2003: Bellingham, WA.

33. H. Fabian, et al, "Diagnosing benign and malignant lesions in breast tissue sections by using IR-microspectroscopy," Biochim Biophys Acta **1758**, 874-82 (2006).

34. D.T. Dicker, et al, "Differentiation of Normal Skin and Melanoma using High Resolution Hyperspectral Imaging," Cancer Biol Ther **5**, 1033-1038 (2006).

35. K.R. Bambery, et al, "A Fourier transform infrared microspectroscopic imaging investigation into an animal model exhibiting glioblastoma multiforme," Biochim Biophys Acta **1758**, 900-7 (2006).

36. M.E. Martin, et al, "An AOTF-based dual-modality hyperspectral imaging system (DMHSI) capable of simultaneous fluorescence and reflectance imaging," Med Eng Phys **28**, 149-55 (2006).

37. M.E. Martin, et al, "Development of an Advanced Hyperspectral Imaging (HSI) System with Applications for Cancer Detection," Ann Biomed Eng (2006).

38. I.M. Orfanoudaki, et al, "A clinical study of optical biopsy of the uterine cervix using a multispectral imaging system," Gynecol Oncol **96**, 119-31 (2005).

39. S.C. Gebhart, W.-C. Lin, and A. Mahadevan-Jansen, "In vitro determination of normal and neoplastic human brain tissue optical properties using inverse adding-doubling," Phys Med Biol **51**, 2011-2027 (2006).

40. J.W. Pickering, et al, "Double-Integrating-Sphere System for Measuring the Optical-Properties of Tissue," Applied Optics **32**, 399-410 (1993).

41. R.L. Sidman, et al, "High resolution mouse brain atlas," http://www.hms.harvard.edu/research/brain, 1999. Accessed on April 26, 2006.

42. W.-C. Lin, et al, "Intraoperative Application of Optical Spectroscopy in the Presence of Blood," IEEE Journal of Selected Topics in Quantum Electronics **7**, 996-1003 (2001).

CHAPTER V

EXPERIMENTAL AND SIMULATED ANGULAR PROFILES OF FLUORESCENCE AND DIFFUSE REFLECTANCE EMISSION FROM TURBID MEDIA

Abstract

Given the wavelength dependence of sample optical properties and the selective sampling of surface emission angles by non-contact imaging systems, differences in angular profiles due to excitation angle and optical properties can distort relative emission intensities acquired at different wavelengths. To investigate this potentiality, angular profiles of diffuse reflectance and fluorescence emission from turbid media were evaluated experimentally and using Monte Carlo simulation for a range of incident excitation angles and sample optical properties. For emission collected within the limits of a semi-infinite excitation region, normalized angular emission profiles are symmetric, roughly Lambertian, and only weakly dependent on sample optical properties for fluorescence at all excitation angles and for diffuse reflectance at small excitation angles relative to the surface normal. Fluorescence and diffuse reflectance within the emission plane orthogonal to the oblique component of the excitation also possesses this symmetric form. Diffuse reflectance within the incidence plane is biased away from the excitation source for large excitation angles. The degree of bias depends upon the scattering anisotropy and albedo of the sample and results from the correlation between photon directions upon entrance and emission. Given the strong dependence of the diffuse reflectance angular emission profile shape on incident excitation angle and sample optical properties, excitation and collection geometry has the potential to induce distortions within diffuse reflectance spectra unrelated to tissue characteristics.

Introduction

Cancer development often leads to distinct changes in the morphology and biochemistry of tissue such as an increase in nuclear density. As structural and physiological characteristics of tissues govern its interactions with light, the concept of using light propagation characteristics to detect cancer (i.e. optical biopsy) has been extensively investigated over the past two decades [1-6]. Because it can be conveniently, directly and non-invasively detected, light emission from the tissue surface, such as fluorescence or diffuse reflectance, is often used for optical tissue

interrogation. In order to truly assess tissue characteristics, it is important to acquire surface emission in a way that spectral distortions induced by factors other than intrinsic tissue characteristics are excluded.

The ability to discriminate between normal and diseased tissue using optical biopsy methods is typically investigated using fiber-optic probes which acquire emission spectra from a single site on the tissue surface. However, this "single-pixel" method of tissue discrimination limits the information transfer to the clinician. As such, the practical, long-term vision for tissue screening, disease diagnosis, and therapy guidance using optical methods calls for spectral imaging systems to implement tissue discrimination over a two-dimensional area in a single snapshot. Since imaging systems typically acquire emission without tissue contact, using detectors with limited reception angles, there is concern regarding how excitation and collection geometry relative to the tissue surface could induce extrinsic spectral distortions within measured fluorescence and diffuse reflectance data.

If angular profiles of surface emission depend upon sample optical properties, angular emission will vary between the various wavelengths within a spectrum. Consequently, their relative intensities will be modulated by detector collection that is limited to a narrow range of emission angles. Non-contact excitation and detection systems must also contend with sample-specific surface geometry effects that modulate the incident excitation angle between interrogated tissue sites (i.e. between pixels within the image). If angular emission profiles depend upon incident excitation angle, an undulating sample surface can similarly induce spectral distortions within imaging spectra and extrinsic differences between them. Given these possible sources of spectral distortion based upon excitation and collection geometry, there exists a need to characterize fluorescence and diffuse reflectance angular emission as functions of incident excitation angle and sample optical properties to determine if constraints on imaging system geometry are necessary.

The correlations of angular emission characteristics to the optical properties of tissue and to the incident angle of excitation light have not been thoroughly explored in the literature. Using Monte Carlo simulation, Qu et al reported "nearly Lambertian" angular emission profiles for fluorescence and diffuse reflectance when excitation is normal to the tissue surface [7]. Angular emission profiles for diffuse reflectance deviated from Lambertian behavior when the excitation was delivered at oblique angles (30° and 75° with respect to the surface normal) such that the

emission was biased away from the source, indicating that angular emission of diffuse reflectance may be dependent on sample optical properties when the excitation is delivered at an oblique excitation angle. Churmakov et al reported similar roughly Lambertian emission behavior for diffuse reflectance when excited normal to the surface [8]. However, while these results hint at angular emission profiles of diffuse reflectance which are dependent upon incident excitation angle, neither group investigated the correlation between angular emission and sample optical properties or provided a detailed explanation for the behavior of the bias.

Our group is interested in the application of optical methods for the guidance of therapy. In particular, we have developed the use of combined diffuse reflectance and fluorescence spectroscopy for brain tumor demarcation. To transition the early single-pixel system into a clinically viable one, a spectral imaging system is being developed and relevant calibration methods evaluated for brain cancer imaging. A critical issue is one associated with non-normal excitation angles. While the excitation angle can be rigidly controlled in contact-based spectroscopy, imaging the tissue within the resection crater of a deep-seated brain tumor can force delivery of excitation light significantly away from the surface normal if the surgeon is interested in tissue diagnosis along the crater walls. The potential for spectral distortion also exists for a variety of other *in vivo* imaging applications that involve oblique excitation angles. Spectral endoscopy in the colon and lung excite the interior circumference of the tissue walls with the lumen positioned in the image center, creating excitation angles that deviate further from the surface normal toward the center of the images. This lack of control over excitation angle in many such *in vivo* applications drives the current investigation into the potential of spectral distortion induced by excitation-sample-collection geometry within diffuse reflectance and fluorescence spectra.

In this paper, angular emission characteristics of fluorescence and diffuse reflectance are experimentally investigated. The experimental measurements are subsequently verified with Monte Carlo simulations. Specifically, effects of tissue optics and incident excitation angle on the shape of angular emission profiles of fluorescence and diffuse reflectance are explored. While this investigation is not exhaustive in nature, it highlights many behaviors of fluorescence and diffuse reflectance emission and demonstrates a need for caution in diffuse reflectance system design.

Materials and Methods

Experimental Measurement of Angular Emission Profiles

Effect of sample optical properties and incident angle of excitation light on the angular emission profiles of fluorescence and diffuse reflectance were evaluated experimentally using tissue phantoms and a combined fluorescence and diffuse reflectance spectroscopic system, as shown in Figure 1. The spectroscopic system utilizes a halogen lamp (Ocean Optics Inc, Dunedin, FL) and a pulsed nitrogen laser (Spectra-Physics, Mountain View, CA) for excitation of diffuse reflectance and fluorescence, respectively. The excitation light was coupled into a 600 μm core optical fiber and then expanded and collimated at the distal end of the fiber, creating an illumination spot of ~15-mm diameter when excitation was normal to the phantom surface (at $\alpha = 60°$, the long axis was ~30 mm in diameter). A fiber-optic probe was employed to collect the reemitted light from the phantom sample at various angles. To confine its collection angle and area, an extender 35 mm in length with a 1-mm inner diameter was attached to the collection end of the probe, giving the probe a collection cone half-angle equal to 0.82° and a numerical aperture of 0.014. The 75-mm distance between the sample and the collection probe subsequently yielded a collection area 2.14 mm in diameter at $\theta = 0°$. At oblique collection angles, the collection area becomes elliptical with its major-axis diameter increasing by $1/\cos(\theta)$ as the collection angle increases relative to the surface normal. The maximum diameter of the collection region at $\theta = 80°$ was 12.4 mm such that it always resided within the limits of the excitation spot.

The excitation light collimator and the emission collection probe were individually mounted onto two mechanical arms rotating concentrically (see Figure 1), such that the observation area was consistently centered within the excitation spot. The optical axis of the excitation light and the long axis of the emission collection probe were aligned parallel to the axes of their corresponding mechanical arms to prevent the observation area of the probe from shifting laterally as the observation angle varied. Fluorescence or diffuse reflectance light collected by the probe was sent to a spectrometer (Ocean Optics Inc) controlled by a computer to effectively observe the wavelength (i.e. optical property) dependence of the angular emission profiles of fluorescence and diffuse reflectance. A petri dish 10 mm deep by 35 mm in diameter was filled to hold the tissue phantoms prepared for this study. Monte Carlo simulation was used

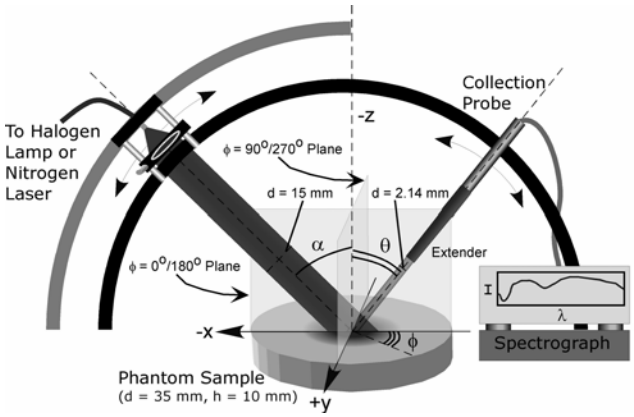

Figure 1. Schematic for experimental measurement of fluorescence and diffuse reflectance angular emission profiles as a function of emission angle θ. The diagram depicts measurement along the Φ = 0°/180° plane for a possible range of excitation angles (α) between 0° and 90°. The collection sub-system was rotated 90° with respect to the sample to measure profiles along the depicted Φ = 90°/270° plane. An extender on the end of the collection probe limited its numerical aperture and confined collection to a narrow range of emission angles at each angular position.

to verify that the dimensions of the phantom produced a semi-infinite medium for the angular profile measurements. The top of the petri dish was aligned with the x-y plane of the experimental setup (see Figure 1) to further prevent lateral shift of the observation spot while interrogating the angular emission profile from the sample.

Tissue phantoms utilized in this experimental study were prepared using polystyrene microsphere suspension (Polysciences Inc, Warrington, PA) as the base. To cover the range of scattering coefficients and anisotropy factors typically found in soft tissue [9], four microsphere suspensions were prepared for diffuse reflectance measurements as shown in Table 1a. Based upon Mie scattering calculations [10], these suspensions provided various scattering coefficients and anisotropy factors over the collected spectral range (400 – 800 nm). For fluorescence measurements, two phantom samples were created according to Table 1b with various fluorophores to provide a wide range of scattering coefficients and anisotropy factors over the fluorescence emission spectra.

For each phantom sample, fluorescence or diffuse reflectance spectra were acquired over an angle from θ = -80° to θ = 80° in 10º increments, at excitation angles of α = 0º and 60º, along the orthogonal emission planes equal to Φ = 0°/180° and 90°/270°. Some emission angles could not be measured due to specular reflectance from the phantom surface or obstruction between the excitation optics and the collection probe. Five emission spectra were collected from each combination of excitation and collection angles to ensure reproducibility, and the mean spectrum

Table 1. Tissue phantoms for experimental measurement of (a) diffuse reflectance and (b) fluorescence angular emission profiles. The polystyrene microspheres in the fluorescence phantoms were 0.954 μm in diameter.

Phantom	Microsphere Diameter (μm)	Microsphere Conc. (mg/g)	λ (nm)	μ_s (cm^{-1})	μ_a (cm^{-1})	g
1	0.954	15	400 - 800	790 - 330	0.02 - 0.18	0.938 - 0.897
2	0.954	5	400 - 800	265 - 110	0.02 - 0.18	0.938 - 0.897
3	0.535	20	400 - 800	955 - 245	0.02 - 0.18	0.906 - 0.761
4	0.535	7.5	400 - 800	360 - 90	0.02 - 0.18	0.906 - 0.761

(a)

				Excitation (λ = 337 nm)			Emission			
Phantom	Microsphere Conc. (mg/g)	Fluorophore(s)	Fluorophore Concentration	μ_s (cm^{-1})	μ_a (cm^{-1})	g	λ (nm)	μ_s (cm^{-1})	μ_a (cm^{-1})	g
1	5	NADH	10 mg/mL (14.1 mM)	272	189.6	0.936	400 - 600	390 - 260	3.32 - 0.18	0.938 - 0.922
2	15	Stilbene 420	0.1 mg/mL (0.18 mM)	815	8.2	0.936	400 - 550	790 - 590	0.46 - 0.18	0.938 - 0.928
		Rhodamine Chloride 610	0.1 mg/mL (0.21 mM)	815	1.9	0.936	570 - 650	560 - 465	16.8 - 0.18	0.925 - 0.918

(b)

was calculated. The mean intensities of fluorescence or diffuse reflectance at various emission angles were grouped such that angular emission profiles as functions of θ could be formed for each combination of excitation angle, emission plane, and wavelength (optical properties). Measured angular profiles were multiplied by cos(θ) to correct for changes in observation area of the collection probe with respect to θ. Angular emission profiles were further normalized to their corresponding peak emission intensity to facilitate comparisons of angular emission profile shape among various excitation angles and sample optical properties.

A metric was developed to quantify the symmetry of the experimentally measured angular emission profiles. The metric calculates the mean percent difference (MPD) between the positive- and negative-angle emission intensities measured in this study:

$$MPD(\%) = \frac{1}{N}\sum_{k=1}^{N=8}\left(\frac{I(\theta = +10^0 * k) - I(\theta = -10^0 * k)}{I(\theta = +10^0 * k) + I(\theta = -10^0 * k)} * 100\right). \quad (2)$$

A perfectly symmetric profile would have a MPD value equal to zero; a profile skewed toward positive angles would have a positive MPD; and a profile skewed toward negative angles would have a negative MPD. MPD values were calculated for all experimentally measured emission profiles, but the angle pairs were limited to those present in all profiles (θ = ±20°, ±30°, and ±40°) to prevent bias between MPD measurements due to larger noise contributions at smaller emission intensities. MPD values were then plotted as a function of reduced scattering coefficient (μ_s') for the various excitation-collection geometries of diffuse reflectance and fluorescence emission. The regression coefficient (R^2) of a least-squares line fit to the MPD vs. μ_s' data and the correlation coefficient (ρ) between the two parameters were calculated for each

excitation-collection geometry to quantify the dependence of the profile MPD, and thus any bias in the profile, on the reduced scattering coefficient of the sample.

Theoretical Validation

To validate the experimental measurements, a Monte Carlo simulation model for fluorescence and diffuse reflectance in biological media was developed based on the principles of Jacques and Wang [11] to be capable of:

1) Arbitrary incident angles (α) of the excitation light,
2) Fluorescence photon generation and propagation,
3) Simultaneous diffuse reflectance and fluorescence monitoring as a function of position (x,y) and escape angles (θ, Φ).

The excitation and collection geometry utilized in this model is defined as shown in Figure 2. Consistent with traditional Monte Carlo simulations for light propagation [11], the sample surface is defined along the x-y plane with the z-dimension indicating depth within the sample. Excitation light is defined by its beam radius ® and by its incident angle (α) relative to the surface normal (i.e. negative z-axis) within the x-z plane.

The photon initialization routine in the simulation model was modified to accommodate non-normal excitation angles, which eliminate the symmetry of emission with respect to the radial axis. To simulate a collimated excitation beam, the initial direction cosines of the photon

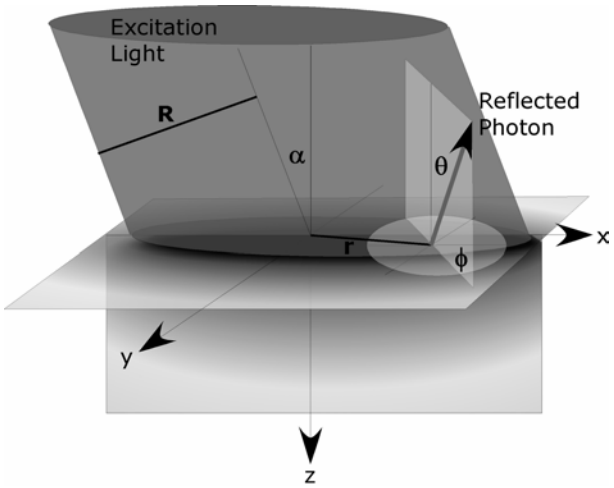

Figure 2. Geometry assignments for Monte Carlo simulation of light propagation in tissue.

are calculated using:

$$\begin{aligned} ux &= (n_0/n_1)\sin(\alpha) \\ uy &= 0 \\ uz &= \cos(\alpha_R) \end{aligned} \tag{1}$$

where n_0 and n_1 are the refraction indices of the incident and sample media, respectively, and α_R is the refraction angle of the incident light as determined by Snell's Law. Each simulation measured the impulse response of the tissue to the angled excitation light by consistently placing the initial photon position at the origin. The tissue emission response to a finite-width excitation beam was subsequently acquired by convolving the impulse response with the spatial profile of the excitation beam on the tissue surface. The excitation profile was elliptical with minor- and major-axis radii equal to R and R/cos(α), respectively.

Fluorescence photon generation occurs after every absorption event of an excitation photon. A fluorescence photon, with an initial weight equal to the product of the user-specified quantum yield of the tissue layer and the excitation photon weight absorbed by the tissue, is generated at the location of the absorption event. If its initial weight is larger than 10^{-4}, the fluorescence photon is propagated and its direction cosines can be randomly calculated using isotropic ($g = 0$) scattering equations (i.e. isotropic generation). The propagation of the fluorescence photon can be tracked using a stepsize and direction defined by user-specified emission-wavelength absorption and scattering coefficients until the photon is terminated due to insufficient weight or tissue escape.

Photon emission is described using four variables: 1,2) its position (x,y) with respect to the origin; 3) its angle (θ) relative to the surface normal; and 4) its angle (Φ) within the x-y plane relative to the negative x-axis; thus diffuse reflectance and fluorescence emission are recorded as four-dimensional functions. Exit position is uniformly and isotropically (with respect to x and y) divided into emission bins whose number and extent are specified by the user. Emission angles were varied from [0, π/2] for θ and [0, 2π] for Φ to cover the entire emission hemisphere. To normalize the surface area and solid angle of each bin and to convert emission weights to units of $W/cm^2/Sr$ (assuming that N photons provided 1 W of power), the intensity in each emission bin is scaled by $(2\pi\ N\ r\ \sin\theta\ \Delta r\ \Delta\theta\ \Delta\Phi)^{-1}$, where Δr, $\Delta\theta$, and $\Delta\Phi$ are the uniform bin widths (in *cm*, *rad*, and *rad*, respectively) for the (x, y), θ, and Φ dimensions.

Eight single-slab Monte Carlo simulations were run to determine the effects of scattering, incident excitation angle, and emission plane on diffuse reflectance and fluorescence angular

Table 2. Monte Carlo simulations of (a) diffuse reflectance and (b) fluorescence angular emission profiles along the $\phi = 0°/180°$ and $\phi = 90°/270°$ emission planes for $\alpha = 0°$ and $\alpha = 60°$ excitation angles.

g	μ_s' (cm^{-1})	A	A'	α (deg)	N
0.9	10	0.909	0.500	**0**	6×10^{11}
0.9	10	0.909	0.500	**60**	6×10^{11}
0.9	80	0.988	0.889	**0**	1×10^{10}
0.9	80	0.988	0.889	**60**	1×10^{10}

(a)

Excitation Wavelength			Emission Wavelength							
μ_s (cm^{-1})	μ_a (cm^{-1})	g	μ_s (cm^{-1})	μ_a (cm^{-1})	g	μ_s' (cm^{-1})	A	A'	α (deg)	N
100	10	0.9	70	7	0.86	10	0.909	0.588	**0**	1.5×10^{9}
100	10	0.9	70	7	0.86	10	0.909	0.588	**60**	1.5×10^{9}
800	10	0.9	560	7	0.86	80	0.988	0.920	**0**	5×10^{7}
800	10	0.9	560	7	0.86	80	0.988	0.920	**60**	5×10^{7}

(b)

emission profiles (Table 2). The limits of the scattering coefficients employed in the simulations were chosen to coincide with the scattering extremes typically found within soft tissue, while the absorption and anisotropy coefficients were maintained at average soft-tissue values [9]. The ratio of optical properties at the fluorescence excitation and emission wavelengths was based on the general trend of Mie scattering and oxy- and deoxy-hemoglobin absorption at the wavelengths which correspond to NADH brain tissue autofluorescence (λ_{em} = 460 nm) under ultra-violet excitation (λ_{ex} = 360 nm) [12].

A uniform collimated beam with a diameter of 1 cm was used for excitation. The slab thickness was set to 5 cm to prevent transmission and subsequently maximize emission of each photon. The slab index of refraction was set to 1.4 to mimic soft tissue [13]. Changes in quantum yield were assumed to modify the intensity but not the direction of fluorescence photon emission; therefore, the quantum yield was set to 1.0 for all simulations in which fluorescence was simulated. Emission position was tracked within 50 spatial bins between –2.5 mm and 2.5 mm along the x- and y-dimensions. Emission direction was divided into 30 bins for $\theta \in [0, \pi/2]$ and 48 bins for $\Phi \in [0, 2\pi]$.

Statistical independence of each excitation photon allowed the computations for each simulation to be expedited by distributing them among 18, 2.4 GHz processors of a 9-node UNIX cluster using Message Passage Interface (MPI) routines. The number of photons for the various cases of incident excitation angle and sample optical properties varied from 10 billion to 4 trillion photons for diffuse reflectance simulation and 50 million to 1.5 billion photons for

fluorescence. Simulation times varied (from several hours to several days) depending upon fluorescence generation, the number of photons simulated, the incident excitation angle, and the sample optical properties. Regardless of parameters, simulations required roughly two additional hours of computation time to compile the emission results from the various nodes of the cluster.

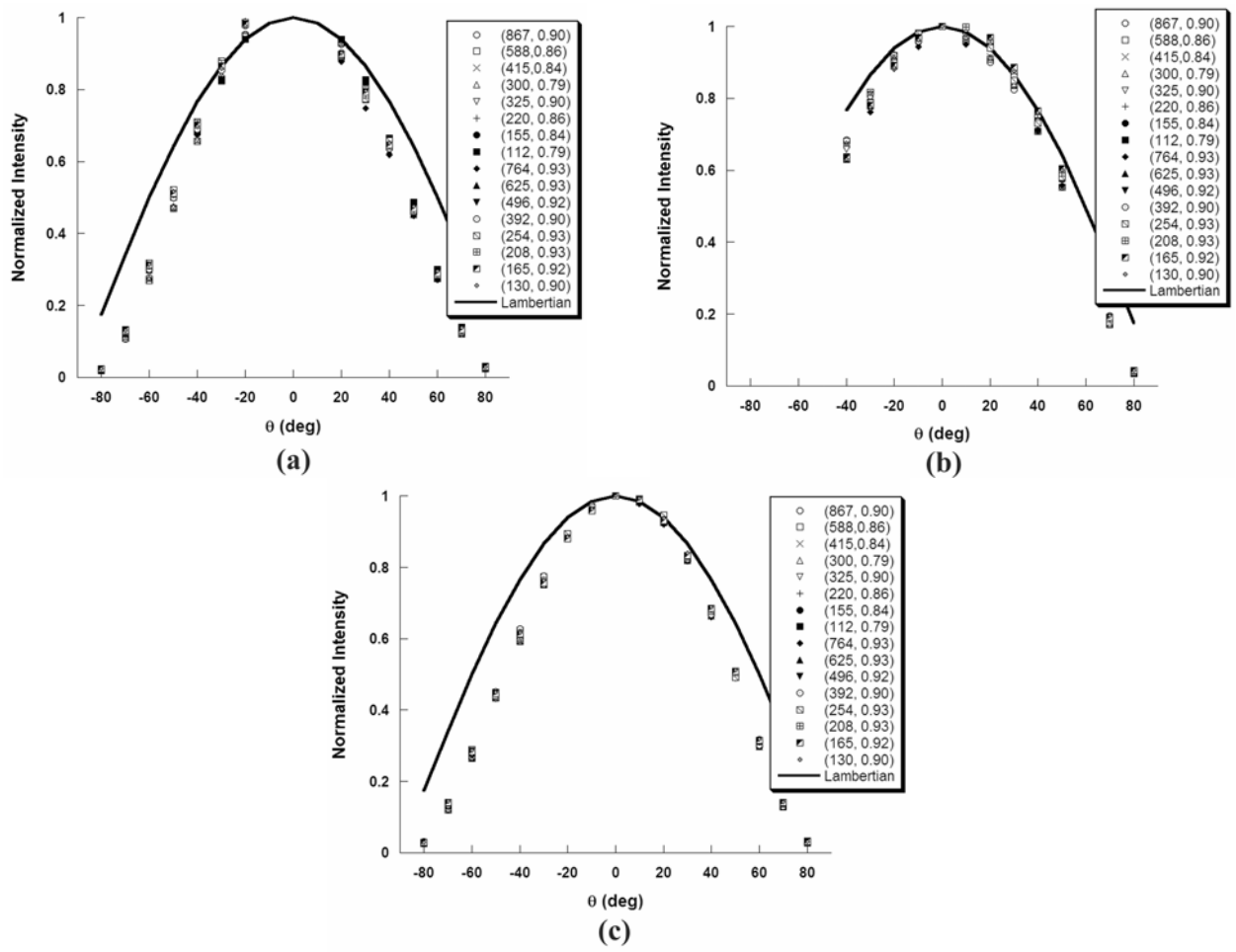

Figure 3. Experimentally measured angular profiles for diffuse reflectance emission: (a) $\alpha = 0°$ excitation, both emission planes; (b) $\alpha = 60°$ excitation, $\Phi = 0°/180°$ plane; (c) $\alpha = 60°$ excitation, $\Phi = 90°/270°$ plane. Multiple curves in each plot represent discrete detected wavelengths and optical properties (μ_s, g shown in the legend) for the phantom samples.

Results

Experimental Measurement of Angular Emission Profiles

The experimentally measured angular emission profiles of diffuse reflectance and fluorescence are shown in Figures 3 and 4. Figure 5 depicts the MPD values as a function of reduced scattering coefficient (μ_s') for the various excitation-collection geometries of diffuse reflectance and fluorescence emission. In general, diffuse reflectance along the incidence plane (Φ = 0°/180°) possesses a consistent angular distribution over a broad range of sample optical properties for α = 0° (Figures 3a and 5a). Noticeable data spreading is found in the experimental

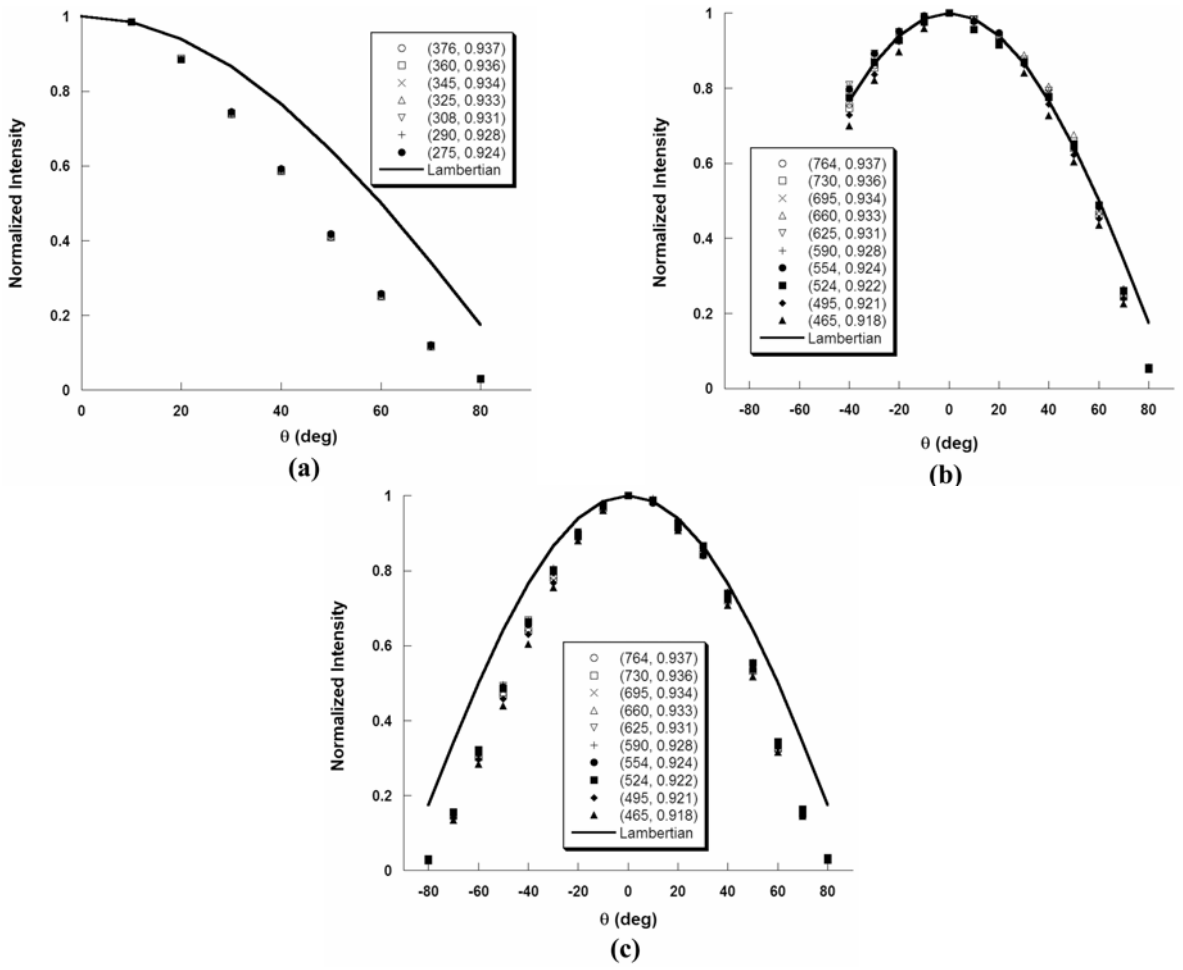

Figure 4. Experimentally measured angular profiles for fluorescence emission: (a) α = 0° excitation, both emission planes; (b) α = 60° excitation, Φ = 0°/180° plane; (c) α = 60° excitation, Φ = 90°/270° plane. Multiple curves in each plot represent discrete detected wavelengths and optical properties ($\mu_{s,em}$, g shown in the legend) for the phantom samples at the emission wavelength. The measurements for plot (a) were acquired from fluorescence phantom 1 described in Table 1b. The measurements for plots (b) and (c) were acquired from fluorescence phantom 2.

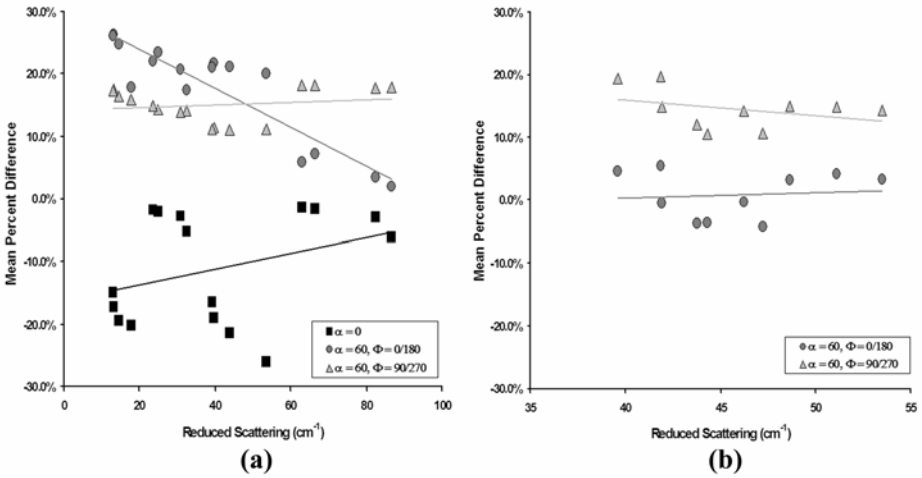

Figure 5. Mean percent difference versus reduced scattering for various excitation angles and emission planes of experimentally measured (a) diffuse reflectance and (b) fluorescence. Regression lines were calculated using a least-squares fit.

data; however, there was no correlation between the MPD of the profile and the reduced scattering coefficient of the sample ($R^2 = 0.12$, $\rho = 0.34$). In other words, the angular emission profile of diffuse reflectance seems to be optical-property independent at $\alpha = 0°$.

For large-angle excitation of diffuse reflectance ($\alpha = 60^o$ – Figures 3b & c), an optical-property dependence of the angular emission is evident within the incidence plane (Figure 5a). The positive MPD values for the $\Phi = 0°/180°$ emission plane, observed (but not shown) for all sample solutions and all wavelengths, indicate a diffuse reflectance emission skewed toward positive emission angles, opposite the excitation source. As the reduced scattering coefficient increases, the asymmetry in the angular emission profile decreases, behavior that is clearly depicted in Figure 5a and further demonstrated by the magnitude of the regression and correlation coefficients ($R^2 = 0.85$, $\rho = -0.91$). The $\alpha = 60°$, $\Phi = 0°/180°$ excitation-collection geometry of diffuse reflectance is the only geometry with a regression coefficient above 0.13 and a correlation coefficient magnitude greater than 0.36.

The optical-property dependence of the angular emission profile of diffuse reflectance is only observed within the incidence plane (Figures 3c and 5a). While on average the MPD values for the $\Phi = 90°/270°$ plane are similar to those for the $\Phi = 0°/180°$ plane, the symmetry of the angular emission profile in the $\Phi = 90°/270°$ plane is not affected by the optical properties of the phantom ($R^2 = 0.04$, $\rho = 0.20$).

Fluorescence along both emission planes is consistent over a broad range of optical properties (Figures 4 and 5b). Since the most extreme excitation angle ($\alpha = 60°$ - Figures 4b & c) yields unbiased, symmetric fluorescence within the incidence ($R^2 = 0.01$, $\rho = 0.11$) and orthogonal ($R^2 = 0.13$, $\rho = -0.36$) emission planes, fluorescence behavior was subsequently characterized only for positive emission angles and only within the incidence plane for $\alpha = 0°$

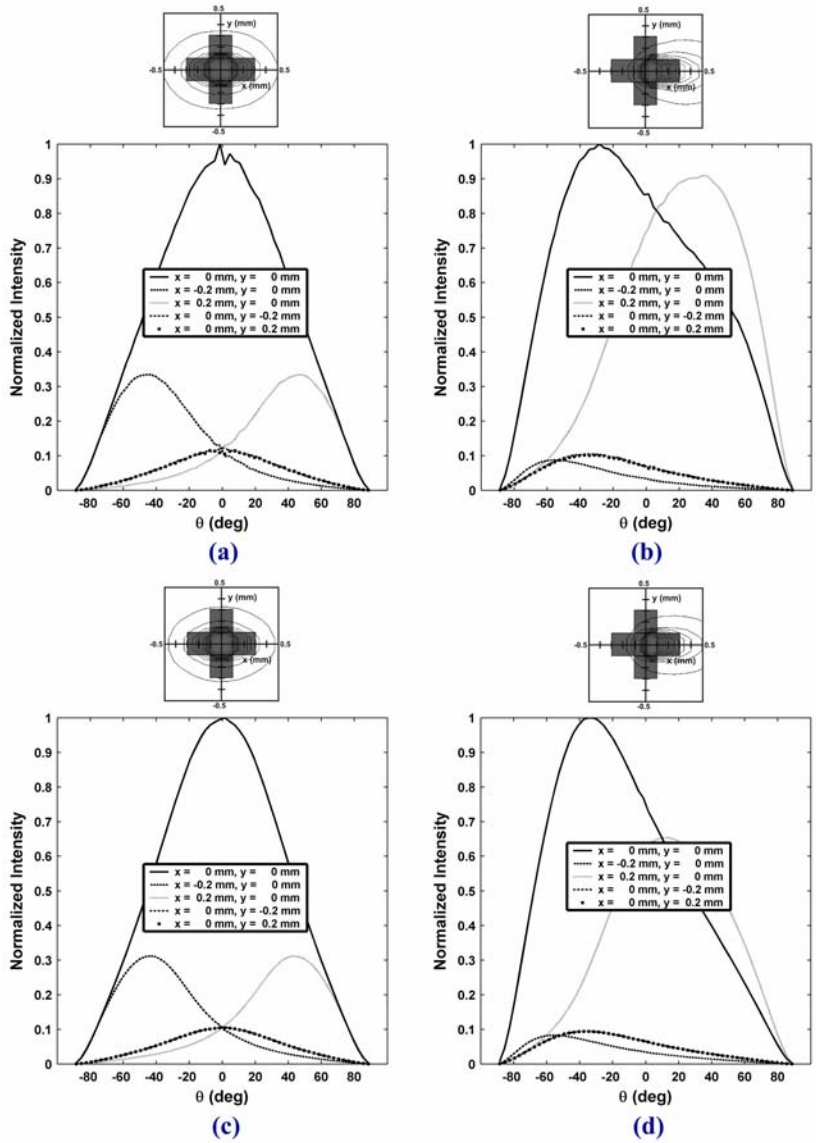

Figure 6. Angular emission profiles produced by Monte Carlo simulation versus spatial position within the impulse response: (a) diffuse reflectance after 0° excitation, (b) diffuse reflectance after 60° excitation, (c) fluorescence after 0° excitation, (d) fluorescence after 60° excitation. The header of each figure depicts the five emission regions from which the angular emission profiles were calculated as well as a contour of the impulse response integrated over all emission angles. The profiles derive from the $\Phi = 0/180°$ emission plane with simulation parameters (at the excitation wavelength for fluorescence): $\mu_s = 100$ cm^{-1}, $\mu_a = 10$ cm^{-1}, $g = 0.9$.

excitation (Figure 4a). Therefore, no MPD values were calculated for these profiles.

Theoretical Validation

Figure 6 outlines the spatial dependence within representative diffuse reflectance and fluorescence impulse responses. Mean profiles are integrated over the five shaded areas shown in the header of each figure. No emission regions outside the central 1 mm by 1 mm area of the impulse response were used because the largest full-width at half maximum (FWHM) of the four impulse responses was 174 μm. The mean angular emission profiles have been normalized with respect to the peak of the (x = 0, y = 0) profile to maintain the relative emission levels of the five emission regions.

For $\alpha = 0°$ excitation, the mean diffuse reflectance and fluorescence profiles from the regions centered about the origin are symmetric about the surface normal. The mean profiles from regions centered along the y-axis are similarly symmetric. However, the regions along the x-axis on either side of the origin are mirror images of one another, skewed away from the spatial origin of the impulse response.

For $\alpha = 60°$ excitation, the diffuse reflectance and fluorescence profiles from the regions centered about the origin are no longer symmetric. The oblique excitation angle shifts the point of maximum emission intensity roughly 100 μm from the origin along the positive x-axis and skews the profiles from regions centered along the y-axis slightly toward negative emission angles. The profile from the region centered along the positive x-axis remains skewed away from the spatial origin.

Figure 7 outlines the representative spatial dependence of angular emission profiles of diffuse reflectance and fluorescence within the excitation area along the sample surface. Only a 60° excitation profile is shown because the minor-axis of the profile can be used to indicate the response after 0° excitation. All profiles are individually normalized to a peak emission intensity of 1.0. Figures 7a and c indicate that the angular emission profile is consistent when the emission region is well within the limits of the excitation profile. This consistent profile is equivalent to the summation profile over the entirety of the impulse response and therefore results when the emission point can be described as surrounded by a semi-infinite excitation area. This description fails to apply near the edges of the excitation spot, as indicated in Figures 7b and d. In these regions, portions of the impulse response are no longer included in the integrated emission

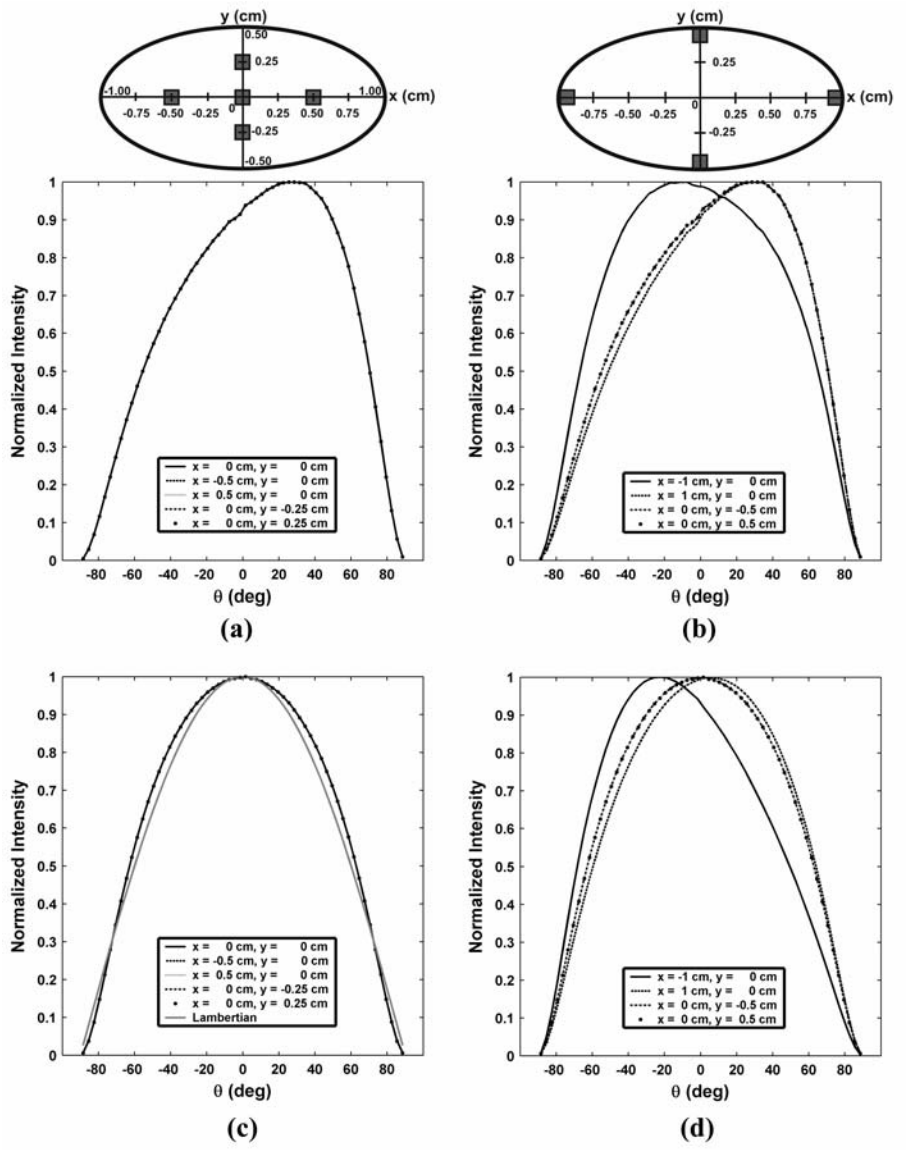

Figure 7. Angular emission profiles produced by Monte Carlo simulation versus spatial position within the excitation spot: (a) diffuse reflectance within the spot interior, (b) diffuse reflectance along the spot edges, (c) fluorescence within the spot interior, (d) fluorescence along the spot edges. The profiles were integrated over 1 x 1 mm surface areas (shown in the headers of Figures 7a and b) and derive from the $\Phi = 0/180°$ emission plane with simulation parameters (at the excitation wavelength for fluorescence): $\mu_s = 100\ cm^{-1}$, $\mu_a = 10\ cm^{-1}$, $g = 0.9$, $\alpha = 60°$.

response, resulting in profiles disparate from the profiles in the interior of the excitation area. The extent of these edge effects inside the boundaries of the excitation profile will depend upon the optical properties of the sample and will be related to the FWHM of the impulse response. Since spectral imaging systems can be designed to exclude emission collection from the outer regions of the excitation spot, and thus prevent these edge effects, the remainder of the

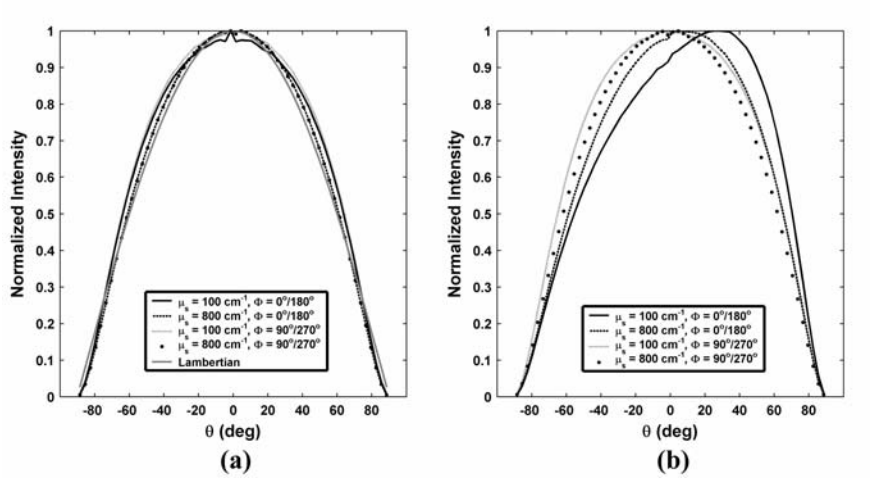

Figure 8. Representative angular emission profiles of diffuse reflectance produced by Monte Carlo simulation: (a) $\alpha = 0^o$ excitation, (b) $\alpha = 60^o$ excitation. An absorption coefficient of $\mu_a = 10$ cm^{-1} and an anisotropy coefficient of g = 0.9 were used for all simulations.

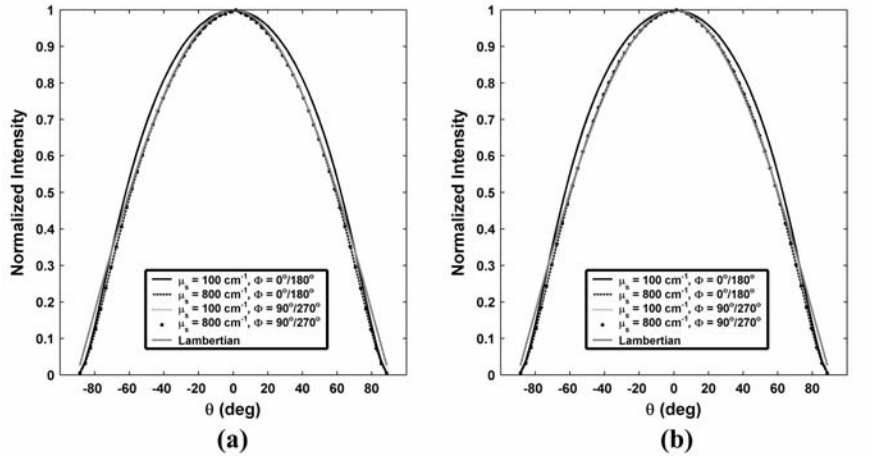

Figure 9. Representative angular emission profiles of fluorescence produced by Monte Carlo simulation: (a) $\alpha = 0^o$ excitation, (b) $\alpha = 60^o$ excitation. Scattering coefficients shown correspond to the excitation wavelength. Scattering at the emission wavelength was consistently equal to 70% of scattering at the excitation wavelength. Absorption coefficients for all simulations were set to 10 cm^{-1} for excitation and 7.0 cm^{-1} for emission. An anisotropy coefficient of g = 0.9 was used for all simulations for excitation and emission.

simulation results will concentrate on angular emission profiles integrated over the emission region depicted in Figure 7a located at the center of the excitation area.

Figures 8 and 9 show representative angular emission profiles of diffuse reflectance and fluorescence, respectively. The MPD values for these profiles are outlined in Table 3. While the profiles in Figures 8a, c & d are symmetric about the surface normal, the optical-property dependent skewing phenomenon of diffuse reflectance emission within the incidence plane of the excitation appears in the simulation result for a large excitation angle ($\alpha = 60°$, Figure 8b). The

Table 3. Mean percent difference (MPD) of diffuse reflectance (Rd) and fluorescence (F) angular emission profiles for two excitation angles (α), two reduced scattering coefficients (μ_s'), along the two emission planes (Φ). All simulations employed g = 0.9 for the scattering anisotropy. The μ_s' values correspond to the excitation wavelength.

Emission	α	Φ	$\mu_s' = 10$ cm^{-1}	$\mu_s' = 80$ cm^{-1}
Rd	0°	0/180	-0.08%	0.03%
		90/270	0.04%	-0.02%
	60°	0/180	13.38%	5.45%
		90/270	0.03%	0.05%
F	0°	0/180	0.08%	0.19%
		90/270	0.02%	0.01%
	60°	0/180	0.08%	0.17%
		90/270	0.04%	0.00%

effect of reduced scattering on skewing implied by the simulation model, however, is less than that derived from the experimental results under the same conditions. The mean percent differences (MPDs) for simulated diffuse reflectance emission after 60° excitation decrease from 13.4% to 5.5% when the reduced scattering increases from 10 cm^{-1} to 80 cm^{-1}; whereas the MPDs of the experimental data decrease from 26.2% to 3.5% over a similar increase in μ_s' (13 cm^{-1} to 82 cm^{-1}). The average MPD for the unskewed profiles (n = 6) is 0.01%, demonstrating a great degree of symmetry. This gives cause to believe that the corresponding experimentally measured diffuse reflectance profiles would be similarly symmetric if not for measurement noise and error.

The diffuse reflectance simulation results also show that angular emission profiles from samples with low scattering properties (μ_s' = 10 cm^{-1}) possess a greater profile width than profiles from samples with high scattering (μ_s' = 80 cm^{-1}), regardless of the emission plane or incident excitation angle. For the profiles in Figure 8 which demonstrate no skewing, the full-width at half-maximum (FWHM) values are significantly larger (Δ = 6.0°, $p < 0.001$, paired t-test, n = 3) for μ_s' = 10 cm^{-1} profiles than μ_s' = 80 cm^{-1} profiles. For the skewed profile from the Φ = 0°/180° emission plane after α = 60° excitation, the FWHM of the μ_s' = 10 cm^{-1} profile is 0.8° narrower than the μ_s' = 80 cm^{-1} profile, possibly due to the disparate degree of skewing between them.

As suggested by the simulation model (Figure 9) and consistent with experimental observations, angular profiles of fluorescence emission are not affected by tissue scattering properties, excitation angle, or observation plane. The average MPD value for the profiles in Figure 9 (n = 8) is 0.07%, again giving cause to believe that the asymmetry in the experimentally measured fluorescence profiles was due to measurement noise and error. Similar to diffuse

reflectance, unskewed angular emission profiles (n = 4 pairs) of simulated fluorescence with lower reduced scattering coefficients ($\mu_{s,em}$' = 7 cm^{-1}) possess higher FWHM values (Δ = 6.1°, p < $1x10^{-5}$) than profiles with higher reduced scattering ($\mu_{s,em}$' = 56 cm^{-1}), suggesting that this phenomenon is intrinsic to the tissue properties of the sample and not specific to diffuse reflectance.

The skewing behavior in diffuse reflectance emission profiles for oblique incident excitation angles was investigated relative to the sample scattering coefficient, absorption coefficient, and anisotropy factor. Monte Carlo simulation was employed for this investigation due to its capability to vary the magnitude of one optical property coefficient while holding the

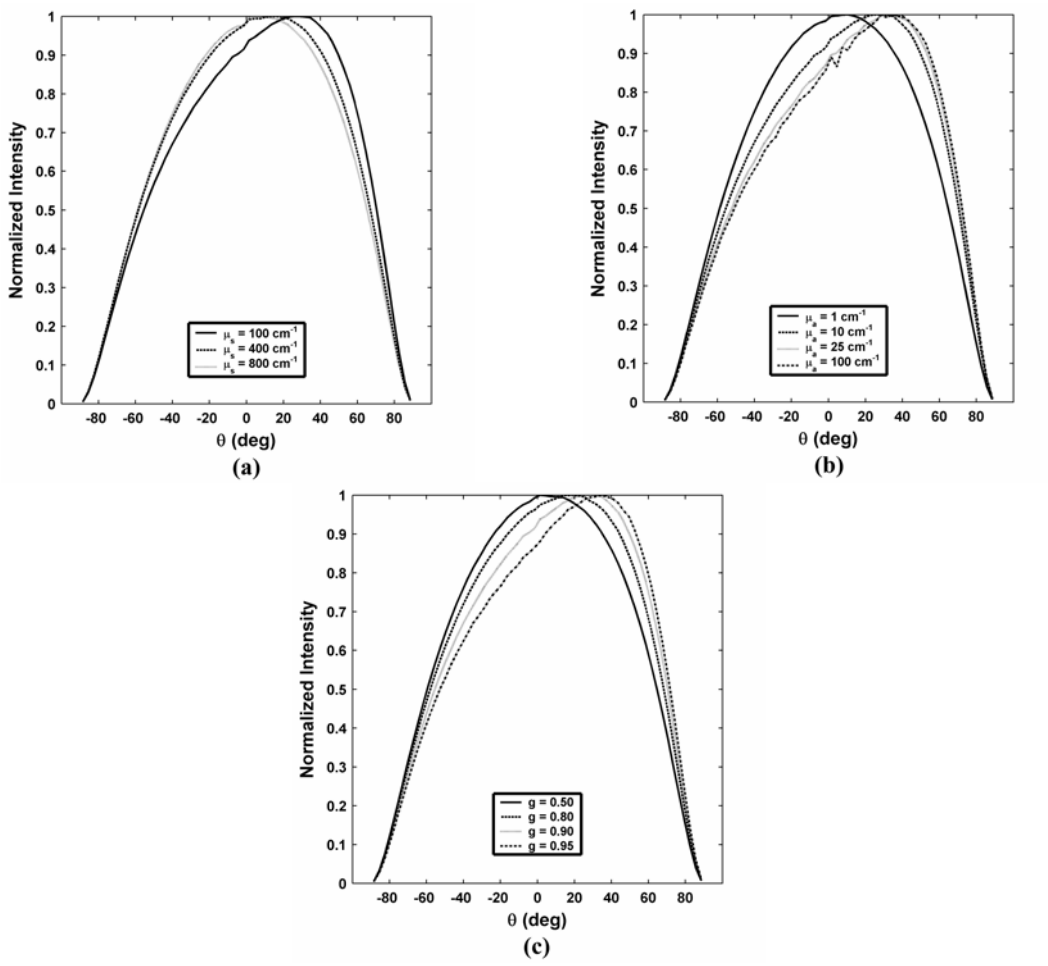

Figure 10. Simulated diffuse reflectance angular emission profiles within the incidence plane at α = 60° excitation and for: (a) varying scattering coefficients, (b) varying absorption coefficients, and (c) varying anisotropy coefficients. When not varied, the other optical property coefficients were held constant at μ_s = 100 cm^{-1}, μ_a = 10 cm^{-1}, and g = 0.9.

Table 4. Monte Carlo simulations to investigate the effects of optical properties (μ_s, μ_a, and g) on diffuse reflectance angular emission profiles along the $\phi = 0°/180°$ emission plane for $\alpha = 60°$ excitation.

μ_s (cm^{-1})	μ_a (cm^{-1})	g	μ_s' (cm^{-1})	A	A'	α (deg)	N
100	10	0.9	10	0.909	0.500	60	6×10^{11}
400	10	0.9	40	0.976	0.800	60	1×10^{11}
800	10	0.9	80	0.988	0.889	60	1×10^{10}
100	**1**	0.9	10	0.990	0.909	60	1×10^{11}
100	**10**	0.9	10	0.909	0.500	60	6×10^{11}
100	**25**	0.9	10	0.800	0.286	60	2×10^{12}
100	**100**	0.9	10	0.500	0.091	60	4×10^{12}
100	10	**0.5**	50	0.909	0.833	60	3×10^{11}
100	10	**0.8**	20	0.909	0.667	60	4×10^{11}
100	10	**0.9**	10	0.909	0.500	60	6×10^{11}
100	10	**0.95**	5	0.909	0.333	60	6×10^{11}

other two constant. The simulations are outlined in Table 4. Figure 10 outlines the results, demonstrating that the "degree" of skewing increases as the scattering coefficient decreases, as the absorption coefficient increases, and as the anisotropy factor increases.

The mathematical definitions of optical parameters such as reduced scattering ($\mu_s' = \mu_s[1-g]$), albedo ($A = \mu_s/[\mu_s+\mu_a]$), and reduced albedo ($A' = \mu_s'/[\mu_s'+\mu_a]$) play against one another the effects of scattering, absorption, and anisotropy on skewing behavior. For example, increasing the scattering coefficient lowers skewing while increasing absorption amplifies it. Since proportionately increasing scattering and absorption yields a consistent albedo, skewing behavior may be constant for a constant albedo, regardless of the scattering and absorption coefficient magnitudes. Similar arguments can be made for reduced scattering and reduced albedo. To investigate these possibilities, three additional sets of Monte Carlo simulations (Table 5) were

Table 5. Monte Carlo simulations to investigate the effects of reduced scattering coefficient (μ_s'), albedo (A), and reduced albedo (A') on diffuse reflectance angular emission profiles along the $\phi = 0°/180°$ emission plane for $\alpha = 60°$ excitation.

μ_s (cm^{-1})	μ_a (cm^{-1})	g	μ_s' (cm^{-1})	A	A'	α (deg)	N
10	10	0	**10**	0.500	0.500	60	2.4×10^{12}
20	10	0.5	**10**	0.667	0.500	60	2.4×10^{12}
50	10	0.8	**10**	0.833	0.500	60	1.2×10^{12}
100	10	0.9	**10**	0.909	0.500	60	6×10^{11}
100	10	0.9	10	**0.909**	0.500	60	6×10^{11}
800	80	0.9	80	**0.909**	0.500	60	1×10^{11}
800	10	0.9	80	**0.988**	0.889	60	1×10^{10}
100	1.25	0.9	10	**0.988**	0.889	60	1×10^{11}
100	10	0.9	10	0.909	**0.500**	60	6×10^{11}
50	25	0.5	25	0.667	**0.500**	60	5×10^{11}
800	10	0.9	80	0.988	**0.889**	60	1×10^{10}
400	25	0.5	200	0.941	**0.889**	60	5×10^{10}

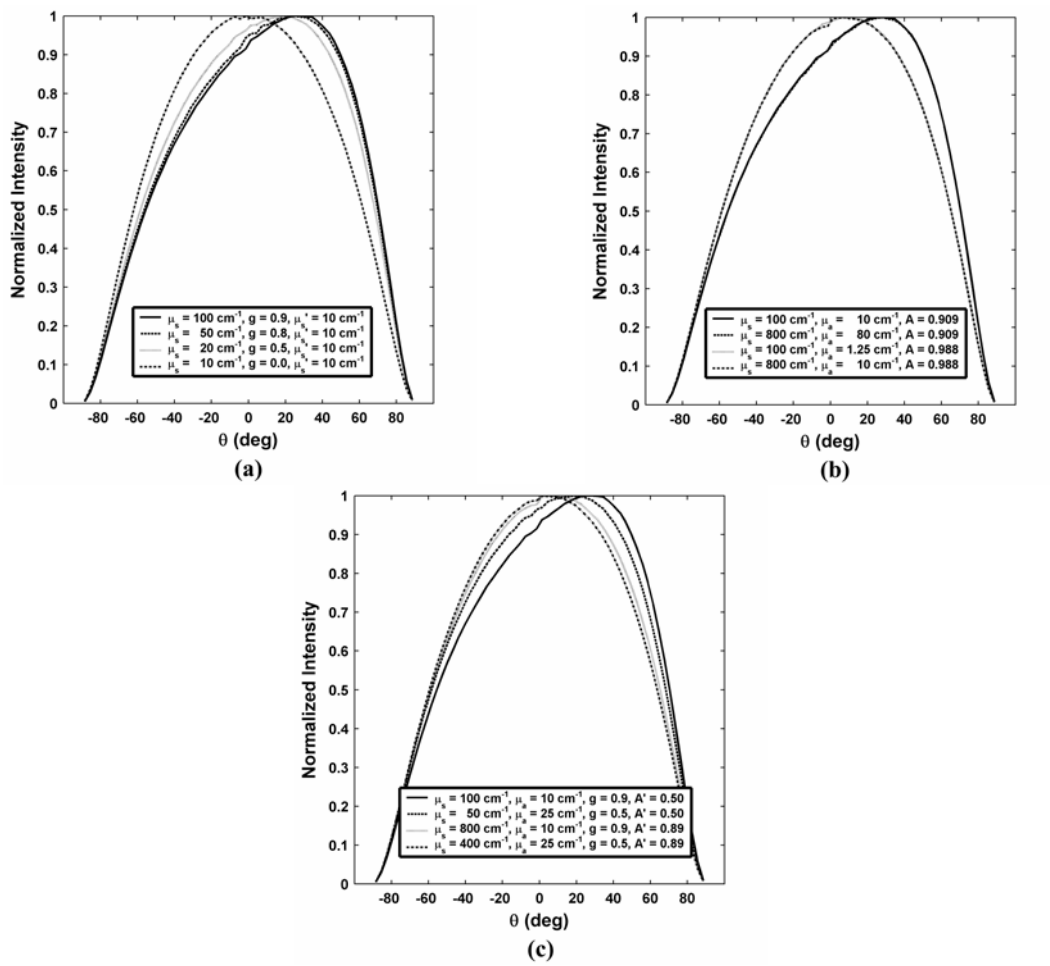

Figure 11. Simulated diffuse reflectance angular emission profiles within the incidence plane at α = 60° excitation and for: (a) constant reduced scattering, μ_s' = 10 cm^{-1}; (b) two cases of constant albedo, A = 0.909 and 0.988; and (c) two cases of constant reduced albedo, A' = 0.5 and 0.889.

run to determine if consistent values of these optical parameters produce consistent emission profiles regardless of the magnitudes of the individual optical property coefficients.

The first set of simulations (Figure 11a) maintained constant reduced scattering coefficients (μ_s' = 10 cm^{-1}) by adjusting the scattering coefficient and anisotropy factor. The observed increase in profile skewing despite the increase in the scattering coefficient demonstrates that the effect of the anisotropy overpowers the effect of scattering. The second set of simulations measured the skewing for two scenarios each of two different albedos (A = 0.909 and 0.988) and show that profile skewing is constant between scenarios with equivalent albedos and that skewing increases as the albedo decreases (Figure 11b). This suggests that profile skewing responds to changes in scattering and absorption via their effect on the sample albedo

and that consistent profile skewing only requires consistent albedo and anisotropy factors. The final set of simulations measured profile skewing for two cases each of two different reduced albedos (A' = 0.5 and 0.889) by manipulating the scattering coefficient, absorption coefficient, and anisotropy factor. The profiles (Figure 11c) demonstrate that profile skewing is not consistent with reduced albedo and that the skewing follows no trend with either the albedo or the anisotropy factor, instead most likely involving a complex interplay between the two.

It was previously indicated in this paper that an optical property dependence of angular emission profiles can lead to a change in spectral shape dependent upon the excitation-collection geometry of the imaging system. Since the experimental and simulation results demonstrate that the angular emission profiles of diffuse reflectance emission are optical property dependent within the incidence plane, Monte Carlo simulation was used to model imaging spectra under the four excitation-collection geometries emphasized in this paper. Diffuse reflectance emission was simulated with α = 0° and 60° excitation for wavelengths 400 nm to 700 nm in 20 nm increments. The sample optical properties at the simulated wavelengths (Figure 12a) were modeled after glioma brain tissue using *in vitro* spectrophotometer measurements of diffuse reflectance and transmission measurements from 58 glioma samples [12]. Reduced scattering

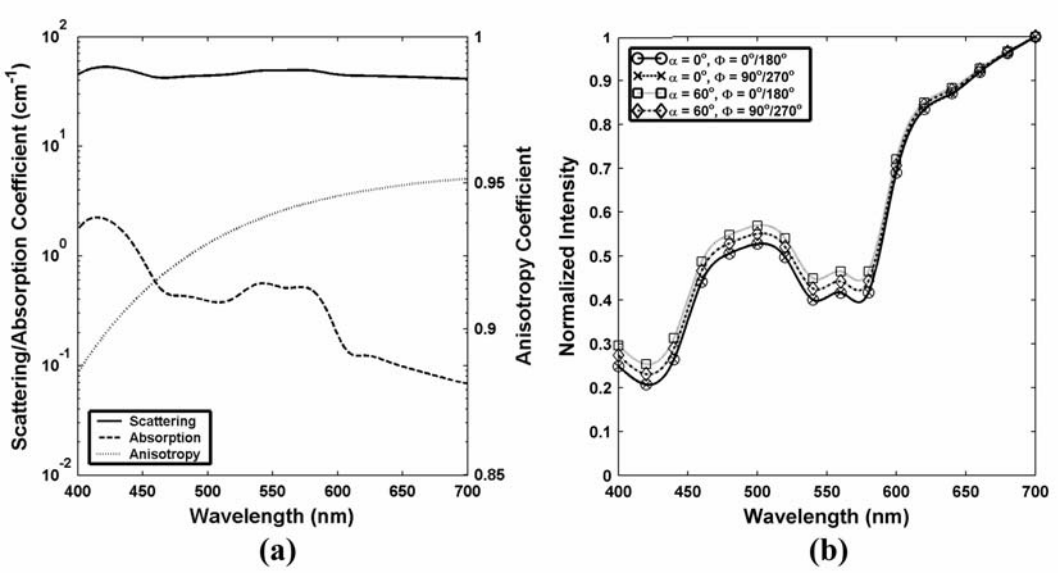

Figure 12. Demonstration of spectral distortion due to the optical property dependence of angular emission profiles: (a) sample optical property spectra employed in spectral imaging simulation, (b) normalized diffuse reflectance spectra for four excitation-collection geometries.

and absorption spectra were calculated from the reflectance and transmission spectra using an inverse-adding doubling method [14]. Sample anisotropy values were taken from anaplastic astrocytoma data published by Yaroslavsky et al [15] and used to determine sample scattering from the reduced scattering spectra.

Diffuse reflectance emission was recorded as a four-dimensional function similar to the angular profile simulations. To simulate collection from an f/3.86 (NA = 0.26) camera lens positioned at $\theta = 45°$, emission intensities for each excitation-collection geometry at each wavelength were calculated by integrating the respective emission profiles from $\theta = 30°$ to 60°. The four simulated spectra were normalized to a peak of one. The resultant spectra (Figure 12b) demonstrate as expected that collection within the incidence plane after $\alpha = 60°$ excitation distorts the shape of the diffuse reflectance spectrum. However, unexpectedly, the spectrum from the orthogonal emission plane after $\alpha = 60°$ excitation also deviates from the $\alpha = 0°$ spectra.

Discussion

Many studies have investigated fluorescence and diffuse reflectance emission as a function of radial position [16-18]; however, there are only a handful of papers that have addressed how sample optical properties and incident excitation angle affect the angular profiles of fluorescence and diffuse reflectance emission [7, 8, 19, 20]. This information can be critical to design of spectral imaging systems for tissue diagnosis because angular profile dependence on incident excitation angle and/or sample optical properties can induce extrinsic distortions within imaging spectra.

For the case where emission is collected within the limits of a semi-infinite excitation spot, we demonstrated both experimentally and theoretically that the optical properties of a sample have little or no influence on the angular emission profile of diffuse reflectance when the incident angle of the excitation light is normal to the tissue surface ($\alpha = 0°$) or when emission occurs within the $\Phi = 90°/270°$ plane orthogonal to the incident excitation plane. For these cases, angular emission profiles are symmetric about the surface normal ($\theta = 0°$) and slightly underestimate a Lambertian profile at all emission angles.

For large excitation angles ($\alpha = 60°$), the angular emission profile of diffuse reflectance loses its symmetry within the incident excitation plane with emission that is biased away from the incident light. The bias, or skewing, of the angular emission profile is found to be dependent

on sample optical properties. From the results in Figure 11, skewing for oblique excitation angles depends solely upon the albedo ($A = \mu_s/[\mu_a + \mu_s]$) and scattering anisotropy (g) of the sample, with the degree of skewing inversely related to the albedo and directly related to the anisotropy factor. As such, the effects of variations in scattering and absorption on skewing are related to how they modulate the sample albedo, regardless of their absolute magnitudes.

Unlike diffuse reflectance, angular emission profiles of fluorescence are symmetric in shape and independent of sample optical properties. They show no alteration as the excitation angle changes. These observations have been confirmed both experimentally and theoretically. Since the diffuse reflectance simulations demonstrate that anisotropy is one of the major players in determining angular emission behavior, the isotropic local generation of fluorescence within the sample is most likely responsible for its symmetric emission profile. It decouples the photon propagation direction, and hence its emission angle, from the incident excitation angle, regardless of the number of scattering events before emission.

The skewing observed in diffuse reflectance emission was previously reported by Qu et al [7]. Skewing was attributed to the forward-scattering nature of tissue, which reduces the chance for scattering back toward the excitation source relative to scattering away from it. However, Qu et al simulated diffuse reflectance and fluorescence emission for a single sample ($\mu_a = 16.5$ cm^{-1}, $\mu_s = 184$ cm^{-1}, $g = 0.9$) without further investigating a possible dependence of diffuse reflectance skewing on optical properties. A hypothesis to explain this dependence must address: (1) the skewing bias of diffuse reflectance emission away from the excitation source within the incident excitation plane for large excitation angles; (2) the loss of bias within the orthogonal emission plane, at low excitation angles, and for fluorescence emission; (3) equivalent profile skewing degree between samples with similar albedo and anisotropy factors for an oblique excitation angle; (4) increased profile skewing with decreased albedo and increased scattering anisotropy.

The most obvious explanation for optical-property dependent skewing is that it depends upon the degree of correlation between the incident excitation angle and the photon emission angle for a given set of sample optical properties. Fluorescence emission is symmetric because the isotropic nature of its local generation within the tissue automatically decouples the two angles. For diffuse reflectance emission with forward-biased scattering, since each scattering event increases the randomness in photon direction, the correlation between incident and

emission angles as well as the emitted photon energy relates inversely to the mean number of scattering events undergone by the emitted photons. To demonstrate this relationship, the mean number of scattering events was calculated for emission at Φ = 0°, 90°, 180°, and 270° for the various Monte Carlo simulations outlined in Figures 6 through 11. Since the contribution of each photon to the angular emission profile is weighted by its emitted photon energy, the contribution (*SE*) of each photon to the mean number of scattering events (μ_{SE}) calculated over the number of emitted photons (*N*) was similarly weighted by the emitted energy (*w*):

$$\mu_{SE} = \frac{\sum_{i=1}^{N} SE_i w_i}{\sum_{i=1}^{N} w_i} \tag{3}$$

The results outlined in Table 6 demonstrate how excitation angle, emission plane, anisotropy, and albedo affect this metric.

Photons that excite normal to the tissue surface must change direction equal amounts to emit along each of the four emission quadrants outlined in Table 6 (Φ = 0°, 90°, 180°, 270°). As such, the number of scattering events before emission is equal between the quadrants and the photons are equally likely to emit along each of them, resulting in symmetric angular emission profiles within both emission planes regardless of sample optical properties. For an oblique excitation angle, the photon direction is biased toward the Φ = 0° quadrant and away from Φ = 180°. Therefore, less scattering events are needed to emit along Φ = 0°, resulting in larger emitted photon energies and an angular emission profile within the incidence plane which is skewed toward positive emission angles (θ = 0-90°). For emission along the orthogonal emission plane (Φ = 90°/270°) with an oblique excitation angle, photons must change direction an equal

Table 6. Weighted mean number of steps per emitted photon along the four quadrants of the principal emission planes for various simulation parameters. Means were calculated over the 90° range of polar emission angles (θ) within each quadrant.

Simulation Parameters				Number of Steps - Weighted Mean			
α (deg)	μ_s (cm^{-1})	μ_a (cm^{-1})	g	Φ = 0°	Φ = 90°	Φ = 180°	Φ = 270°
0	100	10	0.9	13.9	13.9	13.9	13.9
60	100	10	0.9	12.4	13.1	13.9	13.3
0	100	10	0.5	9.1	9.1	9.2	9.1
60	100	10	0.5	8.3	8.7	9.0	8.8
0	800	10	0.9	52.8	52.8	52.8	52.8
60	800	10	0.9	46.1	48.9	51.9	49.6
0	800	80	0.9	13.9	13.9	13.9	13.9
60	800	80	0.9	12.4	13.1	13.9	13.3

amount to emit along the two quadrants so no relative bias exists between them. Therefore, the mean number of scattering events is equivalent between the two, resulting in symmetric angular emission profiles regardless of sample optical properties. Finally, less skewing is present for lower anisotropy factors because they are able to randomize the photon direction and subsequently decorrelate the incident and emission angles in fewer scattering events, decreasing the disparity in the mean number of scattering events between the $\Phi = 0°$ and 180° quadrants (5.7% difference for g = 0.9 to 4.0% difference for g = 0.5, $\mu_s = 100\ cm^{-1}$, $\mu_a = 10\ cm^{-1}$).

In terms of the relationship between the albedo of the sample and the angular emission profile, it is logical for equivalent albedo values to produce similar degrees of profile skewing. As demonstrated in Table 6, proportionately increasing the scattering and absorption coefficients only shrinks the scale of the simulation and does not change the average number of scattering events undergone by a photon before emission. Equivalent numbers of scattering events translate into equivalent correlations between the incident excitation and ultimate emission angles, equivalent photon emission energies, and equivalent disparities between the $\Phi = 0°$ and $\Phi = 180°$ quadrants, given that there is no change in the anisotropy factor.

The increase in skewing with decreased albedo also relates to the disparity in mean number of photon scattering events (and hence the correlation between entrance and emitted direction) per emitted photon within the diffuse reflectance. Total diffuse reflectance from the tissue surface is composed of what Qu et al term "nearly diffuse reflectance" and "diffuse reflectance." "Nearly diffuse reflectance" results from photons which are emitted after a small number of scattering events and whose emission directions are therefore reasonably correlated to the incident excitation angle within strongly forward-scattering media. "Diffuse reflectance" derives from those photons which are scattered many times and whose emission directions are completely randomized. Therefore, the degree of skewing directly depends upon the relative contributions of "nearly diffuse reflectance" and "diffuse reflectance" to the "total diffuse reflectance" emission profile; an increased "nearly diffuse reflectance" contribution will produce a more highly skewed angular emission profile.

Employing theory developed by Wu et al [21] using photon migration, decreasing the albedo from one to zero causes exponential decreases in the weighted mean number of scattering events per emitted photon, the emitted "diffuse reflectance", and the emitted "nearly diffuse reflectance." However, the exponential decay rate for "nearly diffuse reflectance" is significantly

lower than the rate for "diffuse reflectance," such that the total diffuse reflectance is completely "nearly diffuse" at an albedo of zero for *any* anisotropy and reasonable threshold number of scattering events used to divide these two types of reflectance. Therefore, subsequent to a decrease in albedo, the contribution of the "nearly diffuse reflectance" becomes more dominant in the "total diffuse reflectance" profile, the intensity-weighted mean number of scattering events per emitted photon decreases (as supported by Table 6), and the skewing in the angular emission profile subsequently increases. It is important to note that while Wu's theory was designed for excitation light normal to the tissue surface, non-normal excitation does not qualitatively affect the results in terms of the effect of albedo.

Thorough comparison of the experimental and simulated angular emission profiles uncovers four behaviors which differ between the two sets of results: 1) the degree of skewness in the diffuse reflectance emission profiles after 60° excitation is less pronounced experimentally than in the simulation results; 2) experimental measurement indicates that the emission profiles after low-angle excitation and/or within the $\Phi = 90°/270°$ emission plane are optical property independent while the simulation results suggest that profile width (FWHM) depends on sample scattering; 3) the experimentally measured profiles underestimate Lambertian behavior at all emission angles while the corresponding simulation results closely follow Lambertian emission; 4) simulated angular emission profiles are more symmetric than the corresponding experimental profiles as quantified by the MPD metric.

The marked discrepancy in skewing between the simulation and experimental results most likely relates to the differences in absorption between the two sets of measurements. The absorption of the phantom samples varied from 0.02 to 0.18 cm^{-1} according to optical property measurements using inverse-adding doubling [14]. Therefore, the albedo of the experimental samples varied from 0.9986 to 0.9997 for reduced scattering extremes of 13 and 82 cm^{-1}, while the simulation albedo varied from 0.9091 to 0.9877 for similar scattering extremes (μ_s' = 10 to 80 cm^{-1}). Since skewing increases as albedo decreases, the larger range in albedo for the simulation results creates a more significant change in skewing between the scattering extremes.

According to the experimental results, the angular emission profiles of fluorescence and diffuse reflectance disclosed in this paper are relatively symmetric to normal ($\theta = 0°$) and consistent with optical properties of the phantom samples when excitation is delivered at small excitation angles. However, the simulation results (Figures 8 and 9) suggest otherwise. Samples

with lower scattering properties produce emission profiles that are statistically wider than the profiles from higher-scattering samples. Because of potential experimental errors, it is possible that this small variation in profile width between low- and high-scattering samples was buried in the noise of the experimental data. Further Monte Carlo simulation studies (results not shown) indicate that the emission-profile FWHM is similarly dependent upon sample absorption and anisotropy. While exhaustive investigation of this phenomenon is beyond the scope of the current paper, existing results indicate that the FWHM dependence may be due to change in optical properties or differences in spatially sampling the impulse responses relative to their FWHM values.

Experimentally measured profiles after low-angle excitation and within the $\Phi = 90°/270°$ emission plane underestimate Lambertian behavior at all emission angles, while the corresponding simulation results closely follow Lambertian emission. Two sources of experimental error may be responsible for this difference since both errors cause underestimation at oblique observation angles. First, producing a perfectly uniform excitation spot is near impossible with fiber-optic delivery and spherical focusing optics. The intensity profile of the excitation spot used in this study was visually non-uniform, with its peak intensity positioned at the center of the phantom surface and collection area. Since the collection area of the detection probe increases with the observation angle as $1/\cos(\theta)$, it incorporates regions with lower excitation intensity at oblique observation angles. This reduces the mean excitation irradiance over the collection area and underestimates the emission intensity at larger emission angles. Similarly, when the sample surface is not perfectly aligned to the x-y plane, the observation spot will move laterally along the sample surface as the collection angle increases, subsequently shifting it away from the area of peak excitation and collecting from an excitation area with lower mean excitation irradiance.

Differences in the symmetry of experimental and simulated emission profiles may be due to errors in the measurement of the observation angle itself. Careful inspection of the experimentally measured profiles shows that in some cases, the profiles would be more symmetric about the surface normal ($\theta = 0°$) if the observation angles were uniformly shifted by 2-3°. This shift could be due to rotation of the protractor while positioning the collection arm, incorrect alignment of the collection arm with the angle indicated on the protractor, or a lack of correspondence between the rotation center of the collection arm and the vertex of the protractor.

Normalizing the measured emission intensity by the collection area – which varies as $1/\cos(\theta)$ – only serves to exacerbate this error. While every precaution was taken to minimize the experimental errors outlined above, we acknowledge that no experimental design is perfect, giving rise to inherent errors that may influence the shape of the measured angular emission profiles. Because Monte Carlo simulation is free from the types of errors that plague experimental measurements, we believe the simulated results are more accurate in their depiction of the true angular behavior of fluorescence and diffuse reflectance emission.

The study results indicate that angular emission profiles of diffuse reflectance within the incidence plane after small-angle excitation, diffuse reflectance within the orthogonal emission plane, and all types of fluorescence are consistently symmetric with profile widths that weakly depend on sample optical properties when emission is collected within the limits of a semi-infinite excitation spot. For large excitation angles, the optical-property dependence of angular emission intensity of diffuse reflectance within the excitation plane becomes pronounced. From these results, we would not expect the line-shapes of fluorescence imaging spectra to be significantly affected by the excitation and collection geometry when emission is collected well within the boundaries of the excitation area, whereas the line-shapes of diffuse reflectance spectra could be drastically altered for a large-excitation-angle condition when the sample albedo and/or scattering anisotropy vary significantly across the spectral range. Without significant variation in optical properties, the angular emission profile will be identical for all emission wavelengths and the presence of profile skewing can be removed during routine spectral normalization. However, the deviation in line-shape for the orthogonal emission plane after large-angle excitation from the $\alpha = 0°$ spectra during the spectral imaging simulation (Figure 12b) indicate that there may be other sources dependent on incident excitation angle that also affect the line-shape of diffuse reflectance spectra. One potential source of additional distortion is the magnitude of diffuse reflectance and fluorescence angular emission profiles which is also optical property dependent and therefore could directly affect spectral line-shapes. By normalizing the angular emission profiles for comparison sake, the investigation outlined in this paper was limited to the effects of incident excitation angle and sample optical properties on angular profile *shape*. However, preliminary results during this investigation indicate that the optical property dependence of profile *magnitude* varies with incident excitation angle and relates to the mean number of scattering events (Table 6), and the depth of tissue penetration by

the photons, in much the same manner as the extent of profile skewing. Thus, there is reason to believe that the optical property dependence of angular profile magnitude will similarly affect fluorescence line-shape after oblique-angle excitation. This effect is currently under investigation.

The results indicated in this paper and the conclusions derived therein are particularly relevant for the design and application of tissue spectral imaging. Spectral discrimination algorithms developed for individual tissue types will remain effective for spectral imaging systems if they are capable of faithfully reproducing the reliable and true fluorescence and diffuse reflectance spectra of tissue. Therefore, spectral imaging system development must take into account the possible influence of sample optical properties, incident excitation angle, and edge effects along the boundaries of the excitation area on diffuse reflectance and fluorescence spectral line-shape, most notably when designing angular excitation and collection system geometries relative to tissue surfaces and their variable surface topographies.

Conclusion

When emission is collected from an area surrounded by a semi-infinite excitation region, fluorescence for all excitation angles, low-excitation-angle diffuse reflectance within the incidence plane, and both emission types within the $\Phi = 90°/270°$ plane possess consistent, symmetric angular distributions whose widths are weakly dependent on sample optical properties. For similar collection within a semi-infinite excitation region, diffuse reflectance along the incidence plane after large-angle excitation is biased away from the excitation source. The degree of bias is dependent only upon sample albedo and scattering anisotropy and is related to the correlation between the entrance and emission photon directions. Since the angular distribution of fluorescence is only weakly dependent on sample optical properties, constraints on system geometry are not required for fluorescence spectral imaging to avoid spectral distortions due to angular emission profile shape. Geometry-induced distortions within diffuse reflectance spectra can occur for high-angle excitation when the sample albedo and/or scattering anisotropy vary significantly across the spectral range. In this case, to avoid spectral distortions due to profile shape, diffuse reflectance spectral imaging systems should be designed to minimize incident excitation angles or collect emission from the orthogonal emission plane ($\Phi = 90°/270°$ plane), constraints which can be difficult to control with a variable surface topography.

References

1. Bigio, I.J. and S.G. Bown, *Spectroscopic sensing of cancer and cancer therapy: current status of translational research.* Cancer Biol Ther, 2004. **3**(3): p. 259-67.
2. Sokolov, K., M. Follen, and R. Richards-Kortum, *Optical spectroscopy for detection of neoplasia.* Curr Opin Chem Biol, 2002. **6**(5): p. 651-8.
3. Bigio, I.J. and J.R. Mourant, *Ultraviolet and visible spectroscopies for tissue diagnostics: fluorescence spectroscopy and elastic-scattering spectroscopy.* Phys Med Biol, 1997. **42**(5): p. 803-14.
4. Mahadevan-Jansen, A. and R. Richards-Kortum, *Raman spectroscopy for the detection of cancers and precancers.* Journal of Biomedical Optics, 1996. **1**(1): p. 31-70.
5. Ramanujam, N., *Fluorescence spectroscopy of neoplastic and non-neoplastic tissues.* Neoplasia, 2000. **2**(1-2): p. 89-117.
6. Richards-Kortum, R. and E. Sevick-Muraca, *Quantitative optical spectroscopy for tissue diagnosis.* Annu Rev Phys Chem, 1996. **47**: p. 555-606.
7. Qu, J.Y., Z. Huang, and J. Hua, *Excitation-and-collection geometry insensitive fluorescence imaging of tissue-simulating turbid media.* Applied Optics, 2000. **39**(19): p. 3344-3356.
8. Churmakov, D.Y., I.V. Meglinski, and D.A. Greenhalgh, *Influence of refractive index matching on the photon diffuse reflectance.* Phys Med Biol, 2002. **47**(23): p. 4271-85.
9. Cheong, W.F., *Summary of Optical Properties*, in *Optical-Thermal Response of Laser-Irradiated Tissue*, A.J. Welch and M.J.C. van Gemert, Editors. 1995, Plenum Press: New York. p. 275-304.
10. van de Hulst, H., *Rigorous Scattering Theory for Spheres of Arbitrary Size (Mie Theory)*, in *Light Scattering by Small Particles*. 1981, Dover Publications, Inc.: New York. p. 114-130.
11. Jacques, S. and L. Wang, *Monte Carlo Modeling of Light Transport in Tissues*, in *Optical-Thermal Response of Laser-Irradiated Tissue*, A. Welch and M.v. Gemert, Editors. 1995, Plenum Press: New York. p. 73-100.
12. Gebhart, S., W. Lin, and A. Mahadevan-Jansen, *In vitro determination of normal and neoplastic human brain tissue optical properties using inverse adding-doubling.* Phys Med Biol, 2006. **51**: p. 2011-2027.
13. Welch, A.J., et al., *Propagation of fluorescent light.* Lasers Surg Med, 1997. **21**(2): p. 166-78.
14. Prahl, S., M. van Gemert, and A. Welch, *Determining the optical properties of turbid media by using the adding-doubling method.* Applied Optics, 1993. **32**(4): p. 559-568.
15. Yaroslavsky, A.N., et al., *Optical properties of selected native and coagulated human brain tissues in vitro in the visible and near infrared spectral range.* Phys Med Biol, 2002. **47**(12): p. 2059-73.

16. Farrell, T.J., M.S. Patterson, and B. Wilson, *A diffusion theory model of spatially resolved, steady-state diffuse reflectance for the noninvasive determination of tissue optical properties in vivo.* Med Phys, 1992. **19**(4): p. 879-88.

17. Flock, S.T., et al., *Monte Carlo modeling of light propagation in highly scattering tissue—I: Model predictions and comparison with diffusion theory.* IEEE Trans Biomed Eng, 1989. **36**(12): p. 1162-8.

18. Nilsson, H., et al., *Photon pathlength determination based on spatially resolved diffuse reflectance.* J Biomed Opt, 2002. **7**(3): p. 478-85.

19. Zhang, F.J., et al., *Noninvasive determination of tissue optical properties based on radiative transfer theory.* Optics and Laser Technology, 2004. **36**(5): p. 353-359.

20. McShane, M.J., et al., *Monte Carlo modeling for implantable fluorescent analyte sensors.* IEEE Trans Biomed Eng, 2000. **47**(5): p. 624-32.

21. Wu, J., et al., *Diffuse reflectance from turbid media: an analytical model of photon migration.* Applied Optics, 1993. **32**(7): p. 1115-1121.

CHAPTER VI

COMPARISON OF SPECTRAL VARIATION FROM SPECTROSCOPY TO SPECTRAL IMAGING

Abstract

Optical biopsy has been shown to discriminate between normal and diseased tissue with high sensitivity and specificity. Fiber-optic probe-based spectroscopy systems do not provide the necessary spatial information to guide therapy effectively, ultimately requiring a transition from probe-based spectroscopy to spectral imaging. In this paper, the effect of such a transition on fluorescence and diffuse reflectance lineshape is investigated. Inherent differences in spectral lineshape between spectroscopy and imaging are characterized and much of these differences may be attributed to a shift in illumination-collection geometry between the two systems. Sensitivity of the lineshape disparity is characterized with respect to changes in sample absorption and scattering as well as to changes in various parameters of the fiber-optic probe design (e.g. fiber diameter, beam-steering). Differences in spectral lineshape are described in terms of the relative relationship between the light diffusion within the tissue and the distribution of source-detector separation distances for the probe-based and imaging illumination-collection geometries. Monte Carlo simulation is used to determine fiber configurations that minimize the lineshape disparity between the two systems. In conclusion, we predict that fiber-optic probe designs that mimic a spectral imaging geometry and spectral imaging systems designed to emulate a probe-based geometry will be difficult to implement, pointing toward *a posteriori* correction for illumination-collection geometry to reconcile imaging and probe-based spectral lineshapes or independent evaluation of tissue discrimination accuracy for probe-based and spectral imaging systems.

Introduction

Optical spectroscopy has been extensively investigated for real-time, objective, non-invasive discrimination between normal and diseased tissues [1-3]. Clinically motivated by the desire to improve upon tissue diagnosis, these studies seek to demonstrate that optical spectroscopy is capable of detecting tissue structural and biochemical changes which inherently occur during the progression from normalcy to a diseased state. They typically employ handheld

fiber-optic probes to deliver illumination light to and collect remitted light from a point of interest on the tissue surface, after which a punch biopsy is acquired from the interrogated tissue site. The measured spectra are grouped according to gold-standard histopathologic diagnoses of the biopsy samples and are analyzed to discern spectral differences between the tissue groups. The observed differences are used to develop discrimination algorithms and to determine unbiased estimates of discrimination accuracy between the various tissue classes.

Combined fluorescence and diffuse reflectance spectroscopy has been specifically explored by our research group for differentiation between normal brain and infiltrating tumor margins [4-7] towards guiding intra-operative brain tumor resection, in which extent of tumor margin resection has been repeatedly correlated to patient quality of life and survival rate [8-11]. During craniotomy procedures for glioma resection or temporal lobectomy, multiple gray matter, white matter, tumor core, and tumor margin sites are selected for spectral measurement with a portable spectroscopic system [5]. Discrimination accuracy at these sites is subsequently assessed in a manner similar to the protocol outlined above. Despite only subtle spectroscopic differences between normal and tumor tissues, initial reports using multivariate analysis of fluorescence and diffuse reflectance spectra measured from 184 tissue sites in 35 of more than 125 patients measured to date demonstrate a diagnostic accuracy of 100%, 96%, and 94% for normal, tumor core, and tumor margin tissue samples, respectively, with only 2 out of 35 tumor margin sites misclassified as normal (in review). The results indicate not only the promising capability of combined autofluorescence and diffuse reflectance spectroscopy to provide contrast between normal and tumor tissues in the brain, but also its ability to accurately differentiate infiltrating tumor margins from surrounding normal brain tissue and potentially affect more complete brain tumor resection.

While the methodology described is fairly universal in the field of optical diagnosis and is tailored for retrospective studies designed to assess discrimination accuracy, the instrumentation is often limited in its clinical applicability. Fiber-optic probes produce single-point diagnostic measurements without providing information regarding the spatial extent of disease. This is particularly relevant in the case of therapeutic guidance where spatial information such as the extent of tumor margins is necessary to fully target the diseased tissue. As such, once optical spectroscopy is proven as an effective means of disease detection, researchers often move from fiber-optic probe-based spectroscopy to spectral imaging, which

provides spectroscopic information at every pixel within a two-dimensional field of view for a comprehensive snapshot of tissue pathology. In order to limit complexity of instrumentation, researchers often use fluorescence imaging at specific emission wavelengths to provide spatial information. However, recent studies indicate detailed spectral information is required for true effective classification [12, 13], emphasizing the need for spectral imaging development with full lineshape information for accurate disease demarcation.

For a seamless transition from spectroscopy to imaging, spectral imaging systems would produce tissue spectra which are identical in lineshape to probe-based spectra; otherwise, time and resources spent developing discrimination algorithms based upon spectral differences observed in probe-based data are squandered, since new imaging-based algorithms must be determined. Once discrimination algorithms are successfully developed, spectral imaging instrumentation can be simplified and image acquisition can be expedited by selectively interrogating wavelengths which are deemed diagnostically significant.

Spectral lineshape is modulated by two main factors: the optical properties of the tissue sample and the illumination-collection geometry of the measurement system. While tissue optical properties dictate the light distribution within the tissue, the relative propagation and attenuation of different wavelengths, and the subsequent spatial distribution of remitted light from the tissue surface, the illumination-collection geometry dictates what fraction of the light remitted at each wavelength is collected by the system.

While tissue optical properties are independent of the spectral measurement system, the transition from spectroscopy to spectral imaging involves a drastic shift in the spatial geometry between the illumination and collection regions (Figure 1). Spectroscopy probes typically contain multiple fibers, some of which are used for illumination delivery and the remainder for collection of remitted light. The specific configuration of the probe – e.g. the relative positions of the illumination and collection fibers, the gap between the fiber tips and the tissue surface, and the fiber polish angles – create a unique set of source-detector separation distances relative to the light distribution within the tissue (Figure 1c). While multiple modalities exist for spectral imaging implementation, including line-scanning, tunable-filter, and multiplexing methods, most spectral imaging systems acquire spectral data with non-contact illumination and collection (Figure 1b). When the illumination spot is much larger than the system field of view, as is often the case, each pixel in the image can be treated as a small collection region surrounded by a

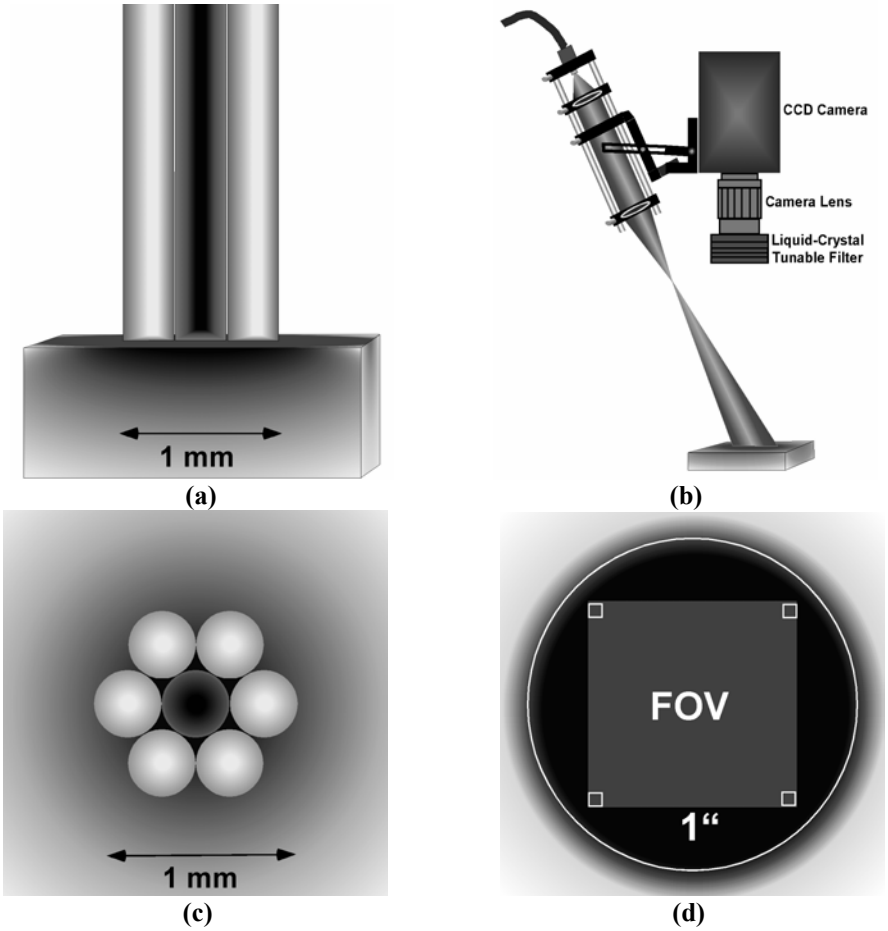

Figure 1. Illumination-collection geometries for typical probe-based spectroscopy and non-contact spectral imaging systems. (a) Contact-based fiber-optic probe with a single illumination fiber and fibers polished normally. (b) Spectral imaging system with non-contact illumination and collection. (c) Cross-section of the probe-tissue interface for a six-around-one probe configuration with a central illumination fiber and six surrounding collection fibers relative to the light distribution in the tissue. (d) Spectral imaging field of view and individual pixels relative to the illumination spotsize and subsequent light distribution.

semi-infinite illumination spot (Figure 1d), and its illumination-collection geometry as a convolution of all possible source-detector separation distances. Therefore, the fraction of remitted light collected by probe-based spectroscopy varies due to changes with optical properties (i.e. wavelength) in the spatial distribution of remitted light relative to the fiber configuration, while the fraction collected by spectral imaging is generally independent of these changes. Thus, spectral imaging lineshape is sensitive to how tissue optical properties affect the total intensity of remitted light, but probe-based spectroscopy lineshape is also sensitive to how they affect its spatial distribution. To our knowledge, a thorough study of the effects of the

transition from probe-based spectroscopy to non-contact spectral imaging on fluorescence and diffuse reflectance lineshape as a function of optical properties has never been conducted.

Previous studies in the literature have investigated fluorescence and diffuse reflectance propagation in tissue, hinting at some of the effects of illumination-collection geometry on fluorescence and diffuse reflectance lineshape. Research into diffuse reflectance propagation in tissue began with one-dimensional depth-resolved investigations in which diffuse reflectance was modeled as a function of optical properties using photon migration theory [14]. Several groups have also simulated or measured radially resolved profiles of diffuse reflectance for wide ranges of optical properties, but the results were used to develop inverse models for *in vivo* optical property determination [15, 16]. The authors concentrated on producing calibrated data for specific collection geometries and did not extend their findings to how profile changes with optical properties might affect clinically measured spectra. Bargo et al [17, 18] measured the collection efficiency of a single illumination-collection fiber and of an illumination-collection fiber pair as a function of optical properties and separation distance, but defined collection efficiency as the fraction of light impinging on the face of the collection fiber that falls within its acceptance cone, without investigating how the absolute intensity of remitted light varies with optical properties (i.e. wavelength) and thereby also affects diffuse reflectance lineshape.

While several studies have demonstrated changes in diffuse reflectance lineshape subsequent to a shift in illumination-collection geometry, the causes for the behavior have not been thoroughly examined. Liu et al [19] simulated and experimentally measured diffuse reflectance for a subset of discrete optical property values and three different probe geometries, but did not discuss how the collection efficiencies of the specific probe geometries varied with wavelength. A subsequent paper from the same research group [20] used one of the investigated probes to demonstrate that fluorescence and diffuse reflectance lineshapes from breast tissue change between three source-detector separation distances. However, the source of the disparities is not discussed other than to ascribe them to probing different depths of the tissue (the spectra from the different separation distances are used as independent inputs to a tissue classification scheme). Not surprisingly, the classification results show that the three sets of spectra yield similar discrimination success rates since there is "no apparent structural change in breast tissue with increasing depth," emphasizing the fundamental difference in terms of

diagnostic utility between changes in lineshape due to tissue morphology/architecture and changes due to illumination-collection geometry.

The only studies in the literature which have examined the combined effects of optical properties and illumination-collection geometry on diffuse reflectance lineshape were conducted by Schmitt and Kumar [21, 22]. Diffuse reflectance spectra were measured in the near infrared for a single illumination-collection fiber pair in an effort to determine how collection of remitted light varied with separation distance (d = 1-6 mm) for various optical properties (μ_a = 0-1.0 mm^{-1}, μ_s' = 0.5-2.0 mm^{-1}). They demonstrated that diffuse reflectance lineshape varies with source-detector separation distance and explained the shifts using diffusion theory. However, diffusion-based predictions broke down at small source-detector separation distances and thus far, no group has validated their results in the visible spectrum where increased scattering and absorption and shorter source-detector separation distances in most fiber-optic probes (d = 0-1 mm) render diffusion theory inaccurate.

Investigations into fluorescence propagation for tissue diagnosis can be divided into two major categories: those that investigate depth-resolved fluorescence [23-28] and those that seek to extract intrinsic fluorescence information from fluorescence measurements [29-33]. Depth-resolved fluorescence investigations predominantly aim to identify probe geometries which will collect fluorescence from specific layers in epithelial tissues, but they rarely worry about how optical properties and probe geometry affect the lineshape. While extracting intrinsic fluorescence information from fluorescence measurements recognizes the effects of optical properties on lineshape and actually seeks to remove those effects, most of the methods seek to minimize the effects of probe geometry by using diffuse reflectance information for fluorescence correction. Since the fluorescence and diffuse reflectance spectra are generally collected with the same illumination-collection geometry, diffuse reflectance lineshape is similarly modulated and can be used to help correct for any wavelength-specific geometry effects.

While depth-resolved and intrinsic fluorescence studies provide knowledge of fluorescence behavior, neither of them give insight into how tissue optical properties and excitation-collection geometry combine to modulate fluorescence lineshape. Surprisingly, while the recent investigations outlined above have strayed from the issue, two of the *first* investigations into fluorescence propagation demonstrated a dependence of fluorescence lineshape on excitation-collection geometry. Richards-Kortum et al [34] compared measured

fluorescence spectra from collection regions inside and outside of the excitation spot, and Keijzer et al [35] simulated and measured fluorescence spectra as a function of radial distance from the source. Both studies found that fluorescence lineshape drastically changes as collection is moved out of and further from the excitation spot. Shifts in lineshape are attributed to increased probing depth as the source-detector separation distance increases, subjecting the fluorescence to greater modulations from sample absorption. Since then, other groups have observed similar results [36, 37], but none have investigated spectral lineshapes measured with traditional fiber-optic probe configurations or non-contact imaging systems.

The goals of this paper are two-fold: 1) to thoroughly examine the behavior of fluorescence and diffuse reflectance lineshape as a function of illumination-collection geometry and tissue optical properties and 2) to determine the specific effects of the transition from fiber-optic probe-based spectroscopy to non-contact spectral imaging on measured lineshapes. Here, we first demonstrate the differences in fluorescence and diffuse reflectance lineshape upon the shift from probe-based spectroscopy to spectral imaging and attribute the spectral differences to a fundamental change in illumination-collection geometry. The sensitivity of the disparity in lineshape to changes in sample absorption and reduced scattering is examined using tissue phantoms with known optical properties. The effects of beam-steered fibers, fiber diameter, and using illumination fibers for collection of remitted light are assessed via experimental measurement and Monte Carlo simulation and subsequently used to determine the ideal fiber-optic probe configuration that minimizes the spectral disparity between spectroscopy and imaging. The results of this investigation provide insight into the behavior of fluorescence and diffuse reflectance lineshape with shifts in illumination-collection geometry and can be used to guide the design and planning of tissue diagnosis studies that rely on optical spectroscopy by aiding in the design of fiber probes that simplify the transition of such studies to spectral imaging.

Materials and Methods

System Descriptions

The probe-based spectroscopy [5] and spectral imaging [38] systems used in this study are employed in the brain tissue diagnosis study and have been described in detail elsewhere; only the

significant details will be repeated here. For spectroscopy measurements, a fiber-optic probe with seven fibers (d = 300 μm, NA = 0.22) in a six-around-one configuration delivered light from a pulsed nitrogen laser (337 nm, 120 μJ per pulse, 20 Hz repetition rate, Spectra-Physics) for fluorescence excitation and from a white-light halogen lamp (6.5 W, Ocean Optics) for diffuse reflectance illumination. Illumination light was delivered by two opposing fibers at the six o'clock and twelve o'clock positions along the outer ring, while the remaining five fibers delivered remitted light, collected from the sample surface, to a spectrometer (S2000-FL, Ocean Optics) for spectral measurement. All seven fibers were polished normally and placed in direct contact with the sample surface during each measurement.

Spectral imaging was performed with a liquid-crystal tunable filter spectral imaging system (Figure 1b) which consisted of three components: a Varispec VIS-20 LCTF (CRI, Inc.), a variable focal-length camera lens (f/3.5, Nikon), and a thermo-electrically cooled CCD camera (PhotonMax, Princeton Instruments) [38]. Images were acquired in a non-contact manner with a 25 mm x 25 mm field of view and an object distance of roughly 180 mm. Light from a 500 W xenon arc lamp, bandpass filtered at 340 nm, was used for fluorescence excitation, while light from a 200 W halogen lamp (Luxtec) was used for diffuse reflectance. A 365 nm dichroic filter coupled both illumination sources into a single, 10-mm-core liquid light guide which delivered the illumination light to the sample. Quartz lenses at the distal end of the light guide focused the illumination light to a spot roughly 50 mm in diameter.

Lineshape Disparity

To demonstrate the lineshape disparity between spectra from probe-based spectroscopy and spectral imaging, fluorescence and diffuse reflectance measurements were acquired with both systems from gelatin-based phantoms designed to optically mimic human white and gray matter brain tissue. The phantoms were developed as part of a separate project (in review), with polystyrene microspheres used for reduced scattering, bovine hemoglobin for absorption, and Stilbene 420 dye for fluorescence. The concentrations of the three components were empirically determined to yield optical property spectra which matched mean reduced scattering, absorption, and fluorescence spectra experimentally measured from human white and gray matter brain tissues. In sum, the white matter and gray matter phantoms contained equivalent levels of absorption and fluorescence, with roughly 3.5-fold higher reduced scattering in the white matter phantom. Probe-based fluorescence and diffuse reflectance spectra were acquired from both tissue phantoms from 400 to 720 nm with a 200-ms integration time and spectral resolution of 10 nm. Corresponding imaging spectra were acquired over the same spectral range with a 10-nm wavelength increment and total image integration times of 8 s and 165 s for diffuse reflectance

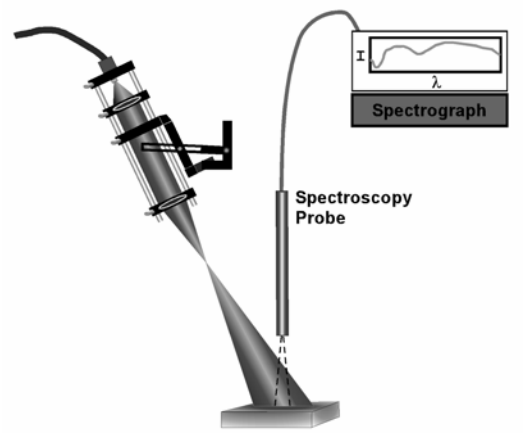

Figure 2. Schematic of probe-based spectroscopy measurement with an imaging excitation-collection geometry.

and fluorescence, respectively. Mean spectra averaged across ten measurements for probe-based spectroscopy and across all pixels within the spectral images were corrected for system sensitivity and the illumination spectrum of the halogen lamp according to a standard calibration procedure using direct-view measurements from a NIST calibration lamp and the white-light halogen lamp [6, 7, 39]. Corrected fluorescence and diffuse reflectance spectra were normalized to a maximum or mean of one, respectively, for comparison of spectral lineshape between systems.

To identify the shift in illumination-collection geometry between the systems as the cause for the observed lineshape disparity, a third set of fluorescence and diffuse reflectance measurements were acquired from the gray matter phantom: probe-based spectra using an imaging illumination-collection geometry (Figure 2). The fiber-optic probe was positioned roughly 25 mm from the sample surface and the illumination optics from the imaging system were used to create an illumination spot on the phantom surface 50 mm in diameter. Given the collection fiber NA = 0.22, this configuration produced a collection region roughly 11 mm in diameter within the 50-mm illumination spot. While this collection region was significantly larger than the 50-μm pixel-limited spatial resolution of the imaging system, it was sufficiently small relative to the illumination spot when considered in terms of photon diffusion.

Effect of optical properties

Two series of gelatin phantoms were created to determine how the disparity in spectroscopy and imaging lineshape is affected by sample optical properties (Table 1). The first

series contained five phantoms with increasing hemoglobin concentrations but equal microsphere concentrations, giving variable absorption but constant reduced scattering at a level between gray and white matter scattering [40]. The second series of five phantoms were created with increasing concentrations of polystyrene microspheres but equal hemoglobin concentrations, giving variable reduced scattering but constant absorption at a level shared by gray and white matter tissue [40]. For each phantom, absorption and reduced scattering spectra were measured at 337 nm for fluorescence excitation and from 400 to 720 nm for fluorescence and diffuse reflectance collection using a single-integrating-sphere spectrophotometer and inverse adding-doubling technique [40-42]. Probe-based spectroscopy and spectral imaging measurements were acquired from each of the ten phantoms with parameters similar to the lineshape study described above. The spectra were corrected for wavelength sensitivity and the halogen illumination spectrum, averaged across ten measurements for spectroscopy and across pixels for imaging, and normalized for comparison purposes.

Effects of probe configuration

Fiber-optic probes are often designed using illumination and collection fibers whose tips are beveled to steer and create overlap between the illumination and collection regions, in an effort to increase the signal collected from the sample [43, 44]. To determine the effect of steered fibers on the disparity between probe-based and imaging spectra, two sets of probe-based spectra were measured from each of the ten phantoms in Table 1. While the first set was acquired with the same probe used in previous experiments, the second set was acquired with a fiber-optic probe (custom-designed by Visionex, Inc.) consisting of the same six-around-one fiber configuration (d = 300 μm, NA = 0.22), but with a central conventional fiber surrounded by six fibers beam-steered toward the central fiber to enhance the collection efficiency [43]. As with previous experiments, ten fluorescence and diffuse reflectance measurements were acquired from each phantom, corrected for wavelength sensitivity and the halogen illumination spectrum, averaged, and normalized for comparison purposes.

The effects of other fiber-probe design parameters on the disparity between probe-based and imaging spectra were investigated. Since many different probe designs exist and probes with other fiber diameters, with other fiber configurations, and with fibers used for simultaneous illumination and collection were not readily available, Monte Carlo simulation was used to

Table 1. Component concentrations and experimentally measured optical properties (specified at 550 nm) for the variable absorption, constant scattering and variable scattering, constant absorption series of tissue phantoms. Hemoglobin and microsphere concentrations are given relative to total phantom volume (15 mL). Microsphere concentration indicates the equal concentrations of 0.1 and 0.5 μm diameter polystyrene microspheres, such that the total microsphere concentration in the phantom was twice the indicated value.

Phantom Series	Phantom Name	Hemoglobin Concentration	Microsphere Concentration	Absorption Coefficient (mm^{-1})	Reduced Scattering Coefficient (mm^{-1})
Variable Absorption, Constant Scattering	12.5 mg	0.833 mg/mL	0.2 mL/mL	0.0663	3.3382
	25.0 mg	1.667 mg/mL		0.1482	3.9416
	37.5 mg	2.500 mg/mL		0.2277	3.8880
	50.0 mg	3.333 mg/mL		0.2903	3.2931
	62.5 mg	4.167 mg/mL		0.3544	3.4767
Variable Scattering, Constant Absorption	0.5 mL	2.5 mg/mL	0.033 mL/mL	0.1812	0.5041
	1.5 mL		0.100 mL/mL	0.2143	1.8291
	2.5 mL		0.167 mL/mL	0.2332	2.9371
	3.5 mL		0.233 mL/mL	0.2118	3.7553
	4.5 mL		0.300 mL/mL	0.2296	4.9926

determine their effects. Diffuse reflectance Monte Carlo simulations were performed for a series of homogeneous, semi-infinite samples whose optical properties formed a grid of optical property pairs (μ_a, μ_s') which spanned the optical properties measured from human brain tissue [40]. For each simulation (i.e. set of optical properties), photons were launched at the origin with a random azimuthal incidence angle whose probability density function was uniformly distributed between zero degrees and the half-angle of the fiber divergence as dictated by its NA (0.22).

Photons were propagated through the tissue, consistent with the principles of Jacques and Wang [45] using an anisotropy factor of 0.85, and their exit from the tissue surface was recorded as a two-dimensional function of radial position and azimuthal angle. Imaging and probe-based diffuse reflectance collection intensities were determined for each optical property pair via convolution of the recorded exit function with functions describing the illumination and collection geometries of the two systems. Piecing these calculated intensities together formed a collection surface as a function of absorption and reduced scattering for each system, and diffuse reflectance spectra were then constructed for a given sample via interpolation using its experimentally measured absorption and reduced scattering spectra.

Monte Carlo diffuse reflectance spectra were constructed for each of the ten tissue phantoms in Table 1 for a spectral imaging geometry and for six-around-one probe configurations (similar to the experimental probe, without beam-steering) with three different

fiber diameters – 110, 220, and 330 μm (core + cladding). Spectra were then created for the same three probe geometries with the illumination fiber included in the collection region. Finally, based upon the experimental and Monte Carlo results, multiple fiber configurations were tested in an attempt to identify the ideal probe configuration that minimizes the disparity between imaging and probe-based spectra.

Results

Lineshape Disparity

Mean fluorescence and diffuse reflectance spectra from gray and white matter tissue phantoms (Figure 3) demonstrate a significant disparity between probe-based spectroscopy and spectral imaging. For diffuse reflectance, imaging spectra show greater intensity contrast

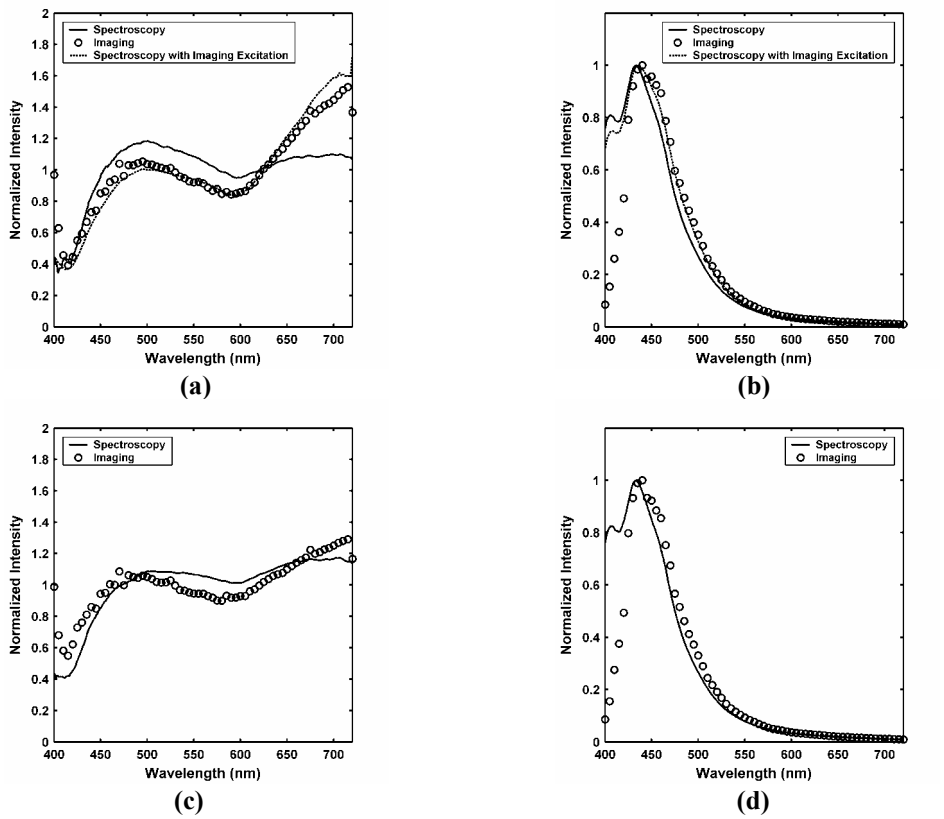

Figure 3. Demonstration of lineshape disparity between probe-based spectroscopy and spectral imaging. (a) Diffuse reflectance spectra from gray matter phantom. (b) Fluorescence spectra from gray matter phantom. (c) Diffuse reflectance spectra from white matter phantom. (d) Fluorescence spectra from white matter phantom.

between the blue/green (400 – 600 nm) and red spectral ranges (600 – 720 nm) than the probe-based spectra for both tissue types. Similarly, the wavelength of peak fluorescence is red-shifted in imaging spectra relative to the probe-based measurements, again indicating greater preference for the red wavelengths relative to the blue/green. These observed differences are more pronounced in gray matter than white matter spectra, suggesting an optical property dependence in the lineshape disparity between the two systems.

Acquiring fluorescence and diffuse reflectance spectra with the probe-based spectroscopy system while using an imaging illumination-collection geometry removed the disparity in spectral lineshape (Figure 3a,b). The red-blue intensity contrast in diffuse reflectance and the peak fluorescence wavelength were shifted on par with the mean imaging spectra, demonstrating that the difference in illumination-collection geometry between probe-based spectroscopy and spectral imaging is responsible for the lineshape disparity observed in Figure 3.

Effect of optical properties

Probe-based spectroscopy and spectral imaging measurements were acquired from all ten phantoms described in Table 1. In an effort to more clearly depict the trends in fluorescence and diffuse reflectance lineshape with optical properties, mean spectra are plotted for only three of the five phantoms in each series. Spectra from the other phantoms consistently follow the trends depicted in the figures.

Since hemoglobin absorption is greater in the blue/green region than the red region of the spectrum, increases in the modulation of spectral lineshape due to hemoglobin absorption, which will be henceforth referred to as absorption modulation, produce greater contrast in the measured intensities between these two regions and are exhibited by higher normalized diffuse reflectance intensities at 720 nm and increased red-shift of the fluorescence peak. Increasing concentrations of hemoglobin in the variable absorption phantoms produce greater absorption modulation for both probe-based and imaging spectra in fluorescence and diffuse reflectance spectra (Figure 4). The modulation of spectral lineshape is consistently larger in imaging than in probe-based spectra, indicating that the photons collected by the imaging system are subject to greater modulation from absorption. This behavior suggests that, on average, imaging photons have increased path lengths before exit from the tissue (i.e. increased tissue interaction) and are more diffuse. While not readily apparent from visual inspection of Figure 4, ratios of probe-based to

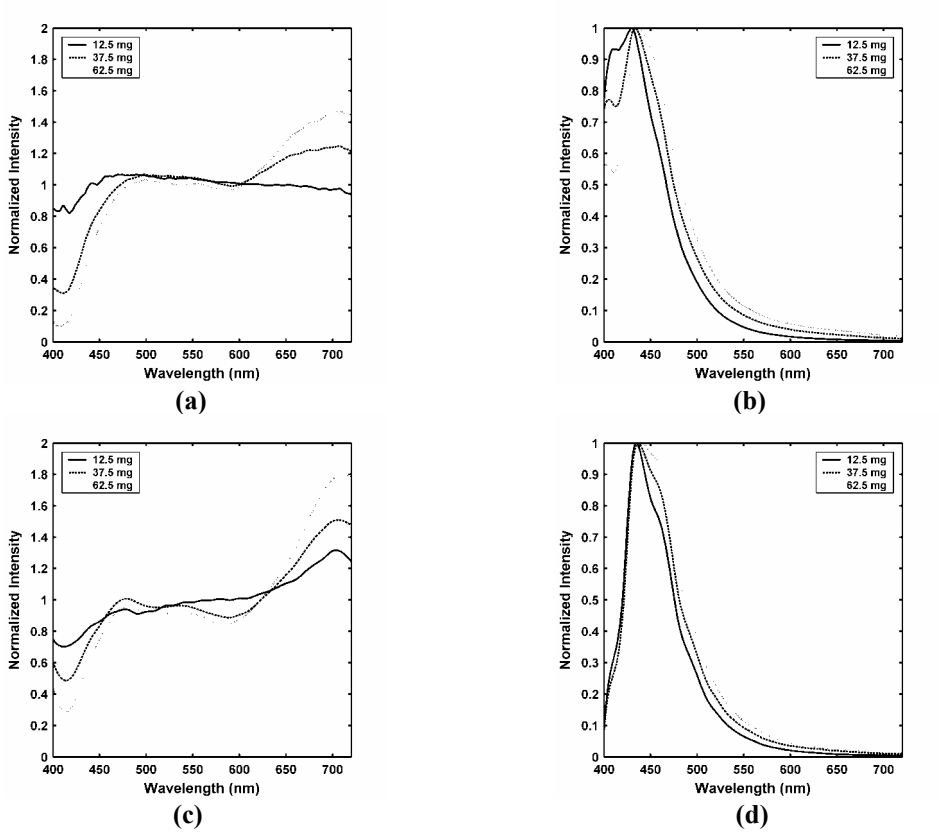

Figure 4. Effect of sample absorption on lineshape disparity between probe-based spectroscopy and spectral imaging. (a) Probe-based diffuse reflectance spectra. (b) Probe-based fluorescence spectra. (c) Imaging diffuse reflectance spectra. (d) Imaging fluorescence spectra.

imaging spectra (results not shown) demonstrate that the disparity in lineshape between the probe-based and imaging systems decreases with increased absorption.

Increases in reduced scattering affect opposing changes in imaging and probe-based spectra for fluorescence and diffuse reflectance (Figure 5). Imaging spectra show decreased absorption modulation with increased scattering, while probe-based spectra show increased absorption effects. This behavior suggests that while the photons collected by the imaging system have shorter path lengths and interact less with the tissue with increased scattering, probe-based photons have increased path lengths and interact more with the tissue. The disparity in lineshape between the probe-based and imaging systems decreases with increased scattering, consistent with results observed in gray and white matter tissue phantoms (Figure 3).

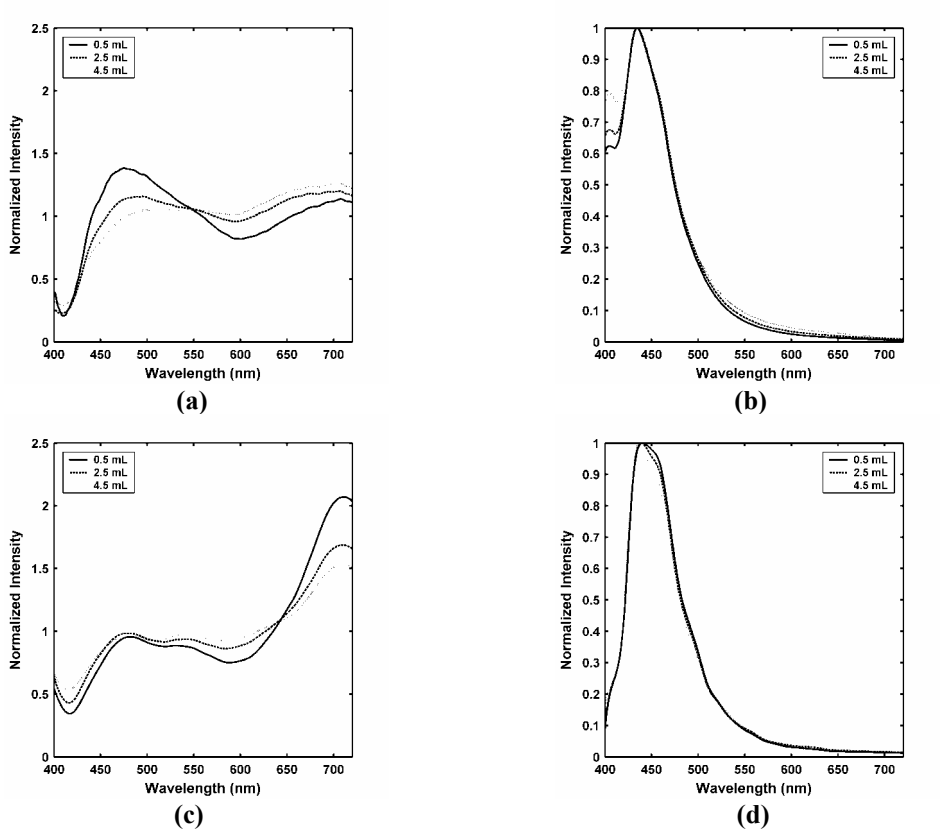

Figure 5. Effect of sample reduced scattering on lineshape disparity between probe-based spectroscopy and spectral imaging. (a) Probe-based diffuse reflectance spectra. (b) Probe-based fluorescence spectra. (c) Imaging diffuse reflectance spectra. (d) Imaging fluorescence spectra.

Effect of probe configuration

While beam-steered fibers have been shown to increase the collection efficiency of fiber-optic probes [43, 44], the comparison between identical probes with and without beam-steering demonstrates that beam-steered fibers increase the disparity between imaging and probe-based spectra (Figure 6). Beam-steered fibers consistently create diffuse reflectance and fluorescence (results not shown) spectra that exhibit less modulation from sample absorption than conventional fibers for variable absorption and scattering. This behavior is consistent with the theory behind the probe design, which aims to create overlapping illumination and collection regions and minimize absorption by shortening photon path lengths through the tissue. Since imaging spectra demonstrate greater absorption modulation than conventional probe-based spectra, reducing photon path lengths and subsequent photon interaction with the tissue using beam-steered fibers only exacerbates the disparity.

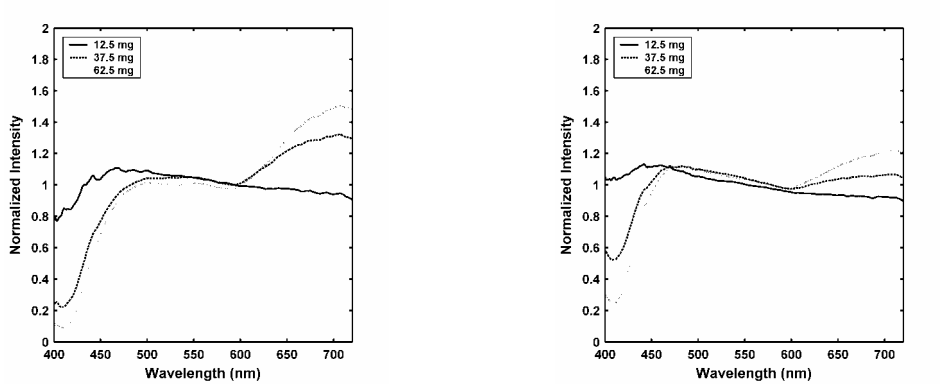

Figure 6. Effect of beam-steered fibers on lineshape of probe-based diffuse reflectance spectra from variable absorption phantoms: (a) without beam-steering (b) with beam-steering.

For fiber-optic probes with conventional fibers (i.e. no beam-steering), decreasing the diameter of the illumination and collection fibers reduces the absorption modulation of diffuse reflectance spectra (Figure 7a-c). Decreasing fiber diameter reduces the collection area of the fiber-optic probe, eliminating photon collection from regions distant from the illumination fiber. Since photon path length, subsequent interaction with the tissue, and absorption increase with source-detector separation distance, shrinking the source-detector separation distances across the probe illumination-collection geometry decreases the lineshape modulation due to absorption within measured spectra. Given that the disparity between imaging and probe-based spectra is characterized by greater modulation of imaging photons, decreased fiber diameter increases the disparity.

Similarly, fiber-optic probes which use illumination fibers for collection of remitted light produce fluorescence and diffuse reflectance spectra with less absorption modulation than probes where the illumination and collection fibers are mutually exclusive (Figure 7c-d). Including the illumination fiber in the collection region biases the population of collected photons towards singly scattered photons which are less diffuse and interact less with the tissue, thereby increasing the disparity between imaging and probe-based spectra. While Monte Carlo fluorescence spectra were not simulated, the changes in fluorescence spectra relative to the changes in diffuse reflectance spectra in Figure 7 are assumed to be consistent with the changes depicted in Figures 4 and 5.

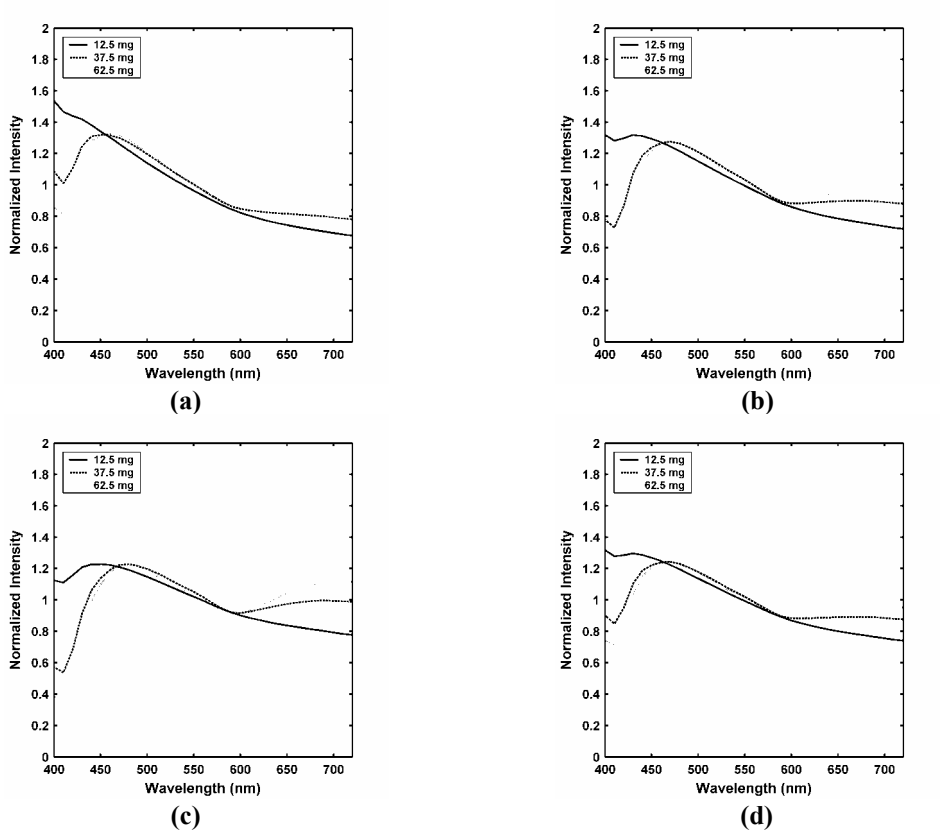

Figure 7. Effect of fiber diameter and using the illumination fiber for collection on Monte Carlo predicted lineshape of probe-based diffuse reflectance spectra from variable absorption phantoms: (a) 110 μm diameter fibers (core + cladding) (b) 220 μm diameter fibers (c) 330 μm diameter fibers (d) 330 μm diameter fibers with illumination fiber used for collection.

To minimize the disparity between imaging and probe-based spectra, the ideal fiber-optic probe configuration must come as close as possible to re-creating an imaging illumination-collection geometry, in which a small collection region falls within a large illumination spot. While this would imply a single collection fiber surrounded by concentric rings of illumination fibers, such a design is impractical since distributing the illumination light across multiple fibers would significantly reduce the illumination irradiance. If viewed in terms of source-detector separation distances, an imaging geometry collects photons across all separation distances ranging from zero to the maximum distance between the pixel location and the edge of the illumination spot, which can often be considered infinite relative to the photon diffusion distance. To mimic this scenario, the collection fibers should extend as far as possible, with uniform coverage as a function of distance from the illumination fiber. For a conventional fiber configuration with a single illumination fiber surrounded by concentric rings of collection fibers

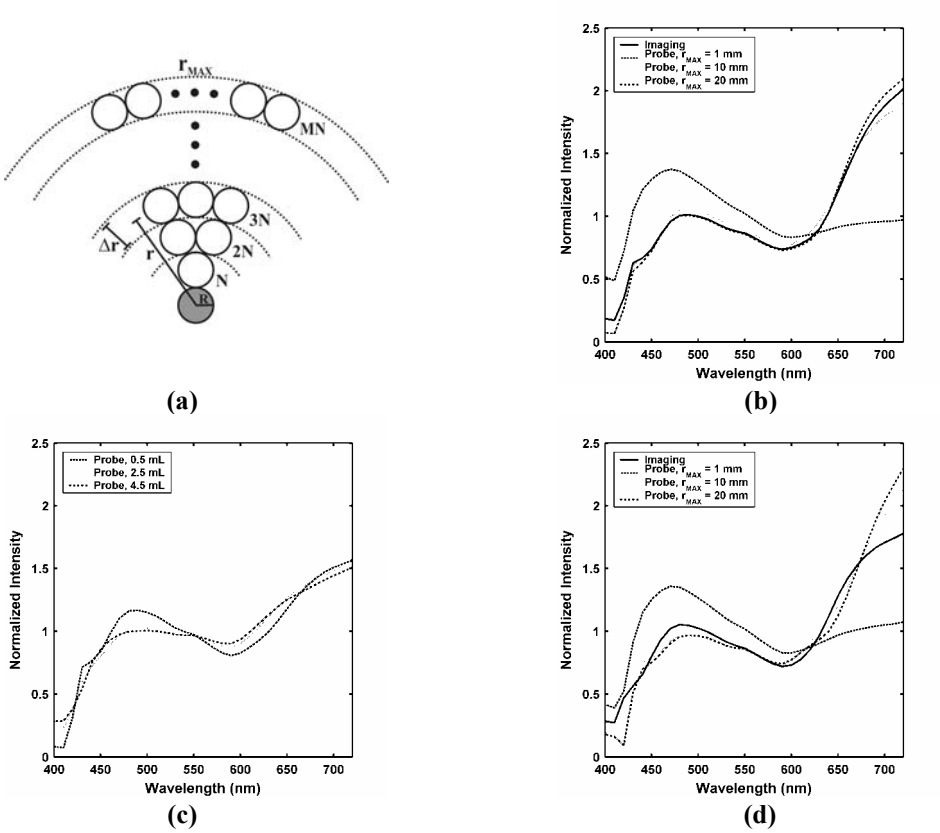

Figure 8. Ideal fiber configuration to minimize the disparity between imaging and probe-based diffuse reflectance lineshapes from variable scattering phantoms: (a) ideal fiber configuration (b) Monte Carlo imaging spectra and probe-based spectra for R = 165 μm, N = 1, and various r_{MAX} values for 0.5 mL phantom (c) Monte Carlo imaging and probe-based spectra for R = 165 μm, N = 1, and r_{MAX} = 5 mm for variable scattering phantoms (d) Monte Carlo imaging spectra and probe-based spectra for R = 165 μm, N = 1, and various r_{MAX} values for 0.5 mL phantom with absorption equal to 133% of μ_a value in (b).

(Figure 8a), each ring of fibers sits within an annulus of width equal to the fiber diameter (2R). Since the area of an annulus of constant width (Δr) increases with radius (r) as $2\pi r\Delta r$, to provide uniform coverage at each source-detector separation distance, the number of fibers within each ring must increase linearly with this distance. Therefore, if the first ring has N fibers, the second ring should have 2N fibers, the third ring 3N fibers, and so on. While ideally this pattern would extend *ad infinitum*, practically it would extend to a point which could be deemed semi-infinite relative to photon diffusion for the given sample optical properties.

Using Monte Carlo simulation to determine the most practical fiber-optic probe design in terms of fiber diameter (R) and extent of coverage (r_{MAX}), the results demonstrate that the fiber geometry must extend out to a point roughly 15 mm from the illumination fiber to minimize the disparity between probe-based and imaging diffuse reflectance lineshape for the lowest

scattering phantom in the variable scattering series (Figure 8b). Since Figure 5 shows opposing trends with increased reduced scattering for probe-based and imaging spectra, the trend for probe-based spectra must reverse itself to emulate imaging lineshape behavior, a transition which occurs at roughly r_{MAX} = 5 mm (Figure 8c). The radial extent of the fiber probe to emulate imaging behavior (Figure 8d) and the transition point (results not shown) are both dependent on the level of sample absorption, decreasing with increasing absorption.

Discussion

The results outlined in this paper demonstrate an inherent disparity between probe-based spectroscopy and spectral imaging in fluorescence and diffuse reflectance lineshape (Figure 3). The results show that the lineshape disparity is due to differences in the illumination-collection geometry of the two systems (Figure 3a,b) and is dependent on the optical properties of the sample. Increased sample absorption leads to greater lineshape modulation due to hemoglobin absorption ("absorption modulation") for both systems with consistently greater modulation in imaging than in probe-based spectra (Figure 4). Increased sample scattering reduces the absorption modulation in imaging spectra while simultaneously increasing absorption effects in probe-based spectra (Figure 5). While more readily apparent with changes in sample scattering, both increased absorption and increased scattering decrease the lineshape disparity between the two systems. Beam-steered fibers (Figure 6), decreasing the fiber diameter (Figure 7a-c), and using the illumination fiber for collection (Figure 7c,d) decrease the absorption modulation in probe-based spectroscopy, thereby increasing the disparity to imaging lineshape.

The first inclination upon comparing the probe-based and imaging spectra shown in Figure 3 is to attribute the lineshape disparity to changes in instrumentation (spectral resolution, illumination sources) and/or errors in wavelength calibration between the probe-based spectroscopy and spectral imaging systems. Before positively identifying the shift in illumination-collection geometry as the true root, each of these causes was investigated to determine its effect on the measured lineshapes. The probe-based spectroscopy system possesses a spectral resolution of roughly 10 nm across its spectral range; the spectral resolution of the spectral imaging system varies from 10 nm at 400 nm to 35 nm at 720 nm. While the disparity in spectral resolution will widen spectral features and increase the contrast between the red and blue wavelengths in imaging measurements, the spectral resolution of the two systems are roughly

equivalent (10-15 nm) at the point of peak fluorescence observed in this study (460 nm), fluorescence peaks are sufficiently wide as to be negligibly affected by spectral resolution, and such an increase in contrast does not explain the complete reversal in the trend of that contrast with changes in scattering between spectroscopy and imaging. Further, shifting from a nitrogen laser to a bandpass-filtered xenon lamp and between halogen lamps were determined to have no effect on measured fluorescence and diffuse reflectance lineshapes, respectively (results not shown), based upon probe-based spectroscopy measurements acquired from a gray matter phantom using the probe-based and imaging illumination sources with a non-contact illumination-collection geometry (Figure 2). Inaccuracies in wavelength calibration were eliminated as the cause for the lineshape disparity using a similar comparison between non-contact imaging and probe-based spectra from a 99% diffuse reflectance standard (Spectralon, LabSphere) illuminated by the halogen lamp from the spectral imaging system.

Once the shift in illumination-collection geometry was identified as the cause for the lineshape disparity, the differences in geometry were theoretically contrasted to those investigated by Richards-Kortum et al [34]. Richards-Kortum et al originally compared spectral lineshapes from a geometry with perfect overlap of the excitation-collection regions to one with adjacent but non-overlapping regions. By concluding that emission should only be collected within the limits of the excitation spot in order to produce spectral lineshapes independent of excitation-collection geometry effects, Richards-Kortum et al suggest that the degree with which the collection region overlaps the excitation spot is paramount in predicting the effects of absorption on spectral lineshape. Since the probe-based geometry in this study produces adjacent but non-overlapping illumination-collection regions and the collection region in the imaging geometry falls completely within the illumination spot, the lineshape investigation in this paper resembles the comparison by Richards-Kortum et al in terms of illumination-collection overlap. However, while the spectra measured by Richards-Kortum et al with perfect overlap show less absorption modulation than the non-overlapping case, the imaging spectra in this study consistently show more absorption effects than the probe-based spectra.

Figure 9 frames the comparison in another way. Rather than concentrate on overlap between illumination and collection, it depicts the relative relationship between impulse response curves and the relative distributions of source-detector separation distances (SDSD) for the experimental illumination-collection geometries of the imaging and spectroscopy measurements

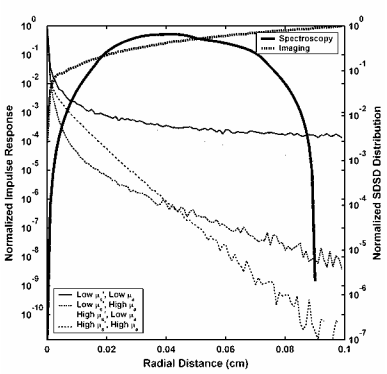

Figure 9. Normalized impulse response and source-detector separation distance (SDSD) distributions for diffuse reflectance. Impulse responses are plotted for four combinations of high and low scattering and absorption (μ_s' = 20 and 1100 cm^{-1}, μ_a = 0.1 and 50 cm^{-1}). Each impulse response was normalized to a peak of one. The imaging and spectroscopy SDSD distributions were calculated for the illumination-collection geometries for the experimental measurements in Figures 4 and 5, with the imaging distribution for a 50 μm pixel at the center of a 25-mm-diameter excitation spot.

in Figures 4 and 5. To highlight the effects of changes with sample optical properties, the impulse response curves were predicted by Monte Carlo simulation for diffuse reflectance emission from four combinations of high and low absorption and scattering. Consistently greater absorption modulation in imaging than probe-based spectra suggests longer photon path lengths before exit from the tissue and subsequently greater interaction of imaging photons with the tissue. As seen in Figure 9, increased tissue scattering effectively shrinks the radial scale of photon diffusion, shortening overall photon path lengths and decreasing photon-tissue interaction. Since the SDSD distribution for imaging extends well beyond the extent of the impulse responses, the imaging system effectively collects the same population of photons regardless of spatial changes in photon diffusion with scattering, and the decrease in photon path lengths produces imaging spectra with decreased absorption modulation consistent with reduced tissue interaction. On the other hand, by shrinking the scale of photon diffusion, increased scattering leads to collection of additional diffuse photons which originally emitted outside the *finite* extent of the SDSD distribution in probe-based spectroscopy, resulting in increased absorption modulation and a shift toward imaging lineshape.

As such, as the scale of photon diffusion decreases relative to the fixed geometry of the fiber-optic probe, probe-based spectroscopy approaches the imaging scenario in which more diffuse photons are collected. Beam-steered fibers, decreasing the fiber diameter, and using the

illumination fiber for collection, all of which bias probe-based photon collection toward photons with shortened path lengths, decrease the effects of absorption modulation and produce spectra with increased disparity to imaging lineshape. These results indicate that rather than on the strict overlap between the illumination and collection regions as proffered by Richards-Kortum et al [34], the lineshape effects from illumination-collection geometry depend on the distribution of source-detector separations relative to the scale of photon diffusion within the tissue. Therefore, the capability for two spectral measurement systems to produce spectral lineshapes equivalent to one another depends on the equality of their illumination-collection geometries, not in terms of illumination-collection overlap but in terms of the overall distribution of source-detector separation distances.

An interesting hypothetical result regarding the lineshape comparison presented by Richards-Kortum et al [34] accurately illustrates the point above. In their paper, fluorescence spectra are initially compared between fiber-based spectroscopy and an *in vitro* non-contact measurement system. The fiber geometry was designed to create 1-mm diameter excitation and collection regions with significant overlap to perfectly mimic the excitation-collection geometry of the non-contact system. It is interesting to note that had the fiber-based system maintained perfect overlap but used 2-mm excitation-collection diameters, the distribution of source-detector separation distances would diverge from the non-contact system since source-detector separation distances for a pair of overlapping excitation-collection regions extend up to the diameter of those regions. Based on the results in this paper, spectra deriving from illumination-collection regions with different diameters would be subject to different levels of absorption modulation and possess different lineshapes, despite perfect illumination-collection overlap.

The effects of absorption and scattering changes on lineshape disparity depend on the relative contributions of the absorption and scattering coefficients to the scale of photon diffusion within the tissue. According to Jacques and Wang, the absorption and scattering coefficients carry equal weight in determining the probability density function for photon stepsize – $p(s) = \mu_t \exp(-\mu_t s)$ where $\mu_t = (\mu_a + \mu_s)$ – and the subsequent photon diffusion scale within the tissue. However, because the scattering coefficient magnitude is significantly larger in most soft tissues (Table 1) [46], changes in absorption affect proportionately smaller changes in the total attenuation coefficient μ_t. Using the optical properties in Table 1, a five-fold change in μ_a across the variable absorption phantoms produces only a 4% increase in μ_t, while a ten-fold

change in μ_s' (and therefore μ_s) produces a 946% increase in μ_t. The unequal effects of changes in absorption and scattering to changes in μ_t and the subsequent scale of photon diffusion demonstrate why large changes in lineshape disparity are apparent across the variable scattering phantoms while the changes with absorption are barely visible.

Despite the fact that the disparate lineshapes of diffuse reflectance and fluorescence make direct comparison difficult, Figures 3 through 5 appear to indicate that the lineshape disparity is less significant in fluorescence than in diffuse reflectance. For equivalent sample optical properties, the fluorescence spectra demonstrate only subtle shifts in the location and width of the emission peak at the same time that diffuse reflectance spectra show large changes in spectral lineshape. While quantitative data is currently unavailable to corroborate this assertion, the differences in lineshape disparity between the two types of spectroscopy most likely trace back to the isotropic nature of fluorescence generation in tissue. Diffuse reflectance photon propagation is entirely subject to forward-biased scattering events, resulting in radially disperse distributions of photon emission. Replacing one of those scattering events with absorption and isotropic photon generation logically results in fluorescence photon emission after fewer scattering events and spatial distributions which are less disperse. As such, the narrow fluorescence distributions relative to diffuse reflectance allows the collection geometry of probe-based spectroscopy to mimic the semi-infinite imaging geometry, with less fluorescence lineshape sensitivity to changes in optical properties.

As outlined in the Results section, the ideal fiber-optic probe configuration that minimizes the disparity between probe-based and imaging spectral lineshape must simulate an imaging illumination-collection geometry. Therefore, given a central illumination fiber surrounded by concentric rings of collection fibers (Figure 8a), the number of collection fibers must increase linearly with the distance from the central illumination fiber. Based on the results in Figure 8b for reduced scattering and absorption spectra which are indicative of human brain tissue, probe-based collection fibers must extend roughly 15 mm to produce diffuse reflectance lineshapes equivalent to spectral imaging (though a less extensive probe could arguably achieve equivalent *fluorescence* lineshapes). While these numbers provide a blueprint for a fiber-optic probe design that minimizes the lineshape disparity from non-contact spectral imaging, it also indicates how far from a given spectral imaging pixel heterogeneities in the tissue will affect measured imaging lineshape. While this paper focuses on spectral lineshape from homogeneous

samples, since photons collected by the imaging system traverse source-detector separation distances up to 10-20 mm, heterogeneous tissue structures in the intervening regions will contribute to the overall imaging lineshape.

The probe-based spectra for r_{MAX} = 10 mm in Figures 8b,d show greater absorption modulation than imaging spectra which involve maximum imaging source-detector separation distances greater than 10-20 mm. Greater absorption modulation in spectroscopy despite shorter maximum source-detector separation distances results from a lack of photon collection within the illumination fiber where source-detector separation distances are short and absorption modulation is minimal. This overshoot in probe-based absorption modulation for probe designs with large r_{MAX} values can be minimized by decreasing the illumination fiber diameter, using the illumination fiber for collection, or decreasing the diameter of the collection fibers (results not shown). However, reducing the illumination fiber diameter reduces the delivered illumination irradiance due to imperfect fiber coupling at the illumination source; using the illumination fiber for collection over-corrects the disparity by over-sampling the source-detector separation distances within the illumination fiber; and reducing the collection-fiber diameter presents a tradeoff between minimizing the lineshape disparity and minimizing the number of collection fibers in the probe. The number of collection fibers for a given fiber diameter (2R), radial extent (r_{MAX}), and number of fibers in the first ring of collection fibers (N) is equal to

$$Number\ of\ Collection\ Fibers = \frac{N}{2} FLOOR\left(\frac{r_{MAX}}{2R}\right)\left[FLOOR\left(\frac{r_{MAX}}{2R}\right)+1\right],$$

where *FLOOR()* indicates rounding down to the nearest integer. For the scenario in Figure 8b with a 330 μm diameter fiber (plus cladding), N = 1, and r_{MAX} = 10 mm, the total number of collection fibers is 465 fibers. If the fiber diameter is decreased to 110 μm, the number of fibers increases to 4095 fibers, creating probe designs which are non-trivial to construct.

Figure 8c demonstrates that as the radial extent (r_{MAX}) of the fiber-optic probe increases, the trend in absorption modulation changes from increased modulation with increased scattering to decreased modulation with increased scattering, similar to the trend in imaging spectra. This behavior indicates that a radial extent exists for which spectral lineshape is independent of changes in sample scattering. These findings are consistent with the results of Schmitt and Kumar [22] who sought to determine a source-detector separation distance for an illumination-collection fiber pair which minimized the measurement sensitivity to background scattering for

NIR absorption spectroscopy. Consistent with the results in this paper (Figures 8b,d), they found that this transition point increases with decreased absorption, so to obtain scattering-independent measurements, the probe configuration must be adaptive for changes in sample absorption.

While much of this paper focuses on how changes in fiber design affect probe-based spectra, several of the issues raised above (large number of collection fibers required, spectral imaging sensitivity to tissue heterogeneities) suggest that changes to the spectral imaging method, rather than to the fiber probe, should be investigated to minimize the lineshape disparity between probe-based and imaging spectra. Since the lineshape disparity is characterized by increased collection of diffuse photons by the imaging system, it can be minimized by limiting the viable source-detector separation distances in the spectral imaging geometry. Three such methods include probe-based spectral imaging, polarization spectral imaging, and a flying-spot scanner.

Geometrically speaking, the most straight-forward solution is a fiber-optic probe designed for spectral imaging. The probe would contain a spatial grid of illumination-collection bundles that serve as image pixels with a fiber configuration for each bundle which mirrors the fiber configuration from probe-based spectroscopy. Such a solution would be an adaptation of the fiber bundle image compression (FBIC) technique developed by McClain et al [47] in which the sample image from a microscope is focused onto one end of a fiber bundle, while the opposite ends of the fibers are aligned parallel to the entrance slit of a CCD-based spectrograph. Each row of the CCD array measures the entire spectrum for a single fiber within the bundle and unique spatial position within the image, yielding an entire spectral image within a single CCD frame. However, implementing the FBIC technique for *in vivo* spectral imaging introduces several complicating factors. Extending FBIC for fiber-based illumination and multi-fiber collection at each pixel requires large fiber bundles coupled to illumination sources and collection fibers precisely aligned at the spectrograph. While the spatial resolution of a FBIC microscope is limited by the fiber diameter and image magnification at the fiber bundle, the spatial resolution of a probe-based imaging system is limited to the width of the existing fiber configuration (660 μm). Since photons have been demonstrated to travel as far as 10-20 mm radially from tissue entry to exit, spectra from the pixel-bundles in the probe must be sequentially acquired to avoid crosstalk between pixels, a process which could prove to be very

time-consuming. Despite these limitations, such a spectral imaging design would ensure perfect replication of the illumination-collection geometry from probe-based spectroscopy.

An alternative imaging solution is co-polarization of the illumination and collected light during spectral image acquisition. It has become common knowledge that polarized photons progressively lose polarization state as they travel through and scatter inside tissue. Several research groups have exploited this behavior to selectively collect photons from various layers (i.e. depths) of epithelial tissues by varying the degree of co-polarization between the illumination light and collection optics [48-51]. Since the disparity between probe-based and imaging spectra results from imaging collection of more diffuse photons, co-polarizing the illumination and collection legs of the system would decrease diffuse photon collection and reduce the disparity. It should be noted that since the disparity is optical property dependent, the degree of co-polarization would depend on *a priori*, spatially resolved optical property information, which cannot be acquired *in vivo* with current methods. Further, polarizing the illumination and collected light reduces the measured signal intensities, though this is mitigated in tunable-filter spectral imaging systems which inherently polarize collected light.

Perhaps the most promising imaging solution is the flying-spot scanner [52], in which spectral information is acquired a pixel at a time while the pixel of interest is raster scanned across the tissue surface. Pixel-by-pixel spectral acquisition prevents crosstalk between pixels due to photon diffusion, and careful design of the excitation and collection optics would allow close replication of a probe-based illumination-collection geometry depending on the complexity of the fiber configuration. The main drawback to a flying-spot scanner is its relatively slow frame rate due to the high number of data acquisitions and the need for precise transitions between pixels. Further, while most flying-spot scanners are designed with common illumination and collection optics to produce perfect overlap while simplifying the optical design, probe geometries with non-overlapping illumination-collection areas would require independent excitation and collection optical trains, leading to increased complexity for the spectral imaging system.

The results outlined in this paper provide a guide for intelligent probe design when a transition to non-contact spectral imaging is the ultimate goal. However, for research groups such as ours, probe-based spectral data has already been acquired from a significant number of patients using a fiber-optic probe which is suboptimal in terms of mimicking an imaging

geometry. Therefore, an essential step in the transition from probe-based spectroscopy to spectral imaging will be to determine whether probe-based and/or imaging spectra can be corrected *a posteriori* for illumination-collection geometry effects to reconcile their lineshapes. While it is beyond the scope of this paper, our group plans to undertake such an investigation in the near future. It should be noted that the clinical applicability for any such correction method will hinge on its independence from *a priori* sample optical property information, which is impossible to acquire for previously measured probe-based spectra and which cannot be determined as a function of spatial position during *in vivo* spectral imaging.

In the absence of spectral correction for illumination-collection geometry, the effect of lineshape disparity on the inputs to tissue discrimination algorithms and subsequent discrimination accuracy must then be investigated. The results outlined here intimate that non-contact spectral imaging systems collect diffuse photons which have longer path lengths and subsequently greater interaction with the tissue of interest before exit, suggesting that the spectral differences observed between normal and diseased tissues in probe-based spectroscopy would be intensified in spectral imaging. While this would presumably increase discrimination accuracy, precedent in the literature indicates that non-layered tissues such as brain and breast render photon diffusion level insignificant [20] in terms of discrimination accuracy. However, for applications which involve multi-layered tissues when deep-layer tissue information has been deemed important to disease diagnosis, collection of diffuse photons, which have been shown to probe greater tissue depths [23, 27, 53], should render spectral imaging more diagnostically accurate. The effect of lineshape disparity on discrimination accuracy is another issue our research group plans to address as we move forward with the transition from fiber-optic probe-based spectroscopy to clinical spectral imaging for brain tumor resection guidance.

Conclusion

The transition from fiber-optic probe-based spectroscopy to non-contact spectral imaging often involves an inherent shift in illumination-collection geometry. This paper has demonstrated that this shift in geometry creates a lineshape disparity between the two systems in fluorescence and diffuse reflectance spectra. The behavior of the lineshape disparity with changes in optical properties and the fiber-optic probe configuration can be explained in terms of the light diffusion within the tissue relative to the distribution of source-detector separation distances for the two

measurement system geometries. Imaging spectra consistently show greater absorption effects than probe-based spectra due to collection of diffuse photons at large source-detector separation distances. Both increased scattering and absorption decrease the diffusion scale of collected photons, increase the diffusion level of probe-based photons, and subsequently decrease the lineshape disparity between imaging and probe-based spectra; however, the high ratio of scattering to absorption magnitude in most soft tissues render the lineshape disparity more sensitive to changes in scattering than absorption. Beam-steered fibers, decreasing the fiber diameter, and using the illumination fiber for collection increases the lineshape disparity by biasing probe-based photon collection towards less diffuse photons. The ideal fiber-optic probe configuration uniformly samples all source-detector separation distances; however, photons collected by the imaging system travel radial distances up to 20 mm, requiring collection fibers to extend beyond limits which may be considered practical. Given further limitations involved with adapting the spectral imaging geometry to minimize the lineshape disparity, future research will investigate methods to correct lineshape for system-specific illumination-collection geometry and the effects of lineshape disparity on tissue discrimination accuracy.

Acknowledgements

We would like to acknowledge the National Institutes of Health for funding this research (RO1 Grant CA85989).

References

1. R. Richards-Kortum and E. Sevick-Muraca, "Quantitative optical spectroscopy for tissue diagnosis," Annu Rev Phys Chem **47**, 555-606 (1996).
2. A. Mahadevan-Jansen and R. Richards-Kortum, "Raman spectroscopy for the detection of cancers and precancers," Journal of Biomedical Optics **1**, 31-70 (1996).
3. N. Ramanujam, "Fluorescence spectroscopy of neoplastic and non-neoplastic tissues," Neoplasia **2**, 89-117. (2000).
4. W.-C. Lin, et al, "Intraoperative Application of Optical Spectroscopy in the Presence of Blood," IEEE Journal of Selected Topics in Quantum Electronics **7**, 996-1003 (2001).
5. W.-C. Lin, et al, "In vivo brain tumor demarcation using optical spectroscopy," Photochem Photobiol **73**, 396-402. (2001).
6. W.-C. Lin, et al, "Brain tumor demarcation using optical spectroscopy; an in vitro study," J Biomed Opt **5**, 214-20. (2000).

7. S.A. Toms, et al, "Intraoperative optical spectroscopy identifies infiltrating glioma margins with high sensitivity," Neurosurgery **57**, 382-91 (2005).

8. M.C. Chamberlain and P.A. Kormanik, "Practical guidelines for the treatment of malignant gliomas," West J Med **168**, 114-20. (1998).

9. A. Kowalczuk, et al, "Quantitative imaging study of extent of surgical resection and prognosis of malignant astrocytomas," Neurosurgery **41**, 1028-36 (1997).

10. M.T. Selch, et al, "Gangliogliomas: experience with 34 patients and review of the literature," Am J Clin Oncol **21**, 557-64. (1998).

11. S.A. Toms, D.Z. Ferson, and R. Sawaya, "Basic surgical techniques in the resection of malignant gliomas," J Neurooncol **42**, 215-26. (1999).

12. W. Stummer, et al, "Fluorescence-guided resection of glioblastoma multiforme by using 5-aminolevulinic acid-induced porphyrins: a prospective study in 52 consecutive patients," Journal of Neurosurgery **93**, 1003-1013 (2000).

13. W. Stummer, et al, "Intraoperative detection of malignant gliomas by 5-aminolevulinic acid-induced porphyrin fluorescence," Neurosurgery **42**, 518-25; discussion 525-6. (1998).

14. J. Wu, et al, "Diffuse Reflectance from Turbid Media - an Analytical Model of Photon Migration," Applied Optics **32**, 1115-1121 (1993).

15. T.J. Pfefer, et al, "Reflectance-based determination of optical properties in highly attenuating tissue," J Biomed Opt **8**, 206-15 (2003).

16. F. Bevilacqua, et al, "In vivo local determination of tissue optical properties: applications to human brain," Applied Optics **38**, 4939-4950 (1999).

17. P.R. Bargo, S.A. Prahl, and S.L. Jacques, "Optical properties effects upon the collection efficiency of optical fibers in different probe configurations," Ieee Journal of Selected Topics in Quantum Electronics **9**, 314-321 (2003).

18. P.R. Bargo, S.A. Prahl, and S.L. Jacques, "Collection efficiency of a single optical fiber in turbid media," Applied Optics **42**, 3187-3197 (2003).

19. Q. Liu, C.F. Zhu, and N. Ramanujam, "Experimental validation of Monte Carlo modeling of fluorescence in tissues in the UV-visible spectrum," Journal of Biomedical Optics **8**, 223-236 (2003).

20. C.F. Zhu, et al, "Use of a multiseparation fiber optic probe for the optical diagnosis of breast cancer," Journal of Biomedical Optics **10**, - (2005).

21. J.M. Schmitt and G. Kumar, "Spectral distortions in near-infrared spectroscopy of turbid materials," Applied Spectroscopy **50**, 1066-1073 (1996).

22. G. Kumar and J.M. Schmitt, "Optimal probe geometry for near-infrared spectroscopy of biological tissue," Applied Optics **36**, 2286-2293 (1997).

23. A.J. Welch, et al, "Propagation of fluorescent light," Lasers Surg Med **21**, 166-78 (1997).

24. T.J. Pfefer, L.S. Matchette, and R. Drezek, "Influence of illumination-collection geometry on fluorescence spectroscopy in multilayer tissue," Medical & Biological Engineering & Computing **42**, 669-673 (2004).

25. T.J. Pfefer, et al, "Selective detection of fluorophore layers in turbid media: the role of fiber-optic probe design," Optics Letters **28**, 120-122 (2003).

26. T.J. Pfefer, et al, "Multiple-fiber probe design for fluorescence spectroscopy in tissue," Applied Optics **41**, 4712-4721 (2002).

27. C.F. Zhu, Q. Liu, and N. Ramanujam, "Effect of fiber optic probe geometry on depth-resolved fluorescence measurements from epithelial tissues: a Monte Carlo simulation," Journal of Biomedical Optics **8**, 237-247 (2003).

28. S.K. Chang, et al, "Analytical model to describe fluorescence spectra of normal and preneoplastic epithelial tissue: comparison with Monte Carlo simulations and clinical measurements," Journal of Biomedical Optics **9**, 511-522 (2004).

29. J. Wu, M.S. Feld, and R.P. Rava, "Analytical Model for extracting intrinsic fluorescence in turbid media," Applied Optics **32**, 3585-3595 (1993).

30. A.J. Durkin, et al, "Relation between Fluorescence-Spectra of Dilute and Turbid Samples," Applied Optics **33**, 414-423 (1994).

31. C.M. Gardner, S.L. Jacques, and A.J. Welch, "Fluorescence spectroscopy of tissue: recovery of instrinsic fluorescence from measured fluorescence," Applied Optics **35**, 1780-1792 (1996).

32. Q.G. Zhang, et al, "Turbidity-free fluorescence spectroscopy of biological tissue," Optics Letters **25**, 1451-1453 (2000).

33. M.G. Muller, et al, "Intrinsic fluorescence spectroscopy in turbid media: disentangling effects of scattering and absorption," Applied Optics **40**, 4633-4646 (2001).

34. R. Richards-Kortum, et al, "Spectral diagnosis of atherosclerosis using an optical fiber laser catheter," Am Heart J **118**, 381-91 (1989).

35. M. Keijzer, et al, "Fluorescence spectroscopy of turbid media: autofluorescence of the human aorta," Applied Optics **28**, 4286-4292 (1989).

36. S. Avrillier, et al, "Influence of the emission-reception geometry in laser-induced fluorescence spectra from turbid media," Applied Optics **37**, 2781-2787 (1998).

37. J. Swartling, et al, "Fluorescence spectra provide information on the depth of fluorescent lesions in tissue," Applied Optics **44**, 1934-1941 (2005).

38. S.C. Gebhart and A. Mahadevan-Jansen, "Liquid-crystal tunable filter spectral imaging designed for brain tumor demarcation," Applied Optics (in review).

39. S.C. Gebhart and A. Mahadevan-Jansen. "Brain tumor demarcation with liquid-crystal tunable filter spectral imaging," in *SPIE Photonics West, Advanced Biomedical and Clinical Diagnostic Systems IV*, San Jose, CA, 2006: Bellingham, WA.

40. S.C. Gebhart, W.-C. Lin, and A. Mahadevan-Jansen, "In vitro determination of normal and neoplastic human brain tissue optical properties using inverse adding-doubling," Phys Med Biol **51**, 2011-2027 (2006).

41. S. Prahl, M. van Gemert, and A. Welch, "Determining the optical properties of turbid media by using the adding-doubling method," Applied Optics **32**, 559-568 (1993).

42. J.W. Pickering, et al, "Double-Integrating-Sphere System for Measuring the Optical-Properties of Tissue," Applied Optics **32**, 399-410 (1993).

43. M.G. Shim, et al, "Study of fiber-optic probes for in vivo medical Raman spectroscopy," Applied Spectroscopy **53**, 619-627 (1999).

44. U. Utzinger and R.R. Richards-Kortum, "Fiber optic probes for biomedical optical spectroscopy," Journal of Biomedical Optics **8**, 121-147 (2003).

45. S. Jacques and L. Wang, "Monte Carlo Modeling of Light Transport in Tissues" in *Optical-Thermal Response of Laser-Irradiated Tissue*, A. Welch and M.v. Gemert, eds. (Plenum Press, New York 1995).

46. W.F. Cheong, "Summary of Optical Properties" in *Optical-Thermal Response of Laser-Irradiated Tissue*, A.J. Welch and M.J.C. van Gemert, eds. (Plenum Press, New York 1995).

47. B.L. McClain, J. Ma, and D. Ben-Amotz, "Optical Absorption and Fluorescence Spectral Imaging Using Fiber Bundle Image Compression," Applied Spectroscopy **53**, 1118-1122 (1999).

48. N. Ghosh, S.K. Majumder, and P.K. Gupta, "Polarized fluorescence spectroscopy of human tissues," Optics Letters **27**, 2007-2009 (2002).

49. Y. Liu, Y.L. Kim, and V. Backman, "Development of a bioengineered tissue model and its application in the investigation of the depth selectivity of polarization gating," Applied Optics **44**, 2288-2299 (2005).

50. K.Y. Yong, et al, "Characterization of layered scattering media using polarized light measurements and neural networks," Journal of Biomedical Optics **8**, 504-511 (2003).

51. A. Myakov, et al, "Fiber optic probe for polarized reflectance spectroscopy in vivo: Design and performance," Journal of Biomedical Optics **7**, 388-397 (2002).

52. N. Ramanujam, et al, "Fast and noninvasive fluorescence imaging of biological tissues in vivo using a flying-spot scanner," IEEE Trans Biomed Eng **48**, 1034-41. (2001).

53. P. Matousek, et al, "Subsurface probing in diffusely scattering media using spatially offset Raman spectroscopy," Applied Spectroscopy **59**, 393-400 (2005).

CHAPTER VII

INTRA-OPERATIVE BRAIN TUMOR DEMARCATION WITH LIQUID-CRYSTAL TUNABLE FILTER SPECTRAL IMAGING

Abstract

Brain tumor resection is currently hindered by significant limitations in the intra-operative localization of tumor margins, which when coupled with conservative resection to minimize neurologic deficit often results in incomplete tumor resection and ultimately tumor recurrence. Autofluorescence and diffuse reflectance spectroscopy have been repeatedly proven capable of discriminating between normal and tumor margin tissues in the brain and other organs but are limited in their ability to guide tumor resection with a series of single-point measurements. This paper describes a preliminary clinical study to assess the feasibility of using autofluorescence and diffuse reflectance spectral imaging for intra-operative brain tumor discrimination and image guidance. Fourteen spectral image sets and thirty-one probe-based spectroscopy measurements were acquired from nine patients undergoing craniotomy for tumor resection or temporal lobectomy. Spectral image acquisition was performed in a clinically viable two-minute timeframe and produced excellent spatial resolution for visualization of fine tissue structures adequate for surgical guidance. Diagnostic algorithms were independently developed for homologous spectral imaging and probe-based spectroscopy data using a non-linear multi-variate framework, and posterior classification probabilities demonstrated perfect optical diagnosis of twenty-eight normal cortex and glioma tissue sites, indicating discrimination accuracy for spectral imaging on par with traditional probe-based spectroscopy. Diagnostic image maps pseudo-colored from classification probabilities for each pixel within the spectral images showed excellent sensitivity and specificity when compared with gross neurosurgical diagnosis of the various tissue regions in the image. While the current-generation spectral imaging system is limited in its geometry and freedom of movement, hindering image acquisition from deep-seated white matter and margin tissues along the walls of the resection cavity, future clinical work will focus on the evaluation of discrimination accuracy at the tumor margins where current tumor localization techniques fail.

Introduction

The American Cancer Society estimates that 18,820 new cases of and 12,820 deaths from brain tumors were reported in the United States in 2006 [1]. Gliomas comprise 40% of primary brain tumors and 78% of malignant tumors, with a five-year survival rate of only 33% and a 12-18 month average survival time and 5.1% three-year survival rate for infiltrating glioblastomas [2]. The current three-prong attack for brain tumor treatment is surgical resection of maximum tumor volume followed by radiation and chemotherapy, despite limited efficacy for these adjunct therapies. The blood-brain barrier often prevents cancer-targeting drugs from reaching the tumor, rendering chemotherapy ineffective; and while surgery and radiation therapy can effectively treat the tumor core, the fingerlike protrusions at the margins of infiltrating tumors make treating the entire tumor near impossible. The extent of surgical resection at these tumor margins for both low-grade and high-grade gliomas has been repeatedly correlated to patient quality of life and mortality [3-7]; however, complete tumor resection is achieved in less than 20% of patients diagnosed with infiltrating gliomas due to limitation in the surgeon's ability to discriminate between normal tissue and tumor margins during surgery. To this end, tools and techniques are constantly being developed to help locate the tumor and identify its margins during a resection procedure, to maximize tumor mass resection without sacrificing neurologic function.

Current methods for intra-operative tumor localization are limited in their ability to differentiate normal brain from tumor margins. Visual inspection can be highly subjective and inconclusive, especially when dealing with low-grade tumors or diffuse tumor margins which often resemble normal neural tissue. On-site pathology is more histologically reliable but is expensive, is far from real-time, and does not spatially demarcate margin extent. Three-dimensional surgical navigation with x-ray computed tomography (CT) or magnetic resonance imaging (MRI) is extremely useful in tumor localization and debulking [8, 9] but limited in its margin sensitivity, as tumor cells have been found outside of delineated image margins in many documented cases [10]. Furthermore, deformation of brain tissue subsequent to craniotomy, retraction, and debulking by as much as a centimeter degrades the accuracy of surgical navigation based upon pre-operative images [11, 12]. Real-time intra-operative ultrasound is not subject to complications from brain deformation and is capable of detecting tumor margins because brain tumors are often hyperechoic relative to normal tissue. But ultrasound imaging is frequently unable to differentiate tumor from peritumoral edema, which is also hyperechoic [13,

14], and poor image resolution hinders correlation between image features and surgical position. Due to the inherent limitations of these adopted tumor visualization techniques, significant residual tumor cells frequently remain after resection [3, 5], emphasizing the need to develop an objective, on-site, real-time imaging system that is capable of detecting the margins of brain tumors with high sensitivity.

The first effort to guide glioma resection in the brain with optical techniques employed exogenous fluorescence subsequent to systemic administration of 5-aminoluvolinic acid (5-ALA) [15, 16], one of the precursors to hematoporphyrins along the heme biosynthesis pathway. Photosensitizers such as 5-ALA when administered systemically or topically have been shown to selectively collect in tumor tissues. While 5-ALA itself is not fluorescent, its porphyrin derivatives exhibit strong red fluorescence in response to blue excitation light, making them useful for photodynamic therapy and potentially as a means to demarcate tumor borders. As mentioned previously, the clinical utility of any technique for glioma resection guidance depends on its ability to highlight infiltrating tumor margins from the surrounding normal brain tissue. To assess this capability *in vivo*, Stummer et al administered 5-ALA to patients before tumor resection surgery and acquired tissue biopsies from fluorescent and non-fluorescent regions along the tumor margins. The presence of fluorescence was correlated to histopathological diagnosis, and the presence of residual porphyrin fluorescence after surgery was correlated to residual gadolinium contrast enhancement in post-operative MRI as a measure of the extent of tumor resection. Over the course of two separate studies which involved 61 patients and 353 biopsy samples, porphyrin fluorescence possessed a sensitivity of 85%, specificity of 98%, positive predictive value (PPV) of 100% and negative predictive value (NPV) of 60% for the presence of tumor cells in the biopsy samples. High diagnostic sensitivity and specificity indicate sensitive detection without false prediction of the presence of tumor, leading to a high PPV which signifies excellent safety to avoid neurologic deficit. However, the low NPV indicates that biopsy samples without fluorescence often contained tumor tissue, suggesting limited efficacy for positive tumor margin demarcation. While the results demonstrate good correlation between residual fluorescence and residual MR contrast enhancement, the correlation simply follows from the fact that margin demarcation with porphyrin fluorescence is limited in much the same manner as with contrast-enhanced MRI. Since gadolinium and 5-ALA are both polar molecules which cannot freely cross the blood-brain barrier [17], contrast enhancement in both modalities

is only present in regions where the blood-brain barrier has been breached, such that neither modality consistently enhances infiltrating tumor margins or low-grade gliomas.

While exogenous contrast methods are spatially correlated to the integrity of the blood-brain barrier, autofluorescence and diffuse reflectance spectroscopy probe intrinsic tissue contrast, giving them the potential to overcome limitations of exogenous contrast by consistently demarcating infiltrating tumor margins based upon the inherent changes in tissue structure and biochemistry subsequent to tumor invasion. Over the past 20 years, the investigation of optical spectroscopy to differentiate between normal and diseased tissues has grown tremendously and been applied for disease detection in a host of bodily tissues [18-20]. Intrinsic fluorescence or autofluorescence spectra have been shown to differ between normal and neoplastic tissues in various organ systems, differences which have been attributed to changes in fluorophore concentration or environment with the progression of disease [21]. While fluorescence spectroscopy provides information about the chemical and morphological composition of tissue, diffuse reflectance spectroscopy yields information about tissue absorption and scattering [22]. During the progression from normal to neoplastic, tissue undergoes many structural as well as chemical changes at the cellular and subcellular level, altering the optical properties of the tissue and thereby enabling tissue discrimination with diffuse reflectance spectroscopy. Thus by combining fluorescence with diffuse reflectance spectroscopy, optical techniques have the potential to be used for brain tumor margin detection.

Optical spectroscopy based on intrinsic tissue changes was first applied for tissue discrimination in the brain by Chung et al *in vitro* [23] and Bottiroli et al *in vivo* [24]. Using fluorescence excitation near 330 nm, both groups observed significant reductions in NADH autofluorescence near 460 nm and Bottiroli et al observed a significant red-shift in the peak fluorescence wavelength in tumor relative to normal brain tissues. However, given the limited number of patients investigated in these studies, true validation of optical spectroscopy as tissue discrimination tool in the brain remained unaccomplished, especially where it was most important, at the tumor margins.

In an effort to determine the clinical utility of optical spectroscopy for tumor resection guidance, our research group is in the middle of a multi-center clinical study to determine the diagnostic accuracy of combined fluorescence and diffuse reflectance spectroscopy for discriminating between normal and tumor margin tissues *in vivo* [25-27]. During craniotomy

procedures for glioma resection or temporal lobectomy, multiple gray matter, white matter, tumor core, and tumor margin sites are selected for spectral measurement with a portable spectroscopic system [26]. Excitation light from a pulsed nitrogen laser (fluorescence) and halogen lamp (diffuse reflectance) are sequentially delivered to a point on the tissue surface by two of seven fibers within a handheld, beam-steered, fiber-optic probe. The remaining five fibers in the probe are used to collect remitted fluorescence and diffuse reflectance from the tissue surface and deliver it to a spectrograph for spectral measurement. Spectra are grouped as normal, tumor core, or tumor margin according to gold-standard histopathological diagnosis of tissue biopsies acquired at the interrogation site and analyzed to determine spectral differences between tissue groups. Despite only subtle spectroscopic differences between normal and tumor tissues, initial reports using multivariate analysis of fluorescence and diffuse reflectance spectra measured from 184 tissue sites in 35 of more than 125 patients measured to date demonstrate a diagnostic accuracy of 100%, 96%, and 94% for normal, tumor core, and tumor margin tissue samples, with only 2 out of 35 tumor margin sites misclassified as normal [25]. These results indicate not only the promising capability of combined autofluorescence and diffuse reflectance spectroscopy to provide contrast between normal and tumor tissues in the brain, but also its ability to overcome the limitations of current tumor margin localization techniques by accurately differentiating infiltrating tumor margins from surrounding normal brain tissue and potentially affecting more complete glioma resection.

While fiber-optic probe-based spectroscopy as previously described is useful for correlating spectral features to histopathological diagnosis at a specific interrogation site, it is limited in clinical applicability since it produces a single-point measurement on the tissue surface without providing the spatial extent of tumor margins, information which is necessary to efficiently guide tumor resection. For optical biopsy to be clinically useful, single-point spectroscopy systems must be extended to spectral imaging in which spectral information is acquired at every pixel within a two-dimensional field of view, yielding spatial and spectral tissue information for a comprehensive snapshot of tissue pathology during surgery. To extend upon the optical spectroscopy results, our research group has developed a clinical, liquid-crystal tunable filter spectral imaging system capable of fluorescence and diffuse reflectance imaging and coupled to an operating microscope for intra-operative *in vivo* imaging. As part of a separate paper [28], the imaging parameters of the system were quantitatively characterized in terms of

linearity, field of view, spatial and spectral resolution, and system sensitivity as a function of wavelength. Functional imaging tests also demonstrated the capability of the system to differentiate between white and gray matter brain tissue and between brain tissue phantoms with disparate levels of exogenous fluorescence. Fluorescence and diffuse reflectance images acquired *in vivo* of a cortical surface glioma revealed excellent visualization of the cortical surface vasculature, but also confirmed the subtle spectral differences in measured lineshape between normal and neoplastic brain tissues originally observed with probe-based spectroscopy. Further, comparisons of fluorescence and diffuse reflectance lineshapes between probe-based spectroscopy and spectral imaging have shown significant disparities in fluorescence and diffuse reflectance lineshape due to inherent differences in excitation-collection geometry, behavior which was thoroughly characterized in a separate paper [29]. These results strongly indicate the need for an independent evaluation specific to spectral imaging of its diagnostic accuracy for normal and tumor tissues in the brain.

This paper describes the results of such a multi-patient clinical study to assess the capability of fluorescence and diffuse reflectance spectral imaging to discriminate between normal and neoplastic brain tissues *in vivo* during tumor resection surgery. Due to geometry constraints for the first-generation spectral imaging system, this preliminary *in vivo* study was limited to image acquisition from tissue areas near the cortical surface of the brain, preventing investigation of deep-seated white matter and tumor margins along the resection cavities. As such, discrimination algorithms were developed to differentiate between normal cortex and tissues from the tumor core, leaving evaluation of tumor margin demarcation with spectral imaging for a future publication. Independent analysis for probe-based spectroscopy and spectral imaging was performed for homologous fluorescence and diffuse reflectance measurements at twenty-eight tissue sites in nine patients. Diagnostic algorithms and their subsequent accuracy are compared between probe-based spectroscopy and spectral imaging to determine the effects of the inherent lineshape disparity characterized in [29]. Ultimately, diagnostic image maps are created and analyzed by applying imaging-specific algorithms to the entirety of imaging data on a pixel-by-pixel basis for a pilot evaluation of the utility of spectral imaging for tumor resection guidance *in vivo*.

Materials and Methods

Homologous spectral imaging and probe-based spectroscopy measurements were acquired from human brain tissue in nine patients undergoing open craniotomy for tumor resection or temporal lobectomy. Spectral imaging was performed with a liquid-crystal tunable filter spectral imaging system which has been described in detail elsewhere [28], so will only be briefly described here. The collection arm of the system was connected to the head of a M690 Wild-Heerbrugg operating microscope (Figure 1a) and consisted of three main components: a liquid-crystal tunable filter (Varispec VIS-20, CRI, Inc.), a variable focal-length camera lens (f/3.5, Nikon), and a cooled CCD camera (PhotonMax, Princeton Instruments) [28]. Light from a 500 W xenon arc lamp, bandpass filtered at 340 nm, was used for fluorescence excitation, while light from a 200 W halogen lamp (Luxtec) was used for diffuse reflectance (Figure 1b). A 365 nm dichroic filter coupled both excitation sources into a single, 10-mm-core liquid light guide which delivered the excitation light to the sample. Electronic shutters allowed automated switching between the excitation sources and quartz lenses at the distal end of the light guide focused the excitation light to a spot roughly 2" in diameter. The system was manually positioned for image acquisition with the tissue surface roughly seven inches from the distal face of the LCTF, creating a 1" x 1" field of view.

The portable, probe-based spectroscopy system (Figure 1c) has been repeatedly used for the clinical brain tumor diagnosis study outlined in the introduction and has been described numerous times in the literature [26], so again, only the relevant details will be repeated here. A fiber-optic probe with seven beam-steered fibers (d = 300 μm, NA = 0.22) in a six-around-one configuration (Figure 1d) delivered light from a pulsed nitrogen laser (VSL-337, Spectra-Physics) for fluorescence excitation (337 nm, 120 μJ per pulse, 20 Hz repetition rate) and from a white-light halogen lamp (6.5 W, LS-1, Ocean Optics) for diffuse reflectance illumination. Illumination light was delivered by two opposing fibers at the six o'clock and twelve o'clock positions along the outer ring, while the remaining five fibers delivered remitted light, collected from the sample surface, to a spectrometer (S2000-FL, Ocean Optics) for spectral measurement. Electronic shutters allowed automated switching between the excitation sources and the probe configuration produced a tissue interrogation area roughly 1 mm in diameter.

A standard measurement protocol was designed for the homologous spectral imaging and probe-based spectral measurements, approved by the Vanderbilt University Institutional Review

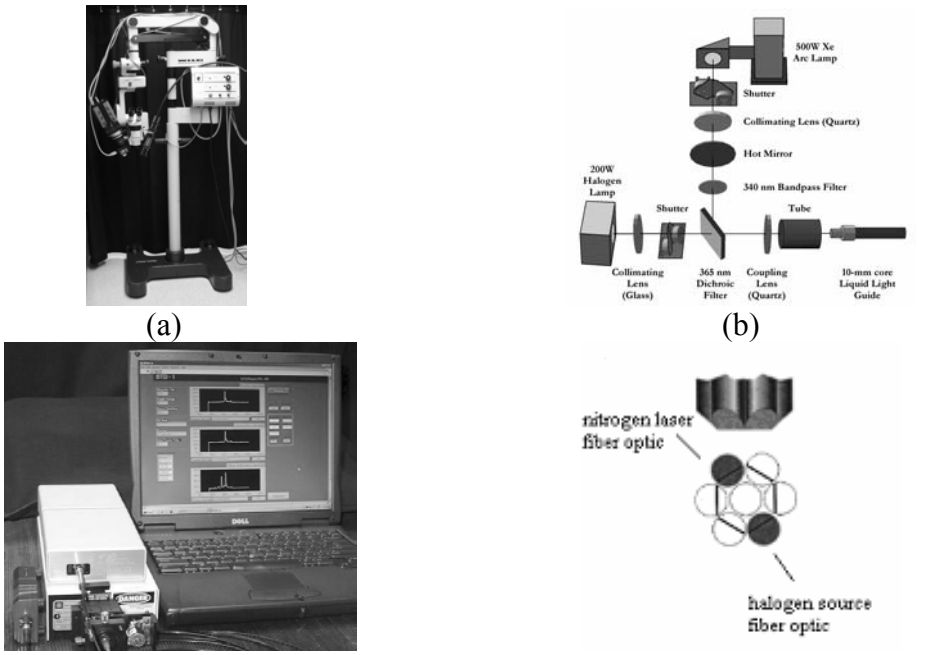

Figure 1. System schematics for the combined fluorescence and diffuse reflectance spectral imaging and fiber-optic probe-based spectroscopy systems used during the clinical study. (a) collection arm of spectral imaging system attached to head of standard operating microscope; (b) excitation optics for spectral imaging system; (c) optical spectroscopy system; (d) distal tip of fiber-optic probe for spectroscopy measurement.

Board, and maintained for all nine patients in the study. The measurements were conducted intra-operatively by the attending neurosurgeon. The spectral imaging system was covered in a sterile drape and the fiber-optic probe was sterilized using a low-temperature plasma method (Sterrad) prior to each study patient. Due to the angled geometry of the spectral imaging system, simultaneous illumination and collection could not be achieved from deep-seated white matter and tumor margin areas along the walls of the resection cavity. As such, fluorescence and diffuse reflectance spectral image sets were limited to the cortical surface and the tumor core for surface-based gliomas and were acquired at various time-points throughout the surgical procedure.

Fourteen image sets were acquired across nine patients, with each image set comprised of fluorescence, fluorescence baseline, diffuse reflectance, and diffuse reflectance baseline images. The spectral range for the images extended from 400 to 720 nm, with a 10-nm increment for diffuse reflectance and its baseline images and an increment which varied between 10 nm around the fluorescence peak to 40 nm in the red region of the spectrum for fluorescence and its baseline images. In an effort to obtain uniform signal-to-noise ratio at all wavelengths, integration times

varied with wavelength according to system sensitivity measured in [28], with total image integration times of 15 and 45 seconds for diffuse reflectance and fluorescence, respectively. To increase measured signals of tissue autofluorescence, 4 x 4 pixel binning was employed for fluorescence and fluorescence baseline imaging. Measured spectra were baseline subtracted and corrected for system sensitivity and integration time as a function of wavelength on a pixel-by-pixel basis. Corrected spectra from 20 x 20 pixel (1 x 1 mm) regions centered about locations interrogated by probe-based spectroscopy were extracted and averaged to create imaging fluorescence and diffuse reflectance spectra homologous to the probe-based spectroscopy measurements described below.

For each image set, one to four sites within the imaging field of view were subsequently selected for probe-based spectral measurement and their locations within the images were recorded. In total, thirty-one image sites were selected across fourteen images for interrogation with probe-based spectroscopy. For each site, three spectra (baseline, fluorescence, diffuse reflectance) were recorded with the fiber-optic probe placed in gentle contact with the tissue surface. A 200-ms integration time was consistently used for all three spectra and all interrogation sites. For grossly abnormal tissues, a tissue biopsy was acquired at each interrogated site, fixed in formalin, and sent to neuropathology for histopathological diagnosis. For grossly normal tissues, opinion of the attending neurosurgeon as to tissue type was recorded. Before spectral analysis, all spectra were baseline subtracted, corrected for system sensitivity as measured by a standard calibration procedure described in [26], smoothed with a moving-average filter, and sub-sampled every 5 nm between 400 and 850 nm.

Spectral analyses were independently performed on homologous imaging and fiber-optic-probe spectra from the thirty-one tissue sites to characterize significant spectral differences between tissue groups using a multi-step method which has been described in detail elsewhere [25]. Briefly, diagnostic features were extracted from the spectra (normalized according to the process described in [25]) using the recently formulated theory of nonlinear Maximum Representation and Discrimination Feature (MRDF) to perform dimensionality reduction while simultaneously maximizing spectral separation between diagnostic groups. Subsequent classification of the extracted nonlinear features into respective tissue categories was based on the theory of Sparse Multinomial Logistic Regression (SMLR), a Bayesian machine-learning

framework of statistical pattern recognition which produces posterior probabilities that a given spectral dataset falls into each histology group.

The scaffold for diagnostic evaluation was performed in a leave-one-out cross-validation scheme to prospectively test its accuracy in an unbiased manner. All spectra from a given patient were excluded during algorithm training and then used for algorithm validation to prevent intra-patient spectra from appearing in both the training and validation datasets. The process was repeated for the spectral datasets for each of the nine patients to determine imaging and spectroscopy optical diagnoses for all tissue samples in the measured population. Sensitivity, specificity, PPV, and NPV metrics were determined for probe-based spectroscopy and spectral imaging by comparing optical to gold-standard histopathological or gross neurosurgical diagnoses. Finally, all spectral datasets were used to retrain the diagnostic algorithm and determine representative algorithms for the spectroscopy and spectral imaging systems.

The discrimination algorithm trained upon spectral imaging data was applied individually to each pixel within the spectral images acquired from all nine patients to create diagnostic image maps. The diagnostic maps were analyzed in terms of "diagnostic noise" in the images (i.e. the presence of isolated pixels for a given histology classification), the classification of structures (e.g. blood vessels, specular reflectance) falling outside the normal and tumor histology groups, the effect of superficial blood contamination, and most importantly, the posterior classification probabilities of pixels along boundaries between tissue regions of differing histology.

Results

Histopathological diagnosis of abnormal tissues and neurosurgical diagnosis of grossly normal tissues classified the 31 tissue sites interrogated by spectral imaging and fiber-optic-probe spectroscopy as normal brain cortex (n = 16), primary tumor tissue (n = 12), normal white matter (n = 1), a mix of cortex and tumor (n = 1), and a non-diagnostic tissue sample (n = 1) which was grossly diagnosed by the surgeon as tumor at the time of measurement. Given the paucity of white matter and margin tissue samples within the interrogated population, the latter three samples were excluded from the discrimination analysis and diagnostic algorithms were subsequently optimized to differentiate between normal brain cortex and primary tumor tissues.

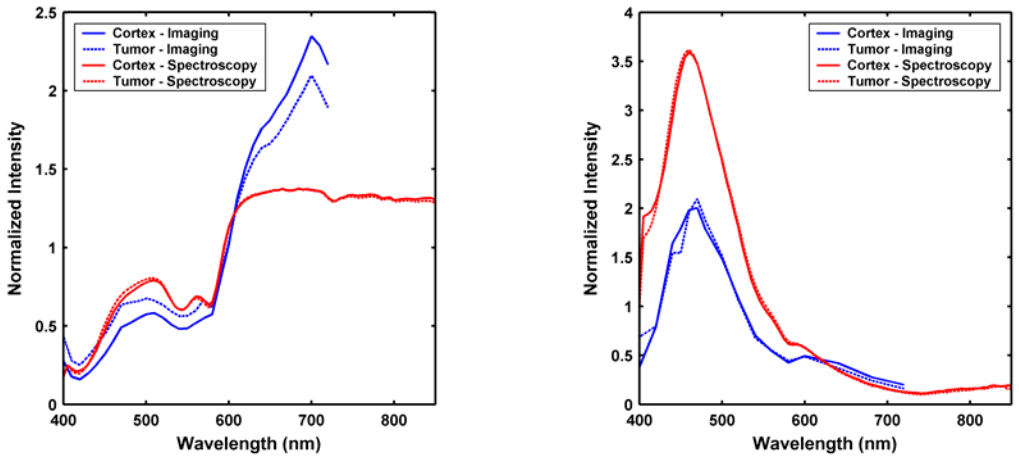

Figure 2. Normalized (a) diffuse reflectance and (b) fluorescence spectra averaged across 16 cortex and 12 tumor interrogation sites measured with spectral imaging and fiber-optic-probe spectroscopy.

Mean fluorescence and diffuse reflectance spectra for normal cortex and primary tumor tissues (Figure 2) reveal subtle differences between the tissue groups, especially in the case of fiber-optic-probe spectroscopy. Both tissue groups exhibit characteristic hemoglobin absorption within diffuse reflectance spectra and peak fluorescence emission near 460 nm, indicative of NAD(H) fluorescence. Consistent with results from a previous comparison of fiber-optic-probe and imaging spectra [29], imaging fluorescence is slightly red-shifted relative to fiber-optic-probe spectroscopy and the contrast between the red and blue regions is consistently larger in imaging diffuse reflectance spectra. These spectral differences are indicative of longer photon path lengths in the tissue for spectral imaging due to a broader distribution of source-detector separation distances in the imaging illumination-collection geometry.

The results from leave-one-out cross-validation demonstrate perfect classification (100% sensitivity, specificity, PPV, NPV) of the 28 tissue samples for both spectral imaging and fiber-optic-probe spectroscopy (Figure 3). The need to run independent spectral analyses for probe-based spectroscopy and spectral imaging is underscored by the discrimination results when probe-based the diagnostic algorithm trained upon probe-based spectroscopy data was subsequently applied to spectral imaging data for validation (Figure 3c). The decreased sensitivity (75%), specificity (81%), PPV (75%), and NPV (81%) values presumably stem from the inherent disparity in lineshape described above between spectral imaging and probe-based spectroscopy.

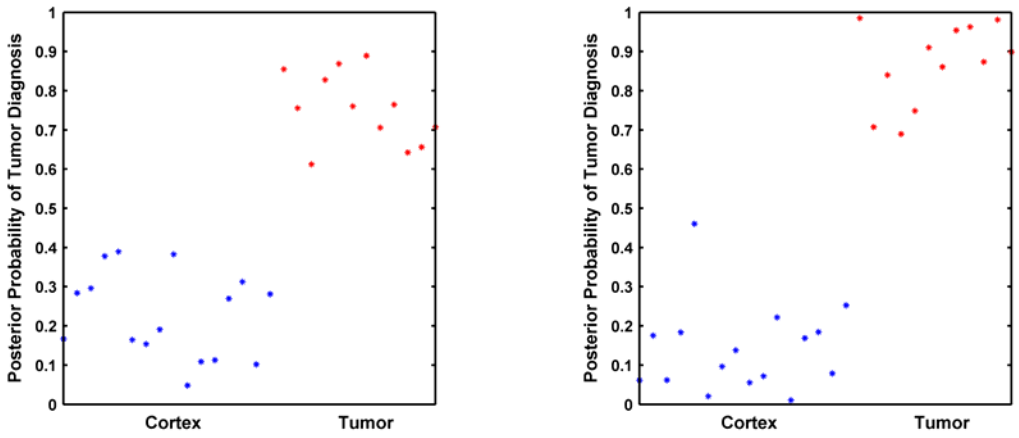

(a)

(b)

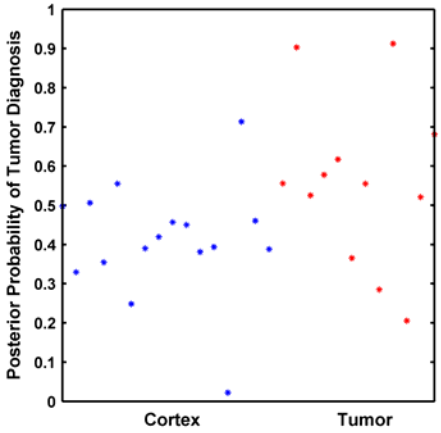

(c)

Figure 3. Posterior probabilities for tumor diagnosis using the MRDF-SLMR technique for diagnostic algorithm development. Individual probabilities are shown for the 16 cortex (blue) and 12 tumor (red) interrogation sites using (a) leave-one-out cross-validation with spectral imaging data, (b) leave-one-out cross-validation with fiber-optic-probe spectroscopy data, and (c) algorithm training with fiber-optic-probe spectroscopy data and algorithm validation with spectral imaging data.

Disparities between spectral imaging and fiber-optic-probe spectroscopy are further highlighted when diagnostic algorithms trained upon the spectroscopy and imaging datasets are applied to diagnose the three samples (white matter, mix of cortex and tumor, non-diagnostic) excluded from the analysis (Table 1). Spectral imaging classifies the white matter sample as definitively normal, the tumor/cortex mix as slightly tumor, and the non-diagnostic sample as non-diagnostic. Probe-based spectroscopy classifies the white matter and cortex/tumor mix samples as definitively tumor and the non-diagnostic sample as definitively normal.

Table 1. Posterior probabilities for three samples excluded from discrimination analysis using discrimination algorithms developed from spectral imaging and fiber-optic-probe spectroscopy data. Posterior probabilities above 0.5 indicate a diagnosis of tumor while probabilities below 0.5 indicate normal cortex.

	Spectral Imaging	Spectroscopy
white matter	0.0183	0.9713
cortex + tumor	0.5654	1.000
non-diagnostic, grossly tumor	0.5096	0.0157

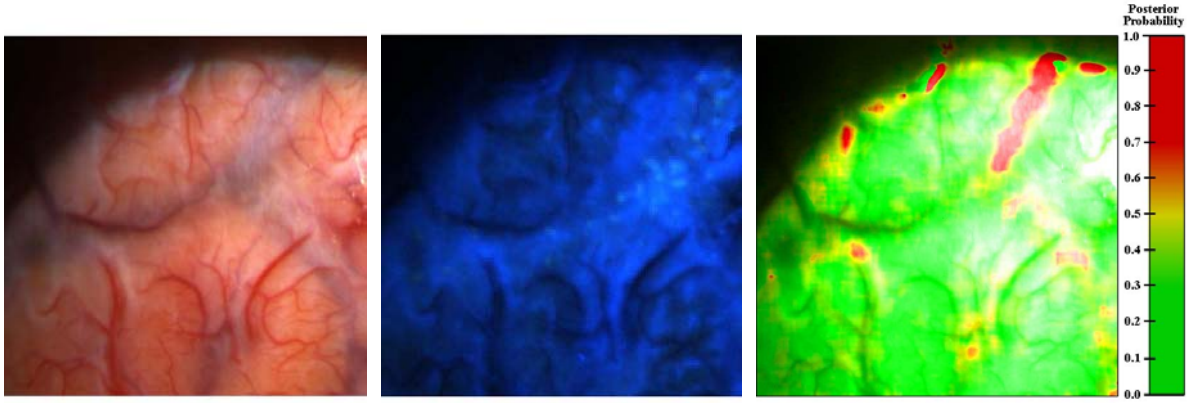

(a) (b) (c)

Figure 4. (a) Diffuse reflectance, (b) fluorescence, and (c) discrimination images acquired from the normal cortical surface of a brain tumor patient. Color information in (a,b) is derived from a direct integration of measured intensities in the spectral imaging data. Pseudo-color in the discrimination image is derived from posterior probabilities on a pixel-by-pixel basis with green indicating normal cortex (p = 0.0), yellow indicating a non-diagnostic transition zone (p = 0.5), and red indicating tumor (p = 1.0).

Example diffuse reflectance and fluorescence spectral images from a brain tumor patient demonstrate the spatial resolution achieved during spectral brain imaging (Figure 4). The images were acquired from a region of completely normal cortex and show excellent visualization of the pial microcirculation along the cortical surface as well as the underlying major blood vessels. Applying the diagnostic algorithm trained upon imaging data produces a diagnostic image map (Figure 4c) with good specificity. Misclassifications are limited to tissue areas containing major blood vessels, which are not expressly handled by the classification algorithm.

Figure 5 shows a second example of diffuse reflectance, fluorescence, and diagnostic images from a tissue region of mixed normal cortex and tumor tissue. As in Figure 4, tissue regions containing major blood vessels as well as image regions with specular reflectance are consistently classified as tumor tissue. Outside of these regions, the diagnostic map shows excellent sensitivity and specificity with good spatial correlation in the classifications (i.e. minimal “diagnostic” noise). The diagnostic algorithm consistently classifies the tumor tissue to

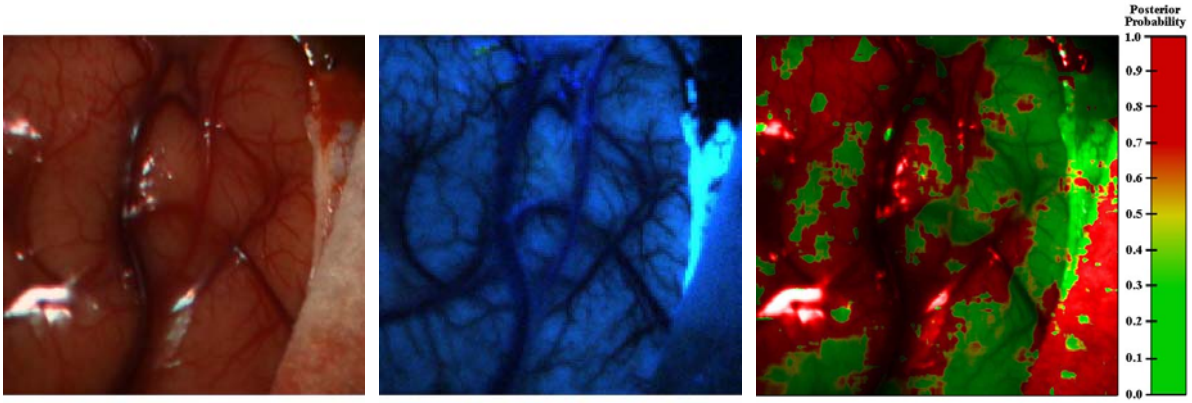

(a) (b) (c)

Figure 5. (a) Diffuse reflectance, (b) fluorescence, and (c) discrimination images acquired from an infiltrating glioma in a brain tumor patient. The tissue to the left of the major blood vessel bisecting the image was grossly classified as tumor by the neurosurgeon. The tissue to the right of the vessel was classified as normal. Color information in the images is derived identically to Figure 4.

the left of the major blood vessel as tumor, with only small regions of normal. The classification algorithm performs even better when applied to the normal cortex to the right of the blood vessel, with only minor pockets of tumor classification evident within the image. It is important to note that the tissue classifications in the diagnostic maps are being compared to the gross tissue diagnosis of the attending neurosurgeon for the various tissue regions in the images, which should not be confused with gold-standard histopathological diagnosis of the tissue biopsies.

Discussion

Surgical resection of brain tumors and their infiltrating margins is currently limited by the surgeon's ability to differentiate between normal and tumor tissue during surgery. Visual similarities between the tissues make such differentiation difficult with direct observation, and pre-operative imaging modalities such as CT and MRI provide poor intra-operative guidance due to problems with tissue deformation during surgery. Current intra-operative tumor localization methods such as ultrasound and contrast-enhanced, intra-operative MRI are limited in their specificity or produce tissue contrast from a breach in the blood-brain barrier, which is often intact in margin tissue. Given the relatively low success (20%) for complete resection of a brain tumor and its associated margins, there exists a distinct need for a real-time, objective imaging tool capable of discriminating between normal and tumor tissue to guide tumor resection surgery.

Preliminary results with optical biopsy methods such as fluorescence and diffuse reflectance have shown promise for brain tumor discrimination from normal white and gray matter; however, the majority of such methods have employed fiber-optic probes for light delivery and collection, limiting the diagnostic throughput to a series of single-point tissue measurements. True clinical utility for tumor resection guidance requires spatial resolution of the diagnostic spectral information in the form of spectral imaging. This paper reports preliminary clinical experience with a dual-mode fluorescence and diffuse reflectance spectral imaging system to differentiate between normal cortex and infiltrating glioma tissues in nine human patients. The results demonstrate excellent sensitivity and specificity on par with fiber-optic probe spectroscopy for this dataset of twenty-eight tissue samples. The spectral images possess high spatial resolution capable of visualizing fine structures down to the brain microvasculature, vastly superior to intra-operative ultrasound, and more than adequate for guidance of surgery with resection tools such as bipolar electro-cautery devices short of direct laser tissue ablation. The spectral images intra-operatively interrogate the tissue within a clinically viable two-minute image acquisition time which stands to be improved as light sources become more powerful, detectors more sensitive, and the diagnostic algorithm more defined to minimize the number of spectral bands which must be interrogated for accurate tissue classification.

Visual similarities between normal and tumor tissues in the brain derive from subtle differences in absorption and scattering across the visible spectrum, in turn producing only subtle differences in diffuse reflectance and fluorescence spectra. As such, accurate spectral discrimination between these tissues requires a sophisticated feature extraction and classification technique. While optical biopsy methods have traditionally employed linear frameworks such as principal component analysis for feature extraction and linear discriminant analysis for feature-set classification, this paper uses a non-linear Maximum Representation and Discrimination Feature extraction technique which is more robust in its ability to draw discrimination boundaries between spectral clusters from different tissue classifications in multi-dimensional spectral space. Further, the Sparse Multinomial Logistic Regression method for spectral diagnosis provides posterior probabilities for each tissue classification, which can be exploited to create diagnostic maps with pseudo-color which conveys not only the classification at each spatial position, but also the confidence in the classification, rather than the simple binary (normal vs. tumor) or trinary (normal vs. tumor vs. margin) outputs of traditional thresholding

methods. Moreover, probabilistic feedback can be extremely useful in clinical situations to judiciously compensate for asymmetric misclassification costs and variable class proportions, and to explore fusion of diagnostic outputs with other probabilistic sources of information before applying decision criteria.

Given that tissue classification in this preliminary study was limited to normal cortex versus tumor tissue, further research work is required to take full advantage of the capability of MRDF-SLMR to perform simultaneous multi-class tissue classification. The geometry and limited freedom of movement for the current generation spectral imaging system restricted image acquisition from superficial tissue regions, preventing interrogation of deep-seated white matter and margin tissues along the walls of resection cavities. Our research group is currently evaluating alternative interfaces which would afford more versatility in terms of image acquisition from hard-to-reach tissue areas. In the construction process for the current imaging system, direct coupling to the camera port of a neurosurgical microscope was also investigated for direct correlation between the neurosurgical field and the imaging system field of view. However, light loss through the microscope collection optics reduced collection power for such an interface by up to 45-fold over a direct-view imaging system such as the one ultimately employed in this clinical study. A more attractive option remains to be coupling the collection optics of the imaging system to the distal end of a fused-silica fiber bundle within a flexible endoscope. The flexibility of the fiber bundle would permit access to deep-seated tissue regions while maintaining spatial resolution of the collected light, which would be collimated through the filter at the bundle's distal end and subsequently focused onto the detector.

Future clinical studies on the efficacy of dual-mode spectral imaging for brain tumor resection guidance will incorporate image acquisition from white matter and more importantly, margin tissues where previous imaging efforts have failed to produce reliable and accurate contrast from normal brain tissue. Clinicians often use magnetic resonance imaging with gadolinium contrast to determine post-operatively whether any tumor regions survived resection. As described in the introduction, a research group from the University of Munich has undertaken a prospective clinical study to assess the efficacy of tumor resection guidance using 5-ALA fluorescence. Both imaging methods rely on the principle of selective collection of exogenous contrast agents within tumor tissue, a phenomenon which only occurs in regions of the brain where the blood-brain barrier has been breached, such as in the core of an aggressive tumor.

Image contrast correlating to the integrity of the blood-brain barrier affords excellent positive predictive values, which are important for surgical guidance in the brain to minimize removal of normal brain tissue and disruption of neurologic function. However, the blood-brain barrier is often intact at tumor margins and in low-grade gliomas, plaguing exogenous-contrast imaging methods with poor negative predictive values in these tissues and resulting in unresected margins which ultimately lead to tumor recurrence. Future clinical studies with a next-generation spectral imaging system will focus on tissue discrimination at the tumor margins, with the hope that probing intrinsic tissue contrast as opposed to collection of exogenous contrast agents will overcome limitations with contrast-enhanced MRI and photosensitizer fluorescence methods and affect more complete brain tumor margin resection.

Future research work is also planned by our research group to ultimately determine the biological basis for spectral differences observed between normal and tumor tissues. One disadvantage with many sophisticated multi-variate feature extraction techniques such as principal component analysis and MRDF is their "black-box" treatment of spectral classification, preventing true interpretation of results and correlation of classification outcome to meaningful morphologic, cellular, and sub-cellular tissue changes with the progression from normal to tumor. Through well-designed experiments, we hope to ultimately shed some light on the spectral changes observed during our clinical probe-based spectroscopy and spectral imaging studies.

Conclusion

The clinical study presented in this paper represents a step toward the development of spectral imaging as a tool for intra-operative guidance of brain tumor margin resection. Dual-mode fluorescence and diffuse reflectance imaging in a clinically viable timeframe was proven capable of producing high-resolution spatial images of brain tissue while discriminating between glioma and normal cortical tissues with accuracy on par with probe-based spectroscopy. The MRDF-SMLR framework for classification algorithm development produced perfect classification of twenty-eight tissue biopsy samples from nine patients. Posterior classification probabilities were calculated for each pixel within the fourteen image sets to produce diagnostic image maps with excellent sensitivity and specificity when compared with gross neurosurgical diagnosis. While additional clinical and research work is required to assess the capability of

tissue discrimination at the tumor margins and in deep-seated white matter regions and to determine the biological basis for spectral differences between normal and tumor tissues, the results from this preliminary clinical study indicate promise for optical biopsy to affect more complete brain tumor margin resection without sacrificing neurologic function, to ultimately improve patient morbidity and mortality from brain cancer.

Acknowledgements

We would like to acknowledge funding from the National Institutes of Health for this research work (Grant R01 CA85989) and the entire nursing staff of the Vanderbilt University Medical Center Department of Neurosurgery for the help with this research study.

References

1. A. Jemal, et al, "Cancer statistics, 2006," CA Cancer J Clin **56**, 106-30 (2006).
2. C.B.T.R.o.t.U. States, "Primary Brain Tumors in the United States Statistical Report, 1998-2002 Years Data Collected," http://www.cbtrus.org, 2005-2006. Accessed on April 27, 2006.
3. M. Ammirati, et al, "Effect of the extent of surgical resection on survival and quality of life in patients with supratentorial glioblastomas and anaplastic astrocytomas," Neurosurgery **21**, 201-6. (1987).
4. M.C. Chamberlain and P.A. Kormanik, "Practical guidelines for the treatment of malignant gliomas," West J Med **168**, 114-20. (1998).
5. A. Kowalczuk, et al, "Quantitative imaging study of extent of surgical resection and prognosis of malignant astrocytomas," Neurosurgery **41**, 1028-36 (1997).
6. M.T. Selch, et al, "Gangliogliomas: experience with 34 patients and review of the literature," Am J Clin Oncol **21**, 557-64. (1998).
7. S.A. Toms, D.Z. Ferson, and R. Sawaya, "Basic surgical techniques in the resection of malignant gliomas," J Neurooncol **42**, 215-26. (1999).
8. R.J. Maciunas, *Interactive Image-Guided Neurosurgery*. 1993, Park Ridge, IL: American Association of Neurological Surgeons.
9. R.J. Maciunas, *Minimally Invasive Therapy of the Brain*, ed. A.D. Salles and R. Lufkin. 1997, New York: Thieme Medical Publishers, Inc.
10. P.D. LeRoux, et al, "A comparison between preoperative magnetic resonance and intraoperative ultrasound tumor volumes and margins," J Clin Ultrasound **22**, 29-36. (1994).
11. D.L. Hill, et al, "Measurement of intraoperative brain surface deformation under a craniotomy," Neurosurgery **43**, 514-26; discussion 527-8. (1998).

12. N.L. Dorward, et al, "Postimaging brain distortion: magnitude, correlates, and impact on neuronavigation," J Neurosurg **88**, 656-62. (1998).

13. L.M. Auer and V.V. Velthoven, *Intraoperative Ultrasound Imaging in Neurosurgery: Comparison with CT and MRI*. 1990, Berlin: Springer-Verlag.

14. J.E. Knake, et al, "Neurosurgical applications of intraoperative ultrasound," Radiological Clinics of North America **23**, 73-90 (1985).

15. W. Stummer, et al, "Fluorescence-guided resection of glioblastoma multiforme by using 5-aminolevulinic acid-induced porphyrins: a prospective study in 52 consecutive patients," Journal of Neurosurgery **93**, 1003-1013 (2000).

16. W. Stummer, et al, "Intraoperative detection of malignant gliomas by 5-aminolevulinic acid-induced porphyrin fluorescence," Neurosurgery **42**, 518-25; discussion 525-6. (1998).

17. L. Terr and L.P. Weiner, "An autoradiographic study of delta-aminolevulinic acid uptake by mouse brain," Exp Neurol **79**, 564-8 (1983).

18. R. Richards-Kortum and E. Sevick-Muraca, "Quantitative optical spectroscopy for tissue diagnosis," Annu Rev Phys Chem **47**, 555-606 (1996).

19. N. Ramanujam, "Fluorescence spectroscopy of neoplastic and non-neoplastic tissues," Neoplasia **2**, 89-117. (2000).

20. A. Mahadevan-Jansen and R. Richards-Kortum, "Raman spectroscopy for the detection of cancers and precancers," Journal of Biomedical Optics **1**, 31-70 (1996).

21. J.R. Lakowicz, *Principles of Fluorescence Spectroscopy*. 1983, New York: Plenum Press.

22. I.J. Bigio and J.R. Mourant, "Ultraviolet and visible spectroscopies for tissue diagnostics: fluorescence spectroscopy and elastic-scattering spectroscopy," Phys Med Biol **42**, 803-14. (1997).

23. Y.G. Chung, et al, "Diagnostic potential of laser-induced autofluorescence emission in brain tissue," J Korean Med Sci **12**, 135-42. (1997).

24. G. Bottiroli, et al, "Brain tissue autofluorescence: an aid for intraoperative delineation of tumor resection margins," Cancer Detect Prev **22**, 330-9 (1998).

25. S.K. Majumder, et al, "A probability-based multi-class diagnostic algorithm for iIn-vivo optical separation of tumor margin and tumor from normal human brain tissue," Applied Spectroscopy ((in review)).

26. W.-C. Lin, et al, "In vivo brain tumor demarcation using optical spectroscopy," Photochem Photobiol **73**, 396-402. (2001).

27. S.A. Toms, et al, "Intraoperative optical spectroscopy identifies infiltrating glioma margins with high sensitivity," Neurosurgery **57**, 382-91 (2005).

28. S.C. Gebhart and A. Mahadevan-Jansen, "Liquid-crystal tunable filter spectral imaging designed for brain tumor demarcation," Applied Optics (in review).

29. S.C. Gebhart and A. Mahadevan-Jansen, "Comparison of spectral variation from spectroscopy to spectral imaging," Applied Optics (in press).

CHAPTER VIII

CONCLUSIONS AND FUTURE DIRECTIONS

Summary

This dissertation presents the translation from fiber-optic probe-based spectroscopy to non-contact spectral imaging for the clinical application of optical biopsy to intra-operative brain tumor and margin demarcation for surgical resection guidance. Specifically, it presents the design, construction, and *in vitro* and *in vivo* testing of a dual-mode liquid-crystal tunable filter spectral imaging system capable of combined fluorescence and diffuse reflectance imaging for spectral discrimination between normal, tumor core, and tumor margin tissues during brain tumor resection surgery. Parallel to spectral imaging system development, a thorough investigation into the effects of the translation from spectroscopy to imaging on measured fluorescence and diffuse reflectance lineshapes is presented. The investigation was designed to ascertain whether diagnostic algorithms developed for tissue differentiation from probe-based spectra should be blindly applied to imaging data or algorithms must be optimized for imaging spectra to achieve accurate tissue diagnosis. The results of these investigations demonstrate that inherent shifts in excitation-collection geometry between probe-based spectroscopy and spectral imaging induce significant changes in measured lineshape. While the effects of these lineshape changes on discrimination accuracy are yet to be determined, imaging-specific discrimination algorithms are presented and shown to be capable of spectrally discriminating between gray matter and tumor core tissues with high sensitivity and specificity. In sum, combined fluorescence and diffuse reflectance spectral imaging can achieve intra-operative brain tumor and margin demarcation with high accuracy, excellent spatial resolution, and minimal disruption to the surgical environment and has the potential to overcome the limitations in current methods of brain tumor margin localization. The following sections summarize the important phases of this research.

Measurement of Brain Tissue Optical Properties

A dearth of optical property coefficient data currently exists within the literature for human brain tissues. Previous brain tissue optical property studies are either limited in the

prediction of true soft tissue behavior (Kubelka-Munk) or in the number of tissue sample measurements (inverse Monte Carlo), opening the door for bias in the measurements. The goal of this study was to complement the handful of inverse Monte Carlo optical property spectra present in the literature and correlate measured optical property measurements to differences between normal and tumor tissues within diffuse reflectance spectra acquired *in vivo* with probe-based spectroscopy. Reflectance and transmission spectra were measured from 400 to 1300 nm for eighty-seven white matter, gray matter, and glioma tissue samples using a single integrating-sphere spectrophotometer. The measurements were subsequently converted to absorption and reduced scattering spectra using an inverse adding-doubling technique. The optical property spectra were grouped according to tissue histology and Student's t-tests were used to determine wavelengths at which the optical properties were significantly different between tissue groups.

Mean absorption spectra were dominated by hemoglobin absorption bands in the visible and water absorption bands in the near-infrared with roughly equivalent levels between white matter, gray matter, and glioma tissues. Reduced scattering decreased with wavelength evident of Mie scattering with levels which were highest in white matter and lowest in gray matter. Ultimately, correlation of optical property measurements to diffuse reflectance spectra revealed that while the shape of diffuse reflectance spectra is predominantly dictated by hemoglobin absorption, the relative intensity between tissue groups is determined by reduced scattering, relationships which are investigated in greater detail in chapter 6.

In terms of the utility of these measurements in the two other phases of my research project, the mean optical property spectra were used to develop white matter, gray matter, and tumor tissue phantoms in chapter 4 for spectral imaging system testing *in vitro*. The concentrations of hemoglobin and polystyrene microspheres for absorption and reduced scattering, respectively, were empirically determined by comparing phantom optical property measurements to the mean measured optical property spectra from this study. To determine whether the translation from probe-based spectroscopy to spectral imaging affects measured lineshape, the mean optical property spectra from this study provided bounds on brain tissue absorption and reduced scattering coefficients, which were used to investigate the effects of optical property changes on observed behaviors via tissue phantoms and Monte Carlo simulation of fluorescence and diffuse reflectance. However, more importantly, the agreement observed between the diffuse reflectance spectra measured *in vivo* and the diffuse reflectance spectra

predicted by Monte Carlo simulation using optical property spectra measured *in vitro* provided the foundation for many of the aforementioned experiments because it demonstrated that spectroscopy and spectral imaging behavior within tissue phantoms or biopsy samples could be accurately predicted via Monte Carlo simulation using optical property measurements.

Spectral Lineshape Effects of the Translation from Probe-Based Spectroscopy to Spectral Imaging

Extending fiber-optic probe-based spectroscopy to non-contact spectral imaging involves a drastic shift in excitation-collection geometry for spectral measurement. While probe-based spectroscopy exerts a consistent interface between the probe and tissue surface, non-contact spectral imaging involves incident excitation and emission collection angles which vary from pixel to pixel with surface topography. While probe-based spectroscopy measures spectra across sub-millimeter source-detector separation distances dictated by the fiber configuration within the probe, macroscopic spectral imaging measures across distances potentially as large as several centimeters. The goal of this phase of the research project was to ascertain whether these differences in measurement geometry induce changes in diffuse reflectance and fluorescence lineshape. The motivation behind such an investigation stems from the desire for spectral imaging to produce identical lineshapes as probe-based spectroscopy, because in such an ideal case, spectral discrimination algorithms developed from the 125+-patient spectral dataset acquired using probe-based spectroscopy could be blindly applied to clinical spectral imaging data for accurate tumor demarcation.

This phase of the research project was divided into two studies: one which investigated the effects of incident excitation and emission collection angles (chapter 5) and one which investigated the effects of the distribution of source-detector separation distances (chapter 6). The effects of these measurement parameters were determined as functions of optical properties within fluorescence and diffuse reflectance spectra.

Non-contact spectral imaging of brain tissue during surgery often involves a variable sample surface topography which creates spatial variations in incident excitation and emission collection angles across the pixels of the image. If angular emission profiles vary with sample optical properties and/or incident excitation angle, the unique excitation-collection geometry of the imaging system relative to the tissue surface has the potential to induce spectral distortions extrinsic to tissue optical properties. The goal of this study was to characterize angular emission

profiles of fluorescence and diffuse reflectance as functions of incident excitation angle and sample optical properties to determine whether constraints on imaging system geometry are necessary to avoid geometry-specific spectral distortion. Fluorescence and diffuse reflectance emission intensity were experimentally measured and predicted via Monte Carlo simulation as functions of azimuthal and polar emission angles, azimuthal incident excitation angle, sample scattering, absorption, and anisotropy coefficient, and combined optical property parameters reduced scattering, albedo, and reduced albedo.

For a spectral imaging geometry which collects emission from a small pixel region within a semi-infinite excitation spot, emission is roughly Lambertian with azimuthal angle for: 1) fluorescence independent of excitation-collection geometry, 2) diffuse reflectance when excited at an azimuthal angle close to the surface normal, and 3) diffuse reflectance within the plane defined by polar angles orthogonal to the polar incident excitation angle. For large oblique incident excitation angles, diffuse reflectance emission is skewed away from the excitation source within the incident excitation plane due to singly scattered and semi-diffuse photon emission. The degree to which emission is skewed from Lambertian behavior is related to the degree of correlation between incident and emission photon directions and can be predicted from the sample albedo and anisotropy coefficient, with increased skewing for decreased albedo and increased anisotropy. Based upon these results, while variations in angular fluorescence emission will not affect spectral lineshape due to angular system geometry or a variable surface topography of the sample, distortions can be induced in diffuse reflectance spectra at pixels with large incident excitation angles if the sample albedo or scattering anisotropy varies significantly across the spectral range of interest.

The implications of these results for our spectral imaging system design are difficult to determine since it involves the interplay of three parameters: incident excitation angle, sample albedo, and sample anisotropy. Further, the optical property measurements in chapter 3 combine the independent contributions of scattering coefficient and anisotropy to the reduced scattering coefficient. Using scattering anisotropy values measured by Yaroslavsky et al [1] to estimate scattering from reduced scattering, the albedo and scattering anisotropy of white matter, gray matter, and glioma tissue vary over the 400 to 700 nm spectral range as:

Tissue Type	Albedo	Anisotropy
White Matter	0.961 – 0.998	0.76 – 0.86
Gray Matter	0.929 – 0.992	0.86 – 0.90
Glioma	0.954 – 0.998	0.88 – 0.96

From these ranges, it can be argued that gray matter and glioma tissue are susceptible to spectral distortion due to the large variation in albedo for gray matter and the large variation in anisotropy for glioma tissue. While white matter possesses an equally large change in anisotropy, the anisotropy values are more isotropic and the albedo values are higher than those for glioma tissue, both of which reduce profile skewing. It should be noted that the effects of variations in albedo and anisotropy will partially offset one another since increases in anisotropy, which affect increased profile skewing, are universally accompanied by increases in albedo, which have the opposite effect.

Multiple studies have established that measured fluorescence and diffuse reflectance lineshape varies with excitation-collection geometry and with the separation distance within an excitation and collection fiber pair, behavior which forms the basis behind optical property measurement from bulk tissues *in vivo*. While several studies in the literature have examined the effect of various excitation-collection geometries on measured spectral lineshape, none have investigated the effect of the geometry shift from probe-based spectroscopy to non-contact spectral imaging. After initial comparisons of imaging and probe-based spectroscopy demonstrated significant lineshape disparities in fluorescence and diffuse reflectance spectra, the source of the disparities were definitively attributed to the shift in the relative relationship between the excitation and collection regions of the two systems. While probe-based spectroscopy collects emission from tissue regions adjacent to the excitation spot, spectral imaging collects emission from a small region within a large excitation spot. The goal of this study was to explore and describe the behavior of the lineshape disparity between probe-based and imaging spectra as a function of sample optical properties and changes to the fiber configuration in the probe. Probe-based and imaging fluorescence and diffuse reflectance spectra were acquired from two series of gelatin-based phantoms with variable absorption and scattering, respectively, based on the brain tissue optical properties measured in chapter 3. The effect of various fiber configuration parameters such as beam-steering, fiber diameter, and using the

excitation fiber for collection were examined through experimental measurement and Monte Carlo simulation.

The behavior of the lineshape disparity between probe-based spectroscopy and spectral imaging with changes in optical properties and fiber-optic probe configuration can be explained in terms of the light diffusion within the tissue relative to the distribution of source-detector separation distances for the two measurement system geometries. Imaging spectra consistently show greater absorption effects than probe-based spectra due to collection of diffuse photons at large source-detector separation distances. Both increased scattering and absorption decrease the diffusion scale of remitted photons, increase the diffusion level of photons collected by probe-based spectroscopy, and subsequently decrease the lineshape disparity between imaging and probe-based spectra; however, the high ratio of scattering to absorption magnitude in most soft tissues renders the scale of photon diffusion and subsequently the lineshape disparity more sensitive to changes in scattering than absorption. Beam-steered fibers, decreasing the fiber diameter, and using the excitation fiber for collection increases the lineshape disparity by biasing probe-based photon collection towards less diffuse photons. The ideal fiber-optic probe configuration to minimize the lineshape disparity uniformly samples all source-detector separation distances; however, photons collected by the imaging system travel radial distances up to 20 mm, requiring collection fibers to extend beyond limits which may be considered practical.

Our research group has completed probe-based fluorescence and diffuse reflectance spectral acquisition from over 125 patients, entrenching our probe-based excitation-collection geometry to the fiber configuration described in [2]. As such, strategies for the translation to spectral imaging are limited to: using a spectral imaging geometry which limits the collection of diffuse photons, correcting probe-based or spectral imaging lineshapes for excitation-collection geometry *a posteriori*, or developing imaging-specific discrimination algorithms to differentiate between normal and tumor tissue *in vivo*. As described in chapter 6, the adaptations to non-contact spectral imaging are either exceedingly complex to implement (spectral imaging fiber probe) or require *a priori* tissue optical property information (co-polarized excitation and collection). For these reasons, chapter 4 focuses on the capability of our non-contact spectral imaging system design to spectrally discriminate between tissue types independent of probe-based discrimination algorithms, while chapter 7 concentrates on developing imaging-specific

discrimination algorithms and investigating the effects of the lineshape disparity on diagnostic accuracy when probe-based discrimination algorithms are applied to imaging data. Since the lineshape disparity between probe-based spectroscopy and spectral imaging varies with sample absorption and scattering, correction of probe-based and/or spectral imaging lineshapes *a posteriori* requires tissue optical property information and is a point of future research for our research group.

Liquid-Crystal Tunable Filter Spectral Imaging for Brain Tumor Demarcation

Current brain tumor localization techniques have significant limitations in their clinical ability to guide tumor resection, especially at the brain tumor margins where diffuse numbers of brain tumor cells and an intact blood-brain barrier make normal and margin tissue visually indistinguishable and render exogenous imaging contrast agents ineffective. Past studies have demonstrated that optical discrimination methods based upon intrinsic tissue information as probed by combined autofluorescence and diffuse reflectance spectroscopy can successfully discriminate between normal, tumor core, and tumor margin tissues in the brain. The next step for clinical implementation of such technology for tumor resection guidance is the extension of fiber-optic probe-based spectroscopy to spectral imaging to spatially demarcate tumor core and margin borders. A successful transition from spectroscopy to clinical macroscopic imaging depends upon two main factors: 1) reasonable image acquisition time despite significant decreases in excitation irradiance due to larger target areas and 2) accurate, sensitive spectral discrimination between tissue types, most notably at tumor margins where other tumor localization methods fail. The goal of this phase of the research project was to develop a spectral imaging system for clinical use and to characterize the system in terms of traditional imaging parameters (field of view, resolution, etc), imaging speed, and capability to spectrally discriminate between brain tissue types *in vivo*.

This phase of the research project was again divided into two studies. The first study (chapter 4) describes the design and characterization of a dual-mode liquid-crystal tunable filter spectral imaging system capable of intra-operative fluorescence and diffuse reflectance imaging, assesses its imaging speed for brain tissues *in vitro* and *in vivo*, and **qualitatively** determines its spectral discrimination capability. Given the need to develop tissue discrimination algorithms specific to spectral imaging data, the second study (chapter 7) describes a clinical investigation

designed to determine the efficacy of tumor demarcation for surgical resection guidance, by acquiring fluorescence and diffuse reflectance images *in vivo*, correlating spectral features to histopathological diagnosis of tissue biopsy samples, developing diagnostic algorithms based on observed spectral differences between tissue types, and **quantitatively** assessing diagnostic accuracy for brain tissue discrimination *in vivo*.

Subsequent to the quantitative comparison of three benchtop spectral imaging systems [3], a liquid-crystal tunable filter spectral imaging system was designed for clinical implementation of dual-mode fluorescence and diffuse reflectance imaging. After thoroughly describing the design of the clinical imaging system, a battery of tests are employed to quantitatively characterize the imaging parameters in terms of linearity of measured intensities to emission intensity and integration time, imaging field of view as a function of object distance, spatial and spectral resolution, and system sensitivity as a function of wavelength. A series of functional tests acquire fluorescence and diffuse reflectance images from gelatin-based phantoms designed to optically mimic white matter, gray matter, and glioma tissues, mouse brain tissue *in vitro*, and human cortical tissue *in vivo.* The images are used to qualitatively assess the ability of the spectral imaging system to produce autofluorescence and diffuse reflectance images capable of spectral discrimination between brain tissues in a reasonable timeframe for the clinical environment.

The spectral imaging system is characterized by measured intensities which are linear with sample emission intensity and integration time, a one-inch field of view for a seven-inch object distance, spectral resolution which is linear with wavelength, spatial resolution which is pixel-limited, and sensitivity functions which provide a guide for the distribution of total image integration time between wavelengths. Functional testing demonstrated good spatial and spectral contrast between brain tissue types, the capability to spectrally discriminate between white and gray matter in the brain, the *in vivo* acquisition of adequate fluorescence and diffuse reflectance intensities within a two-minute imaging timeframe, and the importance of hemostasis to acquired signal strengths and imaging speed. The simple design of the spectral imaging system around a liquid-crystal tunable filter, its linearity of measured intensity with emission intensity and integration time, and its pixel-limited spatial resolution make it a very versatile imaging system. It can acquire spectral information at specific wavelengths deemed diagnostically significant, employ integration times which vary with wavelength to acquire good signal-to-noise across the

spectral range of interest, and utilize pixel binning to increase signal levels without sacrificing discrimination guidance. These results provided direction as we embarked upon the second part of this phase of the research project, a large clinical study to determine the efficacy of combined fluorescence and diffuse reflectance spectral imaging to spectrally discriminate between normal and glioma tissues in the brain for tumor demarcation and surgical resection guidance.

The goal of this study was to quantitatively determine the diagnostic accuracy of the clinical spectral imaging system to optically discriminate between normal and tumor core and margin tissues in the face of: fewer wavelength samples and lineshape disparities relative to probe-based spectra, the loss of absolute intensity information, and crosstalk between pixel regions from photon diffusion. Fluorescence and diffuse reflectance spectral images were acquired from the cortical surface, tumor core, and margin tissues at various points in the surgical resection procedure. Several sites within each image were selected for probe-based spectroscopy interrogation and subsequent biopsy acquisition (if neoplastic). Imaging and probe-based spectra were grouped according to tissue type as determined by gold-standard histopathological diagnosis of the biopsy samples and were analyzed using a non-linear multi-variate framework to determine spectral differences between tissue groups. Discrimination algorithms were developed for each system, unbiased diagnostic accuracy was determined using the leave-one-out cross-validation method, and accuracies were compared between the systems. Imaging-specific algorithms were subsequently applied to all pixels within the fluorescence and diffuse reflectance images to create diagnostic image maps.

The imaging system proved capable of acquiring high-intensity spectral images within a clinically viable two-minute imaging timeframe with spatial resolution more than adequate for visualization of fine tissue structures such as the microvasculature and for surgical guidance with traditional resection tools. While mean imaging and probe-based spectra for twenty-eight normal cortex and tumor samples demonstrated only subtle differences between tissue classes and lineshape disparities consistent with results previously described, the diagnostic algorithm development achieved perfect classification accuracy for all twenty-eight tissue samples for both optical detection methods, indicating discrimination accuracy for spectral imaging on par with traditional probe-based spectroscopy. Diagnostic image maps produced from individual classification of the totality of pixels within the spectral image sets possessed excellent spatial correlation between classification regions, i.e. little to no diagnostic noise, with good sensitivity

and specificity compared to gross neurosurgical diagnosis. Tissue regions containing major blood vessels and image regions containing specular reflectance were consistently classified as tumor tissue. These results indicate excellent promise for dual-mode autofluorescence and diffuse reflectance spectral imaging as a clinical tool for intra-operative tumor and margin demarcation for surgical resection guidance.

Conclusions

In conclusion, the studies described in this dissertation form the basis for the transition from probe-based spectroscopy to spectral imaging for clinical applicability of spatial disease demarcation and subsequent therapy guidance. While the studies focused on and were optimized for brain tissue diagnosis and tumor margin demarcation, many of the results apply to optical discrimination in any turbid medium. The following have been shown:

1. Liquid-crystal tunable filter spectral imaging is capable of intra-operatively acquiring autofluorescence and diffuse reflectance spectral images in a clinically viable timeframe with sufficient spectral contrast between normal cortex and tumor tissues for discrimination accuracy on par with traditional probe-based spectroscopy.
2. Posterior classification probabilities from the multi-variate MRDF-SMLS framework can be exploited to create diagnostic image maps with excellent spatial correlation of diagnostic regions as well as sensitivity and specificity for tumor demarcation, indicating significant promise as a tool for surgical resection guidance.
3. The inherent shift in excitation-collection geometry upon the transition from probe-based spectroscopy to non-contact spectral imaging induces a significant disparity in fluorescence and diffuse reflectance lineshapes between the two systems. While multi-patient clinical studies with probe-based spectroscopy are still useful to prove the principle that optical biopsy is capable of discriminating between normal and diseased tissue states or when spatial information is not required for clinical applicability, the lineshape disparity necessitates development of tissue discrimination algorithms specific to spectral imaging data via independent clinical study.
4. Large incident excitation angles have the potential to induce spectral distortions extrinsic to tissue optical properties when the sample albedo and/or anisotropy vary significantly across the spectral range of interest.

5. Relative to probe-based spectroscopy, spectral imaging tissue discrimination takes place in the face of several confounding factors: decreased signal-to-noise ratio due to significantly reduced excitation irradiances, loss of absolute intensity information, potential spectral distortion due to angular excitation-collection geometry and variable surface topography, crosstalk between pixels due to photon diffusion, and spectral information at fewer wavelengths.
6. Monte Carlo simulation is capable of accurately predicting fluorescence and diffuse reflectance spectra for any excitation-collection measurement geometry given a set of sample optical property spectra.

Future Directions

Given the limited patient population and restriction to cortical surface and surface-based tumor tissues in the preliminary clinical study, further research work is required to fully assess the capabilities of the imaging system for brain tumor and tumor margin demarcation. Alternative imaging interfaces must be investigated for improved positioning and versatility to gain better access to deep-seated white matter, margin tissues, and the walls of narrow resection cavities. Future clinical studies should focus on tissue discrimination at the tumor margins, with the hope that probing intrinsic tissue contrast will overcome limitations with current exogenous-contrast imaging methods and affect more complete brain tumor margin resection.

As mentioned in the introduction, the main limitation to 5-ALA fluorescence guided tumor resection was its lack of sensitivity at tumor margins due to an intact blood-brain barrier [4]. Since extent of margin resection has been repeatedly cited as the main prognostic factor for patient quality of life and mortality, the ultimate assessment for clinical utility of the LCTF spectral imaging system will be its sensitivity to the presence of diffuse tumor cells within the tumor margins. Because spectral imaging contrast with autofluorescence and diffuse reflectance derives from intrinsic changes in tissue structure and biochemistry with tumor invasion, it is not limited by the blood-brain barrier and has the potential to detect the presence of very low levels of infiltrating tumor cells. To determine the sensitivity of tumor demarcation to tumor invasion, spectral imaging diagnosis must be correlated to histological quantification of coalescent tumor cells in biopsy samples. A tumor invasion model which produces a gradient of tumor cell concentration between normal and tumor core tissue would be useful to quantify system

sensitivity. Understanding the basis behind the system sensitivity to tumor invasion and development of a tissue model to quantify that sensitivity would aide from a thorough understanding of the biological bases behind the spectral signature differences observed between normal and tumor tissues in the brain, a topic of imminent experimental investigation in this research project.

Once the accuracy and sensitivity of tumor margin demarcation is established retrospectively, the next logical step is to conduct a prospective study of the efficacy of brain tumor margin demarcation for surgical resection guidance. Unlike in a retrospective study, a prospective study asks neurosurgeons to make surgical decisions based upon spectral imaging diagnoses and tumor margin demarcation. Using the 5-ALA fluorescence guided resection study as a model, the study would correlate spectral image diagnosis to histopathological diagnosis of sample biopsies at tumor margins to determine the baseline diagnostic accuracy of spectral imaging during the study. Since tumor margins located near eloquent cortical areas cannot be resected for reasons of safety, the patient population can be stratified based upon the presence of residual margin tissue as predicted by spectral imaging. Extent of margin resection as predicted by spectral imaging could then be correlated to two endpoints, gadolinium contrast enhancement of tumor margins in post-operative MR images and patient survival time, to determine the benefit of spectral imaging guidance of tumor margin resection.

This study in this dissertation on the effects of incident excitation angle, emission collection angles, and sample optical properties focused solely on angular emission profile **shape**. However, results in that study from a Monte Carlo simulation of diffuse reflectance spectral imaging indicate that variations in angular emission profile **amplitude** with optical properties and incident excitation angle may induce distortions in spectral lineshape extrinsic to sample optical properties. Despite consistently Lambertian emission profiles independent of optical properties, incident excitation normal to the tissue surface and large-angle incident excitation with emission collected along the plane orthogonal to the polar angle of excitation produced disparate diffuse reflectance spectra. The underlying cause of this behavior obviously influences diffuse reflectance lineshape, could affect fluorescence lineshape as well, and should be examined in order to fully investigate the effects of spectral imaging excitation-collection geometry on measured lineshapes. Fortunately, Monte Carlo simulation data already exists from the previous study, from which absolute angular emission profiles can be constructed for

fluorescence and diffuse reflectance. Unfortunately, experimental data to validate these simulation results will prove to be difficult to obtain since careful attention must be paid to excitation irradiances, detection solid angles, and other details which can affect absolute measured intensities.

A significant future direction for any engineering system is improvement over time as the technology of different system components moves forward. One of the main areas of improvement for the liquid-crystal tunable filter spectral imaging system is imaging speed, which is dictated by collection sensitivity, excitation irradiances, and the number of wavelength interrogations necessary for diagnosis. Collection sensitivity of the imaging system can be improved as CCD technology advances with higher quantum yield chips and by incorporating the newest generation of liquid-crystal tunable filters with increased transmission capability. Excitation irradiances can be improved by using higher power excitation sources and liquid light guides with higher throughput. Most importantly, one of the reasons LCTF spectral imaging was chosen for clinical implementation was its random access filter tuning capability. As the diagnostic algorithm for accurate brain tumor margin demarcation is finalized, this capability will allow image acquisition at only those wavelengths which are deemed diagnostically significant and thus improve the imaging speed.

A second main area of improvement for the spectral imaging system is in its clinical interface, not only in terms of clinical convenience but also in terms of clinical versatility. The current system is attached to the side assembly of an operating microscope designed from ophthalmologic applications, requiring the neurosurgeon to stop the surgery, remove the neurosurgical microscope from the surgical field, and position the spectral imaging scope for image acquisition. A better interface for the spectral imaging system would be through direct incorporation into the neurosurgical microscope. Such an alternative was originally investigated by our research group with the imaging system coupled to the camera port of neurosurgical scope. However, a comparison between an interface at the camera port and the current interface with a direct view of the tissue surface realized a 30- to 40-fold increase in signal intensity with the direct view system due to greater solid angle of emission collection and a beamsplitter used to split the sample image between the neurosurgical microscope oculars and the camera port (Appendix B). Given the weak nature of tissue autofluorescence for macroscopic imaging, it was not feasible to acquire autofluorescence images within a reasonable timeframe with the

neurosurgical microscope interface. As the technology improves to allow better collection sensitivity and higher excitation irradiances, direct incorporation of LCTF spectral imaging into operating microscopes may become a possibility. In terms of clinical versatility, experience during the clinical tumor demarcation study revealed that excitation and collection at oblique angles from the optical axis of the operating microscope prevents illumination and visualization of tissue regions at the bottom or along the walls of deep resection cavities. While simply incorporating the spectral imaging system into the neurosurgical microscope which possesses greater freedom of movement than the ophthalmologic scope would ameliorate the problem, adding a contact-based fiber-optic probe or flexible endoscope for spectral acquisition (with or without spatial resolution) from these tissue regions would greatly improve the clinical versatility of the spectral imaging system.

The ultimate goal for spectral imaging development has always been to incorporate diagnostic spectral images into a surgical navigation system to allow tracking of resection instruments within diagnostic image space. Surgical navigation systems allow surgeons to dynamically correlate the position of anatomic structures within their visual field to features within images loaded into the surgical navigation platform. The most recent generation of neurosurgical microscopes have begun interfacing with surgical navigation systems to track the location of the microscope head in physical space, retrieve the relative position of the microscope focal plane, and extrapolate and display the position of the focal plane within the brain. Once direct incorporation of the spectral imaging system into the microscope is achieved, importing spectral images into the surgical navigation platform would be easily realized. However, while importing spectral images into the surgical navigation system would be useful to correlate features between spectral images and images from other modalities, the utility of surgical navigation with spectral images to may be diminished. Surgical navigation with MR and CT images is useful because features in CT/MR images do not visually resemble their physical counterparts. For spectral imaging, diffuse reflectance information can be easily used to construct images which resemble the visual appearance of tissue, as demonstrated in chapters 4 and 7. Therefore, assuming enough feature contrast in the diffuse reflectance image to localize and orient the spectral imaging field of view, correlating features in the diagnostic image to physical position along the brain tissue surface should be relatively straight-forward without the help of a surgical navigation system.

References

1. A.N. Yaroslavsky, et al, "Optical properties of selected native and coagulated human brain tissues in vitro in the visible and near infrared spectral range," Phys Med Biol **47**, 2059-73. (2002).
2. W.-C. Lin, et al, "In vivo brain tumor demarcation using optical spectroscopy," Photochem Photobiol **73**, 396-402. (2001).
3. S.C. Gebhart, et al. "Instrumentation considerations in spectral imaging for tissue demarcation: comparing three methods of spectral resolution," in *SPIE Photonics West, Spectral Imaging: Instrumentation, Applications, and Analysis III*, San Jose, CA, 2005: Bellingham, WA.
4. W. Stummer, et al, "Intraoperative detection of malignant gliomas by 5-aminolevulinic acid-induced porphyrin fluorescence," Neurosurgery **42**, 518-25; discussion 525-6. (1998).

APPENDIX A

INSTRUMENTATION CONSIDERATIONS IN SPECTRAL IMAGING FOR TUMOR DEMARCTION: COMPARING THREE METHODS OF SPECTRAL RESOLUTION

Abstract

Multiple methodologies exist to implement spectral imaging for tissue demarcation and disease diagnosis. In this paper, benchtop acousto-optic tunable filter (AOTF), liquid-crystal tunable filter (LCTF) and Fourier interferometric spectral imaging systems were quantitatively compared in terms of imaging speed of soft tissue autofluorescence. Optical throughput, image signal-to-noise ratio (SNR), and collagen autofluorescence imaging in chicken breast were assessed. Within this comparison, the Fourier system possessed the largest optical throughput (~50%) relative to the tunable-filter imaging systems; however, its throughput advantage failed to correlate to improved image SNR over the LCTF system. Further, while the autofluorescence imaging capability of the Fourier system exceeded that of the LCTF system for comparable total image integration times, the LCTF is capable of producing equivalent autofluorescence SNR with superior SNR when interrogations at only a few wavelengths are required and the random access filter tuning of the LCTF can be exploited. Therefore, the simple, rugged design and random-access filter-tuning capability of LCTF-based spectral imaging makes it best-suited for clinical development of soft tissue autofluorescence imaging.

Introduction

Optical spectroscopy, specifically combined fluorescence and diffuse reflectance spectroscopy, has been shown to discriminate between normal, neoplastic, and margin tissue in the brain and other organs [1-4]. Substantial work has been published expanding optical spectroscopy methods for spectral imaging development [5-19], but none have quantitatively addressed which spectral imaging modality is best-suited for tissue autofluorescence imaging in the operating room. We believe a spectral imaging system that acquires fluorescence and diffuse reflectance information can bolster brain tumor margin resection. However, given the multiple methodologies that exist to implement spectral imaging (e.g. tunable-filter, Fourier

interferometric, line-scanning, Hadamard transform), we sought to answer the outstanding question of "which modality?" before beginning clinical development.

The clinical utility of spectral imaging systems should be judged on two major criteria. First, to apply a diagnostic algorithm developed during a large clinical trial using a fiber-based, single-pixel spectroscopy system, spectral imaging must be capable of faithfully reproducing the fluorescence and diffuse reflectance spectra from the single-pixel system. Second, given the large cost associated with image acquisition time in the operating room, a premium is placed on the speed with which the system can image weak emission signals such as tissue autofluorescence while providing accurate spectral information for tissue diagnosis. While the factors that affect spectral line-shapes measured by non-contact imaging systems are currently under investigation by our research group, this paper seeks to quantitatively assess the imaging speed of a variety of spectral imaging systems.

The quantitative comparison in this paper is limited to imaging systems that resolve the wavelength dimension of the spectral image across acquisition of multiple CCD frames. These imaging systems can be grouped into two major categories – tunable-filter and Fourier interferometric systems – based upon how they resolve the spectral dimension. Tunable-filter based spectral imaging systems [11, 19, 20] directly parse the wavelength dimension of the spectral image between the CCD frames. They employ an electronically tunable bandpass filter, such as an acousto-optic tunable filter (AOTF) or a liquid-crystal tunable filter (LCTF), to diffract or pass, respectively, one band of the emission spectrum to the CCD camera at a time. Therefore, to build the spectral image, a frame of CCD data is acquired for each tuning wavelength of interest within the spectral image. The major drawback to tunable-filter systems is the inherent tradeoff between spectral resolution and system optical throughput. Since only one band of the collected emission is passed to the CCD camera at a time, the majority of collected emission is lost.

Liquid-crystal tunable filters are constructed from a stack of linear polarizers with interspersed layers of liquid crystals sandwiched between birefringent crystals. The retardance (R) of each stage, defined as the product of its thickness (d) and the difference between its ordinary (n_o) and extraordinary (n_e) indices of refraction – $R = d(n_o - n_e)$ – can be modulated by applying a voltage to the liquid crystal and changing its extraordinary index of refraction. Altering the stage's retardance affects the phase delay between the ordinary and extraordinary

light rays emerging from the stage, thereby changing its transmission (T) as a function of wavelength (λ) – $T = 0.5\cos^2(x)$ where $x = dR/\lambda$. The stage thicknesses (d) in the filter stack are often selected to produce a binary series of retardances such that all of the stages transmit the selected passband while destructive interference at the other wavelengths "trims" the stopband light. The number of stages employed in the filter (10 in current LCTFs) dictates the width of the passband and the degree of stopband attenuation.

Acousto-optic tunable filters apply radio-frequency (RF) acoustic waves to modulate the index of refraction of the filter crystal. If the incident wavelength satisfies a momentum-matching condition based upon the frequency of the RF wave, the linear polarization states of the incoming light are diffracted to the opposite state and the light is deflected upon its exit from the crystal, with two symmetrically diffracted passband beams and a transmitted zero-order stopband beam exiting the filter. Since the diffracted and zero-order beams must be separated in any type of imaging setup, the optical design of AOTF systems require either:

1) a long distance between the filter and CCD camera to allow physical separation of the diffracted and zero-order beams; or,
2) orthogonally oriented polarizers on either side of the filter to pre-polarize the input light and allow only the orthogonally oriented passband to reach the camera.

Although AOTF diffraction efficiency is on the order of 90-95% for pre-polarized input light (and 70% for unpolarized light), both beam separation solutions result in a loss of at least 50% of the light collected from the sample.

Fourier interferometric spectral imaging [13] indirectly resolves the spectral dimension of a spectral image by multiplexing the emission wavelengths. Rather than isolating and measuring individual spectral bands of a signal as tunable-filter systems do, multiplexing methods weigh the spectral components in groups using orthogonal basis functions and measure the total intensity of each weighted group. Measuring multiple spectral components simultaneously and back-calculating their intensities from the weighted measurements provides greater optical throughput than filter-based systems, ideally leading to a subsequent increase in SNR for equivalent integration times.

Fourier-based imaging systems use Michelson or Sagnac interferometers where the optical path difference (OPD) between two beams created and subsequently recombined by a 50/50 beamsplitter is varied between successive CCD frames. Varying the OPD modulates the

interference pattern seen by the CCD camera, building interferograms at each pixel as the OPD is shifted and the CCD frames are acquired. After complete image acquisition, each pixel interferogram represents the Fourier transform of the pixel spectrum and can be individually converted to such via the inverse Fourier transform. Employing a beamsplitter-based interferometer for multiplexing provides a theoretical system optical throughput of 50% over the entire spectrum.

The comparison in this paper was limited to three spectral imaging systems (Fourier, AOTF, and LCTF) which resolve the spectral dimension of the image across multiple CCD frames since all three require excitation of the entire sample surface during image acquisition. The three systems employed equivalent optics for sample excitation and emission collection and the same CCD camera for image acquisition. Experiments were designed to assess imaging speed in terms of optical throughput, image signal-to-noise ratio (SNR), and collagen autofluorescence imaging to determine which imaging system is most amenable to therapy guidance in the operating room.

Materials and Methods

In an effort to assess the spectral imaging modality most suitable for intraoperative brain tissue imaging, three benchtop spectral imaging systems were assembled and compared. The first system was based on a Fourier interferometry camera from Applied Spectral Imaging (Carlsbad, CA). The other two were tunable-filter based systems using a LCTF from CRI (Woburn, MA) and a Brimrose AOTF (Baltimore, MD), respectively. Given the ultimate goal of developing a clinical imaging system capable of rapidly imaging weak emission signals, the imaging system characteristics of most interest were: (1) optical throughput of the imaging system, where optical throughput refers to the fraction of light collected by the imaging system which is ultimately detected by the camera; (2) signal-to-noise ratio, defined as the ratio of the image intensity mean (signal) to its standard deviation (noise) at each wavelength; and (3) soft-tissue autofluorescence imaging capability. Experiments were first conducted at Oak Ridge National Laboratory to compare equivalent AOTF and LCTF imaging systems. Similar experiments were then performed at Vanderbilt University to compare Fourier and LCTF systems.

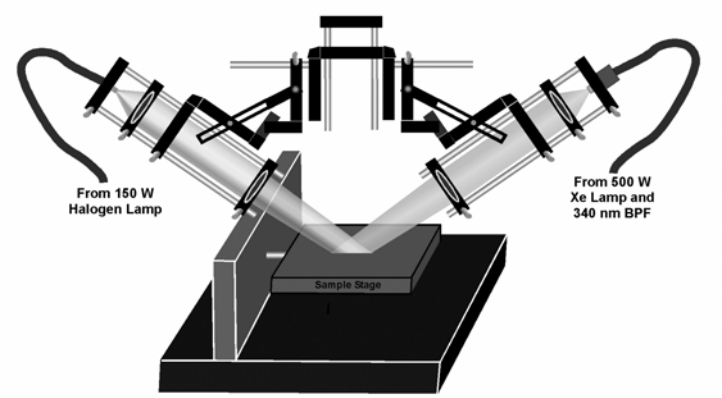

Figure 1. Schematic of excitation optics for comparison of benchtop spectral imaging system comparison.

Excitation Optics

To facilitate a direct and fair system comparison, the three imaging systems employed identical excitation optics (Figure 1) for fluorescence and diffuse reflectance excitation over the visible range of the spectrum (400 to 720 nm). The system consisted of separate legs for white light (diffuse reflectance) and ultraviolet illumination (fluorescence). For diffuse reflectance imaging, the broadband visible output from a 150 W halogen lamp was coupled into a 6 mm diameter liquid light guide (LLG). For fluorescence imaging, the broadband ultraviolet output from a Thermo-Oriel (Stratford, CT) 500 W Xe arc lamp reflected off a 280 nm dichroic mirror, passed through a 330-345 nm band-pass filter, and was coupled into another LLG. The large-diameter LLGs were chosen over fiber-optic light delivery to provide better coupling efficiency from the characteristically large lamp filaments of the illumination sources. Both illumination legs contained distal collimating and focusing lenses for practical adjustment of the illumination spot sizes on the sample. Illuminating the sample from roughly a 45º angle prevented specular reflectance of the white light and UV sources from entering the imaging systems.

Imaging Systems

AOTF vs. LCTF

Above the collection optics, an acousto-optic tunable filter (TEAF 10-0.45-0.70-S) was sandwiched between two orthogonally oriented polarizers and followed by an iris diaphragm (Figure 2a) for maximum rejection of the zero-order (stopband) image. The filter possessed a peak diffraction efficiency of 90-95% of pre-polarized light and an operating spectral range

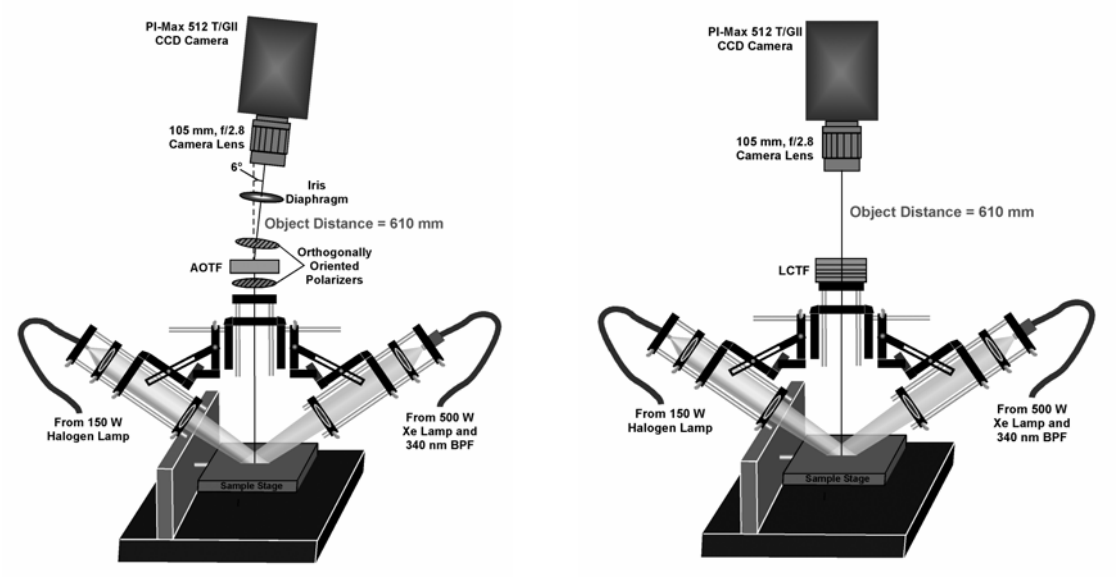

(a) **(b)**

Figure 2. Schematics of benchtop (a) acousto-optic and (b) liquid-crystal tunable-filter spectral imaging systems constructed at Oak Ridge National Laboratory.

between 450 and 700 nm. The optics distal to the AOTF were oriented at a 6º angle relative to the central axis of the AOTF to direct the diffracted beam to an intensified CCD camera (Princeton Instruments, PI-Max 512 T/GII, Trenton, NJ). The beam was collected by a 105 mm, f/2.8 camera lens (Nikon) and focused onto a 512 x 512 array of 19 μm square pixels. The camera was thermoelectrically cooled to -20ºC during all measurements. With this configuration, the sample stage was located roughly 610 mm (24 in.) from the camera lens.

For the LCTF setup (Figure 2b), the camera and lens were aligned with the aperture of the liquid-crystal tunable filter (VariSpec VIS). The filter possessed a maximum passband transmission of pre-polarized light equal to 60% with a spectral range of 400 to 720 nm. For comparison sake, the collection lens was maintained at an object distance of 610 mm from the sample.

Fourier vs. LCTF

An 80 mm, f/3.5 camera lens (Sigma) was attached to a commercially available Fourier Sagnac-interferometric imaging system (SpectraCube) and aligned with the center of the excitation optics (Figure 3a). The imaging system had an operating spectral range between 350

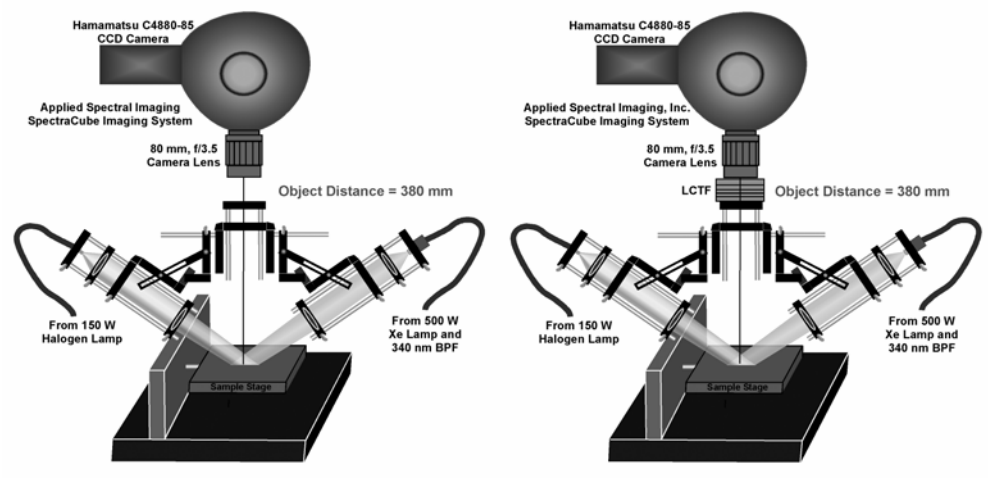

Figure 3. Schematics of benchtop (a) Fourier and (b) liquid-crystal tunable-filter spectral imaging systems constructed at Vanderbilt University.

and 1100 nm and a 656 x 494 array of 9.9 μm square pixels (Hamamatsu, C4880-85). The system possessed an object distance between sample and lens of roughly 380 mm (15 in.).

To acquire a direct comparison of the LCTF and Fourier imaging systems using the same collection optics, CCD camera, and object distance, the direct-image mode of the SpectraCube system was exploited for LCTF imaging. The tunable filter was placed in front of the 80-mm collection lens (Figure 3b) and the SpectraCube controller program was used to acquire a 16-bit TIFF image at each tuning wavelength to build the LCTF spectral image.

Comparison Experiments

AOTF vs. LCTF

Relative optical throughput measurements were performed between the imaging systems by acquiring spectral images of a 99% reflectance standard under white-light excitation and comparing the mean image intensities over consistent 25 x 25 pixel regions. Images were acquired for each system with a 1-second integration time at each tuning wavelength across the spectral range of each filter. Signal-to-noise ratios (SNR) were calculated across the same 25 x 25 pixel regions, where the SNR was defined as the ratio of the mean image region intensity to its standard deviation (i.e. 1/COV) at each tuning wavelength. While small regions were utilized to minimize the effect of non-uniform illumination on the intensity standard deviation, it should be noted that any illumination variations were consistent between the two systems.

To assess the autofluorescence imaging capability of the systems, and to correlate this capability to their relative optical throughput and image SNR, fluorescence images of chicken breast and adipose tissue were acquired. Chicken tissue was chosen as the soft-tissue phantom for two reasons: 1) its collagen autofluorescence peaks around 510 nm, which falls within the tuning range of the Brimrose AOTF, and 2) strict guidelines at Oak Ridge National Laboratory prohibited the use of *ex vivo* animal or human tissues in laboratory experiments without an arduous approval process.

Ten images at 2-second integration per image were acquired at each tuning wavelength to give a total integration time of 20 s per wavelength. The wavelength was varied across the individual spectral ranges of the filters in 10 nm increments, except around the expected collagen fluorescence peak (λ = 510 nm) where a sampling of 2 nm was used. Baseline corrections were applied to the images and the mean spectral intensity at each pixel was calculated for grayscale image display. Representative fluorescence spectra were then calculated from three 15 x 15 pixel image regions corresponding to chicken muscle tissue, chicken adipose tissue, and background emission outside the illumination area. Signal-to-noise ratios were calculated for the three regions at the wavelengths of peak fluorescence emission.

Fourier vs. LCTF

Optical throughput measurements were performed between imaging systems by acquiring spectral images of a 99% reflectance standard under combined halogen- and xenon-lamp (with the bandpass filter removed) excitation. To obtain a true optical throughput measurement of the LCTF as a function of wavelength, a 200 x 200 pixel Fourier spectral image of the reflectance standard was acquired without the LCTF in place using a 20-ms integration time per frame, acquiring 2330 frames with 3 interferometer steps between frames. With the LCTF replaced along the collection leg, similar Fourier images were acquired with the same interferometer and integration settings for tuning wavelengths from 400 to 720 nm in 10 nm increments. The optical throughput (T) for each tuning wavelength of the LCTF was computed at each pixel in the image using

$$T = \frac{1}{\sum_{i=1}^{N} (\Delta\lambda)_i} \sum_{i=1}^{N} (\Delta\lambda)_i \frac{(I_{filter})_i}{(I_{100\%})_i}, \quad (1)$$

where N is the number of wavelengths in the Fourier spectral image, $(\Delta\lambda)_i$ is the mean wavelength spacing between λ_{i-1}, λ_i, and λ_{i+1}, $(I_{filter})_i$ is the spectral intensity at the ith wavelength in the Fourier image with the LCTF in place, and $(I_{100\%})_i$ is the spectral intensity at the ith wavelength in the Fourier image with the LCTF removed. The optical throughput was calculated for and averaged over every pixel within the 200 x 200 image and the mean-throughput calculation process was repeated for every LCTF tuning wavelength.

To measure the optical throughput of the Fourier system as a function of wavelength, 200 x 200 pixel, 16-bit TIFF images of the 99% reflectance standard were acquired using direct-imaging mode (i.e. no fringes) with the LCTF in place and tuned to 400 to 720 nm in 20 nm increments. The integration times varied between 75 and 1000 ms depending upon the transmission of the LCTF to acquire adequate signal for the 100% throughput measurements. At each LCTF tuning wavelength, the fringe position was manually adjusted to the positions used during Fourier spectral imaging to build the interferogram. With the SpectraCube controller program set to fringe mode, sixty-four fringe frames were manually exported to 16-bit TIFF images with 40 interferometer steps between frames. The optical throughput (T) of the Fourier interferometer for each LCTF tuning wavelength was computed at each pixel in the image using

$$T = \frac{\frac{1}{N}\sum_{i=1}^{N=64}\left(I_{fringe}\right)_i}{I_{100\%}}, \tag{2}$$

where $N = 64$ is the number of fringe images acquired at each LCTF tuning wavelength, $(I_{fringe})_i$ is the spectral intensity at the pixel of interest in the ith fringe image, and $(I_{100\%})_i$ is the spectral intensity at the pixel of interest in the 100% direct-mode image. For each tuning wavelength, the optical throughput was calculated for and averaged over every pixel within the 200 x 200 image.

To calculate the image SNR of the LCTF and Fourier imaging systems for the same emission input, spectral images were acquired of the 99% reflectance standard using equivalent total image acquisition times. LCTF frames were acquired as 16-bit TIFF images with 21-ms integration per frame using the direct-imaging mode of the SpectraCube controller software at tuning wavelengths of 400 to 720 nm in 10 nm increments. To achieve equivalent spectral sampling, spectral resolution, and total image integration time, a Fourier spectral image was acquired using 231 frames, 30 interferometer steps between frames, and 3 ms integration per frame. SNR metrics were calculated for both imaging systems across 25 x 25 pixel regions in the

middle of the images. Similar to the AOTF/LCTF comparison, the SNR was defined as the ratio of the mean image region intensity to its standard deviation (i.e. 1/COV).

To assess the autofluorescence imaging capability of the systems, and to correlate this capability to their optical throughput and image SNR, fluorescence images of chicken breast and adipose tissue were acquired. The spectral sampling and interferometer settings for the two systems were maintained from the SNR measurements and the total spectral image integration time for was held constant at 330 s (1430 ms per frame for Fourier, 10 s per tuning wavelength for the LCTF) for comparison purposes. A major advantage of LCTF imaging is the random-access tuning capability of the LCTF allows the system to only interrogate the wavelengths necessary for tissue diagnosis. To compare Fourier and LCTF imaging when only 3 wavelengths are required for tissue diagnosis, an additional Fourier image with a 30 s total integration time was acquired. Baseline corrections were applied to the three images and the mean spectral intensity at each pixel was calculated for grayscale image display. Representative fluorescence spectra were then calculated from three 25 x 25 pixel image regions corresponding to chicken muscle tissue, chicken adipose tissue, and background emission outside the illumination area. Signal-to-noise ratios were calculated for the three regions at the wavelengths of peak fluorescence emission.

Results

AOTF vs. LCTF

The relative optical throughput measurements from the benchtop AOTF and LCTF spectral imaging systems (Figure 4) demonstrate that the mean image intensity of the LCTF was consistently higher than the AOTF. While the throughput of both filter systems peaked in the red and bottomed out in the blue regions of the visible spectrum, the AOTF throughput possessed a dynamic range of 100 while the LCTF throughput possessed a larger dynamic range of 250. The ratio of the LCTF throughput to the AOTF throughput was lowest at 504 nm, due to a resonance-type transmission for the AOTF at that wavelength, and highest at 470 nm due to a sharp drop in AOTF throughput below 500 nm. It should be noted that the dynamic range in optical throughput for the systems incorporates the spectral variation in excitation intensity and CCD quantum efficiency.

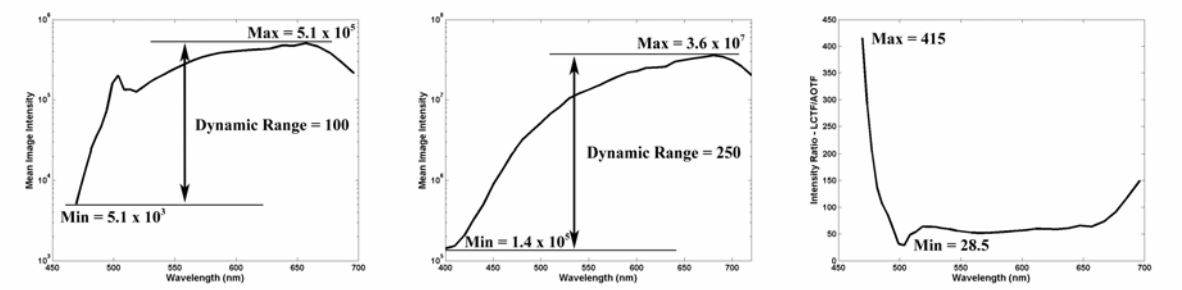

(a) **(b)** **(c)**

Figure 4. Relative optical throughput measurements for the benchtop (a) AOTF and (b) LCTF spectral imaging systems constructed at Oak Ridge National Laboratory. (c) Throughput advantage for LCTF imaging over the AOTF.

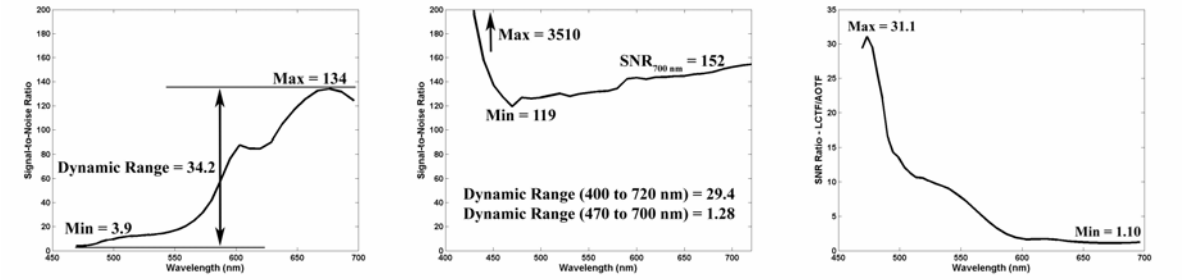

(a) **(b)** **(c)**

Figure 5. Signal-to-noise ratio (SNR) measurements for the benchtop (a) AOTF and (b) LCTF spectral imaging systems constructed at Oak Ridge National Laboratory. (c) SNR advantage for LCTF imaging over the AOTF.

The signal-to-noise ratio measurements from the tunable-filter imaging systems (Figure 5) demonstrate that the larger throughput of the LCTF results in larger signal-to-noise ratio than the AOTF. While the shape of the AOTF SNR and the LCTF-advantage spectra correlate reasonably well with their respective throughput spectra, the LCTF SNR is fairly constant over the 470 to 700 nm spectral range, regardless of 14-fold increase in throughput, and the maximum LCTF SNR occurs at the wavelength with the lowest throughput. These and several other behaviors within the SNR results suggest a curious relationship between system throughput and image signal-to-noise ratio which will be discussed in the next section.

Within the collagen autofluorescence images (Figure 6), both tunable-filter systems show fluorescence peaks between 500 and 520 nm where expected. However, the AOTF mean spectra are dominated by the throughput resonance of the filter at 504 nm while the fluorescence peaks of the LCTF spectra are significantly wider and red-shifted by ~15 nm. As expected from the SNR and throughput advantages of the LCTF over the AOTF (63.7-fold throughput and 10.6-fold SNR at 518 nm), the autofluorescence image from the LCTF system possesses higher image

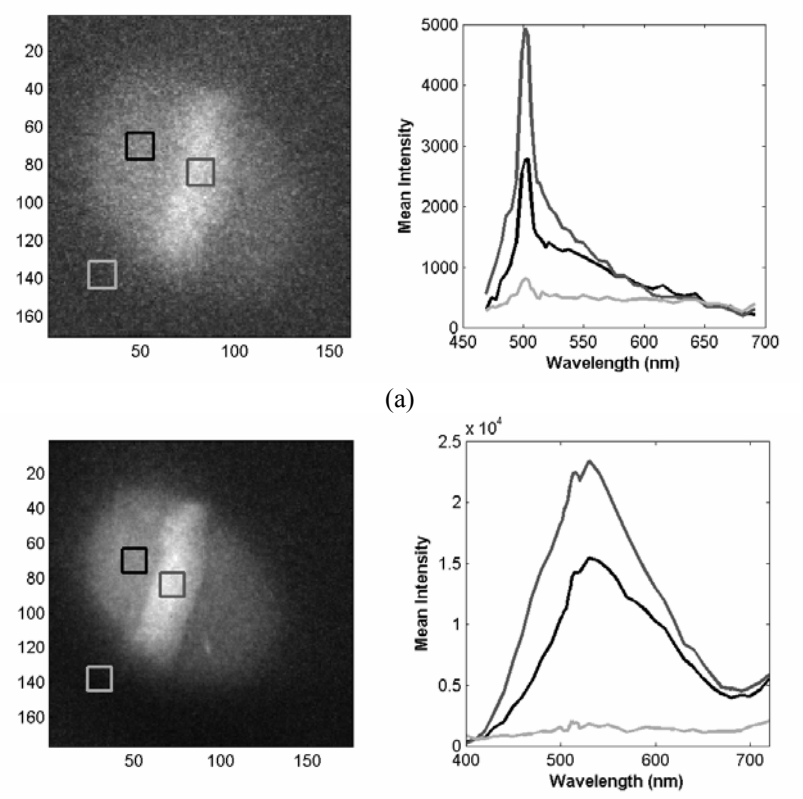

Figure 6. Autofluorescence images of chicken breast from the (a) AOTF and (b) LCTF imaging systems with mean spectra from regions corresponding to background, muscle (black), and adipose tissue.

Table 1. Signal-to-noise ratios for tunable-filter autofluorescence images of chicken muscle, adipose tissue, and background.

	AOTF			LCTF		
	Signal	**Noise**	**SNR**	**Signal**	**Noise**	**SNR**
Muscle	2788	413.2	**6.75**	15456	1109.4	**13.9**
Fat	4937	596.5	**8.28**	23427	1978.1	**11.8**
Background	797.9	287.0	**2.78**	1805.6	693.52	**2.60**

intensities than the AOTF with equivalent background noise between the two. The signal-to-noise ratios at the fluorescence peaks (Table 1) further underscore the superior autofluorescence imaging capability of the LCTF system.

Fourier vs. LCTF

The optical throughput measurements from the benchtop Fourier and LCTF spectral imaging systems (Figure 7) demonstrate that the Fourier system enjoys a considerable throughput advantage over the LCTF. As expected from a beamsplitter-based interferometer, the Fourier throughput was consistently near 50% with slightly lower values in the blue region of the

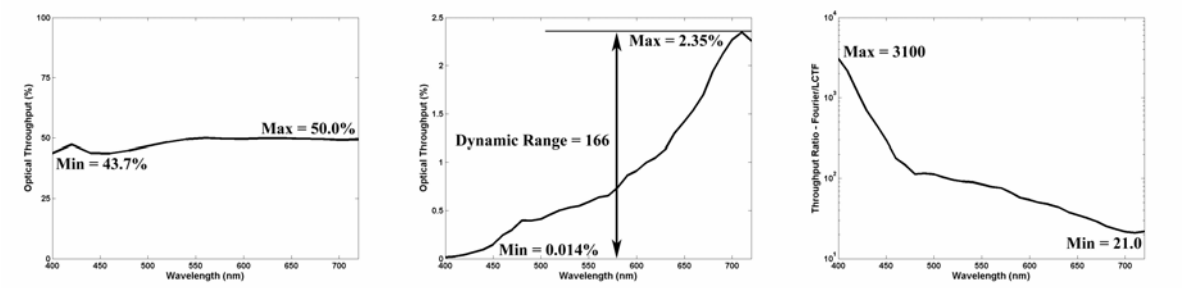

(a) **(b)** **(c)**

Figure 7. Optical throughput measurements for the benchtop (a) Fourier and (b) LCTF spectral imaging systems constructed at Vanderbilt University. (c) Throughput advantage for Fourier imaging over the LCTF.

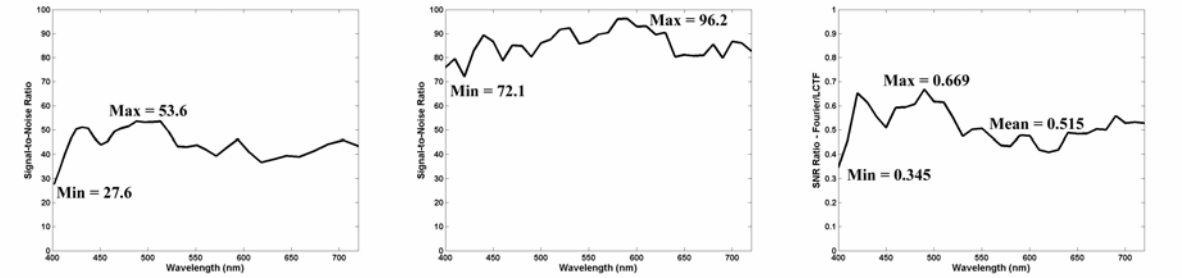

(a) **(b)** **(c)**

Figure 8. Signal-to-noise ratio (SNR) measurements for the benchtop (a) Fourier and (b) LCTF spectral imaging systems constructed at Vanderbilt University. (c) SNR advantage for Fourier imaging over the LCTF.

spectrum. The LCTF throughput possessed a dynamic range of roughly 150-fold that was lowest at 400 nm and peaked at 2.65% at 710 nm. As such, the throughput advantage for the Fourier system was greatest at 400 nm (3100-fold) and lowest in the red region (21-fold).

The signal-to-noise ratio measurements from the two imaging systems (Figure 8) demonstrate that while the Fourier system possesses a considerable throughput advantage over the LCTF, it does not correlate to an advantage in SNR. The SNR for both systems were relatively consistent with wavelength, varying less than two-fold between their maximum and minimum values. However, the SNR of the LCTF system averaged twice as large as the Fourier SNR. Consistent with the AOTF-LCTF comparison the large dynamic range of the LCTF throughput failed to correlate to a large dynamic range in SNR. Contrary to the AOTF-LCTF results, the SNR for the LCTF below 450 nm was consistent with the other tuning wavelengths.

The three autofluorescence spectral images (Figure 9) of chicken breast show fluorescence peaks around 520 nm. Due to the equivalent spectral resolutions of the two systems, the fluorescence peaks have roughly the same width for all three images, but the LCTF peaks are slightly red-shifted. As expected from the throughput advantage of the Fourier interferometer, the grayscale Fourier autofluorescence image after 330 s integration (Figure 9a) possesses

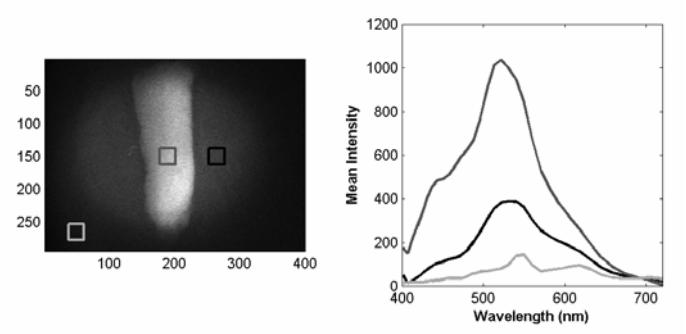

(a)

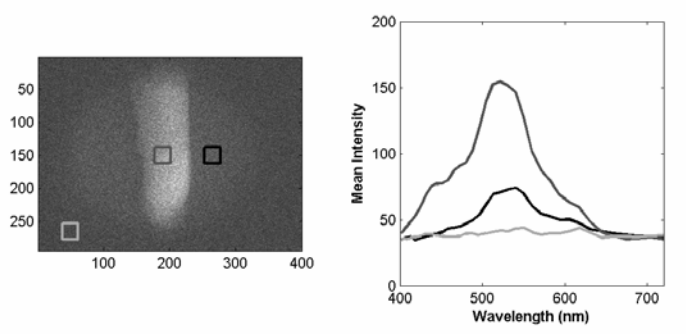

(b)

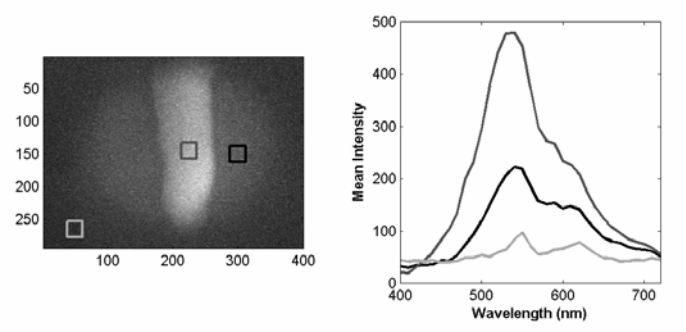

(c)

Figure 9. Autofluorescence images of chicken breast from the (a,b) Fourier and (c) LCTF imaging systems with mean spectra from regions corresponding to background, muscle (black), and adipose tissue. Images (a) and (c) were acquired with 330 s total integration times while image (b) was acquired with a 30 s integration time.

Table 2. Signal-to-noise ratios for Fourier and LCTF autofluorescence images of chicken muscle, adipose tissue, and background.

	Fourier (330 s integration)			Fourier (30 s integration)			LCTF		
	Signal	Noise	SNR	Signal	Noise	SNR	Signal	Noise	SNR
Muscle	391	34.1	**11.5**	74.5	34.1	**2.18**	222	32.6	**6.82**
Fat	1039	96.5	**10.8**	155	39.3	**3.95**	480	42.7	**11.2**
Background	81.6	24.8	**3.29**	41.8	26.3	**1.59**	82.6	30.3	**2.73**

superior clarity and higher image intensities than the LCTF image (Figure 9c) for equivalent levels of background noise. However, there appears to be no considerable difference in spectral quality, consistent with the SNR results. Further, reducing the integration time for the Fourier system to 30 s, equal to the LCTF integration for three wavelengths, creates an image with lower

quality than the LCTF image and reduces the spectral intensities below the LCTF spectra. The signal-to-noise ratios at the fluorescence peaks (Table 2) for the three images further underscore these results.

Discussion

The optical throughput, image signal-to-noise ratio, and collagen autofluorescence imaging experiments were designed to assess the relative speed with which three different spectral imaging systems were capable of capturing high-quality soft-tissue autofluorescence images. The relative optical throughput comparison between the tunable-filter imaging systems was designed to measure the relative amounts of light that reach the CCD camera under consistent imaging conditions (e.g. excitation irradiance, sample emission, integration time). This throughput is affected by three aspects of the system: 1) the peak transmission of the filter at the tuning wavelength, 2) the passband width (i.e. full width at half maximum – FWHM) of the filter, and 3) light lost via the other optical components. Therefore, while the AOTF is known to possess a higher peak transmission than the LCTF for similarly polarized light, the throughput advantage of the LCTF seen in this comparison must be due to the other two sources of throughput loss.

There is an inherent tradeoff between the spectral resolution of the individual filters and the light throughput of the filter that skews the throughput results toward a filter with a broader passband. The FWHM of the LCTF passband is nominally 20 nm at 550 nm and monotonically increases quadratically with wavelength across the spectral range of the filter. Combining this with a peak transmission that is higher in the red region than in the blue explains the 150-fold dynamic range measured for the LCTF throughput. The passband width of the AOTF varies from 1.7 to 6.2 nm across its spectral range while its peak transmission varies between 70% and 90% for polarized light. The increased spectral resolution of the LCTF increases the spectral range and amount of light admitted to the camera relative to the AOTF, giving it an unfair advantage in such a comparison.

Modeling the normalized passband transmission (i.e. without the effect of peak transmission) as a Gaussian function and integrating it over wavelength, the ratio of light passed by the LCTF to that diffracted by the AOTF is equal to the ratio of their passband FWHM values (derivation not shown). While the multiplicative nature of a correction for this effect would not

change the signal-to-noise ratio metrics (i.e. the mean and standard deviation of the intensities would be equally modulated and would therefore cancel in the COV calculation), the mean intensity data of the images should be normalized for the higher spectral resolution of the LCTF. To correct the relative throughput for spectral resolution, the advantage values (Figure 4c) should be divided by $FWHM_{LCTF}$ / $FWHM_{AOTF}$ at each wavelength. However, the maximum dispersion ratio is only 20.2 ($FWHM_{AOTF}$ = 1.7, $FWHM_{LCTF}$ = 34.3 at 720 nm) while the minimum throughput advantage is 28.5. Given the intensity ratio of 31.4 at 500 nm and that $FWHM_{LCTF}$ = 16.5 mm at that wavelength, the LCTF throughput advantage is at least 9.7 near the collagen autofluorescence peak. Similarly, after spectral resolution correction at 700 nm, the LCTF throughput advantage is reduced (at most) from 150 to 7.9. Therefore, while the respective spectral resolution values for the two filters explains part of the LCTF throughput advantage, the remainder must be due to light lost at the polarizers and iris diaphragm of the AOTF imaging system when blocking the stopband image.

Spectral resolution correction is not necessary for the LCTF vs. Fourier comparison since the Fourier system accepts all wavelengths of light simultaneously with a beamsplitter which sends half of the collected light to the CCD camera and the other half back toward the sample. Therefore, no tradeoff exists between its spectral resolution and the amount of light detected by the camera. However, the Fourier throughput was consistently less than the expected 50% in the blue region of the spectrum. While the exact reason for this behavior is unknown, it may relate to the number of interferometer steps (30) between frames used during the throughput measurement. The separation between interferogram fringes for light in the blue region is roughly 100 interferometer steps while the separation in the red region is 180 steps. Therefore, using 30 steps between frames provides fewer than 4 samples per fringe in the blue region, as opposed to the six samples per fringe in the red region, and could result in throughput underestimation.

While an advantage in optical throughput for a given imaging system was expected to produce a corresponding advantage in image signal-to-noise ratio and thus superior autofluorescence images, the relationships between the three gauges of imaging speed were not so straightforward. However, a Fourier throughput advantage over the LCTF that averages 300 over the spectral range of the filter produces a two-fold *dis*advantage in image signal-to-noise

ratio. Further, the SNR of the LCTF imaging system peaks for a tuning wavelength of 400 nm where the imaging system possesses the smallest throughput.

A possible explanation for the disadvantage in Fourier SNR relative to the LCTF is disparate interferogram sampling between pixels within the Fourier image. The interferometry fringes run vertically along the columns of the spectral image such that each column within a fringe image corresponds to a unique position within the interferogram. This disparity in starting position within the interferogram produces unique interferogram sampling and multiplexing schemes for each column as the interferograms are built. This in turn creates small changes in the pixel spectra, thereby reducing the Fourier signal-to-noise ratio. Oversampling the interferogram with a large number of frames and small number of steps between frames could help minimize the disparity in sampling with spatial position; however, to maintain a consistent total image integration time, the integration time per frame must be proportionally decreased and could exacerbate the effects of readout noise from the CCD camera on the image spectra. Since 30 interferometer steps between frames were used for the Fourier SNR and autofluorescence imaging measurements, this same effect could be responsible for the qualitatively similar image spectra and spectral SNR between the LCTF and Fourier systems.

For the SNR measurements, 1000 LCTF acquisitions with 1 ms integration times were acquired to accrue the 1 second total integration time per wavelength. Given the 250-fold reduction in optical throughput of the LCTF from the red to the blue regions of the spectrum, the mean intensity for each acquisition decreases from 36,000 to 140 across the same range. If the readout noise is directly and asymptotically related to the pixel intensity, one can imaging that the low intensities at 400 nm would create less readout noise with correspondingly increased signal-to-noise ratios, producing a curve similar in shape to the one in Figure 5b. Whatever the cause for this anomalous increase in SNR at the wavelength of minimum throughput, the robustness of the SNR and throughput measurements would be improved by acquiring and subtracting a baseline measurement from the spectral images. While no ambient light was present during image measurement, such a correction would remove the effects of camera dark current which could be substantial at wavelengths with lower throughput.

A major drawback to any filter-based imaging system is the inherent trade-off between the system's optical throughput and its spectral resolution. The transmission of liquid-crystal devices ranges from 5% (at 400 nm) to 60% (at 700 nm) of pre-polarized light across the visible

spectrum. Throughput can be improved by increasing the spatial resolution (commercially available at different resolution settings), but could result in "spectral distortion" in the form of low-pass filtering if trying to resolve narrow emission peaks. While the AOTF has increased transmission rates of pre-polarized light, an AOTF spectral imaging system must separate the stopband and passband beams. Using orthogonally oriented polarizers to create a single passband diffraction beam and block the stopband beam automatically decreases the beam signal by 50% and may require an additional iris diaphragm to complete the job since the stopband beam intensity dwarfs the passband. Using increased path length for physical beam separation only collects one of the passband beams (loss of 50%) and decreases the solid angle of the detector with respect to the emission source. Given these constraints, the throughput of an LCTF spectral imaging system is superior to AOTF imaging given the less than two-fold differences in peak transmission, the larger LCTF passbands available, and the lack of constraints on object distance and separation between the filter and CCD camera.

The advantage to LCTF spectral imaging system over Fourier imaging is the simplicity in optical design and system control. The system requires only a camera lens to focus the transmitted light onto the CCD focal plane with no worry about moving parts or the vibration artifacts they may cause. While the system comparison in this paper maintained a constant image integration time, considerable overhead is expended in Fourier spectral image acquisition time for spectral extraction using the inverse fast Fourier transform at every spatial pixel within the image. This process requires N^2 additions or multiplications at each pixel for N interferogram frames, a process that can become computationally intensive for a highly resolved image. While the LCTF system possessed no post-processing computational cost, the Fourier system required approximately 3 seconds to extract the pixel spectra from a 512 x 512 image zero-padded to 128 samples, further offsetting its throughput advantage. Also, the relationship between interferogram and spectral sampling is not intuitive, to the point where we found that certain combinations of interferogram sampling parameters lead to incomplete spectra or images which contain spatial harmonics running vertically across the final spectral image. Foremost, as seen in these experiments, variations in interferogram sampling between columns in the image create small changes in the image spectra, and Fourier imaging must acquire full spectral image information rather than interrogating only the wavelengths required for tissue diagnosis. Assuming that only 2 to 3 wavelengths are needed across a fluorescence spectrum, the

interrogation time for LCTF imaging can be increased 10 to 15 times per interrogation to partially offset the Fourier throughput advantage and produce higher signal-to-noise ratios.

Conclusion

One of the main challenges facing any autofluorescence spectral imaging system will be to achieve adequate signal-to-noise ratio with sufficient imaging speed. Addressing this challenge, the results outlined in this paper highlight advantages of the LCTF spectral imaging system over equivalent AOTF and Fourier systems. The LCTF enjoys increased relative optical throughput and SNR over the AOTF with a significant edge in the blue region of the visible spectrum. These advantages yield superior autofluorescence imaging capability and LCTF spectra with higher image SNR at the collagen autofluorescence peak. Conversely, while the Fourier system possessed a throughput advantage of roughly 100-fold over the LCTF system in the 500 nm region, the average LCTF SNR from 400 to 720 nm was twice that of the Fourier system, and tissue images with equivalent integration times produced qualitatively similar results. Moreover, random access filter tuning by the LCTF system allows interrogation to be limited to the wavelengths required for tissue diagnosis, thereby increasing the allowable integration time per interrogation. Dividing the total LCTF image integration time between three wavelengths overcomes the throughput advantage of the Fourier system, producing autofluorescence images with higher spectral intensities and SNR values at the autofluorescence peak. Based on these results, our research group believes that of the three imaging systems compared in this paper, LCTF spectral imaging is best-suited for autofluorescence imaging.

Acknowledgements

We would like to thank Oak Ridge National Laboratory for allowing us to perform the comparison of tunable-filter spectral imaging systems, the entire laboratory of Tuan Vo-Dinh for their help with those experiments, and the National Institutes of Health for their financial support of this research [RO1 Grant CA85989].

References

1. I.J. Bigio and S.G. Bown, "Spectroscopic sensing of cancer and cancer therapy: current status of translational research," Cancer Biol Ther **3**, 259-67 (2004).

2. N. Ramanujam, "Fluorescence spectroscopy of neoplastic and non-neoplastic tissues," Neoplasia **2**, 89-117. (2000).

3. R. Richards-Kortum and E. Sevick-Muraca, "Quantitative optical spectroscopy for tissue diagnosis," Annu Rev Phys Chem **47**, 555-606 (1996).

4. K. Sokolov, M. Follen, and R. Richards-Kortum, "Optical spectroscopy for detection of neoplasia," Curr Opin Chem Biol **6**, 651-8 (2002).

5. S. Andersson-Engels, et al, "Preliminary evaluation of two fluorescence imaging methods for the detection and the delineation of basal cell carcinomas of the skin," Lasers Surg Med **26**, 76-82 (2000).

6. C.S. Betz, et al, "Autofluorescence imaging and spectroscopy of normal and malignant mucosa in patients with head and neck cancer," Lasers Surg Med **25**, 323-34 (1999).

7. B.W. Chwirot, et al, "Detection of melanomas by digital imaging of spectrally resolved ultraviolet light-induced autofluorescence of human skin," Eur J Cancer **34**, 1730-4. (1998).

8. M.A. D'Hallewin, L. Baert, and H. Vanherzeele, "Fluorescence imaging of bladder cancer," Acta Urol Belg **62**, 49-52. (1994).

9. J. Hewett, et al, "The application of a compact multispectral imaging system with integrated excitation source to in vivo monitoring of fluorescence during topical photodynamic therapy of superficial skin cancers," Photochem Photobiol **73**, 278-82. (2001).

10. C.C. Hoyt, et al, "Remote biomedical spectroscopic imaging of human artery wall," Lasers Surg Med **8**, 1-9 (1988).

11. O. Khait, S. Smirnov, and C.D. Tran, "Multispectral imaging microscope with millisecond time resolution," Anal Chem **73**, 732-9. (2001).

12. B.L. McClain, J. Ma, and D. Ben-Amotz, "Optical Absorption and Fluorescence Spectral Imaging Using Fiber Bundle Image Compression," Applied Spectroscopy **53**, 1118-1122 (1999).

13. K. Potter, et al, "Imaging of collagen and proteoglycan in cartilage sections using Fourier transform infrared spectral imaging," Arthritis Rheum **44**, 846-55. (2001).

14. J.N.Y. Qu, H.P. Chang, and S.M. Xiong, "Fluorescence spectral imaging for characterization of tissue based on multivariate statistical analysis," Journal of the Optical Society of America a-Optics Image Science and Vision **19**, 1823-1831 (2002).

15. N. Ramanujam, et al, "Fast and noninvasive fluorescence imaging of biological tissues in vivo using a flying-spot scanner," IEEE Trans Biomed Eng **48**, 1034-41. (2001).

16. G. Siboni, et al, "Spectral imaging of MC540 during murine and human colon carcinoma cell differentiation," J Histochem Cytochem **49**, 147-53. (2001).

17. M.G. Sowa, et al, "Visible-near infrared multispectral imaging of the rat dorsal skin flap," Journal of Biomedical Optics **4**, 474-481 (1999).

18. C.A. Spibey, P. Jackson, and K. Herick, "A unique charge-coupled device/xenon arc lamp based imaging system for the accurate detection and quantitation of multicolour fluorescence," Electrophoresis **22**, 829-36. (2001).

19. C.D. Tran, "Development and analytical applications of multispectral imaging techniques: an overview," Fresenius J Anal Chem **369**, 313-9. (2001).

20. C. Balas, "A novel optical imaging method for the early detection, quantitative grading, and mapping of cancerous and precancerous lesions of cervix," IEEE Trans Biomed Eng **48**, 96-104. (2001).

APPENDIX B

COMPARISON OF MEASURED INTENSITIES BETWEEN MICROSCOPE-COUPLED AND DIRECT-VIEW SPECTRAL IMAGING SYSTEMS

Motivation

The original proposal for this dissertation outlined a clinical interface in which the liquid-crystal tunable filter spectral imaging system is directly coupled to the camera port on the Zeiss operating microscope that neurosurgeons at Vanderbilt University Medical Center employ during tumor resection surgery. Direct coupling to the microscope aligns the imaging and microscope fields of view for streamlined diagnostic imaging and minimal disruption to the surgical procedure. While the spectral imaging system described in this dissertation is coupled to a Wild-Heerbrugg operating microscope, the Wild operating microscope is designed for ophthalmologic applications and is not employed during brain tumor resection surgery. This creates a more cumbersome spectral imaging implementation since the neurosurgical microscope must be removed from the surgical field, the Wild microscope wheeled into its place, and the tissue target of interest re-localized with the oculars before spectral image acquisition is possible. This unwieldy protocol for spectral image acquisition reduces its efficiency, making neurosurgeons less likely to exploit the capabilities of spectral imaging diagnosis.

Methods

A direct-view system coupled to the side assembly of a separate microscope was ultimately chosen for clinical implementation based upon a quantitative comparison of imaging speeds between such a system and one coupled to the camera port of a Zeiss operating microscope. The direct-view system (Figure 1a) consisted of the VIS-20 liquid-crystal tunable filter connected to the variable focal-length camera lens and PhotonMax CCD camera. The system was supported by an aluminum arm connected to the top of a standard optical table, creating a 90° angle between the optical axis of the imaging system and the table surface. The microscope-coupled system (Figure 1b) was connected to the camera port of a Zeiss OPMI Vario/NC2 operating microscope outfitted with f170 oculars. The VIS-20 tunable filter was mounted between the microscope camera port and an 85-mm focal length camera adapter. The

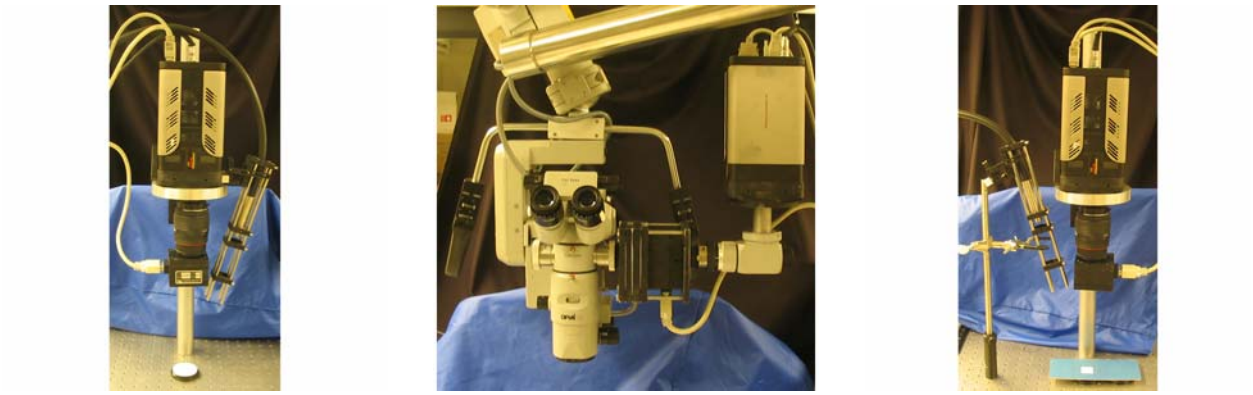

(a) **(b)** **(c)**

Figure 1. (a) Direct-view and (b) microscope-coupled LCTF spectral imaging systems. (c) Experimental setup for quantitative comparison between interfaces.

distal end of the camera adapter connected to the PhotonMax CCD camera. System focusing was dually controlled by the focusing optics of the microscope and the camera adapter.

To compare effective imaging speed between the two systems, image intensities were measured given equivalent samples and integration times. For the sample, a 99% Spectralon diffuse reflectance standard was illuminated by the halogen lamp used for diffuse reflectance excitation in the imaging system. A 10 mm x 10 mm square aperture was used to cover the reflectance standard to form a clearly defined sample for both imaging systems. Baseline and diffuse reflectance spectral images were acquired with both systems from 400 to 720 nm in 10 nm increments and a 10 ms integration time per wavelength for the direct-view system and 100 ms integration times for the microscope-based system. Measured spectra were baseline subtracted and corrected for the lamp spectrum and system sensitivity on a pixel-by-pixel basis. The spectra were corrected in a way so as to maintain the mean measured intensity across the spectrum for each pixel. The corrected spectra were then summed, rather than averaged, over the sample aperture such that differences in field of view and the subsequent number of pixels involved would not play a role in the measured intensities. A ratio of the summed spectra was calculated, taking into account the 10-fold difference in integration time between systems. The comparison was repeated for object distances of 8”, 10”, and 12” between the reflectance standard and the front face of the LCTF or the collection lens of the operating microscope.

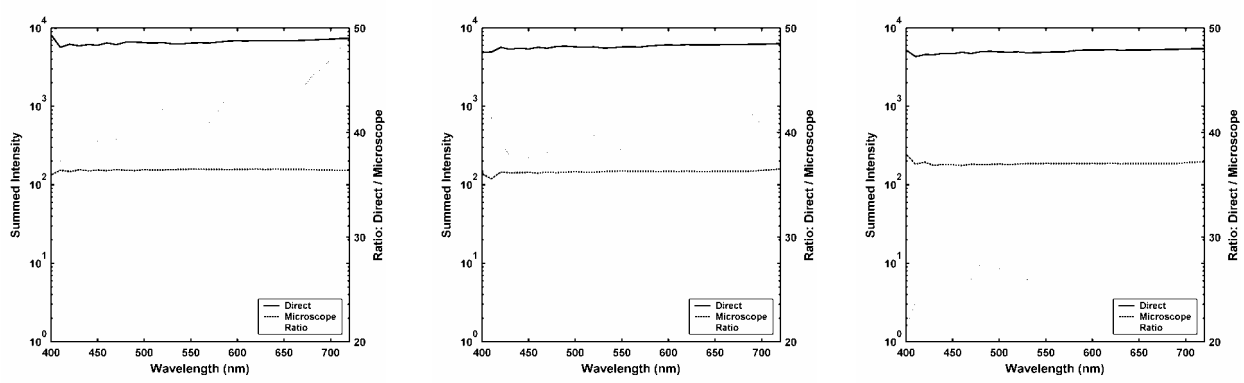

Figure 2. Comparison spectra for the direct-view and microscope-coupled LCTF spectral imaging systems for object distances of (a) 8", (b) 10", and (c) 12".

Results

The corrected, summed spectra for each of the systems as well the ratio between them for each of the object distances are outlined in Figure 2. The corrected spectra for both systems are consistently uniform with wavelength, with coefficients of variation across the summed spectra that vary between 3% and 7.5%. The direct-view imaging system measures summed intensities which are consistently higher than the microscope-coupled system. The direct-view spectra decrease with object distance while the microscope-coupled spectra increases slightly, resulting in a decreased ratio between the two as object distance increases. The mean ratios across the spectral range of interest for the 8", 10", and 12" object distances are 43.2, 39.8, and 27.0, respectively.

Discussion

The spectral uniformity for both systems indicates that the spectral correction procedure properly normalizes for the excitation spectrum of the halogen lamp and the detection sensitivity of the spectral imaging system.

The direct-view spectra decrease in intensity with object distance because the solid angle of the collection lens decreases with object distance. Given a constant aperture size and object distance for the collection lens, the solid angle should vary non-linearly with object distance (d) as $1/d^2$. However, the mean spectral intensities for the three object distances actually vary linearly with *d* (results not shown).

While the intensity ratios decrease with increased object distance, the mean intensities for the microscope-coupled system show no trend with *d*. While the collection solid angle for the microscope-coupled system also decreases with object distance, the optical throughput of the imaging system is more complex than a simple relationship to the collection solid angle. The field of view of the microscope-coupled system is consistently limited by one of the apertures along the light path from the collection lens to the camera. While the square aperture for the sample was inside the field of view of the microscope-coupled imaging system for all three object distances, the effective numerical aperture of the system may be a complex function of the focusing optics on the microscope and camera adapter.

Most importantly, the measured intensities for the direct-view spectral imaging system were consistently 25-45 times greater than equivalent measurements with the microscope-coupled system. Given the fact that the microscope uses a 50/50 beamsplitter to split the collected light between the oculars and the camera port, a two- to three-fold difference between the systems was expected. While that kind of marginal difference in imaging speed could be overcome by the convenience of direct imaging with a microscope-coupled system, requiring *in vivo* autofluorescence image acquisition times to increase 35-fold from 45 seconds to 25 minutes is excessive. For these reasons, a microscope-coupled spectral imaging system is not a reasonable option at this time. However, as mentioned in the future directions, as LCTF, CCD, and excitation source technology improves and depending upon a more efficient interface for microscope coupling, incorporation LCTF spectral imaging directly into the operating microscope design may become feasible in the future.

Some of the reasons for the greater-than-expected intensity ratios between the imaging systems are 1) while the microscope uses a wide collection lens, it uses separate, significantly smaller apertures for each ocular with a beamsplitter along each path, and 2) while we cannot be sure where along the light path the field of view is aperture-limited (rather than array-limited), the bottleneck may occur at one of the apertures along the large distance between the camera port and the camera adapter, resulting in significant loss of light due to spectral imaging system design. Various focal length collection lenses were inserted between the microscope head and LCTF to determine if an extra focusing stage would improve the field of view, but every lens tested resulted in an inability to focus the system on the sample.

Conclusion

Given the current state of LCTF, CCD, and excitation source technology, direct-view LCTF spectral imaging is a more attractive option for clinical implementation, despite the burden of an imaging field of view which is decoupled from the surgical field as viewed through the operating microscope. Hopefully, future advances in spectral imaging technology and/or operating microscope design will allow for direct incorporation of the benefits of spectral imaging diagnosis into neurosurgical operating microscopes without significant loss of imaging speed and quality.